2009

Synthesis and Characterization of Transition Metal and Metal Oxide Nanoparticles Using Dendritic Complexes

Elisabeta Mitran
Louisiana State University and Agricultural and Mechanical College, emitra1@tigers.lsu.edu

SYNTHESIS AND CHARACTERIZATION OF TRANSITION METAL AND METAL OXIDE NANOPARTICLES USING DENDRITIC COMPLEXES

A Dissertation

Submitted to the Graduate Faculty of the
Louisiana State University and
Agricultural and Mechanical College
in partial fulfillment of the
requirements for the degree of
Doctor of Philosophy

in

the Department of Chemistry

by
Elisabeta Mitran
B.S., University of Bucharest, 1995
M.S., University of Bucharest, 1997
May 2010

DEDICATION

This dissertation is dedicated to:

My husband, Cristian Nedelea

and

My son, Gabriel Nedelea

ACKNOWLEDGMENTS

I would like to thank my advisor, Dr. Robin L. McCarley, for giving me the opportunity to work under his guidance and for all his help and support during my graduate studies.

To the McCarley research group, thank you for all of your help. I am glad that I had the opportunity to work with a group of people that are able to get along so well with one another. I wish you all success and happiness in whatever you pursue in life.

Thank you to my committee members, Dr. Barry Dellinger, Dr. Erwin Poliakoff, and Dr. Bin Chen, for all the great and informative discussions during our meetings and for all of your help. I also want to thank the Dean's representative, Dr. Huiming Bao, for giving his time and agreeing to serve on my committee.

To the Dellinger research group, thank you for allowing me to do part of my research in your lab. To Dr. Slawo Lomnicki and Hongyi Wu, thank you for all the advice and guidance in conducting the catalytic reactions research.

I would like to thank my husband, Cristian, for his undying support and love. Thank you for believing in me and making this journey in the USA with me. Thank you for your patience and your support with our son. I sincerely could not have done this without you. Thank you to my son, Gabriel, for being a good boy and always understanding that Mammy has to go to school. I would also like to thank our families for their constant support. I never thought it could be so hard to leave home. I love all of you more than I can express.

I would also like to send a special acknowledgment to all those who helped me in my graduate work here at LSU.

TABLE OF CONTENTS

LIST OF TABLES

LIST OF FIGURES

LIST OF SCHEMES

ABSTRACT

The research in this dissertation focuses on the synthesis and characterization of metal/metal oxide nanoparticles in solution and on surfaces with a high degree of control over size and size dispersity; such well-defined nanoparticles were made using metal ion-dendrimer complexes and silica-supported organometallic dendrimers. The metal oxide-based materials can be used as laboratory surrogates for combustion-generated nanoparticles to assess their role in mediating pollutant formation.

Nickel nanoparticles with low size dispersity were prepared by a dendrimer-ligand-based method employing five generations amine-terminated poly(propylene imine) dendrimer, DAB-Am_n. After coordination, borohydride reduction of Ni(II) ion-dendrimer complexes yielded Ni(0) nanoparticles, as determined by X-ray photoelectron spectroscopy (XPS). The diameter of the Ni nanoparticles (l.85–2.70 nm) was found to be inversely proportional to dendrimer generation and the NH_2:Ni(II) ratio.

Silica-supported iron oxide nanoparticles were prepared by impregnation of silica with ferrocenoyl dendrimers, DAB-$(NHCOFc)_n$, followed by thermal treatment. XPS and thermogravimetric analysis indicated that thermal decomposition at 450 °C in the presence of air results in formation of silica-supported Fe_2O_3 nanoparticles and successful removal of organic materials from the silica surface. Control over nanoparticle diameter (2.50–3.31 nm) was shown to be possible by manipulating the dendrimer generation, calcination temperature, and the metal loading on the silica support. Fe_2O_3/SiO_2 nanoparticles were used as laboratory surrogates in mediating monochlorobenzene decomposition and conversion to byproducts. Surface-mediated reactions of monochlorobenzene with Fe_2O_3/SiO_2 were studied under pyrolytic and oxidative conditions between 300–550 °C. Fe_2O_3/SiO_2 prepared by incipient wetness of silica support with iron(III) nitrate was also studied. The results obtained under pyrolysis conditions indicate

that the Fe_2O_3 nanoparticles promote furans formation and other chlorinated byproducts. Fe_2O_3 nanoparticles obtained from ferrocenoyl dendrimers were found to have higher activity in the production of furans than those catalysts obtained from iron nitrate precursors, with the smallest nanoparticle being the most active. Fe_2O_3 nanoparticles had different properties under pyrolytic and oxidative conditions. Under oxidative conditions iron oxide-mediated monochlorobenzene destruction, rather than the formation of furans and chlorinated byproducts was observed. From a general synthesis point-of-view, my work has significance for and impact on the field of nanoparticle formation and the environment.

CHAPTER 1

INTRODUCTION

1.1 Research Goal and Aims

The goal of my research is to develop a general synthesis method for production of metal and metal oxide nanoparticles with controlled size and composition, using metal ion-dendrimer complexes in solution or on surfaces. These particles can be used as laboratory surrogates for combustion-generated nanoparticles to assess the role of surface-condensed metal oxides in mediating the formation of surface-associated pollutants.

Over the past decade, one of the greatest environmental concerns is the effect of combustion-generated fine particles on human health and the environment. It has been found that the particles with the most demonstrable health impacts are in the nanometer regime.[1-3] Therefore, understanding the conditions under which nanoparticles are formed and the reactions that they catalyze can be used to control their emission and reduce their overall environmental impact.

It is well known that the optical, electrical, magnetic, and catalytic properties of metal nanoparticles are sensitive to their size and shape.[4] As a result of the novel properties of nanomaterials in comparison with bulk materials, the ability to make well-defined nanomaterials that have a very narrow size distribution is an important goal for the catalysis and environmental community. Significant progress has been made to produce spherical nanocrystals with a very low size distribution by using template-based methods. These methods utilize precursors composed of metal ion-containers, such as micelles, dendrimers, and organometallic complexes.[4-6] The reactivity of supported metal oxide nanoparticles is closely related to their size and dispersity. The small size of nanoparticles maximizes the surface area, which plays an important role in their fundamental properties. Therefore, tuning the particle size and size

dispersity provides a possibility to control the catalytic activity of nanoparticles.

This research work describes the synthesis of nanoparticles with a controllable size (less than 3 nanometers) and low size dispersity. Poly(propylene imine) dendrimers (known as PPI or DAB-Am$_n$) were chosen as a template for the preparation of metallic nanoparticles due to their abilities to form metal-ion complexes in solution, and assemble on a number of metal and metal oxide surfaces.[7-10] Nickel metal and iron oxides were selected as transition metal/metal oxides and silica as the supporting surface based on the fact that they are important constituents in the combustion-generated processes for formation of particulate matter.[11-14] Transition metals such as iron and copper are responsible for the biological activity of airborne particles.[15] Because transition metals and their oxides are known to promote formation of polychlorinated dibenzo-*p*-dioxin (PCDD) and dibenzofurans (PCDF) formation,[16,17] the question arises: is it important to know the effects the corresponding nanoparticles have on combustion processes?

The first aim of my research was to synthesize well-defined Ni nanoparticles in solution using a dendrimer-ligand-based method employing amine-terminated poly(propylene imine) dendrimers, DAB-Am$_n$. The dendrimers have -NH_2 functional groups at their periphery that can coordinate Ni(II) from solution. After coordination, chemical reduction of metal ion-dendrimer complexes by sodium borohydride yielded Ni(0) nanoparticles. The size of the nanoparticles was controlled by varying the ratio of metal ion to dendrimer and the generation of the dendrimer (number of periphery –NH_2 groups). The nanoparticles obtained were characterized by UV/Vis spectroscopy, X-ray photoelectron spectroscopy (XPS), and high-resolution transmission electron microscopy (HR-TEM).

The second aim of my research was the synthesis of monodisperse silica-supported iron oxide nanoparticles using organometallic dendrimers. Ferrocenoyl-functionalized poly(propylene imine) dendrimers, DAB-(NHCOFc)$_n$, were used as the precursor for the synthesis of

silica-supported iron oxide nanoparticles. After adsorption of DAB-$(NHCOFc)_n$ dendrimer on the silica support, thermal treatment at different temperatures was used to remove residual organic material and to yield the iron oxide particles. Deposition and activation conditions are very important in preparation of monodisperse nanoparticles. Ideal activation conditions should be forcing enough to remove the dendrimers and mild enough to prevent metal oxide particle agglomeration. The dendrimer precursors permit control over the average particle size, particle size distribution, and monodispersity of nanoparticles on the silica support. In order to address the possible issue of metal oxide particle growth due to agglomeration during formation of iron oxide nanoparticles on silica surfaces, different generations of ferrocenoyl-functionalized dendrimer and different activation temperatures were studied. Less dense populations of the iron oxide nanoparticles on silica surfaces were made by adsorbing the dendrimers from solutions at low concentration (low metal oxide loading). Decomposition of the supported ferrocenoyl-modified dendrimers was investigated by thermogravimetric analysis (TGA) and XPS. The sizes of the resulting nanoparticles were determined by HR-TEM and their oxidation state by XPS.

The ultimate aim of this research was to assess the role of silica-supported iron oxide nanoparticles in mediating the formation of surface-associated pollutants from pyrolysis/combustion of monochlorobenzene. The combustion experiments were carried out under pyrolytic and oxidative conditions using a system for thermal diagnostic studies (STDS). The byproducts formed by monochlorobenzene decomposition in the temperature range 300–550 ºC, for 5 min reaction time, were identified by gas chromatography-mass spectrometry (GC-MS) that was interfaced in-line with the thermal reactor. It was found that iron oxides nanoparticles promote formation of furans versus dioxins.

The methods described in this dissertation allow for synthesis of metal/metal oxide

nanoparticles in solution and on surfaces with exquisite control over size and size dispersity. To date, there are only a limited number of methods that allow for such outcome.[9,18,19] From a general synthesis point of view, my work also has significance for and impact on the field of nanoparticles formation, as it is general in nature.

1.2 Dendrimers in Synthesis of Metal and Metal Oxide Nanoparticles

Dendrimers have intrinsic properties, such as regular and highly-branched, three-dimensional architecture, narrow size distribution, uniform dense terminal functional groups at high generation number, and porosity, that make them very useful materials today in nanotechnology and nanoscience.[20-22] They are produced in an iterative sequence of reaction steps, either divergent or convergent, in which each additional reaction leads to a higher generation dendrimer.[21,22] In the divergent approach, the dendrimer is built starting from the central core out to the periphery.[21,22] In the convergent approach the synthesis starts by assembling the periphery groups around the central core.[21,22]

Poly(propylene imine), PPI, dendrimers were first synthesized by Vögtle et al.[23] in 1978, by the divergent method. They were able to synthesize only generation one and two dendrimers. Later, in 1993, two research groups, Wörner and Mülhaupt[24] and de Brabander-van denBerg and Meijer,[25] modified the Vögtle approach to synthesise PPI dendrimers up to five generations in size. The PPI dendrimer is composed of a diaminobutane (DAB) core that is extended with propylene imine units, as shown in Scheme 1.1. These dendrimers are termed DAB-Am$_n$, where *n* indicates the number of primary amine groups at the periphery. The repetitive reaction sequence in the synthesis of DAB-Am$_n$ dendrimer involves a Michael addition of two equivalents of acrylonitrile to a primary amine, followed by hydrogenation of the nitrile groups to primary amines.[26]

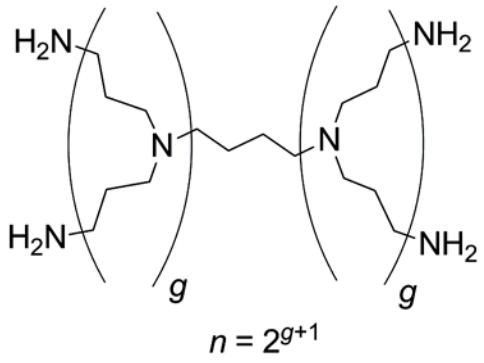

Scheme 1.1 Generation *g* DAB-Am$_n$ dendrimer

DAB-Am$_n$ dendrimers are available up to generation five, and the number of -NH_2 functional groups on the dendrimer surface (periphery) increases exponentially as a function of generation (Table 1.1), resulting in geometrical change from an open structure for lower generation to a close-packed spherical structure for higher generations. The dimension of the dendrimers, as determined by small-angle neutron scattering (SANS) and viscosimetry, shows a linear increase with the generation number.[27]

Table 1.1 Physical characteristics of DAB-Am$_n$ dendrimers.

Dendrimer generation	Number of primary amine groups	Number of interior tertiary amines	Molecular weight (g mole^{-1})	Radius of gyration (nm)[27]
1	4	2	316.5	0.44
2	8	6	773.3	0.69
3	16	14	1686.8	0.93
4	32	30	3513.9	1.16
5	64	62	7168.1	1.39

Dendrimers are able to act as hosts for a variety of ions and molecules because of their three-dimensional structure and multiple internal and external functional groups. Dendrimers can act as hosts for metals, with coordinating centers on the periphery, interior or throughout all layers.[20] The driving force for encapsulation of various guests within dendrimers can be based on diverse interactions such as electrostatic, complexation reaction, steric confinement, and weaker forces like van der Waals, hydrogen bonds, and hydrophobic forces. A polar protic

solvent interacts favorably with the dendrimer through intermolecular hydrogen bonding, promoting the formation of an extended, unfolded conformation.[26] Due to the fact that the dendrimers have a variety of reactive groups along the periphery, it is possible to add almost any desired moiety as end groups and obtain dendrimers with desired structural characteristics.

The synthesis of nanoparticles using dendrimers can be realized by their formation either inside the dendrimer (intradendrimer encapsulated nanoparticles) or outside surrounded by many molecules of dendrimer (interdendrimer-stabilized nanoparticles).[28] Metal-containing dendrimers have been used for a number of different nanofabrication methods, because they combine the structural features of dendrimers with the function of metals.[28,29] Poly(propylene imine) and poly(amidoamine), PAMAM, dendrimers are the most used templates in nanoparticle synthesis. Both Crooks' and Esumi's groups demonstrated the versatility of PAMAM dendrimers in the synthesis of metallic (Pt, Pd, Cu, Ni, Au, Ag, Ru, Fe) and bimetallic (PdAu, PdPt, AuAg) nanoparticles in solution.[19,29-38] The first step of the synthesis typically involves the complexation of metal ions with the functional groups of the dendrimer in either the periphery, interior, or through all layers. After complexation, an excess of reducing agent (usually $NaBH_4$ or hydrazine) is added to the solution (with vigorous stirring), resulting in the formation of zerovalent metallic nanoparticles. Knecht et al.[35] prepared Ni nanoparticles with diameters smaller than 3.0 nm (average of 55 and 147 atoms) by using sixth-generation PAMAM dendrimers partially functionalized on their periphery with alkyl groups. But, there was no demonstration of nanoparticle size control by use of different dendrimer generation or other parameters.

DAB-Am$_n$ dendrimers have been shown to form well-defined stoichiometric complexes with a variety of transition metal ions, where the subunits of the periphery can serve as strong tridentate coordinating sites.[7,8,39] The possibilities are rich and diverse, as it has been shown, that

DAB-Am$_n$ dendrimers can bind metal ions to their peripheral primary amines, and a variety of metal nanoparticles, including those of Cu,[9,40] Ni,[40] Co,[40] Ag,[38,41-44] Au,[36,37,43-48] Pt,[38,44] Pd,[38] Fe[49] and metal oxide nanoparticles (SnO_2)[50] have been synthesized. The McCarley group has synthesized well dispersed (1.98 to 3.71 nm diameter) Cu(0) nanoclusters[9] using an approach wherein the metal ions are first complexed with the dendrimer, and then reduced by borohydride to form metallic nanoclusters. It was found that the complexation of Cu(II) by DAB-Am$_n$ dendrimers in methanol at room temperature occurs in a site-selective way wherein dipropylenetriamine (dpt) end groups of dendrimer act as very strong coordinating units. A significant decrease in nanoparticle size was obtained by tuning the dendrimer generations and the ratio of primary amines to Cu(II) ions in the dendrimer precursor.

The same conclusion, that the size of nanoparticles can be controlled by the molar ratio of dendrimer to metal, was reported by Luo[46] for the synthesis of gold nanoparticles. In this study gold nanoparticles were prepared by exposing a DAB-Am$_{16}$-$HAuCl_4$ aqueous solution to sunlight without any other reducing agent. The formation of gold nanoparticles in the Luo study takes place by a redox reaction between dendrimer and Au(III).[46] In solution the dendrimer becomes protonated and facilitated electron transfer from Au(III) to the amine groups of the dendrimer, and the sunlight accelerated the electron transfer rate. The increase of the molar ratio (dendrimer:Au from 1:1 to 16:1) leads to a decrease in particle size (from an average size of 10 nm to 2 nm) and a decrease in particle size distribution. In a similar way, Sun and Luo[47] synthesized gold nanoparticles from DAB-Am$_{16}$-$HAuCl_4$ in aqueous solution by microwave radiation. They were able to control nanoparticle size (3–7 nm in diameter) by varying the dendrimer-metal molar ratio. Esumi and co-workers prepared gold nanoparticles by wet chemical reduction with $NaBH_4$[36] and laser irradiation.[37] They were interested in comparing both DAB-Am$_n$ dendrimers and PAMAM dendrimers in the synthesis of gold nanoparticles and

their catalytic activity for the reduction of 4-nitrophenol. The results revealed that the Au nanoparticles are between 2–4 nm in diameter for both dendrimers, and they found no dependence of generation number on the gold particle size.[36] They irradiated the gold-dendrimer nanocomposites by laser at 532 nm.[37] It was found that in the case of PAMAM dendrimers the gold nanoparticles increase in size with the laser irradiation time, while for the DAB-Am$_n$ dendrimers the gold nanoparticles do not change in size by laser irradiation. This fact was attributed to the formation of densely covered DAB-Am$_n$ dendrimers on the nanoparticle surface. An interesting observation made in their work is that the concentration of the dendrimer required to obtain stable Au nanoparticles is different depending on the dendrimer generation used (more dendrimer is needed for lower generations than for the higher generations). These synthesized gold nanoparticles exhibited activity for the reduction of 4-nitrophenol, but with a higher rate for those made from the PAMAM than those gold nanoparticles made from DAB-Am$_n$ in the lower generation dendrimers. In the case of higher dendrimer generations, no distinct difference in the rate constant was observed.

In other works, Esumi et al.[38,44] reported the synthesis of metal (Ag, Pt, and Pd) nanoparticles using DAB-Am$_n$ or PAMAM dendrimers. The synthesis was carried out in aqueous solution by borohydride reduction of metal salt-dendrimer mixtures. These experiments lead to similar conclusions as observed for the Au nanoparticles discussed above,[36] in that the particle size is independent of the dendrimer generation as well as the concentration of both types of dendrimer. The particle sizes for Ag nanoparticles (5.6–7.5 nm in diameter) were higher than for Pt and Pd nanoparticles (1.2–1.6 and 1.6–2.0 nm), and this was explained by the weak interaction between Ag and dendrimer molecules.[38] Ag nanoparticles do not present any activity in the reduction of 4-nitrophenol, while the 4-nitrophenol reduction rate constants were significantly higher when DAB-Am$_n$ dendrimer–Pt and –Pd nanoparticles were used as catalysts

than in the case with PAMAM dendrimer–Pt and –Pd nanoparticles.

In 2005, Esumi and co-workers prepared Au and Au/Ag nanocomposites by changing the chemical reduction method to UV irradiation in the presence of benzoin.[43] It was found that nanoparticle size can be tuned by changing the concentration of dendrimer and benzoin and the size is not influenced by the type of dendrimer used (PAMAM or DAB-Am$_n$). TEM and DLS techniques were used to measure the size of gold-dendrimer nanocomposites, and they found that the size of nanocomposites measured by DLS is two to four times bigger than that measured by TEM.[43] The authors explained this outcome by the fact that the gold nanoparticles are covered by multilayers of dendrimers. On the contrary, Hayakawa et al.[45] found that the dendrimers are adsorbed on Au nanoparticles as a monolayer, when they prepared gold-dendrimer nanocomposites by laser irradiation. TEM, in combination with DLS and UV-Vis, allowed the conclusion to be made that the diameters of gold nanoparticles tend to decrease with an increase in the dendrimer concentration (PAMAM or DAB-Am$_n$).[45]

Sun et al.[42] prepared silver nanoparticles by simply heating aqueous solutions containing DAB-Am$_{16}$ and $AgNO_3$, without any reducing agent. The DAB-Am$_{16}$ dendrimer serves both as a reducing and protective (anti-agglomeration of nanoparticles) agent. The heat treatment accelerates the electron transfer rate from dendrimer to Ag(I), resulting in the formation of silver nanoparticles. Results from XPS and XRD revealed that the nanoparticles are in coexistence with Ag and Ag_2O. It was found that temperature influences the size of the resulting Ag nanoparticles. From TEM experiments it was shown that there is an increase in the average diameter from 20 to 25 nm with an increase in the temperature from 60 to 100 °C. Au nanoparticles were prepared in a similar way, and it was found that particle size and the nucleation and growth kinetics can be tuned by changing the molar ratio of dendrimer to gold.[48]

In 2007, Luo and Sun[41] used a microwave-based thermal process to prepare dendrimer-protected Ag nanoparticles. An interesting observation made in this study was that by changing the molar ratio of DAB-Am_{16} dendrimer to Ag, not only the size of nanoparticles is changed, but also the shape. As observed in TEM experiments, particle size decreases from an average diameter of 25 nm to 10 nm by increasing the molar ratio from 1:20 to 9:20. At a molar ratio of 3:20, both Ag nanorods and Ag nanoparticles were obtained.

Vohs et al.[49] prepared dendrimer encapsulated Fe catalysts by borohydride reduction of a DAB-Am_{32}-Fe(III) complex in ethanol solution. After separation by centrifugation, the air-dried dendrimer encapsulated Fe samples were used as catalysts for the growth of carbon nanotubes. Chai and co-workers[40] used the same borohydride reduction of DAB-Am_{16} dendrimer-metal complexes to prepare bimetallic (Cu/Ni and Cu/Co) nanoparticles.

Juttukonda et al.[50] compared the use of PAMAM and DAB-Am_n dendrimers, and poly(ethyleneimine) hyperbranched polymers in the synthesis of SnO_2 nanoparticles. An aqueous solution or ethanolic solution of sodium stannate was mixed with the dendrimer/polymer host in a dendrimer:sodium stannate molar ratio of 1:4, folowed by bubbling of gaseous carbon dioxide for 30 min. SnO_2 nanoparticles with diameters between 2.5 and 6 nm (the smallest nanoparticles were obtained with the DAB-Am_n dendrimer) were formed, as shown by TEM and EDS experiments.

DAB-Am_n–modified dendrimers have also been used to prepare metal nanoparticles. Niu and Crooks synthesized dendrimer-encapsulated metal nanoparticles (Cu and Pd) using hexanoyl or palmitoyl-modified DAB-Am_n dendrimers.[51] The main function of the alkyl groups on the modified dendrimers was to solubilize the dendrimer in non-aqueous solution. Encapsulated Cu or Pd nanoparticles were synthesized by introducing first the metal into the dendrimer interior, followed by chemical reduction with $NaBH_4$. In another work, Pd nanoparticles (2–3-nm

diameter) were prepared by chemical reduction of Pd(II) encapsulated into DAB-Am$_n$ dendrimers covalently functionalized with perfluorinated polyether chains on the periphery.[52] These nanoparticles were effective catalysts for Heck coupling reactions. Ooe et al.[53] used triethoxybenzamide-terminated DAB-Am$_n$ dendrimers to prepare Pd nanoparticles of 2–3-nm diameter. Pd(II) was first introduced into the interior of functionalized dendrimer and then reduced with KBH_4 to yield Pd(0) nanoparticles encapsulated within dendrimers. The Ooe-prepared dendrimer-Pd nanoparticles are effective catalysts for substrate-specific hydrogenation of polar olefins.

A combination of characterization techniques (HR-TEM, UV-VIS, DLS, and AFM) were used by Pietsch and co-workers[54] to characterize Au nanoparticles obtained by chemical reduction or auto-reduction of maltose-modified DAB-Am$_n$ dendrimer-Au complexes. It was found that autoreduction (when glycodendrimers are used as reducing agents at room temperature) leads to large Au nanoparticles (1–10 nm in diameter). When $NaBH_4$ was used as reducing agent, small Au nanoparticles with diameters less than 3 nm were obtained. Their results are consistent with the conclusion that the particle size and size distribution can be controlled by the dendrimer generation, with the formation of smaller nanoparticles and narrower size-distributions obtained with higher dendrimer generations.

CdS nanoparticles were prepared by Donners et al.[55] using DAB-Am$_{16}$ dendrimer functionalized with oligo(phenylene vinylene) groups. This synthesis involves the mixing a equimolar amount of cadmium chloride with oligo(phenylene vinylene)-modified dendrimer under inert atmosphere for 30 min, followed by slow addition of hydrogen sulfide or sodium sulfide. The results were compared with the CdS nanoparticles obtained with DAB-Am$_n$ dendrimer functionalized with alkyl groups. It was found that these modified dendrimers do not act as molecular containers but function more as headgroup polymerized surfactants. For

example in chloroform solution, spherical CdS nanoparticles with a controlled size of 3 nm were formed, whereas in a chloroform/methanol mixture, plate-like CdS structures were formed. Furthermore, at the air-water interface, CdS particles were formed with diameters of 20–60 nm organized into a leaf-nerve structure.

Dendrimers can also be used to synthesize supported metal/metal oxide nanoparticles. Supported metal oxide nanoparticles are generally prepared via impregnation of a dendrimer-templated metal onto different supports or sol-gel methods, followed by thermal treatment to yield the metal oxide.[10,56-62] Impregnation of metallic nanoparticles on the surface of solid supports can be achieved by one of the two following methods. In the first method, the dendrimer-encapsulated nanoparticles are first prepared in solution and then chemisorbed onto the substrate surface.[56-59] In the second method, dendrimer molecules are first adsorbed onto the surface of a solid support, then the dendrimer–nanoparticles are prepared directly on the support.[56,62] After impregnation, removal of the dendrimer template is achieved by various thermal treatments in either an oxidizing or reducing environment. A crucial parameter in the synthesis of supported-metal oxide nanoparticles is the activation temperature because the removal of the dendrimer precursor by calcination at high temperatures may result in nanoparticle sintering (diffusion of nanoparticles). It is important to find a temperature sufficiently high so as to remove the dendrimer but not too high to cause growth of the nanoparticles. Deutsch and co-workers studied the decomposition and activation of Pt-dendrimer nanoparticles on silica support by infrared spectroscopy.[59] In-situ monitoring experiments led to the conclusion that oxidation at 425 °C was the most successful temperature for removing PAMAM dendrimer fragments from the Pt surface. Thermogravimetric analysis (TGA) can also be used to monitor the removal of dendrimer.[58] The specific activation conditions likely depend on the metal and support, the metal loading, dendrimer loading and

metal:dendrimer ratios, but 400–500 °C appears to be a good interval of temperature to remove the dendrimer.

Larsen and co-workers prepared Cu-CuO nanoparticles by a sol-gel method using DAB-Am_{64} dendrimer as both chelating and pore-templating agent.[10,63] In a similar way, Rogers et al. prepared mesoporous titanosilicate and vanadosilicate oxidation catalysts.[61] Using a combination of characterization techniques (TGA, BET, PXD, SEM), they showed that the metals are uniformly distributed throughout these silicates, and after calcination at 560 °C, the dendrimer templates are completely removed.

Supported Fe_2O_3 nanoparticles with controlled sizes have been prepared previously using a dendrimer template-based approach.[64-66] Amama et al. used PAMAM dendrimers to deliver complexed Fe(III) ions to different substrates by dip coating.[65,66] The impregnated substrates were then calcined at different temperatures so as to obtain a monolayer of Fe_2O_3 nanoparticles. Plasma-enhanced chemical vapor deposition (PECVD) with the Fe_2O_3 nanoparticles afforded the formation of carbon nanotubes. Their conclusion was similar to that obtained by Choi et al., that silica-supported iron oxide nanoparticles with narrow diameter (1–2 nm) were efficient catalysts for the growth of single-walled carbon nanotubes.[64]

It may be concluded that by using dendrimers, it is possible to prepare nanoparticles in solution and on surface supports with a high degree of control of metal particle size, composition, dispersity, and solubility. But, none of previous works demonstrated that tunable-size nanoparticles with low size dispersity can be achieved by chemical reduction of five different generations of dendrimer. No relationship was found between the primary amine:metal ion ratio in the precursor. In only one reported case for the synthesis of Ni nanoparticles using dendrimers,[35] two different sized Ni nanoparticle (0.8 and 1.2 nm in diameter) were prepared, but using a single generation of partially modified PAMAM dendrimer and two different metal ions

PAMAM ratios.

1.3 Synthesis of Metal and Metal Oxide Nanoparticles

The first step in the formation of nanoparticles involves the process of precipitation of a solid phase from solution. The ideal precipitation process consists of a temporally discrete nucleation followed by a slower controlled growth on the existing nuclei. The nucleation and growth of metal nanoparticles is very sensitive to the reaction conditions. In order for the nucleation to occur, the solution must be supersaturated either by rapid addition of reagents or by dissolving the solute at higher temperature followed by cooling.[4] Nucleation in solution occurs due to the driving force of the thermodynamics, as the supersaturated solution is not energetically stable. In the classical nucleation theory, the free energy of nucleus formation (ΔG_{nuc}) contains two competing terms: one negative, for the favorable formation of bonds in the nucleus, and one positive due to the new surface created.[67] The expression for the free energy of spherical particles is given in Equation (1.1):

$$\Delta G_{nuc} = -\frac{4}{3}\pi r^3 \left|\Delta G_v\right| + 4\pi r^2 \gamma \qquad \textbf{Equation 1.1}$$

were r is the radius of the cluster, ΔG_{v} is the difference in bulk free energy per volume between the old and new phase, and γ is the surface free energy per unit area. The free energy of nucleus has a maximum value at a particular radius, called the critical radius, r^*. For a nucleus with radius smaller than r^*, growth is unfavorable and the nucleus will dissolve, while a nucleus with a radius larger than r^*, growth is favored.[4,67] After the formation of nuclei in solution, the growth process occurs via molecular addition. If the nucleation time is very short followed by a temporally-distinct self-sharpening growth process, nanoparticles with uniform sizes (low size dispersity) are obtained. In many systems, a second growth process occurs, called Ostwald ripening, wherein the larger particles continue to grow at the expense of the smaller particles (dissolution), because of the high surface energy of the small particles.[68] Particles can also grow

by aggregation with other particles, which means that after they grow to a stable size, they will grow again by combining with smaller unstable nuclei.[4]

The synthesis of metal nanoparticles has been studied for over a century, with the main goal being the ability to prepare nanoparticles with very small sizes. The synthetic process must be controlled in such a way that the prepared nanoparticles have the following characteristics: very narrow size distribution, low-size dispersity, identical shape and chemical composition. It is well known that nanoparticles tend to agglomerate to form larger particles. In order to prepare stable and low-size dispersity nanoparticles, collisions between primary particles must be arrested during the reaction.[4] This can be realized by either using surface protecting reagents or quickly cooling the solution. The preparation methods used to generate metal nanoparticles can be grouped into two categories: homogeneous nucleation from liquid or vapor and heterogeneous nucleation on substrates. In the solution method, the established methods involve an aqueous reduction of metal salts in the presence or absence of stabilizing agents. The nanoparticles can be prepared without using any stabilizers. However, control of particle size distribution is limited in this case. The purpose of stabilizers is to mediate nanoparticle growth and to prevent agglomeration and precipitation. Various types of precursors (such as metal chloride, metal acetate, organometallic), reducing reagents (e.g. $NaBH_4$, H_2, hydrazine, polyols), stabilizing agents (such as surfactants, polymers, dendrimers, ligands) have been used to promote and control the reduction, initial nucleation and the subsequent growth of initial nuclei.[4,5,69] Although stabilizing agents play a very important role in the synthesis of metal nanoparticles in solution, the active surface sites of nanoparticles are sometimes blocked by these agents.[70] The main problem to be solved is the removal of stabilizing agents after nanoparticle preparation without altering their structure and properties.

Other methods used to prepare metal and metal oxide nanoparticles in solution are

thermal decomposition, radiation, sol-gel processes, co-precipitation, and electrochemical routes.[4,5] For example, iron oxide nanoparticles with diameters ranging from 4 to 10 nm were prepared by thermal decomposition of metal cupferron complex in hot surfactants.[71] In an attempt to control nucleation and growth of iron oxide nanomaterials, Casula et al.[72] used a delayed nucleation method, in which the initial iron pentacarbonyl precursor is co-injected with an oxidizer (*m*-chloroperoxybenzoic acid) into hot organic solvent containing a fatty acid. In this method, iron pentacarbonyl is slowly converted to an active species, followed by a brief period of nucleation when the concentration of the active species increases.

Heterogeneous nucleation is generally used for the synthesis of supported metal and metal oxide nanoparticles. Traditional routes to prepare supported metal nanoparticles involve impregnation of metal salts onto supports with high surface area, followed by various thermal activation steps.[73,74] These methods typically result in little control over particle size, composition and reproducibility. Several strategies to overcome these problems have been proposed by many researchers, such as the two-step impregnation and the use of protective agents (microemulsions, dendrimers, and encapsulating agents) that offer control and prevent particle agglomeration on the support.[56,75-78] In order to control nucleation and particle growth, Che and co-workers used a two-step procedure in the synthesis of silica-supported Ni catalysts.[75,79] In the first step, nickel "seed" nuclei were prepared by impregnation of nickel nitrate on silica, followed by washing or by ion-exchange and then calcination. In the second step, the silica with nickel nuclei was impregnated again with different concentrations of nickel nitrate. The particle sizes prepared by this method depended on the respective amounts of nickel introduced at each step. The authors proposed a mechanism where particle growth on the nickel nuclei takes place after impregnation and during the drying step of the samples at 90 °C via condensation reactions between the two types of nickel (nickel in strong interaction and nickel in

weak interaction).

The fabrication of metal and metal oxide nanoparticles of low size dispersity can be achieved through many different methods, in solution or on supports, or in gas, liquid, or solid media. In general, two types of templates have been used to prepare metal/metal oxide nanoparticles: a soft template (e.g. surfactants, dendrimers) and a hard template (mesoporous solids, such as silica, MgO, carbon materials).[30,80-83] In the following paragraphs, several examples will be discussed to illustrate the methods used in the fabrication of Ni nanoparticles in solution and iron oxide nanoparticles on solid supports from the last 10–15 years.

1.3.1 Literature Review on Synthesis of Ni Nanoparticles

Ni nanoparticles have been extensively studied in the last decade, because of their current and potential applications in many areas, such as catalysis, conductive and magnetic materials, optoelectronics, and information storage.[84-87] As their properties (magnetic, optical, electronic, and chemical) are dependent on the size and composition, it is important to develop a facile method to synthesise low-size dispersity nanoparticles with different sizes to meet different demands.[4] The preparation of stable Ni metal nanoparticles is relatively difficult because they are easily oxidized, and sometimes alloys are formed instead of pure Ni. Many different factors affect the characteristics of Ni nanoparticles, such as the type of precursor and reducing agent, the temperature, the atmosphere, and the presence of stabilizers. The methods presented in the following sections are discussed in terms of nanoparticle morphology (size, shape, and dispersion), crystalinity, and their catalytic performance in different reactions.

1.3.1.1 Surfactant-Free Ni Nanoparticle Synthesis

Synthesis of Ni nanoparticles can be achievd by simply reducing the Ni salt in aqueous or non-aqueous solution with a reducing agent. For example, Wu and Chen[88] prepared crystalline Ni nanoparticles, in the absence of soluble polymer surfactant, by chemical reduction of $NiCl_2$

with hydrazine in ethylene glycol and an appropriate amount of NaOH. The nanoparticles obtained at 60 °C under inert atmosphere had low size dispersity and an average diameter of 9.2 nm, as shown by TEM. The authors explained that ethylene glycol might act as a protective agent forming a layer via the interaction of the OH groups of the ethylene glycol with Ni nanoparticles, preventing particle aggregation. It was found that the hydrazine/Ni(II) ratio influenced nanoparticle size, resulting in a decrease with increasing the ratio up to 12. At higher ratios, no change in nanoparticle size was observed. Similarly, Bai et al.[89] prepared pure metallic Ni nanoparticles by a modified hydrazine reduction route in ethanol, at different temperatures. They found that ethanol plays a complementary reducing role, leading to nanoparticles with a smooth surface and uniform size (around 50 nm, as determined by field-emission scanning electron microscopy) when the synthesis was carried out at 180 °C. By decreasing the temperature from 180 °C to 60 °C, the size and shape of the particles changed (from smooth 50 nm diameter particles to 150 nm diameter spiky particles). In another work, Duan and Li[90] obtained Ni nanoparticles by spontaneous autocatalytic reduction in alcohol-water solution. Contrary to the other hydrazine reduction experiments described by Bai,[89] this reduction took place at room temperature, leading to crystalline Ni nanoparticles with an fcc structure. TEM observation showed that the Ni nanoparticles obtained (size distribution 30–40-nm diameter) were "soft" aggregates of individual crystalline Ni particles, and they can be broken up by the electron beam in the TEM instrument. Hald et al.[91] reported preparation of spherical Ni nanoparticles with average diameters of 40 to 60 nm by combining two methods, namely the use of a continuous flow supercritical reactor and hydrazine reduction of $NiSO_4$. The SEM images revealed that the size of nanoparticles can be tuned from 60 to 40 nm by decreasing the temperature from 350 to 150 °C. This synthetic method is fast and high yielding (being able to prepare ~1.5 g Ni nanoparticles per hour), inexpensive and presents the advantage that the

reaction parameters (pressure, temperature, flow rate and reactant concentrations) can be changed continuously to control the size of the nanoparticles.

Ni nanoparticles with different morphologies (spherical, star-shaped, and flower-shaped) were obtained by Libor and Zhang[92] by reducing nickel acetate with hydrazine in aqueous solution. They were able to control the crystal shape by controlling reaction temperature and aging time, which affect crystal nucleation and growth. Similarly, Ni et al.[93] prepared crystalline Ni nanoflowers by hydrazine reduction of a mixture of nickel chloride and dimethylglyoxime. An interesting observation made in their work was that spherical particles were formed first (flower centers), and petals grew radially from the spherical particle surfaces, as shown by field-emission scanning electron microscopy and TEM. This control of nanocrystal shape can be explained by the fact that two chemical reactions are matched. The production of spherical nanoparticles that occurs first, results from the $Ni(N_2H_4)_3^{2+}$ complex; these particles act as nucleation sites for the growth of sword-like petals that originate from reduction of the $Ni(dmg)_2$ complex. The size of the nanoflowers can be tuned by adjusting the molar ratio of these two complexes. The crystalline Ni nanoflowers exhibit an enhanced coercivity (173.2 Oe) and a decreased saturation magnetization (*Ms*) value (30.8 emu g^{-1}) as compared with that of bulk Ni materials.

Roy et al.[94,95] prepared Ni nanoparticles by reducing Ni ions with $NaBH_4$ in aqueous media, at room temperature and ambient atmosphere. The nanoparticles obtained were Ni in a tetragonal crystal structure (as determined from X-ray diffraction patterns) when the samples were annealed in air at different temperatures (due to the presence of interstitial oxygen atoms). When the samples were annealed in argon or hydrogen gas at 973K, the X-ray diffraction pattern indicated an ordering of Ni in the nanocrystal as an fcc structure. Due to the existence of both paramagnetic and ferromagnetic properties, the authors concluded that the nanoparticles present

a core-shell structure, where a Ni core is ferromagnetic and the NiO shell is antiferromagnetic/paramagnetic. Furthermore, the magnetic properties changed from paramagnetic to ferromagnetic with increasing the $NiCl_2$ concentration at room temperature.[95] The same conclusion that the Ni nanoparticles are in a core-shell structure of Ni-NiO with different magnetic properties, was arrived at by Nayak et al.[96] when they used a combination of borohydride chemical reduction and gaseous reduction. First, the Ni nanoparticle precursor was reduced with $NaBH_4$ in aqueous media, followed by gaseous reduction with H_2-Ar (2%-98%) at different temperatures. TEM micrograph revealed nanoparticles with different shapes (spherical, ellipsoidal, cylindrical, hexagonal, and polyhedral) and sizes (ranging from 20 to 120 nm in diameter) indicating that the growth of nanoparticle was not controlled. Kudlash et al.[97] were able to prepare low-size-dispersity Ni nanoparticles (average size between 2 and 6 nm) by the interphase reduction of Ni oleate precursor with $NaBH_4$ (in hexane-water system), without any protective agent. In this synthesis it was important to keep the two phases separated (not intermixed). The authors claim that oleic acid (in hexane dispersion) or sodium oleate (in aqueous dispersion) acts as an unusual surfactant, forming a protective layer around the particle surface preventing particle aggregation. By analysis of X-ray diffraction pattern, the resultant Ni nanoparticles adopted a crystalline metallic Ni fcc structure, with some admixture of nickel boride. It was found that the average diameter of Ni nanoparticles decreased with increased $NaBH_4$ concentration (from 5- to 20-fold moll excess) and approached a nearly constant value when greater than 20-fold excess.

Liu et al.[98] prepared Ni-B amorphous alloy nanoparticles by borohydride reduction of nickel acetate in organic/aqueous solvent mixtures (methanol or ethanol in water (1:1)). Different reaction parameters (reduction temperature, gas atmosphere, stirring speed, and solvent) were studied, and the results indicated that the average particle size changes drastically

(10–50-nm diameter) upon changing these parameters. XPS investigations showed that Ni-B alloy nanoparticles were obtained under all conditions investigated. They also studied the catalytic activity of these nanoparticles and found that the particles with the smallest size (10–20-nm diameter) present higher activity for hydrogenation of *p*-chloronitrobenzene.

In the view of these results, it may be concluded that the main advantage of reduction without protective agents is that a large amount of nanoparticles can be synthesized using relatively inexpensive reactants. However, the control of particle size distribution is limited by the agglomeration process that occurred during particle synthesis.

1.3.1.2 Surfactant-Templated Ni Nanoparticle Synthesis

The use of surfactants for the synthesis of metallic nanoparticles has received considerable attention because of the ability of surfactants to self-assemble into well-defined structures. Surfactants are molecules that possess both polar and non-polar moieties (a polar hydrophilic head and a hydrophobic hydrocarbon chain).[99] The shape of the surfactant plays a crucial role in the final assembly formed, which in turn influences the shape of the nanomaterial. For example, if the surfactant molecule has a very large polar head and a small chain, normal micelles are formed, while when the surfactant has a small polar head and branched hydrocarbon chains, spherical reverse micelles are formed (called water-in-oil droplet). The size of reverse micelles increases linearly with the amount of water added in the system. Upon adding more water or oil, a new phase transition occurs, and the shape and dimension of the aggregate changes, thereby leading to channels or cylinders.[99] The synthesis of nanocrystals by using colloidal solutions was pioneered by Pileni, who showed that crystalline nanoparticles can be obtained by controlling the reaction parameters.[69] It was demonstrated that the surfactant template is not the only parameter controlling the nanocrystal morphology; another key parameter is the selective adsorption of surfactant molecules during crystal growth.[69]

The number of papers dealing with surfactant-templated synthesis of Ni nanoparticles has increased in recent years. Once the right microemulsion conditions are obtained, nanoparticle synthesis consists of mixing two water-in-oil microemulsions, one containing the salt of the metal and the other containing the reducing agent.[80] After mixing the two microemulsions, the interchange of the reactants occurs as a result of the continuous coalescence and decoalescence process, resulting in nanoparticles surrounded by water and stabilized by surfactant. The nucleation and growth takes places inside of the droplets, resulting in the control of final size of the particles. The most commonly used surfactants in Ni nanoparticle synthesis are hexadecylamine (HDA),[100,101] trioctylphosphine oxide (TOPO),[101-103] sodium succinate,[104] sodium dodecyl sulfate (SDS),[97] oleic acid,[70,97,105-107] cetyl-trimethyl-ammonium bromide (CTAB),[108-112] sodium dodecylbenzene sulfonate (SDBS),[113] sodium bis(2-ethyl-hexyl)-sulfosuccinate (AOT),[114-116] trioctylphosphine (TOP),[70,102,106,107,114] trioctylamine (TOA),[70,106] tetrabutylammonium bromide (TBAB),[109] tetraethylammonium bromide (TEAB)[109], hexadecylamine,[117] 1-adamantanecarboxylic acid (ACA).[103]

The synthesis of Ni nanoparticles in the presence of surfactants has been done by reduction of Ni salts with different reducing agents such as sodium borohydride, hydrazine, polyols, and hydrogen gas. These methods will be discussed with regard to reducing agent type in the following pages.

- **Preparation of Ni Nanoparticles by Reduction with $NaBH_4$**

Among the various synthetic techniques, chemical reduction with sodium borohydride is widely used for the preparation of Ni nanoparticles. However, the chemistry of the borohydride reduction is complex and not fully understood. In 1994, Glavee et al.[118] performed a significant amount of work to determine the general trends in borohydride reduction of first-row, transition-metal ions in aqueous and nonaqueous media. It was found that the mechanism and

the end product depend drastically on the reaction conditions such as aqueous or nonaqueous media, inert or ambient atmosphere, all of which determine if the resulting material is a metal or a mixture of metal, metal oxide and metal borides.[94,118]

The control of nanoparticle size by the use of a surfactant template was demonstrated by Hou et al.[100] Low-size-dispersity Ni nanoparticles (3.7 nm diameter) were prepared by reduction of Ni(II) with $NaBH_4$ in the presence of hexadecylamine (HDA), which acts as a stabilizer and solvent. Later, they prepared Ni nanoparticles, tuned from 3 to 11 nm in diameter, by using two surfactants in the system, namely hexadecylamine and trioctylphosphine oxide (TOPO).[101] It was found that the introduction of HDA into the Ni colloidal synthesis system was an effective approach to obtain smaller low-size-dispersity nanoparticles. The X-ray diffraction patterns indicated an ordering of Ni atoms in a cubic structure, and the XPS data revealed the presence of a very small amount of oxygen on the Ni nanoparticle surfaces that originates from the organic layer coated on the surface of the Ni nanoparticles. These nanoparticles also present a superparamagnetic behavior as indicated by magnetic measurements.

Recently Khanna et al.[104] synthesized Ni nanoparticles coated by hydrophilic surfactant (sodium succinate) in aqueous media using either $NaBH_4$ or sodium formaldehyde sulfoxylate (SFS) as reducing agents. An interesting observation made in this work was that the choice of reducing agent is crucial to the success of the synthesis. The use of SFS leads to crystalline Ni nanoparticles, while reduction by $NaBH_4$ leads to the formation of nearly amorphous Ni nanoparticles. The explanation proposed for these results was the ability of SFS to act as a slow reducing agent as well as a secondary surfactant. The size of the nanoparticles estimated by HR-TEM was around 10 nm diameter. In another work, Sidhaye and co-workers synthesized Ni nanoparticles in the presence of sodium dodecyl sulfate (SDA) as surfactant and oleic acid as capping agent.[105] It was found that the presence of oleic acid is very important for the stability

of Ni nanoparticles, and also at an optimum concentration of SDS and oleic acid, crystalline Ni nanoparticles having a hexagonally close-packed (hcc) structure were obtained (with an average size around 30 nm diameter).

Microemulsion systems are also a suitable way for obtaining uniform and size controllable Ni nanoparticles. For example, the ternary water-in-oil microemulsion (water/cetyl-trimethyl-ammonium bromide/*n*-hexanol) yields surfactant-stabilized NiB particles with a size distribution in the range 3–8-nm diameter.[108] It was found that the particle size depends on the concentration of Ni salt, the amount and speed of addition of borohydride, and the reaction temperature. The as-prepared nanoparticles were compared with NiB catalyst (prepared by reducing nickel acetate in aqueous solution with $NaBH_4$) in the hydrogenation of carbonyl and olefinic groups, and the results revealed that the nanoparticles prepared by the microemulsion method (3–8-nm diameter) are more active in these reactions than the NiB catalyst (20–50-nm diameter). You-Xian et al.[113] also obtained Ni-B alloys (with a wide size distribution, 20–40-nm diameter) when the quaternary water-in–oil microemulsion (water/sodium dodecylbenzene sulfonate/*n*-pentanol/*n*-heptane was used. The experimental results showed that the nanoparticle size depends on the size of the emulsion droplets, aging time, concentration of water and surfactants (and their molar ratio).

Legrand et al.[114] prepared ~5-nm diameter Ni nanoparticles by using functionalized AOT (sodium bis(2-ethyl-hexyl)-sulfosuccinate) reverse micelles. They demonstrated by XPS that the reduction of the Ni precursor with $NaBH_4$ in functionalized AOT reverse micelles does not yield zero valent Ni metal nanoparticles. A mixture of Ni and Ni boride with undetermined stoichiometry was obtained. The reaction was studied under air and nitrogen conditions and it was observed that in open air the final product is a mixture of Ni and Ni-B, while under nitrogen

it is Ni_2B. This is further confirmed by magnetic measurements that lead to observation of paramagnetic behavior for samples obtained under nitrogen.

These studies indicated that microemulsions are effective microreactors to prepare uniform and size-controllable Ni nanoparticles. However, the final size does not depend solely on the size of the microemulsion droplets, but also on many other factors, such as the concentration of surfactants, the Ni salt precursor used, and the Ni to $NaBH_4$ mole ratio.

- **Preparation of Ni Nanoparticles by Reduction with Hydrazine**

Hydrazine is a powerful reducing agent. Temperature and time of the nickel reduction reaction are two parameters that influence the size and shape of the final product. Ni nanoparticles were synthesized by reducing Ni salt precursors with hydrazine at elevated temperature (60–100 °C) in the presence of surfactants. Cetyl trimethyl ammonium bromide (CTAB) surfactant is the most used in this synthetic route. Abdel-Aal et al.[111] prepared Ni nanoparticles by hydrothermal reduction of nickel chloride with hydrazine. They showed that the particle size (determined by SEM) ranges from 55 nm to 250 nm and depends on three variables: concentration of $NiCl_2$, concentration of CTAB surfactant, and hydrothermal reaction time. The concentration of CTAB surfactant plays an important role in controlling the particle size and also the morphology of the Ni nanoparticles, by affecting the nucleation rate. In another work, Singla et al.[109] prepared low-size-dispersity Ni nanoparticles in aqueous media using three surfactants: CTAB, tetraethylammonium bromide (TEAB), and tetrabutylammonium bromide (TBAB). It was found that when CTAB is used alone the final product consist is a mixture of nickel hydroxide and nickel nanoparticles. When CTAB is used in combination with TEAB and TBAB, only pure Ni nanoparticles (average size 16-nm diameter) with fcc structure were obtained. This finding was explained by the fact that CTAB alone is not able to cap efficiently the Ni nanoparticles in aqueous media. Infrared spectra indicated that in the presence of low

concentrations of TEAB and TBAB, the CTAB has a better capping effect because first TEAB and TBAB were adsorbed on the nanoparticles surface, followed by CTAB. The Ni nanoparticles prepared by this method showed catalytic activity in the reduction of *p*-nitrophenol. Crystalline Ni nanoparticles with an fcc structure were also synthesized by Chen et al.[112] by the reduction of $NiCl_2$ with hydrazine in water-in-oil microemulsion (water/CTAB/ *n*-hexanol). The final size of the nanoparticles can be tuned from 14.3- to 4.2-nm diameter by increasing the CTAB to *n*-hexanol ratio and hydrazine concentration. The magnetic measurements showed that Ni nanoparticles exibit a superparamagnetic comportment. Zhang et al.[110] prepared needle-like Ni nanoparticles when they used water-in-oil microemulsions with the same cationic surfactant CTAB (water/CTAB, *n*-butanol/*n*-octane). The size of the nanoparticles was affected by the size of the microemulsion droplets and the ratio of oil/surfactant.

Stable Ni nanoparticles were prepared by a solvothermal reduction with hydrazine.[119] In the presence of oleylamine, ferromagnetic Ni(0) nanoparticles having an fcc structure were obtained, and their size can be tuned from 40 to 100 nm by varying the solvothermal reaction time. The solvothermal reaction takes place in two steps: in the first step Ni-oleylamine complexes are formed at 85 °C, then, in the second step the Ni-oleylamine complexes react with hydrazine under alkaline conditions at 100 °C to produce spherical Ni nanoparticles. Their catalytic activity was successfully investigated in the hydrogenation of nitrobenzene to aniline.

- **Preparation of Ni Nanoparticles by Reduction with Polyol (Alcohols Containing Multiple Hydroxyl Groups)**

Ni nanoparticles with controlled size and structure can be produced by polyol reduction. In the polyol method, the Ni precursor is suspended in a liquid polyol and heated to an elevated temperature that can reach the boiling point of the polyol. During this heating process, the nickel precursor is reduced by the polyols and metal particles are formed. The polyol serves as reducing agent, solvent, and stabilizing agent. Ningthoujam et al.[120] studied the reduction

mechanism of Ni(II) to Ni(0) from three nickel precursors ($NiCl_2$, NiO powder, and $Ni[(NH_3)_6]Cl_2$ complex) using ethylene glycol as reducing agent. TEM revealed that particle size can be controlled by the type of Ni precursor, with the smallest particle size (50-nm diameter) obtained from $Ni[(NH_3)_6]Cl_2$ complex in the presence of oleic acid. An interesting observation made in this work was that the $Ni[(NH_3)_6]Cl_2$ complexes with or without oleic acid stabilizer is a better precursor for the synthesis of Ni nanoparticles, because of the short reaction time, lower reduction temperature, and smaller nanoparticle sizes compared to those formed from $NiCl_2$ and NiO precursors.

De Biasi et al.[106] and Rinaldi et al.[70] prepared colloidal Ni nanoparticles with a small diameter (5.3 nm) and narrow size distribution by reduction of $Ni(CH_3COO)_2$ with 1,2-dodecanediol in the presence of three surfactants (trioctylamine, trioctylphosphine, and oleic acid). The magnetic properties were studied intensively, and it was found that above 23 K the nanoparticles have two magnetic phases, paramagnetic and ferromagnetic, that can be attributed to different factors, such as non-coherent cluster magnetization inversion, intra-cluster interactions that generate an effective internal field, and the local ordered regions within each particle.[106] Furthermore, supported Ni nanoparticles were prepared by impregnation of two different supports (silica and active carbon) with the synthesized colloidal Ni nanoparticles,[70] at room temperature and under N_2 atmosphere. These surfactants were indispensable for the stabilization of the colloidal Ni nanoparticles, as well as for the control of their size and shape, but they were difficult to remove. The presence of surfactants on the Ni nanoparticles and supported Ni nanoparticle surfaces was confirmed by XPS. It was found that the silica-supported Ni nanoparticles are not catalytically active in the hydrogenation of cyclohexene and in the steam reforming of ethanol because the active sites were blocked by the capping surfactants.

- **Preparation of Ni Nanoparticles by Radiation-Induced Reduction**

Radiolytic reduction of reverse micelles containing Ni precursors can be also used to prepare Ni nanoparticles. For example, Gornostaeva and co-workers[115,116] studied the preparation of Ni nanoparticles and silica-supported Ni nanoparticles in reverse micelles, using AOT as surfactant and isooctane as the solvent, with γ-irradiation as "reducing agent". The influence of different reaction parameters (ratio $[H_2O]/[AOT]$, addition to the reaction of NH_3 vapors and/or ethanol) on nanoparticle synthesis was studied by UV-Vis spectroscopy. The Ni nanoparticles prepared by this method had a wide size distribution (from 1 to 100-nm diameter) and are not stable in the presence of air.

1.3.1.3 Preparation of Ni Nanoparticles Using Polymers/Capping Agents

The surface of Ni nanoparticles can be stabilized in solution by the adsorption of different polymers or capping agents that interact with the nanoparticle surface and prevent agglomeration. Wang et al.[121,122] prepared Ni nanoparticles (with an fcc structure) by chemical reduction of $NiCl_2$ with hydrazine in the presence of hydroxyethyl carboxymethyl cellulose (HECMC) as stabilizing agent. HECMC prevents particles agglomeration by interaction with Ni nanoparticles. The presence of the polymer and the oxide layer on the particle surface was confirmed by infrared spectroscopy and XPS analyses. The diameter of the nanoparticles increased from 15 to 83 nm with an increase in Ni precursor concentration from 0.8 to 1.2 M and an increase in reaction temperature from 65 to 80 °C. Magnetic measurements indicated that the Ni nanoparticles obtained were ferromagnetic, and the presence of HECMC and the oxide layer on the nanoparticles surface weakens the magnetism. A similar experiment was performed by Chen et al.[123] but with dodecanethiol as stabilizer.

Poly(*N*-vinilpyrrolidone), PVP[124-126] was also used as a protective agent in the synthesis of Ni nanoparticles. Couto et al.[124] reported the synthesis of Ni nanoparticles in air by a

modified polyol route using $NaBH_4$ as reducing agent and PVP as a stabilizer. By using a combination of characterization techniques they were able to determine the role of stabilizer, and the nature and size of the nanoparticles. These techniques indicated an atomic arrangment of Ni nanocrystals in fcc structure with an average diameter of 3.8 nm. It was found that the carbonyl groups from PVP strongly coordinate to the nanoparticle surface. Other experiments[125] lead to the same kind of results. Sun et al.[126] prepared Ni, Co, and Fe nanoparticles by using a rapid expansion of supercritical fluid solutions and chemical reduction methods. The results showed that the size and size distribution of nanoparticles were not influenced by the concentration of PVP in the reaction. The only parameter that affects the size of the nanoparticles is the temperature of the supercritical fluid solution.

Hou and Gao[127] used a solvothermal process to prepare PVP-coated Ni nanoparticles with an average diameter of 15 nm and possessing superparamagnetic behavior. In the same way, they prepared iron nanoparticles. XPS and X-ray diffraction demonstrated that PVP passivates the surface of the nanoparticles, thereby preventing their oxidation. PVP-stabilized Ni nanoparticles were prepared by Xu et al.[128] by reduction of Ni(II) salts with hydrazine under microwave irradiation. It was found that an appropriate amount of Na_2CO_3 and NaOH in ethylene glycol was necessary for the reduction, and the particle formed were uniform Ni nanoflowers with an average diameter of 50 to 100 nm.

1.3.1.4 Preparation of Ni Nanoparticles by Other Reduction Methods

The preparation of Ni nanoparticles by hydrogen reduction has also been used mainly due to the easy control of process conditions. Domínguez-Crespo et al.[129] synthesized Ni nanoparticles by an organometallic approach. The $Ni(COD)_2$ (COD = cycloocta-1,5-diene) was dissolved in THF in the presence of the two stabilizers 1,3-diaminopropane (DAP) and anthranilic acid (AA). The mixture was pressurized for 20 h at 70 °C under hydrogen. The

prepared Ni nanoparticles were used to prepare electrode materials, and their catalytic performance on the hydrogen evolution reaction was studied. They found that the size, morphology and electrochemical properties of Ni nanoparticles are dependent on the nature and quantity of the stabilizer used. TEM micrographs confirmed the formation of crystalline Ni nanoparticles, with an average diameter ranging from 5 to 14 nm when DAP was used as the stabilizer, and larger particles resulted (5 nm to 500-nm diameter) when AA was used as the stabilizer. With almost the same experimental procedure but with poly(vinylpyrrolidone) of different molecular weights (K30, M 40 000 and K 90, M 360 000) as stabilizers at room temperature, Ely et al.[130] prepared Ni nanoparticles. It was found that the magnetic properties of the Ni nanoparticles strongly depend on the PVP chain length and the nature of the solvent.

Crystalline Ni nanoparticles with a wide size (ranging from 31 to 106 nm) can be obtained by H_2 reduction of the metal chloride in the gas phase.[131] The kinetics of gas-phase reduction of $NiCl_2$ conversion and the associated rate constants were studied over a large temperature range in a tubular furnace reactor by manipulating concentrations of the reactants. The reaction was first order with respect to $NiCl_2$ concentration, and the conversion and the rate constant were dependent on the reaction temperature.

Alonso et al.[132] generated Ni nanoparticles (0.75–2.88-nm diameter) by the reduction of $NiCl_2$ with lithium powder in the presence of 4,4,-di-*tert*-butylbiphenyl (DTBB) at room temperature under argon. These nanoparticles have high reactivity and versatility in the reduction of a variety of ketones and aldehydes. In another work, Zhang and co-workers[133] prepared monodisperse nickel and cobalt nanoparticles in dimethylformamide (DMF) at 160 °C. In this synthesis, DMF acted not only as solvent but also as reducing agent, involving the oxidation of DMF to a carboxylic acid that causes the reduction of metal ions. The X-ray diffraction patterns indicated an fcc structure of for the Ni nanoparticles (average diameter of

100 nm). Magnetic measurements confirmed that the nanoparticles were ferromagnetic and had an enhanced coercivity and decreased saturation magnetization compared with bulk Ni materials.

1.3.1.5 Preparation of Ni Nanoparticles by Thermal Decomposition

Thermal decomposition has been used to prepare metal nanoparticles with different sizes and shapes. This method involves solubilization of nickel precursors in different solvents under an inert atmosphere at elevated temperature and subsequent crystallization of particles from the fluid. During this synthesis, parameters such as temperature, solvent, surfactants/stabilizers usually have important effects on the structure of the nanocrystals. Zhang et al.[134] used thermal decomposition of the organometallic precursor, $Ni(acac)_2$, in oleylamine to synthesize nanocrystalline Ni having an fcc structure. Two other methods, seed-assisted and hot-injection, were used to compare the influence of the reaction parameters on the size and magnetic properties of Ni nanoparticles. It was found that smaller nanoparticles were obtained by a direct thermolysis method (22 nm). For seed-assisted and hot injection processes, the size of the nanoparticles was larger, 46 and 59 nm diameters, respectively. All the three methods produced ferromagnetic Ni nanoparticles having an fcc structure. Kim and co-workers[135] studied the preparation of Ni thin films for electrode applications using Ni nanoparticles prepared by thermal decomposition of Ni-oleate complexes. The average diameter of the Ni metallic nanoparticles was tuned from 5.1 to 6.6 nm by varying the decomposition temperature from 350 to 400 °C. The nanoparticles were pure metal (fcc structure) and were stable in air due to surface adsorption of oleate molecules on their surface.

The role of long-chain amines as both solvent and reducing agents has been examined during thermal decomposition methods.[103,107,117] More specifically, fcc and hcp-Ni nanoparticles were prepared by Mourdikoudis and co-workers[103] by thermal decomposition of nickel acetate in primary and tertiary amines. An interesting observation in this synthesis is that the alkylamine

surfactants can be used as the solvent, surfactant and reducing agent. The size of the resulting nanoparticles was controlled between 5 and 120 nm by using additional surfactants, such as 1-adamantanecarboxylic acid and trioctylphosphine oxide. Similar conclusions have been drawn by Luo et al.[102] from a study of nickel acetate thermal decomposition. It was found that the surfactant play an important role in controlling the shape and size of the Ni nanoparticles. Without using alkylphosphine surfactants, the Ni nanoparticles (hcp structure) exhibited an irregular shape and an average diameter of 62 nm. Interestingly, the final size and structure of the nanoparticles depended not only on the presence of surfactant but also on the type and concentration of surfactant (such as trioctylphosphine oxide (TOPO) or trioctylphosphine (TOP)) used in the reaction. For example, when TOPO surfactant was used in the reaction, the hcp Ni nanoparticles were spherical in shape but with larger size (~90 nm diameter). In the case of TOP surfactant the nanoparticles had a spherical shape (with an hcp phase) and smaller size (6.5-nm diameter), reflecting the role of the type of surfactants in controlling the morphology of nanoparticles. Also, a transition from hcp to fcc phase was found with an increase in alkylamine concentration. In another work, Wang and co-workers[117] prepared polycrystalline Ni nanoparticles by the same thermal decomposition of nickel acetate. In their experiment, the surfactant hexadecylamine was used as the solvent, and reducing and stabilizing agent. The size of nanoparticles (average diameter 7 nm) and structures were controlled by experimental factors: molar reactant ratio, reaction time, and reaction temperature. Higher reaction temperature (increasing from 200 to 290 °C) favored the phase transformation from fcc to hcp-Ni. Johnston-Peck et al.[107] were able to prepare Ni(core)/NiO(shell) nanoparticles by intentional oxidation of Ni(0) nanoparticles obtained by thermolysis of nickel acetylacetonate in the presence of oleylamine and trioctylphosphine. The TEM images revealed that depending on the synthesis conditions (amount of reactants and temperature), the size of the nanoparticles could be

controlled from 8 to 24 nm (the NiO shell thickness increased from 1.1–2.6 nm). These nanoparticles had interesting magnetic properties because the Ni core is ferromagnetic and the oxide shell is antiferromagnetic.

1.3.1.6 Preparation of Ni Nanoparticles by Aerosol and Vapor Methods

Other successful routes in the synthesis of Ni nanoparticles involve DC sputtering,[136] spray pyrolysis,[137] arc[138,139] and hydrogen plasma.[140] These methods usually generate highly agglomerated clusters with a broad particle size distribution. In the spray pyrolysis method, two nickel precursors are sprayed into a series of reactors under nitrogen gas containing 10% H_2, where the aerosol solute condenses and the solvent evaporates. Ni nanoparticles (with size distributed from 160 to 450 nm in diameter) were obtained in a residence time of less than 3 sec when the temperature in the second reactor was over 1200 °C.[137] The arc plasma instruments usually consist of an arc melting chamber and a collecting chamber. The bulk metal nickel was heated and melted by the high temperature of the plasma, and the metal vapors (aerosols) were rapidly cooled. The obtained nanoparticles can be collected after a passivation and stabilization period with the working gas.[139] Chang and Su[141] introduced an arc-submerged nanofluidic synthetic system to produce Ni nanoparticles around 20 nm in diameter that were well distributed inside the dielectric liquid.

Laser ablation[142-145] is a promising process for the synthesis of Ni nanoparticles, both in the liquid and gas phases, with or without the presence of surfactants. The variables affecting the particle morphology produced by laser ablation are: the wavelength of laser, the duration of laser pulses, the number of laser shots, and the irradiation time. The nanoparticles may consist of pure Ni[145] or NiO,[144] with the smallest diameter $\geq$ 3 nm.

1.3.1.7 Preparation of Ni Nanoparticles by Hydrolysis Methods

Wang et al.[146] developed a new and relatively simple method for preparing Ni nanoparticles by hydrolysis of Mg_2Ni and Mg_2NiH_4 in water or KOH solution. Results from X-ray diffraction and TEM showed that the final product consists of spherical Ni nanoparticles (with a diameter about 10 nm) and small amounts of $Ni(OH)_2$. Special attention has to be paid to the removal of the hydrolysis products, especially $Mg(OH)_2$, because the final products were contaminated with Mg and oxygen, as shown by X-ray spectroscopy.

1.3.1.8 Preparation of Ni Nanoparticles by Sol-Gel Methods

The sol-gel process for this specific application is based on the hydroxylation and condensation of a nickel precursor in solution resulting in a sol, followed by heating to form gel. Further heat treatment at higher temperature and under an inert atmosphere is required to obtain the final crystalline Ni state. Gong et al.[147] prepared crystalline Ni nanoparticles by a sol-gel method followed by heat treatment at different temperatures (300–400 °C) under argon. It is of interest to note that the particles synthesized at 300 °C have an hcp structure (8–15 nm in diameter), while that obtained at 400 °C have an fcc structure and larger sizes.

1.3.2 Literature Review on Synthesis of Iron Oxide Nanoparticles

Compared with the synthesis of nickel nanoparticles in solution, the approaches used in the preparation of supported iron oxide nanoparticles are not so numerous. These approaches can be grouped as sol-gel, impregnation (such as wetness impregnation, adsorption on the support surface, and impregnation inside of mesoporous materials), and microcontact printing methods.

1.3.2.1 Preparation of Iron Oxide Nanoparticles by Sol-Gel Methods

The sol-gel technique is typically used to prepare iron oxide nanoparticles in an inorganic matrix via the hydroxylation and condensation of molecular precursors in an alcoholic solution.

The hydroxide precursors undergo polymerization by condensation of the hydroxyl network, resulting in a three-dimensional metal oxide gel. After gelation, the solvent is removed by drying. Further heating at different temperatures leads to an ultra-fine powder of iron oxide nanoparticles in an inorganic network. The porous nature of the matrix formed by the sol-gel method minimizes particle aggregation and imposes an upper limit on the size of particles formed. The method seems very simple, but very special attention must be paid to different factors, such as the rates of hydrolysis and condensation, the choice of solvents in the sol-gel process, the removal of solvent, appropriate drying, and calcination temperature. This is because the final product may end up in the form of a nanometer-scale powder or just bulk materials with different chemical and physical properties.

Isolated nanoparticles of γ-Fe_2O_3 in a silica matrix have been prepared by Del Monte et al.[148] using the sol-gel method. In their work, the influence of different factors such as the nature and concentration of the iron precursors and thermal treatment of the gels on the gelation process and the nature of the final product were investigated. It was found that when iron chloride was used as the precursor, the iron oxide obtained after calcination in air at 400 °C for 10 h was α-Fe_2O_3 with a mean crystallite diameter of 40 nm. On the other hand, use of the iron nitrate precursor gave Fe_3O_4 or γ-Fe_2O_3 spinel phase with an estimated particle diameter of 15 nm from X-ray data. The authors explained that γ-Fe_2O_3 was formed through a reduction-oxidation reaction that occurs during the calcination process of the organic material trapped inside the gel pores. Ennas et al.[149] prepared Fe_2O_3-SiO_2 nanocomposites using tetraethoxysilane (TEOS) and iron(III) nitrate in alcoholic solution as gelling precursors. Interestingly, in their work γ-Fe_2O_3 nanoparticles, with an average diameter of 3–4 nm, were formed at low calcination temperatures (150–300 °C). The nanoparticle sizes were found to be slightly increased with increasing temperature, and at high temperature (higher than 900 °C) a transition from γ-Fe_2O_3 to α-Fe_2O_3

was observed and also a transition from antiferro- to ferrimagnetic behavior. The technique was extended by Solinas et al.,[150] who investigated the influence of two factors on the gelation process: temperature and surface of evaporation/volume ratio of the sol. This study showed that depending on these two parameters γ-Fe_2O_3 and/or α-Fe_2O_3 nanoparticles in the silica matrix with different sizes could be obtained. When low surface of evaporation/volume ratios and high temperatures were adopted, the occurrence of γ-Fe_2O_3 was observed, while high surface of evaporation/volume ratios and low temperatures gave α-Fe_2O_3. The interaction of the iron oxides with the silica matrix was studied by infrared and NMR techniques.[151] These spectroscopic studies indicated that the iron oxides interacted with the silica/silanol groups at the surface of the cavities in which they form. At lower heating temperatures, the iron oxide nanoparticles form in the silica matrix and remain in their position, being unable to move around. At higher temperatures, the diffusion of the oxide particles is higher, and the particles coalesce into bigger particles, thus favoring the observed transition from γ- to α-Fe_2O_3. In another work, Chanéac et al.[152] concluded that the silica matrix acts as an anti-sintering agent for iron oxide particles, and their γ structure was retained at temperatures up to 1000 °C.

Ida et al.[153] prepared nanoscopic Fe_2O_3/SiO_2 catalysts by two methods: hydrolysis of a mixed solution of TEOS and iron(III) nitrate in ethylene glycol, followed by calcination at various temperatures, and conventional impregnation of silica powder with an aqueous solution of iron(III) nitrate. EXAFS studies showed that the iron oxide particles prepared by the sol-gel method were γ-Fe_2O_3. On the contrary, the impregnation method produced α-Fe_2O_3 nanoparticles with a broad size distribution.

From all these studies, it can be concluded that γ or α-Fe_2O_3-SiO_2 with different particle size and distribution can be prepared by adequate modification of the initial gel structure through different gelation times, the type and concentration of iron precursors, and heating treatment.

1.3.2.2 Preparation of Iron Oxide Nanoparticles by Impregnation Methods

Silica-supported iron oxide nanoparticles with average sizes ranging from 2.5 to 9.5 nm were prepared by an incipient wetness impregnation method of silica with an aqueous ferric nitrate solution.[154] The total metal oxide loading was varied from 3.22 to 19.32% and the calcination temperature from 400 to 450 °C. X-ray diffraction showed the presence of only α-Fe_2O_3. In a similar way, α-Fe_2O_3 (average size 20 nm) particles were obtained by calcination of an iron-impregnated silica precursor in air at temperatures higher than 400 °C.[74] When the samples are calcined in air at temperatures ≤ 400 °C, γ-Fe_2O_3 nanoparticles are obtained. Small γ-Fe_2O_3 nanoclusters (average diameter 2–3 nm) were also obtained by Rostovshchikova et al.[155] by impregnation of an activated silica gel matrix (AGM) and activated silica matrix (ASM) with iron(III) acetylacetonate, followed by calcination at 400 °C. The nanoclusters obtained possessed catalytic activity in the conversion of chloro olefins. Iron oxide and bimetallic Co-Fe oxide nanoparticles were prepared by O'Shea and co-workers[156] using the same wetness impregnation method on a silica support. The samples were dried at 120 °C overnight and calcined in an air flow at 500 °C for 2 h. The TEM images revealed that the iron oxides form non-uniform aggregates on the silica surface, with sizes ranging from 0.1 to 1 μm. X-ray photoelectron spectroscopy and X-ray diffraction showed the formation of separate Fe_2O_3 and Co_3O_4 in oxide samples and no cobalt-iron mixed oxides.

Ultradispersed diamond powders are also suitable materials for stabilization of iron oxide nanoparticles.[157] Dimitrov et al.[157] prepared iron oxide on ultradispersed diamond by impregnation with iron acetylacetonate in chloroform or iron nitrate aqueous solution. After impregnation, the samples were dried and calcined in Ar or air flow at 377 °C for 1h. It was found that the iron oxide state strongly depends on the diamond surface characteristics and the sample pre-treatment media. Most highly-dispersed nanoparticles, which also present the

highest catalytic activity in methanol decomposition, were obtained for samples obtained from iron nitrate as a precursor with air pre-treatment. Szabo and co-workers[158] prepared magnetic iron oxide nanoparticles on two different clay supports (natural montmorillonite and synthetic laponite) by impregnation with iron(III) chloride. The main differences between these two clays were their lamellar sizes and their cation-exchange capacities. The results revealed that these factors influenced the average nanoparticle size and size distribution, magnetic properties, specific surface area, and porous structure. More specifically, the iron oxides formed on montmorillonite were much larger (around 16-nm diameter), with high surface coverage, and they were dispersed over the clay lamellae. In the case of laponite support, the nanoparticles were very small (ranging from 2 to 3-nm diameter) and they were localized on certain regions of the silicate sheets and near the edges.

Gervasini et al.[159,160] prepared well-dispersed iron oxide nanoparticles on silica and silica-zirconia mixed oxides supports by an equilibrium-adsorption method. They used temperature programmed reduction to study the kinetics of reduction of supported iron oxide nanoparticles. It was found that the reduction path of the iron oxide particles was dependent on the support, as zirconia supports favored complete reduction of iron oxides to metallic iron, while silica induced reduction through wüstite formation. Choi et al.[161] prepared Fe_2O_3/SiO_2 by simply immersing the SiO_2 substrate in an aqueous solution containing $FeCl_3$ and hydroxylamine to yield $Fe(0)/SiO_2$. After the deposition process the substrate was calcined in air at 800 °C to convert the nanoparticles to Fe_2O_3. The Fe_2O_3 nanoparticles were then used to catalyze the growth of single-walled carbon nanotubes by chemical vapor deposition method.

Rostovshchikova et al.[162] prepared iron oxide nanoparticles, with an average diameter of 6 nm, on the surface of ultradispersed poly(tetrafluoroethylene) (UPTFE) granules by thermal destruction of iron(III) formate in a dispersion system UPTFE-mineral oil. The as-synthesized

nanoparticles mainly consist of Fe_3O_4 and Fe_2O_3 phases depending on the activation temperature. In an another work, Gmucová and co-workers[163] described a high-temperature reaction of iron acetylacetonate with 1,2-hexadecanediol in the presence of oleic acid and oleylamine to obtain iron oxide nanoparticles (Fe_3O_4/Fe_2O_3). The as-prepared iron oxide nanoparticles were deposited on a Pt/photovoltaic hydrogenated amorphous silicon (a-Si:H) electrode by a Langmuir-Blodgett technique. Drbohlavova et al.[164] prepared silica-supported iron oxide nanoparticles with average sizes around 140 nm using an easy co-precipitation method. XRD measurements showed the presence of two crystalline phases: orthorhombic ε-Fe_2O_3 as a majority phase (49%) and hematite (24%).

Mesoporous materials, such as silica and carbon, have received significant attention in the synthesis of supported iron oxide nanoparticles. In these cases, the pore size of the supports limits particle growth. Köhn and Fröba[165] prepared transition metal oxide nanoparticles within mesoporous MCM-48 silica by wet impregnation method with iron(III) nitrate, followed by drying and calcination procedures. It was found that the metal oxide nanoparticles were formed almost exclusively within the pore system, and the mesoporous silica structure was still intact after the treatment. When the impregnation was done on two mesoporous silica materials, MCM-41, which has one dimensional channel system, and MCM-48, which has three-dimensional channel systems, highly dispersed α-Fe_2O_3 nanoparticles were obtained.[166] The pore diameter was less than 3 nm for both mesoporous materials. It was found that the iron oxide nanoparticles were distributed in two fractions of species: one fraction with hematite properties with diameters larger than 10–12 nm and located on the outer surface of the mesoporous silica, and another fraction with diameters smaller than 3–4 nm and located inside the pores of the mesoporous material. These iron oxide-modified mesoporous materials presented catalytic activity in the decomposition of methanol. On the contrary, when

mesoporous carbon CMK-3 was used, the iron oxide nanoparticles were mainly distributed within the mesopores.[167]

Tsoncheva et al.[81,82] studied the influence of a variety of mesoporous support (SBA-15, KIT-6, KIT-5, MgO, and CeO_2), that exhibit different 2-D and 3-D channel- or cage-like pore structures, on the state of iron oxide nanoparticles. The data indicated that the pore topology of the support affected the location and dispersion of iron oxide nanoparticles. The most homogeneously dispersed nanoparticles were obtained for a silica host matrix that has a 3-D channel-like structure and pore diameter of 7 nm. For the mesoporuos material with low mesoporous volume and small pore diameters, larger iron oxide nanoparticles were found mainly on the outer surface. The state of iron species presented on the mesoporous support strongly affects their catalytic properties.

Similarly, Alam et al.[83] studied the magnetic properties of iron oxide nanoparticles loaded on mesoporous silica and carbon materials and formed by wetness impregnation. The magnetic properties were found to be strongly influenced by the size of the iron oxide nanoparticles and also by the nature of the mesoporous support (SBA-15, KIT-6, CMK-3, and carbon nanocage) and interactions between iron oxide nanoparticles. The nanoparticles embedded in mesoporous silica had much lower magnetization values (around 10 emu g^{-1}) than those embedded in mesoporous carbon materials (around 40 emu g^{-1}).

Schnitzler et al.[168] prepared silica/carbon and silica/iron oxide nanocomposite by incorporation and pyrolysis of ferrocene into porous Vycor glass (which has nanometrer-sized pores). After impregnation, the ferrocene molecules were oxidized to ferricinium ions by air and the $Si–O^-$ groups on the surface of the pores act as counteranions to stabilize these ferricinium cations. Pyrolysis of the ferricinium-impregnated glass at different temperatures, under Ar or air,

gives rise to different glass/carbon or glass/α-Fe_2O_3 nanocomposite, as shown by TEM, and Raman and EPR spectroscopies.

1.3.2.3 Preparation of Iron Oxide Nanoparticles by Microcontact Printing Methods

Microcontact printing has been used to pattern iron oxide catalysts for the growth of carbon nanotubes. For example, Ding et al.[169] used microcontact printing to prepare uniform patterns of Fe_2O_3 nanoparticles (mean diameter 10–20 nm) on silicon wafers surfaces. The fabricated iron oxide nanoparticles were used as catalysts to grow single-walled carbon nanotubes by both thermal and chemical vapor deposition methods.

1.4 The Role of Metal Oxide Particles in the Formation of Surface-Associated Pollutants in Combustion Processes

Combustion of solid and liquid fuels and incineration processes lead to the formation and emission of chlorinated benzenes and phenols, chlorinated polynuclear aromatic hydrocarbons (PAH), dioxins, furans, and particles with a variety of sizes and compositions.[170-172] Basically, PCDD/Fs are formed in most combustion processes from any combination of C, H, O, and Cl under suitable time and temperature conditions.[170,173] The particulate emission from combustion sources can be classified into three major categories: fly ash, soot, and particles with various composition and structures. Particles produced in the combustion chamber in the gaseous phase undergo inception, coagulation and surface growth and, as a result, their diameters range from 3 to 4 nm for the smallest metallic nanoparticles to a few hundreds of nanometers for the agglomerates.[11] Many studies have shown that transition metals are present in combustion-generated fly ashes and airborne particulate matter.[11-13,174] These particles are thought to play a vital role in the formation of air-borne pollutants via catalytic routes.[11,13,175]

PCDD and PCDFs in combustion processes are generally formed through homogeneous and heterogeneous mechanisms.[16,17,176-178] The homogeneous gas-phase mechanism involves reaction of chlorinated organic precursors at temperatures between 400 and 800 °C. The

heterogeneous formation of PCDD/F occurs in the post-combustion zones at low temperatures (200–600 °C) and involves two routes: *de novo* reaction and transition-metal-mediated surface reaction of organic precursors. *De novo* reactions involve the oxidation and chlorination of elemental carbon in the ash or soot. In the precursor reactions, PCDD/Fs are formed from aromatic precursors, such as chlorobenzenes and chlorophenols, through surface-mediated reactions. In both cases, combustion-generated fly ash is a reactive surface on which reactions occur. The composition of fly ash in municipal solid waste incineration (MSWI) was listed in many papers,[12-14,179,180] and it was shown that the chemical composition and morphology of the fly ash depends on reaction conditions. SiO_2, Al_2O_3, and CaO typically make up the bulk of the fly ash and various metallic species, such as Cu, Ni, Fe, Pb, Zn, Cr, Cd, and V, are present from ppm levels to a few percent by weight.

Many factors that influence the formation of PCDD/Fs in combustion processes are temperature, the residence time, chlorine input, oxygen and feed rate, the presence of ash or soot particles, and precursors.[17] It is known that transition-metal species, especially copper oxides and chlorides, found in native fly ash play an important role in the formation of polychlorinated dibenzo-*p*-dioxins (PCDD) and polychlorinated dibenzofurans (PCDF).[181] Micron-scale particles of metal oxides have a role in mediating the reactions of organics to form both high and low molecular weight species.[182] The formation of PCDD/Fs and some other related compounds, from organic precursors in the presence of supported transition metal oxides, has been confirmed experimentally in the low temperature range of 250–500 °C.[183-185] For PCDD/Fs formed from precursors such as 2-monochlorophenol over iron oxides supported on a silica substrate, Nganai and co-workers found that iron oxides mediate the formation of dioxin and furans.[183] Dibenzo-*p*-dioxin, 1-monochlorodibenzo-*p*-dioxin, dibenzofuran, and 4,6-dichlorodibenzofuran were formed in maximum yields (0.2%, 0.1%, 0.4%, and 0.3%,

respectively) under pyrolytic conditions, over the temperature range 200–500 °C for 1 h reaction time.

The reactions involving precursors will involve their transport to the surfaces, coupled with various reactions on the surface under the influence of metal catalysts, followed by desorption of products. Chlorobenzenes and chlorophenols are some of the model precursors that have been implicated in the formation of PCDD/Fs.[170,172,186-188] The experimental studies of Zimmermann[188] and Blumenstock[187] showed that there is a good correlation between the international toxicity equivalent (I-TEQ) value of PCDD/Fs measured and lower chlorinated benzenes (mono to trichlorobenzene), indicating that chlorobenzene is the best suited surrogate for PCDD/Fs formation.

Studies have primarily focused on surface-mediated formation of PCDD/F from chlorinated phenols as precursors.[183,185,189-192] Very few studies have shown the formation of PCDD/Fs from chlorinated benzenes as precursors. Catalytic combustion of chlorobenzene on 2 wt.% Pt/γ-Al_2O_3 was studied by De Jong et co-workers.[193] The byproducts observed when monochlorobenzene (1000–1500 ppm) was introduced into the feed gas (16% O_2 in nitrogen) to the catalyst bed between 150 and 550 °C, were especially polychlorobenzenes and low levels of PCDD and PCDFs. Upon exposure to tert-butyl chloride, as an additional chlorine source, much higher levels of polychlorinated benzenes and PCDD/Fs are obtained. In this reaction they also used a micropollutant-like mixture, and the results revealed that although the total chlorine input was reduced, the output of PCDD/Fs was higher. Addink et al.[194] studied the formation of PCDD/Fs on fly ash from precursors (such as chlorobenzene, 1,2,4,5-tetrachlorobenzene, pentachlorobenzene and phenol) and carbon model compounds under oxidative conditions. It was found that when HCl was used as a chlorine source in addition to the chloride naturally present in fly ash, both chlorobenzenes and phenol form PCDD/Fs via condensation reactions.

However, other authors[195] found no PCDD/Fs formation from monochlorobenzene combustion in the presence of CuO and HCl. The combustion was conducted at temperatures 300–600 °C in a mixture of air and helium (10% oxygen). Tetrachloroethylene and higher chlorobenzenes were the only products observed in this study.

A detailed study of surface-mediated reactions of 2-chlorophenol, 1,2-dichlorobenzene, and monochlorobenzene with CuO/SiO_2, as a fly-ash surrogate, was reported by Alderman and co-workers,[181] using infrared and X-ray absorption near edge structure spectroscopy (XANES). They determined that chlorinated phenols and chlorinated benzenes chemisorb on the surface of CuO/SiO_2 to form chlorophenolate via H_2O and/or HCl elimination.

Although extensive research has been done to study the formation of PCDD/Fs in combustion processes using micron-scale grains of transition metal oxides no study exist with the nanoscale particles. It is expected that nanoparticles would be at least as active as or even more active than micron-scale particles because they are likely more reactive. The extremely small size of nanoparticles will maximize the surface area exposed to the organic precursor in combustion processes allowing more reaction to occur. Formation of polychlorinated benzenes from combustion of chlorobenzene on supported Pt nanoparticle catalysts was studied by van den Brink et al.[196] Catalysts were prepared by homogeneous deposition precipitation of $H_2[Pt(OH)_6]$ precursor on different supports (γ-Al_2O_3, SiO_2, and ZrO_2 at concentration necessary to yield 2 wt.% Pt on each support) and calcined at different temperatures (500, 600, 700, and 800 °C). The experimental results showed that polychlorinated benzenes were the only byproducts obtained for chlorobenzene combustion carried out under oxidative conditions (15% O_2, 85%N_2). In addition, the amount of polychlorinated benzene correlated with the dispersion of platinium on supports, with very small Pt crystallites (1.6 nm in diameter) being more active for polychlorinated benzene formation. Furthermore, when Pd/γ-Al_2O_3 was used as the catalyst

in this reaction, the conversion of chlorobenzene was lower but the amounts of byproducts were higher.

Thus, based on the known characteristic properties of a number of metal and metal oxide nanoparticles, knowledge of the impact of nanoparticle size and composition on pollutant formation in combustion processes would be highly valuable. This thesis begins to address some aspects of this very large and potentially important area of research.

1.5 References

(1) Donaldson, K.; Li, X. Y.; MacNee, W. Ultrafine (nanometre) particle mediated lung injury. *J. Aerosol Sci.* **1998**, *29*, 553-560.

(2) Nel, A.; Xia, T.; Madler, L.; Li, N. Toxic potential of materials at the nanolevel. *Science* **2006**, *311*, 622-627.

(3) Li, N.; Xia, T.; Nel, A. E. The role of oxidative stress in ambient particulate matter-induced lung diseases and its implications in the toxicity of engineered nanoparticles. *Free Radical Bio. Med.* **2008**, *44*, 1689-1699.

(4) Burda, C.; Chen, X. B.; Narayanan, R.; El-Sayed, M. A. Chemistry and properties of nanocrystals of different shapes. *Chem. Rev.* **2005**, *105*, 1025-1102.

(5) Laurent, S.; Forge, D.; Port, M.; Roch, A.; Robic, C.; Elst, L. V.; Muller, R. N. Magnetic iron oxide nanoparticles: Synthesis, stabilization, vectorization, physicochemical characterizations, and biological applications. *Chem. Rev.* **2008**, *108*, 2064-2110.

(6) Kahn, M. L.; Glaria, A.; Pages, C.; Monge, M.; Saint Macary, L.; Maisonnat, A.; Chaudret, B. Organometallic chemistry: an alternative approach towards metal oxide nanoparticles. *J. Mater. Chem.* **2009**, *19*, 4044-4060.

(7) Bosman, A. W.; Schenning, A.; Janssen, R. A. J.; Meijer, E. W. Well-defined metallodendrimers by site-specific complexation. *Chem Ber-Recl* **1997**, *130*, 725-728.

(8) Vassilev, K.; Ford, W. T. Poly(propylene imine) dendrimer complexes of Cu(II), Zn(II), and Co(III) as catalysts of hydrolysis of p-nitrophenyl diphenyl phosphate. *J. Polym. Sci. Pol. Chem.* **1999**, *37*, 2727-2736.

(9) Floriano, P. N.; Noble, C. O.; Schoonmaker, J. M.; Poliakoff, E. D.; McCarley, R. L. Cu(0) nanoclusters derived from poly(propylene imine) dendrimer complexes of Cu(II). *J. Am. Chem. Soc.* **2001**, *123*, 10545-10553.

(10) Larsen, G.; Noriega, S. Dendrimer-mediated formation of Cu-CuOx nanoparticles on silica and their physical and catalytic characterization. *Appl. Catal., A* **2004**, *278*, 73-81.

(11) Allouis, C.; Beretta, F.; D'Alessio, A. Structure of inorganic and carbonaceous particles emitted from heavy oil combustion. *Chemosphere* **2003**, *51*, 1091-1096.

(12) Quina, M. J.; Bordado, J. C.; Quinta-Ferreira, R. M. Treatment and use of air pollution control residues from MSW incineration: An overview. *Waste Manage.* **2008**, *28*, 2097-2121.

(13) Born, J. G. P.; Mulder, P.; Louw, R. Fly-ash mediated reactions of phenol and monochlorophenols - oxychlorination, deep oxidation, and condensation. *Environ. Sci. Technol.* **1993**, *27*, 1849-1863.

(14) Saffarzadeh, A.; Shimaoka, T.; Motomura, Y.; Watanabe, K. Characterization study of heavy metal-bearing phases in MSW slag. *J. Hazard. Mater.* **2009**, *164*, 829-834.

(15) Smith, K. R.; Aust, A. E. Mobilization of iron from urban particulates leads to generation of reactive oxygen species in vitro and induction of ferritin synthesis in human lung epithelial cells. *Chem. Res. Toxicol.* **1997**, *10*, 828-834.

(16) Altarawneh, M.; Dlugogorski, B. Z.; Kennedy, E. M.; Mackie, J. C. Mechanisms for formation, chlorination, dechlorination and destruction of polychlorinated dibenzo-p-dioxins and dibenzofurans (PCDD/Fs). *Prog. Energy Combust. Sci.* **2009**, *35*, 245-274.

(17) Stanmore, B. R. The formation of dioxins in combustion systems. *Combust. Flame* **2004**, *136*, 398-427.

(18) Esumi, K.; Suzuki, A.; Aihara, N.; Usui, K.; Torigoe, K. Preparation of gold colloids with UV irradiation using dendrimers as stabilizer. *Langmuir* **1998**, *14*, 3157-3159.

(19) Esumi, K.; Suzuki, A.; Yamahira, A.; Torigoe, K. Role of poly(amidoamine) dendrimers for preparing nanoparticles of gold, platinum, and silver. *Langmuir* **2000**, *16*, 2604-2608.

(20) Zeng, F. W.; Zimmerman, S. C. Dendrimers in supramolecular chemistry: From molecular recognition to self-assembly. *Chem. Rev.* **1997**, *97*, 1681-1712.

(21) Klajnert, B.; Bryszewska, M. Dendrimers: properties and applications. *Acta Biochim. Pol.* **2001**, *48*, 199-208.

(22) Bosman, A. W.; Janssen, H. M.; Meijer, E. W. About dendrimers: Structure, physical properties, and applications. *Chem. Rev.* **1999**, *99*, 1665-1688.

(23) Buhleier, E.; Wehner, W.; Vogtle, F. Cascade-chain-like and nonskid-chain-like syntheses of molecular cavity topologies. *Synthesis-Stuttgart* **1978**, 155-158.

(24) Wörner, C.; Mülhaupt, R. Polynitril- und polyaminfunktionalisierte poly(trimethylenimin)-dendrimere. *Angew. Chem.* **1993**, *105*, 1367-1370.

(25) Berg, E. M. M. D. B.-V. D.; Meijer, E. W. Poly(propylenimin)-dendrimere: synthese in größerem Maßstab durch heterogen katalysierte hydrierungen. *Angew. Chem.* **1993**, *105*, 1370-1372.

(26) Adhiya, A.; Wesdemiotis, C. Poly(propylene imine) dendrimer conformations in the gas phase: a tandem mass spectrometry study. *Int. J. Mass Spectrom.* **2002**, *214*, 75-88.

(27) Scherrenberg, R.; Coussens, B.; van Vliet, P.; Edouard, G.; Brackman, J.; de Brabander, E.; Mortensen, K. The molecular characteristics of poly(propyleneimine) dendrimers as studied with small-angle neutron scattering, viscosimetry, and molecular dynamics. *Macromolecules* **1998**, *31*, 456-461.

(28) Chung, Y. M.; Rhee, H. K. Synthesis and catalytic applications of dendrimer-templated bimetallic nanoparticles. *Catal. Surv. Asia* **2004**, *8*, 211-223.

(29) Crooks, R. M.; Zhao, M. Q.; Sun, L.; Chechik, V.; Yeung, L. K. Dendrimer-encapsulated metal nanoparticles: Synthesis, characterization, and applications to catalysis. *Acc. Chem. Res.* **2001**, *34*, 181-190.

(30) Scott, R. W. J.; Wilson, O. M.; Crooks, R. M. Synthesis, characterization, and applications of dendrimer-encapsulated nanoparticles. *J. Phys. Chem., B* **2005**, *109*, 692-704.

(31) Scott, R. W. J.; Datye, A. K.; Crooks, R. M. Bimetallic palladium-platinum dendrimer-encapsulated catalysts. *J. Am. Chem. Soc.* **2003**, *125*, 3708-3709.

(32) Wilson, O. M.; Scott, R. W. J.; Garcia-Martinez, J. C.; Crooks, R. M. Synthesis, characterization, and structure-selective extraction of 1-3-nm diameter AuAg dendrimer-encapsulated bimetallic nanoparticles. *J. Am. Chem. Soc.* **2005**, *127*, 1015-1024.

(33) Knecht, M. R.; Crooks, R. M. Magnetic properties of dendrimer-encapsulated iron nanoparticles containing an average of 55 and 147 atoms. *New J. Chem.* **2007**, *31*, 1349-1353.

(34) Zhao, M.; Crooks, R. M. Intradendrimer exchange of metal nanoparticles. *Chem. Mater.* **1999**, *11*, 3379-3385.

(35) Knecht, M. R.; Garcia-Martinez, J. C.; Crooks, R. M. Synthesis, characterization, and magnetic properties of dendrimer-encapsulated nickel nanoparticles containing <150 Atoms. *Chem. Mater.* **2006**, *18*, 5039-5044.

(36) Esumi, K.; Miyamoto, K.; Yoshimura, T. Comparison of PAMAM-Au and PPI-Au nanocomposites and their catalytic activity for reduction of 4-nitrophenol. *J. Colloid. Interface. Sci.* **2002**, *254*, 402-405.

(37) Esumi, K.; Hayakawa, K.; Yoshimura, T. Morphological change of gold-dendrimer nanocomposites by laser irradiation. *J. Colloid. Interface. Sci.* **2003**, *268*, 501-506.

(38) Esumi, K.; Isono, R.; Yoshimura, T. Preparation of PAMAM- and PPI-Metal (silver, platinum, and palladium) nanocomposites and their catalytic activities for reduction of 4-nitrophenol. *Langmuir* **2004**, *20*, 237-243.

(39) Chai, M. NMR investigation on the complexation of PPI-3 with zinc (II) ions. *Polym. Prepr. (Am. Chem. Soc., Div. Polym. Chem.)* **2004**, *45*, 581-582.

(40) Chai, M. Synthesis and characterization of PPI-3 encapsulated metal nanoparticles. *Polym. Prepr. (Am. Chem. Soc., Div. Polym. Chem.)* **2003**, *44*, 296-297.

(41) Luo, Y.; Sun, X. Rapid, single-step preparation of dendrimer-protected silver nanoparticles through a microwave-based thermal process. *Mater. Lett.* **2007**, *61*, 1622-1624.

(42) Sun, X.; Dong, S.; Wang, E. One-step preparation and characterization of poly(propyleneimine) dendrimer-protected silver nanoclusters. *Macromolecules* **2004**, *37*, 7105-7108.

(43) Esumi, K.; Matsumoto, T.; Seto, Y.; Yoshimura, T. Preparation of gold-, gold/silver-dendrimer nanocomposites in the presence of benzoin in ethanol by UV irradiation. *J. Colloid. Interface. Sci.* **2005**, *284*, 199-203.

(44) Esumi, K. Synthesis and catalytic property of dendrimer-metal nanocomposites. *Polym. Prepr. (Am. Chem. Soc., Div. Polym. Chem.)* **2004**, *45*, 460-461.

(45) Hayakawa, K.; Yoshimura, T.; Esumi, K. Preparation of gold-dendrimer nanocomposites by laser irradiation and their catalytic reduction of 4-nitrophenol. *Langmuir* **2003**, *19*, 5517-5521.

(46) Luo, Y. Size-controlled preparation of dendrimer-protected gold nanoparticles: A sunlight irradiation-based strategy. *Mater. Lett.* **2008**, *62*, 3770-3772.

(47) Sun, X.; Luo, Y. Size-controlled synthesis of dendrimer-protected gold nanoparticles by microwave radiation. *Mater. Lett.* **2005**, *59*, 4048-4050.

(48) Sun, X.; Jiang, X.; Dong, S.; Wang, E. One-step synthesis and size control of dendrimer-protected gold nanoparticles: A heat-treatment-based strategy. *Macromol. Rapid Commun.* **2003**, *24*, 1024-1028.

(49) Vohs, J. K.; Brege, J. J.; Raymond, J. E.; Brown, A. E.; Williams, G. L.; Fahlman, B. D. Low-temperature growth of carbon nanotubes from the catalytic decomposition of carbon tetrachloride. *J. Am. Chem. Soc.* **2004**, *126*, 9936-9937.

(50) Juttukonda, V.; Paddock, R. L.; Raymond, J. E.; Denomme, D.; Richardson, A. E.; Slusher, L. E.; Fahlman, B. D. Facile synthesis of tin oxide nanoparticles stabilized by dendritic polymers. *J. Am. Chem. Soc.* **2006**, *128*, 420-421.

(51) Niu, Y. Preparation of Dendrimer-encapsulated metal nanoparticles using organic solvents. *Chem. Mater.* **2003**, *15*, 3463-3467.

(52) Yeung, L. K.; Crooks, R. M. Heck Heterocoupling within a dendritic nanoreactor. *Nano Lett.* **2000**, *1*, 14-17.

(53) Ooe, M.; Murata, M.; Mizugaki, T.; Ebitani, K.; Kaneda, K. Dendritic nanoreactors encapsulating Pd particles for substrate-specific hydrogenation of olefins. *Nano Lett.* **2002**, *2*, 999-1002.

(54) Pietsch, T.; Appelhans, D.; Gindy, N.; Voit, B.; Fahmi, A. Oligosaccharide-modified dendrimers for templating gold nanoparticles: Tailoring the particle size as a function of dendrimer generation and -molecular structure. *Colloids Surf., A* **2009**, *341*, 93-102.

(55) Donners, J. J. J. M.; Hoogenboom, R.; Schenning, A. P. H. J.; van Hal, P. A.; Nolte, R. J. M.; Meijer, E. W.; Sommerdijk, N. A. J. M. Fabrication of organic-inorganic semiconductor composites utilizing the different aggregation states of a single amphiphilic dendrimer. *Langmuir* **2002**, *18*, 2571-2576.

(56) Sun, L.; Crooks, R. M. Dendrimer-mediated immobilization of catalytic nanoparticles on flat, solid supports. *Langmuir* **2002**, *18*, 8231-8236.

(57) Lang, H. F.; May, R. A.; Iversen, B. L.; Chandler, B. D. Dendrimer-encapsulated nanoparticle precursors to supported platinum catalysts. *J. Am. Chem. Soc.* **2003**, *125*, 14832-14836.

(58) Scott, R. W. J.; Wilson, O. M.; Crooks, R. M. Titania-supported Au and Pd composites synthesized from dendrimer-encapsulated metal nanoparticle precursors. *Chem. Mater.* **2004**, *16*, 5682-5688.

(59) Deutsch, D. S.; Lafaye, G.; Liu, D. X.; Chandler, B.; Williams, C. T.; Amiridis, M. D. Decomposition and activation of Pt-dendrimer nanocomposites on a silica support. *Catal. Lett.* **2004**, *97*, 139-143.

(60) Scott, R. W. J.; Sivadinarayana, C.; Wilson, O. M.; Yan, Z.; Goodman, D. W.; Crooks, R. M. Titania-supported PdAu bimetallic catalysts prepared from dendrimer-encapsulated nanoparticle precursors. *J. Am. Chem. Soc.* **2005**, *127*, 1380-1381.

(61) Rogers, M. C.; Adisa, B.; Bruce, D. A. Synthesis and characterization of dendrimer-templated mesoporous oxidation catalysts. *Catal. Lett.* **2004**, *98*, 29-36.

(62) Bar, G.; Rubin, S.; Cutts, R. W.; Taylor, T. N.; Zawodzinski, T. A. Dendrimer-modified silicon oxide surfaces as platforms for the deposition of gold and silver colloid monolayers: Preparation method, characterization, and correlation between microstructure and optical properties. *Langmuir* **1996**, *12*, 1172-1179.

(63) Velarde-Ortiz, R.; Larsen, G. A poly(propylene imine) (DAP-Am-64) dendrimer as Cu^{2+} chelator for the synthesis of copper oxide clusters embedded in sol-gel derived matrixes. *Chem. Mater.* **2002**, *14*, 858-866.

(64) Choi, H. C.; Kim, W.; Wang, D. W.; Dai, H. J. Delivery of catalytic metal species onto surfaces with dendrimer carriers for the synthesis of carbon nanotubes with narrow diameter distribution. *J. Phys. Chem. B* **2002**, *106*, 12361-12365.

(65) Amama, P. B.; Maschmann, M. R.; Fisher, T. S.; Sands, T. D. Dendrimer-templated Fe nanoparticles for the growth of single-wall carbon nanotubes by plasma-enhanced CVD. *J. Phys. Chem. B* **2006**, *110*, 10636-10644.

(66) Amama, P. B.; Cola, B. A.; Sands, T. D.; Xu, X. F.; Fisher, T. S. Dendrimer-assisted controlled growth of carbon nanotubes for enhanced thermal interface conductance. *Nanotechnology* **2007**, *18*, 385303-385306.

(67) Finney, E. E.; Finke, R. G. Nanocluster nucleation and growth kinetic and mechanistic studies: A review emphasizing transition-metal nanoclusters. *J. Colloid. Interface. Sci.* **2008**, *317*, 351-374.

(68) Murray, C. B.; Kagan, C. R.; Bawendi, M. G. Synthesis and characterization of monodisperse nanocrystals and close-packed nanocrystal assemblies. *Annu. Rev. Mater. Sci.* **2000**, *30*, 545-610.

(69) Pileni, M. P. Nanocrystals: fabrication, organization and collective properties. *C.R. Chimie* **2003**, *6*, 965-978.

(70) Rinaldi, R.; Porcari, A. d. M.; Rocha, T. C. R.; Cassinelli, W. H.; Ribeiro, R. U.; Bueno, J. M. C.; Zanchet, D. Construction of heterogeneous Ni catalysts from supports and colloidal nanoparticles - A challenging puzzle. *J. Mol. Catal. A: Chem* **2009**, *301*, 11-17.

(71) Rockenberger, J.; Scher, E. C.; Alivisatos, A. P. A new nonhydrolytic single-precursor approach to surfactant-capped nanocrystals of transition metal oxides. *J. Am. Chem. Soc.* **1999**, *121*, 11595-11596.

(72) Casula, M. F.; Jun, Y. W.; Zaziski, D. J.; Chan, E. M.; Corrias, A.; Alivisatos, A. P. The concept of delayed nucleation in nanocrystal growth demonstrated for the case of iron oxide nanodisks. *J. Am. Chem. Soc.* **2006**, *128*, 1675-1682.

(73) Canton, P.; Menegazzo, F.; Polizzi, S.; Pinna, F.; Pernicone, N.; Riello, P.; Fagherazzi, G. Structure and size of poly-domain Pd nanoparticles supported on silica. *Catal. Lett.* **2003**, *88*, 141-146.

(74) Alcala, M. D.; Real, C. Synthesis based on the wet impregnation method and characterization of iron and iron oxide-silica nanocomposites. *Solid State Ionics* **2006**, *177*, 955-960.

(75) Che, M.; Cheng, Z. X.; Louis, C. Nucleation and particle growth-processes involved in the preparation of silica-supported nickel materials by a 2-step procedure. *J. Am. Chem. Soc.* **1995**, *117*, 2008-2018.

(76) Singh, A.; Chandler, B. D. Low-temperature activation conditions for PAMAM dendrimer templated Pt nanoparticles. *Langmuir* **2005**, *21*, 10776-10782.

(77) Hayashi, H.; Chen, L. Z.; Tago, T.; Kishida, M.; Wakabayashi, K. Catalytic properties of Fe/SiO_2 catalysts prepared using microemulsion for CO hydrogenation. *Appl. Catal., A* **2002**, *231*, 81-89.

(78) Park, Y.; Kang, T.; Kim, P.; Yi, J. Encapsulation method for the dispersion of NiO onto ordered mesoporous silica, SBA-15, using polyethylene oxide (PEO). *J. Colloid. Interface. Sci.* **2006**, *295*, 464-471.

(79) Cheng, Z. X.; Louis, C.; Che, M. Nucleation and particle growth in the preparation of silica-supported nickel-catalysts by a 2-step procedure. *Z. Phys. D. Atom Mol. Cl.* **1991**, *20*, 445-448.

(80) Holmberg, K. Surfactant-templated nanomaterials synthesis. *J. Colloid. Interface. Sci.* **2004**, *274*, 355-364.

(81) Tsoncheva, T.; Rosenholm, J.; Linden, M.; Kleitz, F.; Tiemann, M.; Ivanova, L.; Dimitrov, M.; Paneva, D.; Mitov, I.; Minchev, C. Critical evaluation of the state of iron oxide nanoparticles on different mesoporous silicas prepared by an impregnation method. *Micropor. Mesopor. Mat.* **2008**, *112*, 327-337.

(82) Tsoncheva, T.; Roggenbuck, J.; Tiemann, M.; Ivanova, L.; Paneva, D.; Mitov, I.; Minchev, C. Iron oxide nanoparticles supported on mesoporous MgO and CeO_2: A comparative physicochemical and catalytic study. *Micropor. Mesopor. Mat.* **2008**, *110*, 339-346.

(83) Alam, S.; Anand, C.; Logudurai, R.; Balasubramanian, V. V.; Ariga, K.; Bose, A. C.; Mori, T.; Srinivasu, P.; Vinu, A. Comparative study on the magnetic properties of iron oxide nanoparticles loaded on mesoporous silica and carbon materials with different structure. *Micropor. Mesopor. Mat.* **2009**, *121*, 178-184.

(84) Gates, B. C. Supported metal clusters: Synthesis, structure, and catalysis. *Chem. Rev.* **1995**, *95*, 511-522.

(85) Lewis, L. N. Chemical catalysis by colloids and clusters. *Chem. Rev.* **1993**, *93*, 2693-2730.

(86) Wang, A.; Yin, H.; Lu, H.; Xue, J.; Ren, M.; Jiang, T. Effect of organic modifiers on the structure of nickel nanoparticles and catalytic activity in the hydrogenation of p-nitrophenol to p-aminophenol. *Langmuir* **2009**, *25*, 12736-12741.

(87) Lee, I. S.; Lee, N.; Park, J.; Kim, B. H.; Yi, Y.-W.; Kim, T.; Kim, T. K.; Lee, I. H.; Paik, S. R.; Hyeon, T. Ni/NiO core/shell nanoparticles for selective binding and magnetic separation of histidine-tagged proteins. *J. Am. Chem. Soc.* **2006**, *128*, 10658-10659.

(88) Wu, S. H.; Chen, D. H. Synthesis and characterization of nickel nanoparticles by hydrazine reduction in ethylene glycol. *J. Colloid. Interface. Sci.* **2003**, *259*, 282-286.

(89) Bai, L.; Yuan, F.; Tang, Q. Synthesis of nickel nanoparticles with uniform size via a modified hydrazine reduction route. *Mater. Lett.* **2008**, *62*, 2267-2270.

(90) Duan, Y.; Li, J. Structure study of nickel nanoparticles. *Mater. Chem. Phys.* **2004**, *87*, 452-454.

(91) Hald, P.; Bremholm, M.; Iversen, S. B.; Iversen, B. B. Surfactant-free synthesis of nickel nanoparticles in near-critical water. *J. Solid State Chem.* **2008**, *181*, 2681-2683.

(92) Libor, Z.; Zhang, Q. The synthesis of nickel nanoparticles with controlled morphology and SiO_2/Ni core-shell structures. *Mater. Chem. Phys.* **2009**, *114*, 902-907.

(93) Ni, X.; Zhao, Q.; Zheng, H.; Li, B.; Song, J.; Zhang, D.; Zhang, X. A novel chemical reduction route towards the synthesis of crystalline nickel nanoflowers from a mixed source. *Eur. J. Inorg. Chem.* **2005**, *2005*, 4788-4793.

(94) Roy, A.; Srinivas, V.; Ram, S.; De Toro, J. A.; Riveiro, J. M. Effect of interstitial oxygen on the crystal structure and magnetic properties of Ni nanoparticles. *J. Appl. Phys.* **2004**, *96*, 6782-6788.

(95) Roy, A.; Srinivas, V.; Ram, S.; De Toro, J. A.; Goff, J. P. A comprehensive structural and magnetic study of Ni nanoparticles prepared by the borohydride reduction of $NiCl_2$ solution of different concentrations. *J. Appl. Phys.* **2006**, *100*, 094307.

(96) Nayak, B. B.; Vitta, S.; Nigam, A. K.; Bahadur, D. Ni and Ni-nickel oxide nanoparticles with different shapes and a core-shell structure. *Thin Solid Films* **2006**, *505*, 109-112.

(97) Kudlash, A. N.; Vorobyova, S. A.; Lesnikovich, A. I. Interphase synthesis and some characteristics of aqueous nickel dispersions. *J. Phys. Chem. Solids* **2008**, *69*, 1652-1656.

(98) Liu, Y. C.; Huang, C. Y.; Chen, Y. W. Hydrogenation of p-chloronitrobenzene on Ni-B nanometal catalysts. *J. Nanopart. Res.* **2006**, *8*, 223-234.

(99) Pileni, M. P. The role of soft colloidal templates in controlling the size and shape of inorganic nanocrystals. *Nat. Mater.* **2003**, *2*, 145-150.

(100) Hou, Y.; Gao, S. Monodisperse nickel nanoparticles prepared from a monosurfactant system and their magnetic properties. *J. Mater. Chem.* **2003**, *13*, 1510-1512.

(101) Hou, Y.; Kondoh, H.; Ohta, T.; Gao, S. Size-controlled synthesis of nickel nanoparticles. *Appl. Surf. Sci.* **2005**, *241*, 218-222.

(102) Luo, X.; Chen, Y.; Yue, G.-H.; Peng, D.-L.; Luo, X. Preparation of hexagonal close-packed nickel nanoparticles via a thermal decomposition approach using nickel acetate tetrahydrate as a precursor. *J. Alloys Compd.* **2009**, *476*, 864-868.

(103) Mourdikoudis, S.; Simeonidis, K.; Vilalta-Clemente, A.; Tuna, F.; Tsiaoussis, I.; Angelakeris, M.; Dendrinou-Samara, C.; Kalogirou, O. Controlling the crystal structure of Ni nanoparticles by the use of alkylamines. *J. Magn. Magn. Mater.* **2009**, *321*, 2723-2728.

(104) Khanna, P. K.; More, P. V.; Jawalkar, J. P.; Bharate, B. G. Effect of reducing agent on the synthesis of nickel nanoparticles. *Mater. Lett.* **2009**, *63*, 1384-1386.

(105) Sidhaye, D. S.; Bala, T.; Srinath, S.; Srikanth, H.; Poddar, P.; Sastry, M.; Prasad, B. L. V. Preparation of nearly monodisperse nickel nanoparticles by a facile solution based methodology and their ordered assemblies. *J. Phys. Chem. C* **2009**, *113*, 3426-3429.

(106) De Biasi, E.; León-Vanegas, A.; Nunes, W. C.; Sharma, S. K.; Haddad, P.; Rocha, T. C. R.; Santos Duque, J. G.; Zanchet, D.; Knobel, M. Complex magnetic internal order in structurally disordered Ni nanoparticles. *Eur. Phys. J. B* **2008**, *66*, 503-508.

(107) Johnston-Peck, A. C.; Wang, J.; Tracy, J. B. Synthesis and structural and magnetic characterization of Ni(Core)/NiO(Shell) nanoparticles. *ACS Nano* **2009**, *3*, 1077-1084.

(108) Chiang, S. J.; Liaw, B. J.; Chen, Y. Z. Preparation of NiB nanoparticles in water-in-oil microemulsions and their catalysis during hydrogenation of carbonyl and olefinic groups. *Appl. Catal. A* **2007**, *319*, 144-152.

(109) Singla, M. L.; Negi, A.; Mahajan, V.; Singh, K. C.; Jain, D. V. S. Catalytic behavior of nickel nanoparticles stabilized by lower alkylammonium bromide in aqueous medium. *Appl. Catal., A* **2007**, *323*, 51-57.

(110) Zhang, D. E.; Ni, X. M.; Zheng, H. G.; Li, Y.; Zhang, X. J.; Yang, Z. P. Synthesis of needle-like nickel nanoparticles in water-in-oil microemulsion. *Mater. Lett.* **2005**, *59*, 2011-2014.

(111) Abdel-Aal, E. A.; Malekzadeh, S. M.; Rashad, M. M.; El-Midany, A. A.; El-Shall, H. Effect of synthesis conditions on preparation of nickel metal nanopowders via hydrothermal reduction technique. *Powder Technol.* **2007**, *171*, 63-68.

(112) Chen, D. H.; Wu, S. H. Synthesis of nickel nanoparticles in water-in-oil microemulsions. *Chem. Mater.* **2000**, *12*, 1354-1360.

(113) You-xian, Z.; Fu, W.-j.; An, X.-q. Preparation of nickel nanoparticles in emulsion. *Trans. Nonferrous Met. Soc. China* **2008**, *18*, 212-216.

(114) Legrand, J.; Taleb, A.; Gota, S.; Guittet, M. J.; Petit, C. Synthesis and XPS characterization of nickel boride nanoparticles. *Langmuir* **2002**, *18*, 4131-4137.

(115) Gornostaeva, S. V.; Fenin, A. A.; Revina, A. A.; Ermakov, V. I. Influence of the composition of the inverse micelle solution on the formation of nickel nanoparticles under the effect of gamma-Rays of Co-60. *Theor. Found. Chem. Eng.* **2008**, *42*, 599-602.

(116) Gornostaeva, S.; Revina, A.; Belyakova, L.; Larionov, O. Synthesis and properties of nickel nanoparticles and their nanocomposites. *Prot. Met.* **2008**, *44*, 372-375.

(117) Wang, H.; Jiao, X.; Chen, D. Monodispersed nickel nanoparticles with tunable phase and size: Synthesis, characterization, and magnetic properties. *J. Phys. Chem. C* **2008**, *112*, 18793-18797.

(118) Glavee, G. N.; Klabunde, K. J.; Sorensen, C. M.; Hadjipanayis, G. C. Borohydride reduction of nickel and copper ions in aqueous and nonaqueous media - Controllable chemistry leading to nanoscale metal and metal boride particles. *Langmuir* **1994**, *10*, 4726-4730.

(119) Xu, R.; Xie, T.; Zhao, Y. G.; Li, Y. D. Quasi-homogeneous catalytic hydrogenation over monodisperse nickel and cobalt nanoparticles. *Nanotechnology* **2007**, *18*, 055602.

(120) Ningthoujam, R. S.; Gajbhiye, N. S.; Sharma, S. Reduction mechanism of Ni^{2+} into Ni nanoparticles prepared from different precursors: Magnetic studies. *Pramana-J. Phys.* **2009**, *72*, 577-586.

(121) Wang, H.; Kou, X.; Zhang, L.; Li, J. Size-controlled synthesis, microstructure and magnetic properties of Ni nanoparticles. *Mater. Res. Bull.* **2008**, *43*, 3529-3536.

(122) Wang, H. Z.; Kou, X. L.; Mang, B.; Li, J. L. Large scale synthesis and characterization of Ni nanoparticles by solution reduction method. *Bull. Mater. Sci.* **2008**, *31*, 97-100.

(123) Chen, L.; Chen, J. M.; Zhou, H. D.; Zhang, D. J.; Wan, H. Q. Synthesis of dodecanethiol monolayer-stabilized nickel nanoparticles. *Mater. Sci. Eng. A* **2007**, *452*, 262-266.

(124) Couto, G. G.; Klein, J. J.; Schreiner, W. H.; Mosca, D. H.; de Oliveira, A. J. A.; Zarbin, A. J. G. Nickel nanoparticles obtained by a modified polyol process: Synthesis, characterization, and magnetic properties. *J. Colloid. Interface. Sci.* **2007**, *311*, 461-468.

(125) Metin, Ö.; Özkar, S. Synthesis and characterization of poly(N-vinyl-2-pyrrolidone)-stabilized water-soluble nickel(0) nanoclusters as catalyst for hydrogen generation from the hydrolysis of sodium borohydride. *J. Mol. Catal. A: Chem* **2008**, *295*, 39-46.

(126) Sun, Y. P.; Rollins, H. W.; Guduru, R. Preparations of nickel, cobalt, and iron nanoparticles through the rapid expansion of supercritical fluid solutions (RESS) and chemical reduction. *Chem. Mater.* **1999**, *11*, 7-9.

(127) Hou, Y.-L.; Gao, S. Solvothermal reduction synthesis and magnetic properties of polymer protected iron and nickel nanocrystals. *J. Alloys Compd.* **2004**, *365*, 112-116.

(128) Xu, W.; Liew, K. Y.; Liu, H.; Huang, T.; Sun, C.; Zhao, Y. Microwave-assisted synthesis of nickel nanoparticles. *Mater. Lett.* **2008**, *62*, 2571-2573.

(129) Domínguez-Crespo, M. A.; Ramírez-Meneses, E.; Montiel-Palma, V.; Torres Huerta, A. M.; Dorantes Rosales, H. Synthesis and electrochemical characterization of stabilized nickel nanoparticles. *Int. J. Hydrogen Energy* **2009**, *34*, 1664-1676.

(130) Ely, T. O. Synthesis of nickel nanoparticles. Influence of aggregation induced by modification of poly(vinylpyrrolidone) chain length on their magnetic properties. *Chem. Mater.* **1999**, *11*, 526-529.

(131) Suh, Y. J.; Jang, H. D.; Chang, H. K.; Hwang, D. W.; Kim, H. C. Kinetics of gas phase reduction of nickel chloride in preparation for nickel nanoparticles. *Mater. Res. Bull.* **2005**, *40*, 2100-2109.

(132) Alonso, F.; Riente, P.; Yus, M. Hydrogen-transfer reduction of carbonyl compounds promoted by nickel nanoparticles. *Tetrahedron* **2008**, *64*, 1847-1852.

(133) Zhang, Z.; Chen, X.; Zhang, X.; Shi, C. Synthesis and magnetic properties of nickel and cobalt nanoparticles obtained in DMF solution. *Solid State Commun.* **2006**, *139*, 403-405.

(134) Zhang, H. T.; Wu, G.; Chen, X. H.; Qiu, X. G. Synthesis and magnetic properties of nickel nanocrystals. *Mater. Res. Bull.* **2006**, *41*, 495-501.

(135) Kim, S.-G.; Terashi, Y.; Purwanto, A.; Okuyama, K. Synthesis and film deposition of Ni nanoparticles for base metal electrode applications. *Colloids Surf., A* **2009**, *337*, 96-101.

(136) Rellinghaus, B.; Stappert, S.; Wassermann, E. F.; Sauer, H.; Spliethoff, B. The effect of oxidation on the structure of nickel nanoparticles. *Eur. Phys .J. D* **2001**, *16*, 249-252.

(137) Jung, K. Y.; Lee, J. H.; Koo, H. Y.; Kang, Y. C.; Park, S. B. Preparation of solid nickel nanoparticles by large-scale spray pyrolysis of $Ni(NO_3)_2 \cdot 6H_2O$ precursor: Effect of temperature and nickel acetate on the particle morphology. *Mater. Sci. Eng., B* **2007**, *137*, 10-19.

(138) Wei, Z.; Yan, P.; Feng, W.; Dai, J.; Wang, Q.; Xia, T. Microstructural characterization of Ni nanoparticles prepared by anodic arc plasma. *Mater. Charact.* **2006**, *57*, 176-181.

(139) Wei, Z.; Xia, T.; Ma, J.; Feng, W.; Dai, J.; Wang, Q.; Yan, P. Investigation of the lattice expansion for Ni nanoparticles. *Mater. Charact.* **2007**, *58*, 1019-1024.

(140) Duan, H.; Lin, X.; Liu, G.; Xu, L.; Li, F. Synthesis of Ni nanoparticles and their catalytic effect on the decomposition of ammonium perchlorate. *J. Mater. Process. Technol.* **2008**, *208*, 494-498.

(141) Chang, H.; Su, H.-T. Synthesis and magnetic properties of Ni nanoparticles. *Rev. Adv. Mater. Sci.* **2008**, *18*, 667-675.

(142) Moon, Y. K.; Lee, J. K.; Kim, J. G.; Jung, M. Y.; Lee, J. B.; Kim, S. H. Sintering kinetic measurement of nickel nanoparticle agglomerates by electrical mobility classification. *Curr. Appl Phys.* **2009**, *9*, 928-932.

(143) Amoruso, S.; Ausanio, G.; de Lisio, C.; Iannotti, V.; Vitiello, M.; Wang, X.; Lanotte, L. Synthesis of nickel nanoparticles and nanoparticles magnetic films by femtosecond laser ablation in vacuum. *Appl. Surf. Sci.* **2005**, *247*, 71-75.

(144) Mahfouz, R.; Cadete Santos Aires, F. J.; Brenier, A.; Jacquier, B.; Bertolini, J. C. Synthesis and physico-chemical characteristics of nanosized particles produced by laser ablation of a nickel target in water. *Appl. Surf. Sci.* **2008**, *254*, 5181-5190.

(145) Zhang, J.; Lan, C. Q. Nickel and cobalt nanoparticles produced by laser ablation of solids in organic solution. *Mater. Lett.* **2008**, *62*, 1521-1524.

(146) Wang, H.; Han, L.; Hu, H.; Northwood, D. O. The hydrolysis behaviour of Mg_2Ni and Mg_2NiH_4 in water or a 6 M KOH solution and its application to Ni nanoparticles synthesis. *J. Alloys Compd.* **2009**, *470*, 539-543.

(147) Gong, J.; Wang, L. L.; Liu, Y.; Yang, J. H.; Zong, Z. G. Structural and magnetic properties of hcp and fcc Ni nanoparticles. *J. Alloys Compd.* **2008**, *457*, 6-9.

(148) delMonte, F.; Morales, M. P.; Levy, D.; Fernandez, A.; Ocana, M.; Roig, A.; Molins, E.; OGrady, K.; Serna, C. J. Formation of γ-Fe_2O_3 isolated nanoparticles in a silica matrix. *Langmuir* **1997**, *13*, 3627-3634.

(149) Ennas, G.; Musinu, A.; Piccaluga, G.; Zedda, D.; Gatteschi, D.; Sangregorio, C.; Stanger, J. L.; Concas, G.; Spano, G. Characterization of iron oxide nanoparticles in an Fe_2O_3-SiO_2 composite prepared by a sol-gel method. *Chem. Mater.* **1998**, *10*, 495-502.

(150) Solinas, S.; Piccaluga, G.; Morales, M. P.; Serna, C. J. Sol-gel formation of γ-Fe_2O_3/SiO_2 nanocomposites. *Acta. Mater.* **2001**, *49*, 2805-2811.

(151) Bruni, S.; Cariati, F.; Casu, M.; Lai, A.; Musinu, A.; Piccaluga, G.; Solinas, S. IR and NMR study of nanoparticle-support interactions in a Fe_2O_3-SiO_2 nanocomposite prepared by a sol-gel method. *Nanostruct. Mater.* **1999**, *11*, 573-586.

(152) Chaneac, C.; Tronc, E.; Jolivet, J. P. Thermal behavior of spinel iron oxide-silica composites. *Nanostruct. Mater.* **1995**, *6*, 715-718.

(153) Ida, T.; Tsuiki, H.; Ueno, A.; Tohji, K.; Udagawa, Y.; Iwai, K.; Sano, H. Characterization of iron-oxide in Fe_2O_3/SiO_2 catalyst. *J. Catal.* **1987**, *106*, 428-439.

(154) Hong, F.; Yang, B. L.; Schwartz, L. H.; Kung, H. H. Crystallite size effect in the selective oxidation of butene to butadiene on iron-oxide .1. Mossbauer, X-Ray, and magnetization characterization of the catalysts. *J. Phys. Chem.* **1984**, *88*, 2525-2530.

(155) Rostovshchikova, T.; Kiseleva, O.; Smirnov, V.; Maksimov, Y.; Suzdalev, I.; Prusakov, V.; Tsodikov, M.; Ikorskii, V. Catalytic conversions of chloroolefines over iron oxide nanoparticles 3. Electronic and magnetic properties of γ-Fe_2O_3 nanoparticles immobilized on different silicas. *Russ. Chem. Bull.* **2006**, *55*, 1768-1774.

(156) O'Shea, V. A. D.; Alvarez-Galvan, M. C.; Campos-Martin, J. M.; Menendez, N. N.; Tornero, J. D.; Fierro, J. L. G. Surface and structural features of Co-Fe oxide nanoparticles deposited on a silica substrate. *Eur. J. Inorg. Chem.* **2006**, 5057-5068.

(157) Dimitrov, M.; Ivanova, L.; Paneva, D.; Tsoncheva, T.; Stavrev, S.; Mitov, I.; Minchev, C. Iron oxide nanoparticles supported on ultradispersed diamond powders: Effect of the preparation procedure. *Appl. Surf. Sci.* **2009**, *255*, 4322-4328.

(158) Szabó, T.; et al. Magnetic iron oxide/clay composites: effect of the layer silicate support on the microstructure and phase formation of magnetic nanoparticles. *Nanotechnology* **2007**, *18*, 285602.

(159) Gervasini, A.; Messi, C.; Ponti, A.; Cenedese, S.; Ravasio, N. Nanodispersed Fe oxide supported catalysts with tuned properties. *J. Phys. Chem. C* **2008**, *112*, 4635-4642.

(160) Messi, C.; Carniti, P.; Gervasini, A. Kinetics of reduction of supported nanoparticles of iron oxide. *J. Therm. Anal. Cal.* **2008**, *91*, 93-100.

(161) Choi, H. C.; Kundaria, S.; Wang, D. W.; Javey, A.; Wang, Q.; Rolandi, M.; Dai, H. J. Efficient formation of iron nanoparticle catalysts on silicon oxide by hydroxylamine for carbon nanotube synthesis and electronics. *Nano Lett.* **2003**, *3*, 157-161.

(162) Rostovshchikova, T.; Korobov, M.; Pankratov, D.; Yurkov, G.; Gubin, S. Catalytic conversions of chloroolefins over iron oxide nanoparticles 2. Isomerization of dichlorobutenes over iron oxide nanoparticles stabilized on the surface of ultradispersed poly(tetrafluoroethylene). *Russ. Chem. Bull.* **2005**, *54*, 1425-1432.

(163) Gmucová, K.; Weis, M.; Nádazdy, V.; Capek, I.; Satka, A.; Chitu, L.; Cirák, J.; Majková, E. Effect of charged deep states in hydrogenated amorphous silicon on the behavior of iron oxides nanoparticles deposited on its surface. *Appl. Surf. Sci.* **2008**, *254*, 7008-7013.

(164) Drbohlavova, J.; Hrdy, R.; Adam, V.; Kizek, R.; Schneeweiss, O.; Hubalek, J. preparation and properties of various magnetic nanoparticles. *Sensors* **2009**, *9*, 2352-2362.

(165) Kohn, R.; Froba, M. Nanoparticles of 3d transition metal oxides in mesoporous MCM-48 silica host structures: Synthesis and characterization. *Catal. Today* **2001**, *68*, 227-236.

(166) Kohn, R.; Paneva, D.; Dimitrov, M.; Tsoncheva, T.; Mitov, I.; Minchev, C.; Froba, M. Studies on the state of iron oxide nanoparticles in MCM-41 and MCM-48 silica materials. *Micropor. Mesopor. Mat.* **2003**, *63*, 125-137.

(167) Huwe, H.; Froba, M. Synthesis and characterization of transition metal and metal oxide nanoparticles inside mesoporous carbon CMK-3. *Carbon* **2007**, *45*, 304-314.

(168) Schnitzler, M. C.; Mangrich, A. S.; Macedo, W. A. A.; Ardisson, J. D.; Zarbin, A. J. G. Incorporation, oxidation and pyrolysis of ferrocene into porous silica glass: a route to different silica/carbon and silica/iron oxide nanocomposites. *Inorg. Chem.* **2006**, *45*, 10642-10650.

(169) Ding, L.; Zhou, W. W.; Chu, H. B.; Jin, Z.; Zhang, Y.; Li, Y. Direct preparation and patterning of iron oxide nanoparticles via microcontact printing on silicon wafers for the growth of single-walled carbon nanotubes. *Chem. Mater.* **2006**, *18*, 4109-4114.

(170) Taylor, P. H.; Lenoir, D. Chloroaromatic formation in incineration processes. *Sci. Total Environ.* **2001**, *269*, 1-24.

(171) Pekarek, V.; Weber, R.; Grabic, R.; Solcova, O.; Fiserova, E.; Syc, M.; Karban, J. Matrix effects on the de novo synthesis of polychlorinated dibenzo-*p*-dioxins, dibenzofurans, biphenyls and benzenes. *Chemosphere* **2007**, *68*, 51-61.

(172) Lavric, E. D.; Konnov, A. A.; De Ruyck, J. Modeling the formation of precursors of dioxins during combustion of woody fuel volatiles. *Fuel* **2005**, *84*, 323-334.

(173) Addink, R.; Olie, K. Mechanisms of formation and destruction of polychlorinated dibenzo-*p*-dioxins and dibenzofurans in heterogeneous systems. *Environ. Sci. Technol.* **1995**, *29*, 1425-1435.

(174) Mohapatra, R.; Rao, J. R. Some aspects of characterisation, utilisation and environmental effects of fly ash. *J. Chem. Technol. Biotechnol.* **2001**, *76*, 9-26.

(175) Kauppinen, E. I.; Pakkanen, T. A. Coal combustion aerosols - a field-study. *Environ. Sci. Technol.* **1990**, *24*, 1811-1818.

(176) Tuppurainen, K.; Halonen, I.; Ruokojarvi, P.; Tarhanen, J.; Ruuskanen, J. Formation of PCDDs and PCDFs in municipal waste incineration and its inhibition mechanisms: A review. *Chemosphere* **1998**, *36*, 1493-1511.

(177) Weber, R. Relevance of PCDD/PCDF formation for the evaluation of POPs destruction technologies - Review on current status and assessment gaps. *Chemosphere* **2007**, *67*, S109-S117.

(178) Altwicker, E. R. Formation of PCDD/F in municipal solid waste incinerators: laboratory and modeling studies. *J. Hazard. Mater.* **1996**, *47*, 137-161.

(179) Cains, P. W.; McCausland, L. J.; Fernandes, A. R.; Dyke, P. Polychlorinated dibenzo-*p*-dioxins and dibenzofurans formation in incineration: Effects of fly ash and carbon source. *Environ. Sci. Technol.* **1997**, *31*, 776-785.

(180) Yokohama, N.; Otaka, H.; Minato, I.; Nakata, M. Evaluation of gas-particle partition of dioxins in flue gas I: Evaluation of gasification behavior of polychlorinated dibenzo-*p*-dioxins and polychlorinated dibenzofurans in fly ash by thermal treatment. *J. Hazard. Mater.* **2008**, *153*, 395-403.

(181) Alderman, S. L.; Farquar, G. R.; Poliakoff, E. D.; Dellinger, B. An infrared and X-ray spectroscopic study of the reactions of 2-chlorophenol, 1,2-dichlorobenzene, and chlorobenzene with model CuO/silica fly ash surfaces. *Environ. Sci. Technol.* **2005**, *39*, 7396-7401.

(182) Khachatryan, L.; Dellinger, B. Formation of chlorinated hydrocarbons from the reaction of chlorine atoms and activated carbon. *Chemosphere* **2003**, *52*, 709-716.

(183) Nganai, S.; Lomnicki, S.; Dellinger, B. Ferric oxide mediated formation of PCDD/Fs from 2-monochlorophenol. *Environ. Sci. Technol.* **2009**, *43*, 368-373.

(184) Lomnicki, S.; Dellinger, B. Formation of PCDD/F from the pyrolysis of 2-chlorophenol on the surface of dispersed copper oxide particles. *Proc. Combust. Inst.* **2003**, *29*, 2463-2468.

(185) Lomnicki, S.; Dellinger, B. A detailed mechanism of the surface-mediated formation of PCDD/F from the oxidation of 2-chlorophenol on a CuO/silica surface. *J. Phys. Chem. A* **2003**, *107*, 4387-4395.

(186) Lavric, E. D.; Konnov, A. A.; De Ruyck, J. Surrogate compounds for dioxins in incineration. A review. *Waste Manage.* **2005**, *25*, 755-765.

(187) Blumenstock, M.; Zimmermann, R.; Schramm, K. W.; Kaune, A.; Nikolai, U.; Lenoir, D.; Kettrup, A. Estimation of the dioxin emission (PCDD/FI-TEQ) from the concentration of low chlorinated aromatic compounds in the flue and stack gas of a hazardous waste incinerator. *J. Anal. Appl. Pyrolysis* **1999**, *49*, 179-190.

(188) Zimmermann, R.; Heger, H. J.; Blumenstock, M.; Dorfner, R.; Schramm, K. W.; Boesl, U.; Kettrup, A. On-line measurement of chlorobenzene in waste incineration flue gas as a surrogate for the emission of polychlorinated dibenzo-*p*-dioxins/furans (I-TEQ) using mobile resonance laser ionization time-of-flight mass spectrometry. *Rapid Commun. Mass Spectrom.* **1999**, *13*, 307-314.

(189) Ryu, J. Y.; Mulholland, J. A. Metal-mediated chlorinated dibenzo-p-dioxin (CDD) and dibenzofuran (CDF) formation from phenols. *Chemosphere* **2005**, *58*, 977-988.

(190) Ryu, J.-Y.; Mulholland, J. A.; Kim, D. H.; Takeuchi, M. Homologue and isomer patterns of polychlorinated dibenzo-p-dioxins and dibenzofurans from phenol precursors: Comparison with municipal waste incinerator data. *Environ. Sci. Technol.* **2005**, *39*, 4398-4406.

(191) Tuppurainen, K.; Asikainen, A.; Ruokojarvi, P.; Ruuskanen, J. Perspectives on the formation of polychlorinated dibenzo-p-dioxins and dibenzofurans during municipal solid waste (MSW) incineration and other combustion processes. *Acc. Chem. Res.* **2003**, *36*, 652-658.

(192) Briois, C.; Ryan, S.; Tabor, D.; Touati, A.; Gullett, B. K. Formation of polychlorinated dibenzo-p-dioxins and dibenzofurans from a mixture of chlorophenols over fly ash: Influence of water vapor. *Environ. Sci. Technol.* **2007**, *41*, 850-856.

(193) De Jong, V.; Cieplik, M. K.; Louw, R. Formation of dioxins in the catalytic combustion of chlorobenzene and a micropollutant-like mixture on Pt/γ-Al_2O_3. *Environ. Sci. Technol.* **2004**, *38*, 5217-5223.

(194) Addink, R.; Cnubben, P. A. J. P.; Olie, K. Formation of polychlorinated dibenzo-*p*-dioxins dibenzofurans on fly-ash from precursors and carbon model compounds. *Carbon* **1995**, *33*, 1463-1471.

(195) Nakka, H.; Fullana, A.; Sidhu, S. Surface catalyzed chlorobenzene transformation reactions in post-combustion zone. *Organohalogen Compd.* **2004**, *66*, 1140-1145.

(196) van den Brink, R. W.; Krzan, M.; Feijen-Jeurissen, M. M. R.; Louw, R.; Mulder, P. The role of the support and dispersion in the catalytic combustion of chlorobenzene on noble metal based catalysts. *Appl. Catal., B* **2000**, *24*, 255-264.

CHAPTER 2

ANALYTICAL TECHNIQUES AND METHODS

2.1 Analytical Techniques

2.1.1 Ultraviolet-visible (UV-vis) Spectroscopy

UV-vis spectroscopy was performed on a Varian Cary 50 Bio UV-vis spectrophotometer. This instrument was equipped with a Xenon flash lamp. The scan rate for each run was 600 nm min^{-1}, with a scan range varying from 300 to 800 nm. Before each run, background subtraction was performed with the solvent system of choice. The measurements were performed in a quartz cell with 1-cm optical path length, and spectra were recorded after stirring.

2.1.2 Nuclear Magnetic Resonance Spectrometry (NMR)

All ferrocenoyl-modified, DAB-$(NHCOFc)_n$, dendrimers were dissolved in deuterated chloroform and characterized with ^1H NMR spectroscopy using a Bruker instrument, AV-400.

2.1.3 Electrospray Ionization Mass Spectrometry (ESI-MS)

An Applied Biosystems SCIEX QStar XL equipped with a quadrupole TOF-MS with ion spray source was utilized to characterize the ferrocenoyl-modified DAB-$(NHCOFc)_n$ dendrimers. Each sample was measured with a mass accuracy of less than 4 parts per million (ppm).

2.1.4 High-Resolution Transmision Electron Microscopy (HR-TEM)

Electron microscopy images were obtained with a JEOL-2010 high-resolution transmission electron microscope. The nanoparticles were first dispersed in methanol, after which a drop of the suspension was placed on a holey carbon coated copper grid (400 mesh from SPI supplies) or a Formvar carbon-coated copper grid (200 mesh from Ted Pella, Inc.), and the solvent was allowed to evaporate. The instrument was operated at an accelerating voltage of 200 KV and different standard magnifications (400–600K). The images were recorded on a negative film for Ni nanoparticles and with a Gatan digital camera for iron oxide nanoparticles. For each

sample, HR-TEM images were taken from different parts of the grid and used to estimate the average diameter and size distribution of particles. The nanoparticles size was measured using an ImageJ program (image processing and analysis JAVA-based software developed by the National Institutes of Health (NIH)), and the histograms were plotted using OriginPro 6.1. The nanoparticle size measurements are mean values calculated from at least 200 measurements.

2.1.5 X-ray Photoelectron Spectroscopy (XPS)

The X-ray photoelectron spectra were obtained using an AXIS 165 X-ray photoelectron spectrometer (Kratos Analytical). The X-ray source used was monochromatic Al Kα radiation (photon energy 1486.6 eV), with a current of 10 mA and a voltage of 15 KV. During analysis, the pressure inside the chamber was held below 2×10^{-9} Torr, and a takeoff angle of 90° was used for all measurements. Survey and high-resolution spectra were obtained for each sample using pass energies of 40 eV and 160 eV, respectively. The samples were degassed in the pretreatment chamber overnight and then moved into the analysis chamber for XPS study. The spectra were acquired by signal averaging of two repeated scans over the same binding energy range in order to increase the signal to noise ratio. To perform the XPS analyses, the Ni nanoparticles were adsorbed onto clean Pt foil substrates for at least 48 h under nitrogen atmosphere. The Pt foil was removed from solution and dried with an argon flow before loading in the instrument. Before measurements, Ni nanoparticles were sputtered with Ar ions for 1 min to remove surface oxidation due to manipulation of samples in air during loading in the instrument. For iron oxide nanoparticles, the samples were prepared by pressing the powdered silica-supported iron oxide nanoparticles onto double-sided adhesive copper tape. A charge neutralizer was used to minimize/eliminate sample charging. For curve fitting, the high-resolution spectra were smoothed using a quadratic Savitzky-Golay method and fitted by applying a Gaussian-Lorentian (GL-30) peak-shape curve fitting. The high-resolution X-ray

photoelectron spectra were plotted using OriginPro 6.1, and when smoothed using an adjacent averaging function in OriginPro 6.1.

2.1.6 Thermogravimetric Analysis (TGA)

Silica-supported iron oxide nanoparticles were examined by thermogravimetry to determine thermal transition temperatures. The TGA experiments were carried out on a Mettler Thermobalance instrument with a heating rate of 10 ºC min^{-1}. Weight changes were recorded as a function of temperature between 25 and 700 ºC in both air and nitrogen environments.

2.1.7 Dynamic Light Scattering (DLS)

The sizes of DAB-$(NHCOFc)_n$ dendrimers were determined by dynamic light scattering using a MALVERN instrument (Zetasizer Nano-ZS ZEN3600), with a 633 nm He-Ne laser. The dendrimers were dissolved in THF by sonication for 30 min, and the solution was then filtered using a Whatman Anatop 10 syringe filter (0.2 μm pores) into a clean quartz cuvette. The measurements were performed in a quartz cell with 1-cm optical path length, and the scattering angle θ was 173°. Z-average diameter (in nm) was calculated for at least 6 scans.

2.1.8 System for Thermal Diagnostic Studies

The system for thermal diagnostic studies (STDS) is a high-temperature, analytical flow reactor system[1] and was used for the study of surface-mediated reaction of monochlorobenzene (MCBz). There are four main components: the control instrumentation console, a thermal reactor compartment, a cryogenic trapping unit, and an analytical instrument for effluent analysis. The STDS consists of a high-temperature fused silica flow reactor inside a furnace whose temperature is controlled by a separate temperature controller. The furnace is housed inside the thermal reactor compartment, namely a gas chromatograph (GC) oven (Varian, CP 3800). The GC oven is designed to act as a temperature control that maintains the temperature of all connections and the lines coming from the injection port to the reactor and the line going

from the reactor to the heated transfer line. The temperature inside the thermal reactor compartment was controlled at a constant temperature of 200 ^{o}C to facilitate transport of gas-phase reactants and products. The flow reactor is made of quartz that is stable at very high temperature and has a length of 18 cm and an inside diameter of 0.4 cm. Helium was used as the carrier gas for pyrolytic conditions, while a mixture of helium-oxygen (20%) was the carrier gas for oxidative conditions. The carrier gas was controlled by a digital flowmeter (Alltech, model 4068) that maintains a constant residence time for monochlorobenzene inside the reactor. A digital syringe pump (KD Scientific, model 100) was used to maintain a constant flow rate of the liquid sample into the injection port of the thermal reactor compartment to help maintain a constant initial concentration of sample inside the flow reactor. This injection port has a temperature controller that vaporizes all liquid samples before entering the flow reactor. The flow reactor effluent is transported through a heated, temperature-controlled transfer line where it is trapped cryogenically at the head of the capillary column of the gas chromatograpy mass spectrometry (GC-MS) system (Varian, Saturn 2000). Liquid nitrogen is used to cryogenically trap gas-phase products at the head of the capillary column (Chrompack, CP SIL 8CB 30m × 0.32 i.d., stationary phase film thickness of 0.25 μm) inside the GC (Varian, CP 3800). Initially, all the products were trapped at the head of capillary column at –60 °C, followed by temperature programmed ramping of the column from –60 °C to 300 °C at 15 °C min^{-1}. Separated products with molecular weights from 40 to 650 amu were analyzed with a mass spectrometer (MS) operating in the full-scan mode. The mass spectral library (NIST 98 version 1.6d) was used to identify the products.

2.2 Theory

2.2.1 Theory on X-ray Photoelectron Spectroscopy (XPS)

X-ray photoelectron spectroscopy (XPS), known also as electron spectroscopy for chemical analysis (ESCA), is a powerful method of surface analysis that provides elemental and chemical state identification for atoms located within the top few atomic layers of a sample. The basic components necessary for XPS instruments (Figure 2.1) are: an X-ray source, a sample/support system, an electron energy analyzer, an electron detector/multiplier, and suitable electronics to convert the detected current into a spectrum.[2]

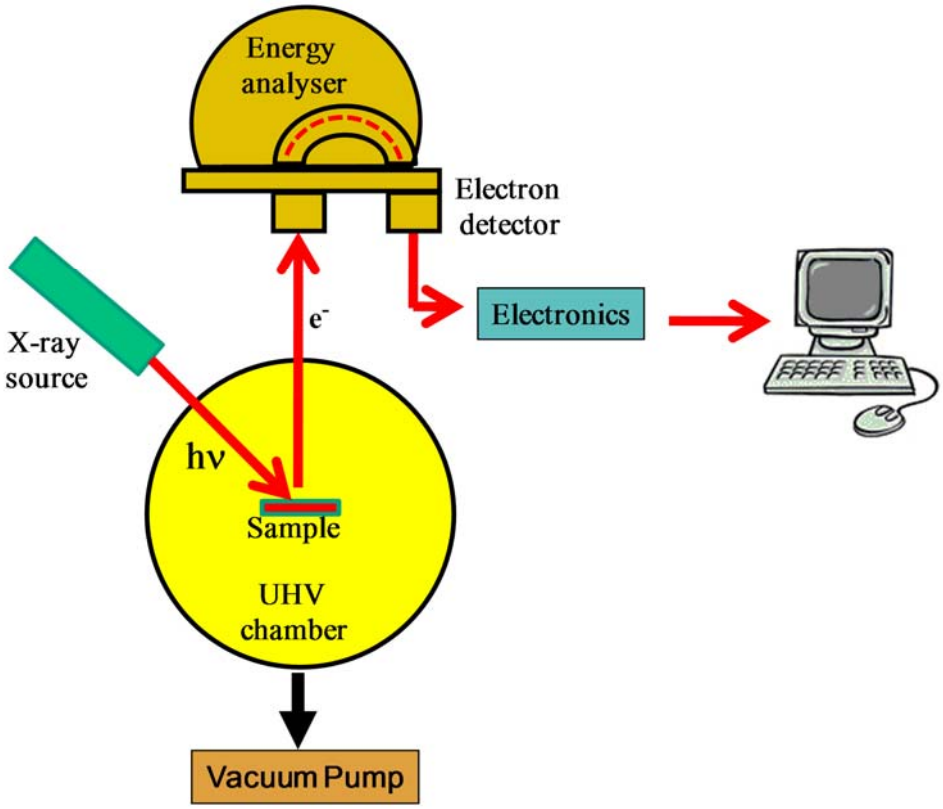

Figure 2.1 Block diagram illustrating the principal components of an X-ray photoelectron spectrometer.

There are many XPS experiments that require additional components, such as: a charge neutralizer, an argon ion gun (that allows samples to be cleaned in vacuum or to study the depth

profile), and a system for heating and cooling the samples. The analysis and detection of photoelectrons requires that the sample to be placed in a high-vacuum chamber.

XPS involves irradiation of the sample in vacuum with X-rays of known energy ($h\upsilon$) that causes photoelectrons to be emitted from the sample surface. Al Kα (1486.6 eV) or Mg Kα (1253.6 eV) X-ray sources are ordinarily used. The spectrum obtained is a plot of the number of emitted electrons per energy interval (photoelectron intensity in counts per second, CPS) versus their binding energy (*BE*). The emitted electrons have a characteristic kinetic energy (*KE*) that can be measured in the instrument, given by:

$$KE = h\upsilon - BE - \Phi_{sp} \qquad \textbf{Equation 2.1}$$

where $h\upsilon$ is the energy of the photon, *BE* is the binding energy of electrons, and Φ_{sp} is the spectrometer work function.[2,3] The spectrometer work function can be compensated electronically, and the basic equation of XPS becomes

$$KE = h\upsilon - BE \qquad \textbf{Equation 2.2}$$

Photoelectrons are emitted from all energy levels of the atom of interest and the lines in the spectrum are labeled according to the energy level from which they originate. The *p*, *d*, and *f* core levels become split upon ionization due to the coupling of the spin and orbital angular momenta of the emitted photoelectron. For example, the *p* level splits into the $p_{1/2}$ and $p_{3/2}$ in the ratio 1:2, the *d* level into $d_{3/2}$ and $d_{5/2}$ in the ratio 2:3, and the *f* level into $f_{5/2}$ and $f_{7/d}$ in the ratio 3:4.[3]

XPS can distinguish between particular elements in different environments. The binding energy value and the shape of a particular band is a function not only of the emitting element, but also of its local environment and chemical state.[4] This results in chemical shifts in binding energy of the core-level electrons that are observed in the XP spectrum. The determination of these chemical shifts is probably the most useful and also the most difficult part in XPS analyses

because of charging effects. Charging occurs due to ejection of electrons that causes a positive charge build-up on nonconductive materials. There are several approaches used to compensate/or determine the extent of charging, such as the use of a charge neutralizer, a thin film of gold evaporated onto the surface of the specimen, "adventitious" carbon presence and one element from the sample that does not have any changes in *BE* and thus its binding energies are used as an internal standard.[3,5]

Along with the qualitative analysis of the sample by XPS, semi-quantitative and possibly quantitative information can also be obtained from the integrated peak. For purposes of chemical state identification, quantitative analysis and for peak fitting, high-resolution scans must be obtained. Occasional cleaning of the analyzed surface is necessary in order to remove adsorbed hydrocarbons, water vapor, and oxide layers that are present on any surface that has been exposed to air, or handled without any special precautions. A common method used for removal of these surface contamination layers is sputtering away the contaminants using an argon ion beam.[4] The impact of the argon ions causes contaminant material to be ejected from the surface and subsequent layers to become exposed and available for analyses. Using this method, the variation of the composition of material with depth can also be monitored.[4]

In addition to the major XPS peaks, a number of minor peaks appear in the XP spectrum, such as X-ray line satellites, shake-up lines, and ghost lines.[2,4] For each major photoelectron peak, small satellite peaks appear, with intensities and spacing characteristic of the particular X-ray anode used.[5] The shake-up lines are due to the fact that the ion will be left in an excited state a few electron volts above the ground state, resulting in a lower kinetic energy of the emitted photoelectron. This results in the occurrence of a satellite a few electron volts higher in binding energy than the main peak.[2] More than one satellite of a principal photoelectron line can also be observed in the spectrum, occurring more often for paramagnetic compounds. One

further source of extraneous peaks in an X-ray photoelectron spectrum results from X-ray radiation from foreign material. These peaks are known as ghost lines and arise from different sources such as Mg impurity in the Al source in a dual anode source, Cu from the anode base structure, or X-ray photons arising from the foil window of the anode interface. Such lines are expected to occur at known positions.[2] In addition to the photoelectrons emitted, Auger electrons are emitted due to relaxation of the energetic ions left after photoemission[2] (the details of Auger electron emission will not be discussed here). XPS is certainly one of the most widely used methods for surface characterization of nanomaterials because it provides the possibility to identify different chemical states for an element as well as to analyze quantitatively the chemical composition in the surface region. Comprehensive and more detailed discussion of XPS can be found in the following references.[2,4,6]

2.2.2 Theory on Transmission Electron Microscopy

Transmission electron microscopy (TEM) has become a powerful and indispensable technique for the characterization of nanostructured materials. A direct imaging of nanoparticles is possible using electron microscopy (TEM). TEM is a unique technique because it can provide information about the morphology (the size, shape and arrangement of the particles), the crystallography (using diffraction to identify crystal class and lattice parameter) and chemical composition (if equipped with energy dispersive X-ray spectroscopy (EDS) and/or electron energy-loss spectroscopy (EELS)) almost simultaneously. The image can be recorded on a film placed below the screen or by using a CCD camera.

Transmission electron microscopes are very similar to conventional light optical microscopes but uses electrons instead of light. The basic components of a TEM instrument are: an illumination system, a specimen stage, an objective lens system, a magnification system, a data recording system, and a chemical analysis system.[7] In Figure 2.2 is presented the schematic

ray path for a transmission electron microscope. The electron path from the electron gun to the camera must be evacuated to 10^{-5} torr or better.[2] The acceleration voltage of TEM instruments is in the 100–500 kV range.[8]

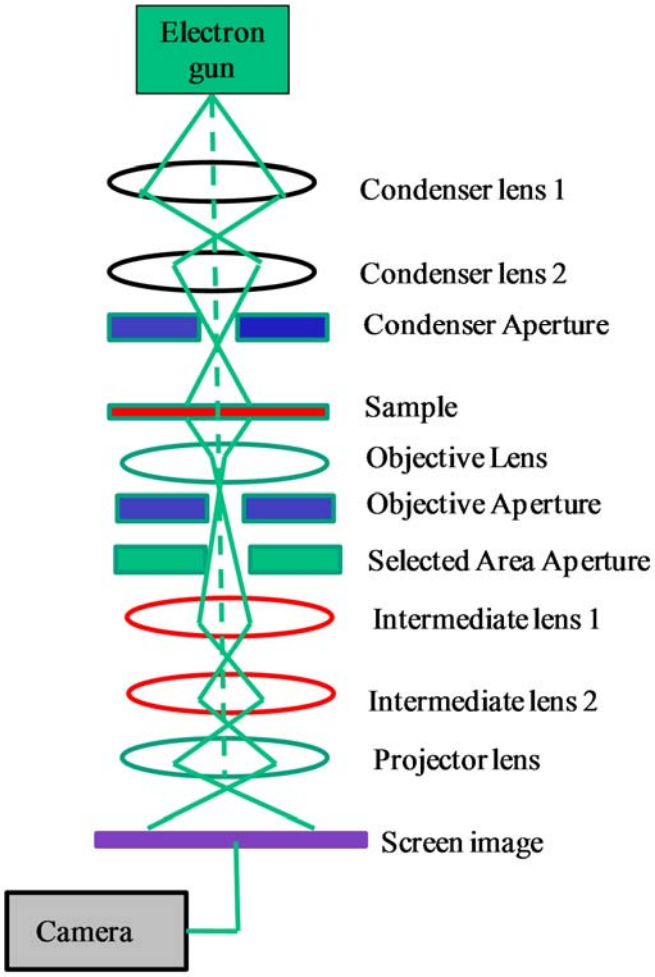

Figure 2.2 Block diagram illustrating the principal components of a transmission electron microscope and the ray path. Adapted from reference [2].

TEM operates in two modes: conventional TEM (CTEM or TEM for short) and high-resolution TEM (HR-TEM). The conventional mode has two imaging modes: bright field (BF) and dark field (DF).[9] In BF, the image is obtained from transmitted electrons, while in DF mode the image is formed from diffracted electrons alone and the central beam is excluded by the objective aperture. In HR-TEM an objective aperture is used that allows several diffracted beams to interfere with the axial transmitted beam to form the image. The size of the objective

aperture determines which diffracted beam contributes to the image formation. In principle, the process of image formation in the HR-TEM can be considered as occurring in two stages. In the first stage incoming or incident electrons undergo interactions with atoms of the specimen, involving both elastic and inelastic scattering processes (therefore the specimen must be very thin, otherwise multiple electron scattering effects become significant).[8,10] In the second stage, the electron wavefunction that leaves from the specimen is transmitted through the objective lens and to the subsequent magnifying lenses of the electron microscope to form the final enlarged image. Electrons that are elastically scattered contribute to the formation of the high-resolution bright field image; the inelastic scattering electrons are less localized.[8] Images in TEM are dominated by three types of contrast: diffraction, phase, and mass-thickness.[7] Diffraction contrast, which is produced by a local distortion in the orientation of the crystal, is ideally suited for imaging defects and dislocations in nanocrystals larger than 15 nm. Phase contrast, which is the basis of HR-TEM, is sensitive to the atom distribution and is produced by the phase modulation of the incident electron wave upon its transmission through a crystal potential. The mass-thickness or atomic number contrast is produced by the different scattering powers of atoms. The image contrast in HR-TEM is a complicated function of particle orientation, internal structure, and electron imaging conditions, and is critically affected by the defocus of the instrument.[11] A particular defocused imaged is recognized by the characteristic image of a crystal defect or the presence of the Fresnel fringe along the edge of the sample.[10]

There are several resolution limits characteristic of HR-TEM, such as interpretable resolution, instrumental resolution, and lattice-fringe resolution.[10] The interpretable resolution, known as point resolution, is determined by the position of the first zero crossover of the phase contrast transfer function at the optimum defocus. The instrumental resolution is determined by the damping produced by the envelope functions. The lattice-fringe resolution, which is

characteristic of a given crystalline material, refers to the finest spacing of the lattice fringes that are visible in HR-TEM images. The HR-TEM has evolved over years to such an extent that the achievement of instrumental resolution close to 0.1 nm is now possible.

One major limitation of TEM is that the image obtained is two dimensional from samples that are three dimensional in nature. An alternative approach is electron tomography, which records TEM images as a function of tilt angle and combines the images to create a 3D reconstruction.[9,11] Despite this limitation, the HR-TEM has proven indispensable in evaluating nanomaterials. A more detailed discussion of TEM can be found in the following references.[2,8]

2.3 References

(1) Rubey, W. A.; Grant, R. A. Design aspects of a modular instrumentation system for thermal diagnostic studies. *Rev. Sci. Instrum.* **1988**, *59*, 265-269.

(2) O'Connor, D. J.; Sexton, B. A.; Smart, R. S. C. *Surface analysis methods in materials science*; 2nd ed.; Springer, **2003**.

(3) Wagner, C. D.; Riggs, W. M.; Davis, L. E.; Moulder, J. F.; Muilenberg, G. E. *Handbook of x-ray photoelectron spectroscopy*; Perkin-Elmer Corporation Physical Electronics Division, Minnesota, U.S.A, **1979**.

(4) Smith, G. C. *Surface analysis by electron spectroscopy measurement and interpretation*; PLENUM PRESS, **1994**.

(5) Chaney, R. L. Recent developments in spatially resolved ESCA. *Surf. Interface Anal.* **1987**, *10*, 36-47.

(6) Drummond, I. W.; Cooper, T. A.; Street, F. J. Four classes of selected area XPS (SAXPS): An examination of methodology and comparison with other techniques. *Spectrochim. Acta* **1985**, *40B*, 801-810.

(7) Wang, Z. L. *Characterization of nanophase materials*; WILEY-VCH, **2000**.

(8) Reimer, L.; Kohl, H. *Transmission electron microscopy: Physics of image formation*; Fifth ed.; Springer: New York, **2008**.

(9) Ertl, C.; Knozinger, H.; Schuth, F.; Weitkamp, J. *Handbook of heterogeneous catalysis*; Second, Completely Revised and Enlarged Edition ed.; WILEY-VCH, **2008**.

(10) Yao, M.; Wang, Z. L. *Handbook of microscopy for nanotechnology*; Kluwer Academic Publishers, **2005**.

(11) Datye, A. K. Electron microscopy of catalysts: Recent achievements and future prospects. *J. Catal.* **2003**, *216*, 144-154.

CHAPTER 3

WELL-DEFINED NICKEL NANOPARTICLES FROM POLY(PROPYLENE IMINE) DENDRIMER-NI(II) COMPLEXES

3.1 Introduction

In the past decade, considerable attention has been paid to metal nanoparticle research because of the unusual properties exhibited by nanoparticles compared to those of larger particles or bulk metal. The development of flexible and precise synthetic routes for metal nanoparticles is an active area of research,[1] but there still exists a great need for the simple, straightforward synthesis of metallic and metal-oxide nanoparticles of tunable size and low size dispersity. Of these preparative methods, the use of metallodendrimers as metal nanoparticle precursors has quickly moved to the forefront. Dendrimers are well suited for synthesis of nanoscopic metals and metal oxides due to their propensity to coordinate/complex a variety of metal ions at the periphery, interior or throughout all layers of the dendrimer "host."[2-5] Poly(propylene imine), PPI or DAB, and poly(amido amine), PAMAM, dendrimers can be used for preparing metallic nanoparticles using an approach wherein the metal ions are coordinated or loaded into the dendrimeric material, followed by chemical reduction to form metallic nanoparticles. The possibilities are rich and diverse, as it has been shown, that amine-terminated PPI dendrimers can bind metal ions to their peripheral primary amines,[6-9] and a variety of metal nanoparticles, including those of Cu,[7,10] Ag,[11-15] Pt,[11,14] Pd,[11] Fe,[16] and Au,[14,15,17-22] have been synthesized using PPI dendrimers.

In addition to their use in applications of technological importance,[8,11,23,24] the role of metal and metal oxide nanoparticles—particularly those containing copper, nickel, and iron—in the production of pollutants has been implicated.[25-27] These nanoparticles are produced by combustion sources as primary particulate emissions or as secondary particles formed by atmospheric chemical reactions.[28] Particles produced in combustion chambers in the gas phase

undergo inception, coagulation and surface growth, and as a result, their size ranges from 2–4 nm for the smallest metallic nanoparticles, to a few hundred nanometers for agglomerates.[29] Under primarily oxidative/oxidative pyrolysis of fuels, metal nuclei or supported metal nanoparticles may form and result in initiation of pollutant production on their surfaces. Ni has been reported at relatively low concentrations of ~0.2 μg g^{-1} in airborne fine particles, whereas Fe and Cu —typically the most abundant transition metals—are present at ~ 1000 and 2 μg g^{-1}.[30] Ni has also been reported to comprise <0.1 % of the weight of nanoparticles from combustion of coal.[31,32] However, along with vanadium, Ni is typically the most abundant transition metal in fuel oil combustion-generated nanoparticles (~13% and 18% for Ni and V, respectively).[29] Thus, based on the characteristic properties of a number of metal and metal-oxide nanoparticles,[1] knowledge of the impact of nanoparticle size and composition on pollutant formation would be highly valuable. Two key factors controlling the properties of nanoparticles are their size and surface properties,[1,33] and they are interrelated because the surface-to-volume ratio increases as the size decreases; being able to control the size of Ni nanoparticles over the 1–3 nm diameter range would allow for probing of possible differences in their propensity to produce different amounts and types of pollutants at the smallest particle sizes found in combustion processes.[29] For example, Van den Brink et al.[34] showed that in comparison to larger-sized Pt particles, supported Pt nanoparticles with very small size were more active in formation of polychlorinated benzene in the catalytic combustion of chlorobenzene. We propose that similar effects with Ni nanoparticles will occur, and there may exist relationships between particle size and both the nature and amount of pollutant products formed during particle-catalyzed reactions.

Nickel nanoparticles have generally been produced by both gas- and liquid-phase processes. Gas-phase methods include hydrogen reduction of $NiCl_2$,[35] hydrogen plasma metal reaction,[36] and DC sputtering in argon,[37] with the smallest nanoparticles having diameters

(d) ≥ 31 nm. Liquid-phase methods—such as microemulsion/surfactant techniques,[38-41] chemical reduction in solution[42-47] or in the presence of heterogeneous supports,[48,49] and organometallic routes,[50] including thermolytic decomposition[51-53]—typically result in nanoparticles with $d \geq 3$ nm, and with size control only for particles above 5 nm.[51,53,54] However, we are unaware of a simple solution method that allows for careful control of Ni particle size over a range of sizes with $d < 3$ nm and with low size dispersity. A promising alternative synthetic methodology employs the use of dendrimers so as to allow control over size, stability, and solubility of nanoparticles with diameters from less than 1 nm up to 4 or 5 nm.[4,5] In the one reported case for Ni(II)-PAMAM, two sizes of nickel nanoparticles with diameters smaller than 3.0 nm (average of 55 and 147 atoms) have been obtained using sixth-generation PAMAM dendrimers functionalized on their periphery with alkyl groups.[55]

I report here, for the first time, the synthesis and characterization of nickel nanoparticles using DAB-Am$_n$ dendrimer-metal ion complexes, the result of which is the size-tunable synthesis of Ni(0) nanoparticles with low size dispersity. Five generations of DAB-Am$_n$ (n = 4, 8, 16, 32, and 64) have been used as multifunctional ligands for Ni(II). The stoichiometry of the predominant DAB-Am$_n$–Ni$_x$ complex was determined using the method of continuous variation applied to UV-visible spectroscopy, and it was found to be at an NH_2:Ni end-group mole ratio (n/x) of 2:1. In addition, I have studied the properties of nickel nanoparticles —using high-resolution transmission electron microscopy (HR-TEM) and UV-visible spectroscopy—that form upon reduction of various DAB-Am$_n$–Ni(II)$_x$ precursors with methanolic $NaBH_4$. The particles are composed of zero-valent Ni (devoid of Ni_2B) and possess a borate impurity as determined from XPS studies. Precise control of Ni nanoparticle size is shown to be possible by manipulating the dendrimer generation, the $NiCl_2$ concentration, and the ratio of primary amines to Ni(II) ions in the dendrimer precursor (n/x). The size of the Ni(0) nanoparticles decreases

with increasing generation of dendrimer and increasing *n*/*x*, as noted by outcomes from HR-TEM studies

3.2 Experimental Section

3.2.1 Materials

Commercial-grade reagents were used without further purification. The poly(propylene imine dendrimers) were obtained from Sigma-Aldrich (generations 1 and 3) and SYMO-Chem (generations 2, 4, and 5) and used as received. $NiCl_2 \cdot 6H_2O$ (99.9%), Ni_2B (30 mesh, 99%), Ni nanopowder (≤100 nm particle size, 99.9% trace metal basis), and $NaBH_4$ were purchased from Sigma-Aldrich. HPLC-grade methanol was from EMD.

3.2.2 UV-Visible Spectroscopy

The measurements were performed in a quartz cell (1-cm optical path length), and spectra were recorded after stirring, using a CARY 50 BIO UV/Visible spectrophotometer. Stock solutions of 5 and 10×10^{-3} M DAB-Am$_n$ dendrimers (with respect to primary amine end group) and 5 and 10×10^{-3} M Ni(II) salt solutions were prepared in methanol to investigate the stoichiometry of the predominant complex. The method of continuous variation (Job plot) was used to determine the stoichiometry.[56,57] Solutions were prepared by mixing aliquots of equimolar solutions of Ni(II) salt and DAB-Am$_n$ dendrimer such that the total concentration of Ni(II) plus dendrimer was constant at 10^{-2} M. All Ni(II) absorbance spectra for Job plots were background corrected.

3.2.3 Preparation of DAB-Am$_n$–Ni(II)$_x$ Complexes and DAB-Am$_n$–Ni(0)$_{NP}$ Nanoparticles

The nomenclature used to describe the dendrimers and dendrimer-nanoparticles in this paper is as follows: poly(propylene imine) dendrimer is DAB-Am$_n$, where *n* is the number of primary NH_2 (Am) end groups; complexes of poly(propylene imine) dendrimer with Ni(II) are

referred to as DAB-Am$_n$–Ni(II)$_x$, where x is n/4, n/2 or n/8; and the poly(propylene imine) dendrimer loaded with metal ions after reduction is referred to as DAB-Am$_n$–Ni(0)$_{NP}$.

The dendrimer-nickel complexes were synthesized in the following mode: the requisite amounts of methanolic solutions of Ni(II) and the corresponding amine-terminated poly(propylene imine) dendrimer were mixed to result in a final Ni(II) concentration of 5×10^{-4} M for the different stoichiometric ratios studied. Investigations of nanoparticle size as a function of nickel chloride concentration (5×10^{-4} M and 2×10^{-3} M) and the NH_2:Ni(II) ratio (n/x) in the dendrimer precursor were also carried out. DAB-Am$_n$–Ni(0)$_{NP}$ were obtained by chemical reduction of DAB-Am$_n$–Ni(II)$_x$ solutions with a 10-fold molar excess of methanolic $NaBH_4$ solution under nitrogen in a glove bag. Immediately upon its preparation (3–5 min), the methanolic $NaBH_4$ solution (0.5 mL) was added to the DAB-Am$_n$–Ni(II)$_x$ solutions drop by drop over a 30 s interval. The reduction resulted in an instantaneous color change of the solution from pale green to black, indicating the formation of nanoclusters of DAB-Am$_n$-Ni(0)$_{NP}$. The nickel nanoparticle solutions are very sensitive to atmospheric air; after exposure to air for times greater than 10 min, the solutions become colorless. If the nanoparticles are kept under nitrogen atmosphere, no change in color is observed for up to the longest time investigated, 2 weeks. The metal nanoparticles obtained were analyzed by UV-visible absorption spectroscopy, X-ray photoelectron spectroscopy (XPS), and high-resolution transmission electron microscopy (HR-TEM).

3.2.4 TEM Images of DAB-Am$_n$–Ni(0)$_{NP}$

Electron microscopy images were obtained with a JEM-2010 high-resolution transmission electron microscope. A drop of the analyte solution was placed on a Formvar carbon-coated copper grid under an inert atmosphere in a glove bag, and the solvent was allowed to evaporate. The sample was exposed to air briefly (less than 60 s) during transfer from the

glove bag to the microscope. The JEM-2010 was operated at an accelerating voltage of 200KV and different standard magnifications (400 and 600K). For each sample, at least 270 particles from different parts of the grid were used to determine the average diameter and size distribution of particles.

3.2.5 X-Ray Photoelectron Spectroscopy (XPS) of DAB-Am$_n$–Ni(0)$_{NP}$

The XPS data were obtained with an AXIS 165 photoelectron spectrometer using a monochromatized Al Kα X-ray radiation source. First, the metal nanoparticles were adsorbed onto clean Pt foil substrates under anaerobic conditions for at least 48 h. The Pt foil was removed from solution and dried with a stream of Ar in a glove bag before loading in the instrument. Samples were stored under Ar in the antechamber overnight and then moved into the analysis chamber for XPS study. A charge neutralizer was used to eliminate the charge effect on the sample surface. Low-resolution survey spectra (40 eV pass energy) were recorded for the 0–1200 eV region to determine the elements present in the sample. High-resolution spectra (160 eV pass energy) were recorded for the Ni 2p and B 1s regions. Before measurements, the samples were sputtered with Ar ions for 1 min (DAB-Am$_n$–Ni(0)$_{NP}$) or 10 min (for the reference standards) to avoid surface oxidation due to manipulation of samples in air during loading into the antechamber. For the XPS analyses, samples of the DAB-Am$_n$–Ni(0)$_{NP}$ produced from DAB-Am$_n$–Ni(II)$_x$ with a Ni(II) concentration of 5×10^{-3} M were used; the use of lower Ni(II) concentrations lead to low signal-to-noise ratio spectra.

3.3 Results and Discussion

3.3.1 Dendrimer-Nickel Complexes: DAB-Am$_n$–Ni(II)$_x$

Different generations of DAB-Am$_n$ dendrimers were examined as possible multifunctional ligands for Ni(II) in methanol solutions. In the absence of dendrimer, Ni(II) exhibits a maximum absorption near $\lambda = 410$ nm and another absorption band that spans 680

to790 nm (corresponding to *d-d* transitions[58]), Figure 3.1. The addition of the three different generations of DAB-Am$_n$ to Ni(II) solutions produced a light green color and is the result of Ni-NH_2 complexation. In the presence of DAB-Am$_n$, the absorption maximum of the *d-d* transition is shifted to 640 nm, and the band at 410 nm is now centered at 400 nm. The band intensities do not change for times up to 90 min (the longest time investigated), indicating that the initially formed complex is stable. As expected, the DAB-Am$_n$ dendrimer does not absorb light to any significant degree in this energy range.

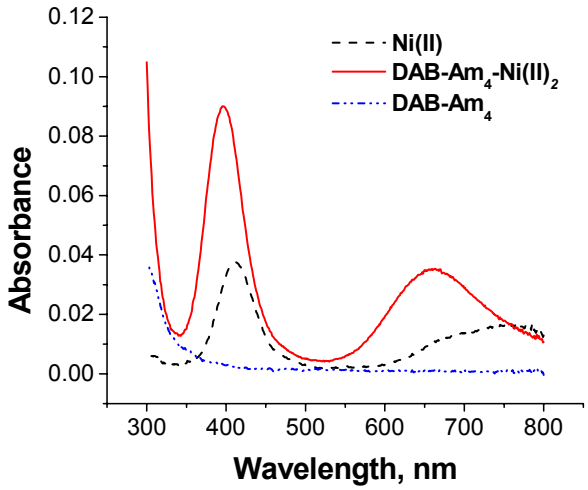

Figure 3.1 UV-visible absorption spectra of 5×10^{-3} M $NiCl_2 \cdot 6H_2O$ in methanol (dashed black line), 5×10^{-3} M $NiCl_2 \cdot 6H_2O$ with DAB-Am_4 fully complexed (solid red line), and DAB-Am_4 dendrimer (2×10^{-2} M in end groups, dotted/dashed blue line).

The method of continuous variation (Job plot) was used to identify the stoichiometry of the predominant Ni(II)-dendrimer complex as a function of dendrimer generation. This was achieved by mixing aliquots of equimolar solutions of Ni(II) and dendrimer such that the total concentration of Ni(II) plus dendrimer remained constant. In order to ensure proper identification of the stoichiometry of the Ni-dendrimer complex, measurements were taken at two wavelengths (640 and 680 nm) using total concentrations of Ni(II) plus dendrimer of 5×10^{-3} M and 1×10^{-2} M. In Figure 3.2 are displayed Job plots for generations 1, 3, and 4 of DAB-Am$_n$ dendrimers in

the presence of various amounts of Ni(II) in methanol. It was observed for all generations investigated that the maximum value in the Job plots occurs at a NH_2:Ni(II) mole ratio of 2:1, a value that is in accord with results from spectrophotometric titrations we carried out (data not shown) and those of others.[6,59]

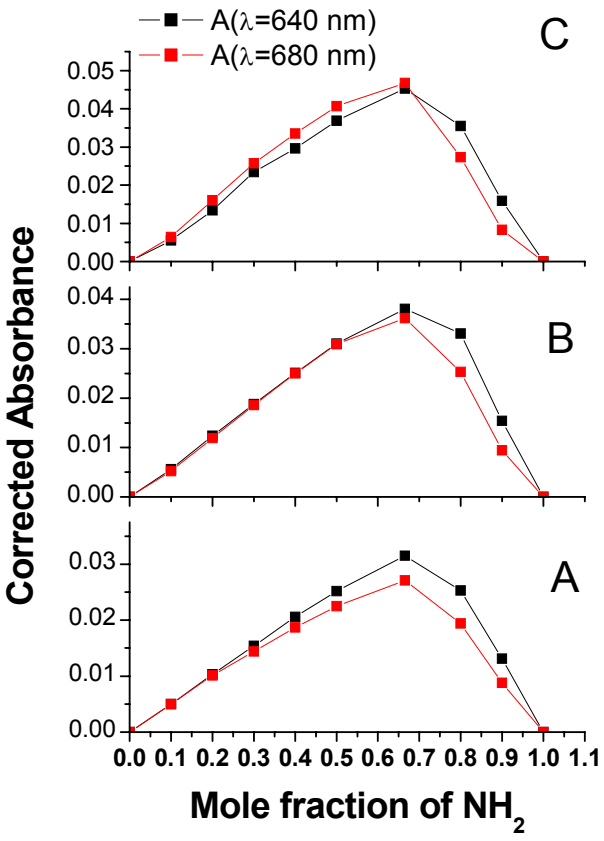

Figure 3.2 Job plots: absorbance at 640 nm and 680 nm as a function of the mole fraction of -NH_2 end groups for DAB-Am_4 (A), DAB-Am_{16} (B), and DAB-Am_{32} (C) with Ni(II). Total concentration of Ni(II) and dendrimer = 1×10^{-2} M. Absorbances were background corrected in all cases.

In prior spectrophotometric titration studies, it was demonstrated that Ni(II) does not complex with the tertiary amine functional groups in the core of DAB-Am_n dendrimers.[6,10,59] In those studies, it was shown that the predominant DAB-Am_4–Ni(II) complex has a 2:1 ratio of NH_2:Ni(II), and there was no evidence of 4:1 complexes. However, all higher generations (n = 8, 16, 32, 64) gave rise to predominant complexes with a 4:1 or 2:1 NH_2:Ni(II) ratio

—depending on the Ni(II) and DAB-Am$_n$ concentrations—supporting the existence of two different complexes,[6,10,59] as has been shown in previous work with Ni(II) and dipropyltriamine, dpt, ligand.[60-62] It was proposed that one of the complexes results from a site with six coordinating nitrogens at high DAB-Am$_n$–Ni(II) ratios, and the other complex comes about from a site with three coordinating nitrogens at lower DAB-Am$_n$–Ni(II) ratios. Based on my results here and those from previous studies,[60-62] I propose that complexation of Ni(II) by DAB-Am$_n$ dendrimers in methanol at room temperature occurs in a site-selective way wherein dipropylenetriamine (dpt) end groups act as very strong coordinating units (Scheme 3.1). This outcome is similar to that we found for Cu(II) with DAB-Am$_n$ dendrimers.[7]

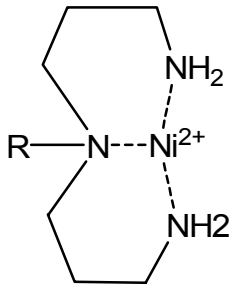

Scheme 3.1 Binding of Ni(II) to the dipropyltriamine, dpt, units of DAB dendrimer (R=dendrimer core; DAB-Am$_n$).

3.3.2 DAB-Am$_n$–Ni(0)$_{NP}$ from DAB-Am$_n$–Ni(II)$_x$: Spectral Properties

Samples obtained from $NaBH_4$ reduction of DAB-Am$_n$–Ni(II)$_x$, (n = 4, 8, 16, 32 and 64; n/x = 4), at fixed concentration of Ni(II) were investigated by UV-visible spectroscopy. In Figure 3.3 are shown the optical spectra of the DAB-Am$_{32}$–Ni(II)$_8$ complex before and after reduction with $NaBH_4$. Upon reduction, the color of the solution changed from light green to black, indicating that DAB-Am$_n$-Ni(II)$_x$ is no longer present in solution. After reduction, the absorbance bands initially present at 400 and 640–680 nm are absent, and instead, a spectrum is found that has a monotonically increasing absorption with shorter wavelengths. I attribute these observations to the formation of Ni nanoparticles, because they are similar to spectroscopic

results for other types of metal nanoparticles.[7,63] Indistinguishable results were observed for the other DAB-Am$_n$–Ni(II)$_x$ complexes.

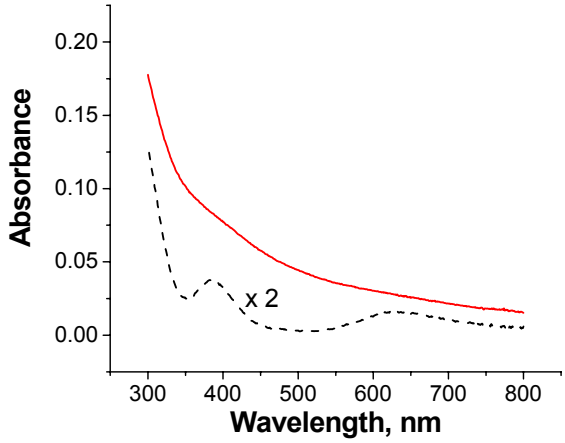

Figure 3.3 Absorption spectra of DAB-Am$_{32}$–Ni(II)$_8$ before (dashed black line) and after (solid red line) reduction with $NaBH_4$ in methanol. [Ni(II)] = 5×10^{-4} M.

As noted in other syntheses of metallic nanoparticles,[42,64] I found that the Ni nanoclusters are not stable in aerobic environments as a result of their spontaneous surface oxidation. When DAB-Am$_n$–Ni(0)$_{NP}$ solutions were exposed to the laboratory ambient for times > 10 min, the color of the solutions slowly dissipated, and this is the result of the oxidation of Ni(0) to Ni(II).[55,65]

3.3.3 DAB-Am$_n$–Ni(0)$_{NP}$ from DAB-Am$_n$–Ni(II)$_x$ via $NaBH_4$ Reduction: Chemical Composition

XPS analyses of reduced DAB-Am$_n$–Ni(II)$_x$ led to more detailed information about the oxidation state of Ni and the possible presence of other elements in the nanoparticles, such as nickel borides that are often observed in borohydride-produced nanoparticles.[40] Both survey (Figure 3.4) and high-resolution spectra for the Ni 2p and B1s regions were acquired. For comparison purposes, commercially available Ni "nanopowder" (diameter ≤ 100 nm) and Ni_2B powder (30 mesh) references were evaluated. Shown in Figure 3.5 is a representative

high-resolution Ni 2p region spectrum of a typical borohydride-reduced DAB-Am_{16}–Ni(II) sample supported on cleaned Pt foil (Figure 3.6).

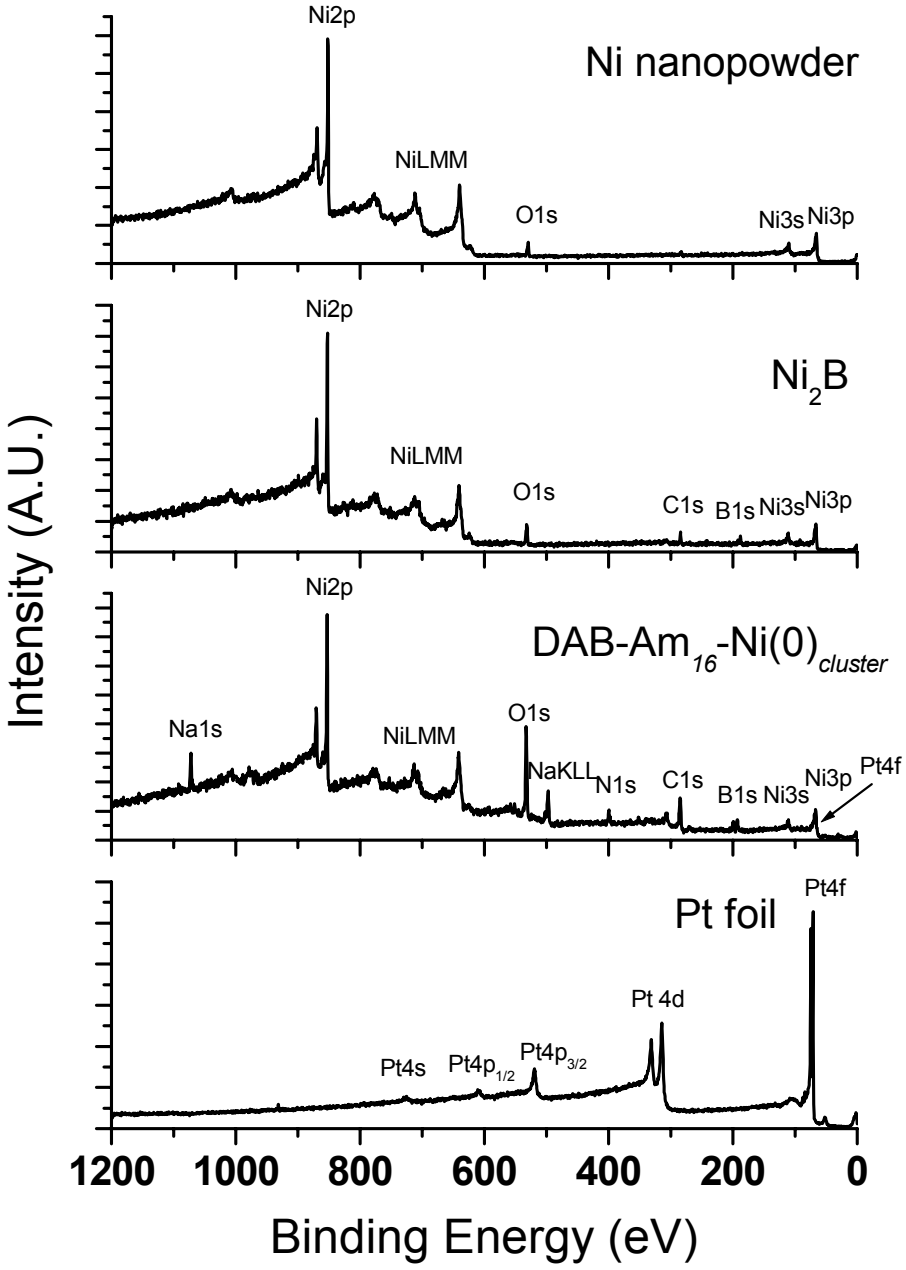

Figure 3.4 X-ray photoelectron survey spectra for clean platinum foil and DAB-Am_{16}-$Ni(0)_{NP}$ supported on platinum foil. For comparison the reference spectra of Ni nanopowder and Ni_2B are included.

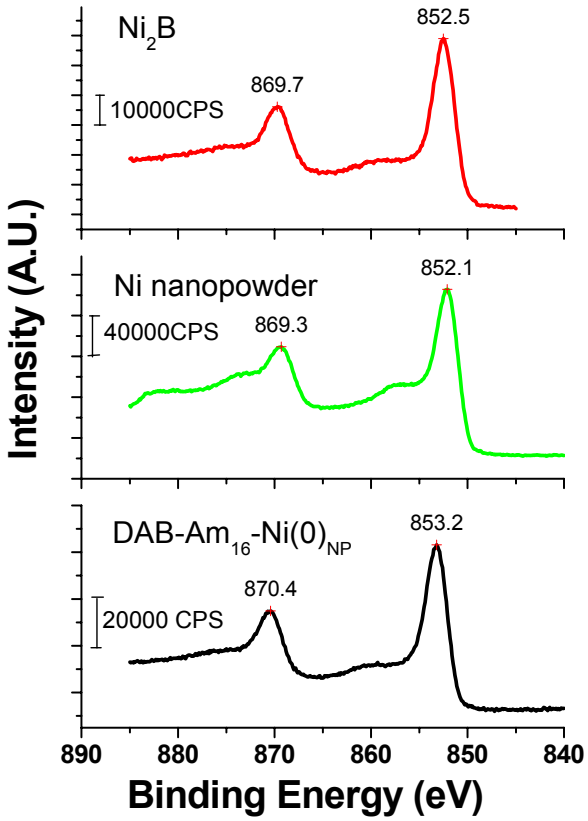

Figure 3.5 Ni 2p high-resolution X-ray photoelectron spectra. Bottom: nickel nanoparticles obtained by reduction of DAB-Am_{16}–$Ni(II)_8$ ($x = n/2$; [Ni(II)] = 5×10^{-3} M); Middle: nickel nanopowder reference (d ≤ 100 nm) ; and Top: Ni_2B reference.

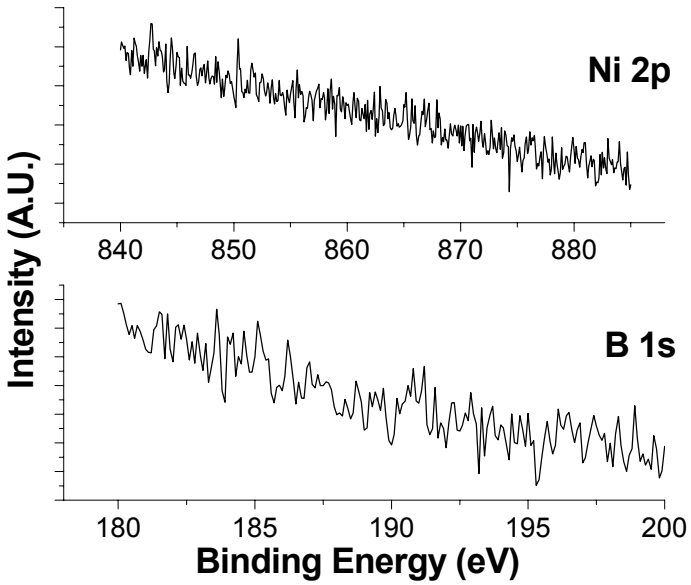

Figure 3.6 High-resolution XPS data for blank platinum foil: Ni 2p and B1s core level regions.

The metallic nature of the Ni atoms in the reduced sample is suggested by the 853.2 eV binding energy of the Ni $2p_{3/2}$ band; however, further examination of the Ni $2p_{1/2}$ and $2p_{3/2}$ and plasmon/shake-up loss satellite transitions[66] are needed due to variability of the instrument's anti-charging feature. Confirmation of the zero-valent state of the nickel in the nanoparticles comes from the observed 17.2 eV binding energy difference between the Ni $2p_{1/2}$ and $2p_{3/2}$ transitions[67] (Figure 3.5) and the 6.0 eV difference in the $2p_{3/2}$ and plasmon/shake-up loss satellite transitions (see Figure 3.5 and peak-fitted spectrum in Figure 3.7), with the latter being extremely sensitive to the oxidation state and environment of the nickel.[66]

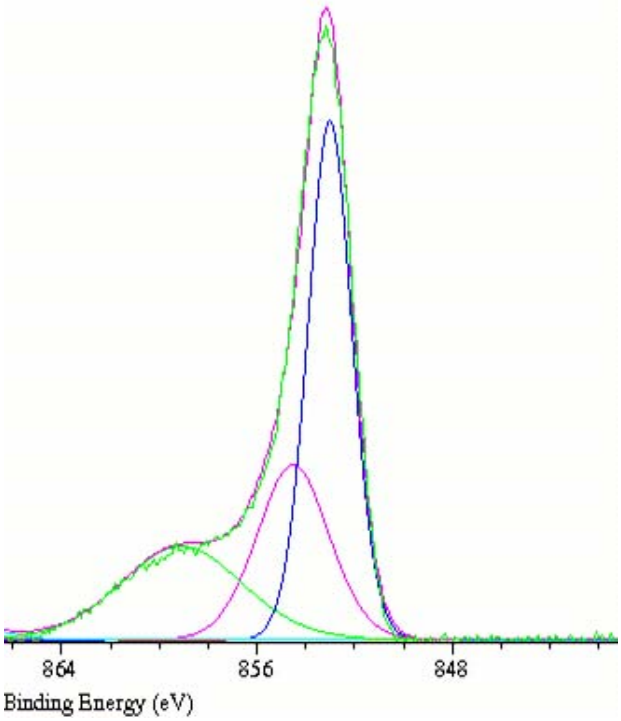

Figure 3.7 Peak-fitted Ni 2p high-resolution X-ray photoelectron spectrum of nickel nanoparticles obtained by reduction of DAB-Am_{16}-$Ni(II)_8$, ($x = n/2$); [Ni(II)] = 5×10^{-3} M. The main band is located at 853.2 eV and the shake-up/plasmon satellite at 859.2 eV. The average size of these Ni nanoparticles determined by HR-TEM was 3.46±0.37 nm (data not shown).

The difference in energy between the Ni $2p_{1/2}$ and $2p_{3/2}$ transitions in NiO has been observed to be 18.4 eV, while that in zero-valent nickel species is 17.4 eV, with the latter in good agreement with the 17.2 eV value observed for the DAB-Am_{16}–$Ni(0)_{NP}$.[67] Importantly, the 6.0

eV difference in the $2p_{3/2}$ and plasmon/shake-up loss satellite transitions (853.2 eV and 859.3 eV) found for the DAB-Am_{16}–$Ni(0)_{NP}$ is in agreement that observed for clean Ni(0) metal, 6.0 eV;[66] NiO has its $2p_{3/2}$ transition centered at 854 eV and its plasmon/shake-up loss satellite located at 861 eV, while $Ni(OH)_2$ exhibits values of 855.4 and 861 eV.[66]

I now turn my discussion to the well-known issue regarding the possible formation of metal borides during the borohydride reduction of metal salts, which has been observed when water or diglyme are used as solvents.[40,65] In Figure 3.8 are presented representative high-resolution X-ray photoelectron spectra of DAB-Am_{16}–$Ni(0)_{NP}$ and the Ni_2B reference in the B 1s region.

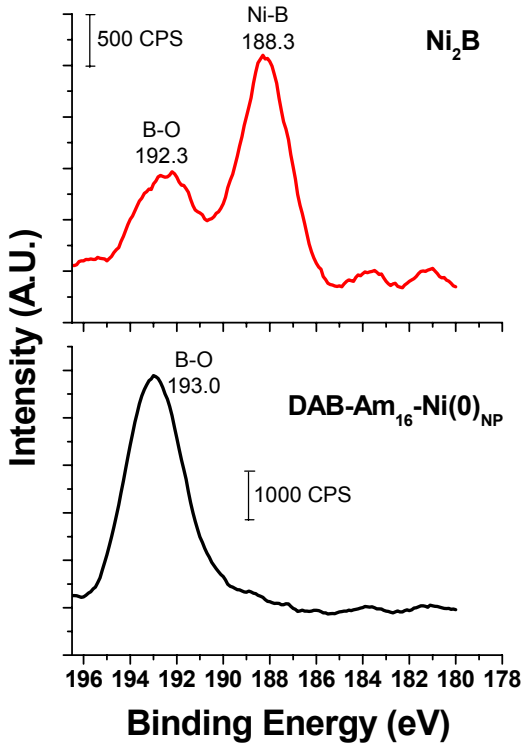

Figure 3.8 B 1s high-resolution X-ray photoelectron spectra. Bottom: nickel nanoparticles obtained by borohydride reduction of DAB-Am_{16}–$Ni(II)_8$ ($x = n/2$; [Ni(II)] = 5×10^{-3} M); and Top: Ni_2B reference.

As expected for the Ni_2B reference, a B–Ni band at 188.3 eV and that for B–O at ~192.3 eV are present, and these values are in agreement with those of Ni-B alloys obtained by

others.[40,68-71] Interestingly and importantly, the spectrum for DAB-Am_{16}–$Ni(0)_{NP}$ does not possess the characteristic B–Ni band at 188.3 eV and thus does not support the presence of any boride (B-Ni) in the Ni nanoparticles. As a result, we conclude that the borohydride reduction of DAB-Am_n–$Ni(II)_x$, under the conditions used here, results in zero-valent nickel nanoparticles free of metal boride. We postulate that this is the result of the methanol solvent employed, as it has been shown that borohydride reduction of Cu(II) in methanol results in Cu(0) particles, and not the boride.[72] However, the spectrum for DAB-Am_{16}–$Ni(0)_{NP}$ does exhibit the characteristic B–O transition centered at 193 eV.[40] Because of the rapid reaction of borohydride with protic methanol to yield either methylboronate or hydrated sodium borate and hydrogen gas,[73] boron-oxygen species will always be present in the borohydride chemical reduction medium. Thus, it can be concluded that the peak at 193 eV for DAB-Am_{16}–$Ni(0)_{NP}$ is most likely associated with the presence of H_3BO_3,[40,67,74] and the borate species is present as a ~10% impurity in the Ni(0) nanoparticles. At this time, the nature of its presence within the Ni(0) nanoparticles is not known, and so I am unable to provide any further chemical/structural information about the Ni(0) nanoparticles.

3.3.4 DAB-Am_n–$Ni(0)_{NP}$ from DAB-Am_n–$Ni(II)_x$ via $NaBH_4$ Reduction: Microscopically Determined Sizes

HR-TEM investigation of DAB-Am_n–$Ni(II)_x$ ($x = n/4$) solutions treated with 10 mole excess of borohydride routinely lead to images such as those in Figure 3.9. It is clear that nanoparticles have formed, as expected from other studies of borohydride treatment of Ni(II) solutions.[42,44] TEM images from control experiments of DAB-Am_n solutions treated with methanolic $NaBH_4$ did not possess any particulates. I first examined the impact of dendrimer generation on $Ni(0)_{NP}$ size at fixed [Ni(II)] and $x = n/4$, as well as BH_4^-:Ni(II). Representative TEM images and particle size distributions for the Ni nanoparticles (DAB-Am_n–$Ni(0)_{NP}$; n = 4, 8, 16, 32, and 64) are shown in Figures 3.9 and 3.10.

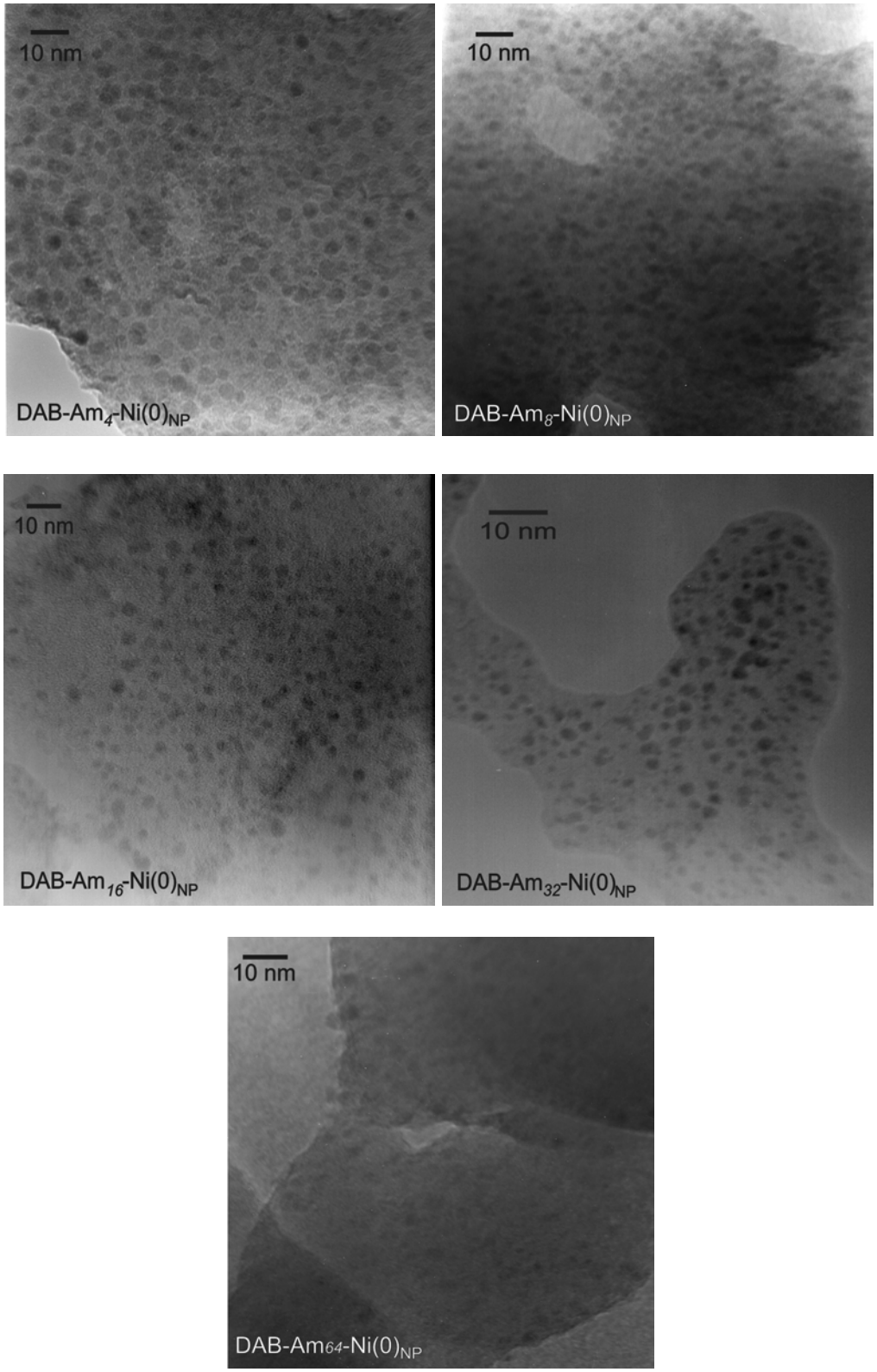

Figure 3.9 Representative HR-TEM of $Ni(0)_{NP}$ formed by $NaBH_4$ reduction of DAB-Am_n–$Ni(II)_x$, $x = n/4$, in MeOH.

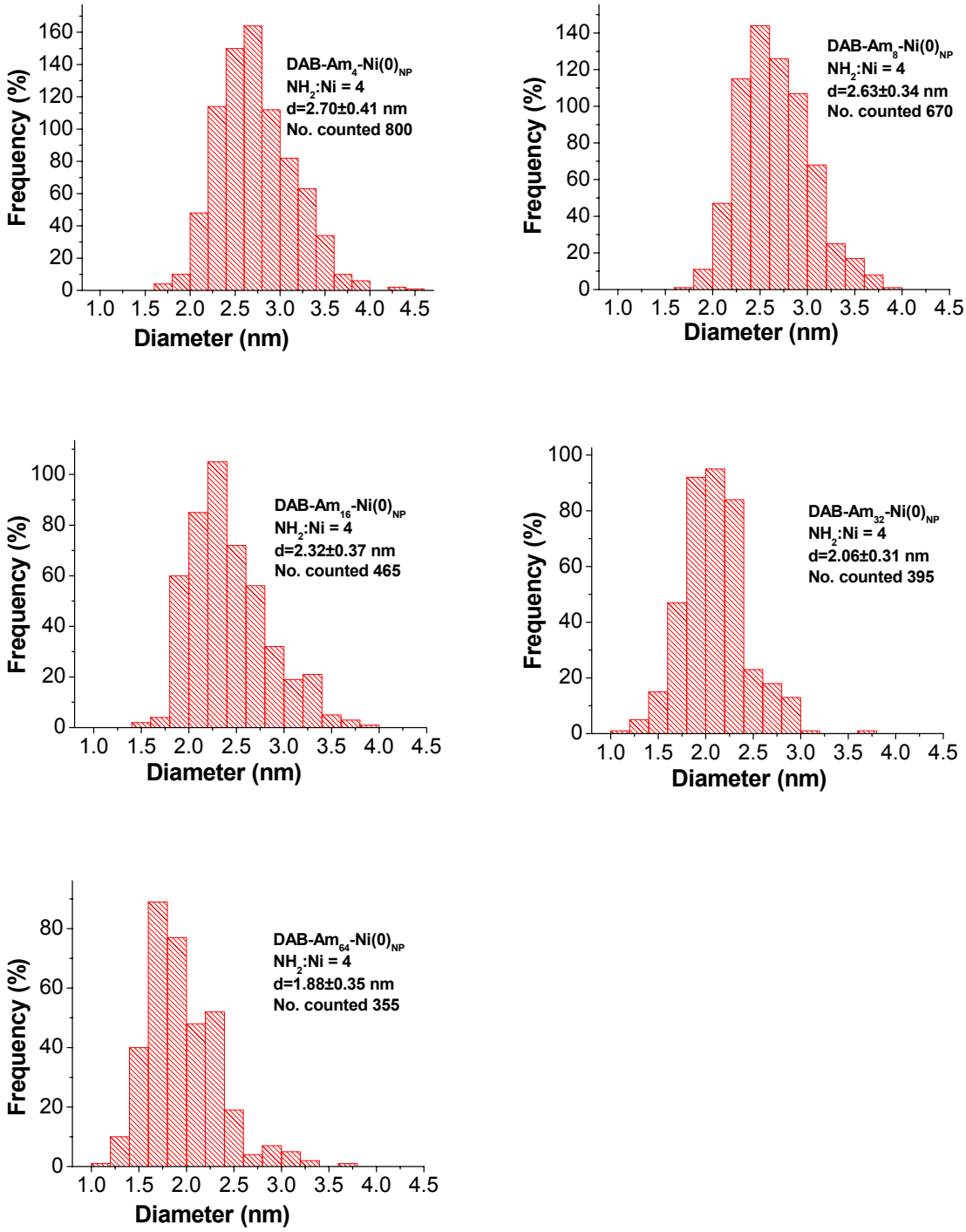

Figure 3.10 Particle size distributions of $Ni(0)_{NP}$ formed by $NaBH_4$ reduction of DAB-Am_n–$Ni(II)_x$, $x = n/4$, in MeOH.

The average diameters of the Ni nanoparticles as a function of dendrimer generation are compiled in Table 3.1, and they range between 2.70 and 1.88 nm, with notably low size dispersities. Upon statistical treatment of the $Ni(0)_{NP}$ diameter data, it was found that the differences in diameters are significant beyond the 99.9% confidence level (*t*-test). It is clear that the particle size decreases with increasing dendrimer generation. Esumi and Amis have observed similar phenomena in the synthesis of Au nanoparticles using PAMAM dendrimers.[75-77] Upon close inspection of the TEM images, although there is apparent uniform particle contrast, we are unable to conclude that there is no indication of Ni(0) core-NiO shell structures.[78]

Investigations of particle size as a function of the NH_2:Ni(II) ratio in the dendrimer precursor and nickel chloride concentration were carried out, Table 3.2. Upon statistical treatment of the $Ni(0)_{NP}$ diameter data, it was found that the differences in diameters are significant beyond the 99.9% confidence level (t-test). From the results in Table 3.2 and Figures 3.11 and 3.12, it is revealed that the size of the DAB-Am_n–$Ni(0)_{NP}$ is affected by variation of the NH_2:Ni(II) ratio at fixed Ni(II) concentration. A significant decrease in $Ni(0)_{NP}$ size (~24%, or 2.26-fold decrease in number of Ni atoms) was obtained by increasing the NH_2:Ni(II) ratio in the dendrimer precursor from 2 to 8 at fixed Ni(II) concentration, (Table 3.2 and Figure 3.11). In addition, there is a roughly 30% increase in particle size with an increase of the [Ni(II)] from 5×10^{-4} to 2×10^{-3} M.

At this point, I turn to a discussion of $Ni(0)_{NP}$ formation from the DAB-Am_n-$Ni(II)_x$ materials upon addition of BH_4^-. From the data in Tables 3.1 and 3.2, it is clear that the size dispersity of the $Ni(0)_{NP}$ is relatively invariant with respect to the various conditions for their preparation. Furthermore, the size dispersity is very small in all cases (10–19%). These results—according to nucleation theory[79]—point to the separation of the nucleation event from

that of the particle growth event, either temporally or spatially. That is to say, the variation in size of the nanoparticles is small because the production of critical nuclei is very near completion before the onset of nuclei enlargement by addition of Ni(0) atoms.

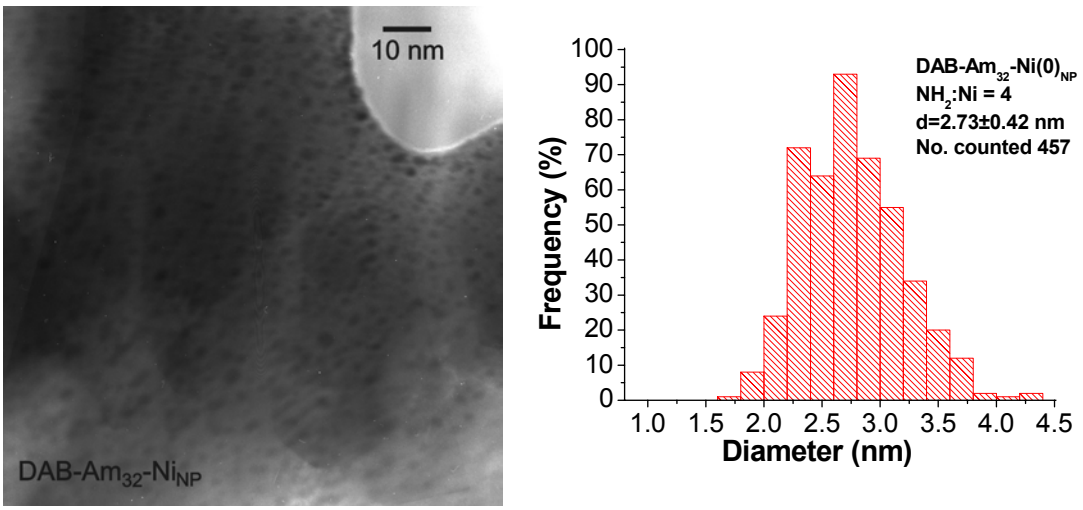

Figure 3.11 HR-TEM image and particle size distribution of nickel nanoparticles obtained by reduction of DAB-Am_{32}-Ni(II)$_8$, ($x = n/4$); [Ni(II)] = 2×10^{-3} M.

Typically, this is achieved by either kinetic (temporal) or steric (spatial) constraints, wherein either reducing agent is added extremely quickly to the metal ion solution *or* the metal ions are sequestered in a fixed volume through use of template molecules/assemblies during the reduction process.[79] Importantly, under the conditions used here, the BH_4^- reducing agent was added at a relatively slow rate (0.5 mL in 30 s); thus the low size dispersities observed here are attributed to a scaffold effect imparted by the DAB-Am_n environment. A strong interaction of the dpt groups of DAB-Am_n with Ni(II)—$K = 2.45 \times 10^7$ for methyl-dpt of Scheme 1(R = CH_3-)[80]—and the resulting Ni(0) surface will result in a small Ni(0)$_{NP}$ size dispersity and Ni(0)$_{NP}$ size, as noted in a study of Pt and Pd nanoparticles produced from a select group of DAB-Am_n (n = 8, 16, 32) at extremely high primary amine:metal ion ratios ($200 \leq n/x \leq 800$).[11]

Table 3.1 Properties of Ni nanoparticles as a function of dendrimer generation upon $NaBH_4$ reduction of methanolic DAB-Am_n–Ni(II)$_x$ (4:1 = n/x) with fixed [Ni(II)] = 5×10^{-4} M (BH_4^-:Ni(II) = 10:1). Mean diameters (± one standard deviation {% size dispersity}) are significantly different beyond the 99.9% confidence level (as judged by application of the *t*-test to the average particle diameters of the next closest-sized particles). The number of particles used for calculating the average and standard deviation is 800, 670, 465, 395, and 355 for the 1st–5th generation dendrimer cases.

Sample	**Average Ni(0)$_{NP}$ Diameter ± 1s{%} (nm)**	**Number of Ni atoms per Ni(0)$_{NP}$[a]**	**Number of DAB-Am_n–Ni(II)$_x$ Required to Make 1 Ni(0)$_{NP}$ [Aggregate Diameter, nm][b]**	**Γ NH_2 on Ni(0)$_{NP}$ (mol cm^{-2})[c]**
DAB-Am_4–Ni(0)$_{NP}$	2.70 ± 0.41 {15%}	963	963 [19]	5.58×10^{-8}
DAB-Am_8–Ni(0)$_{NP}$	2.63 ± 0.34 {13%}	890	445 [24]	5.41×10^{-8}
DAB-Am_{16}–Ni(0)$_{NP}$	2.32 ± 0.37 {16%}	611	153 [21]	4.80×10^{-8}
DAB-Am_{32}–Ni(0)$_{NP}$	2.06 ± 0.31 {15%}	428	54 [17]	4.26×10^{-8}
DAB-Am_{64}–Ni(0)$_{NP}$	1.88 ± 0.35 {19%}	325	20 [14]	3.89×10^{-8}

[a]Calculated according to Leff *et al.* in *J. Phys. Chem.* **1995**, *99*, 7036-7041. [b]The aggregate diameter was computed using the method in footnote *a* and employed estimated DAB-Am_n–Ni(II)$_x$ diameters of 1.15, 1.90, 2.30, 2.72, and 3.14 nm for the n = 4–64 materials. [c]Estimated using the surface area of all nanoparticles generated by reduction and the total amount of dendrimer in solution.

Table 3.2 Properties of Ni nanoparticles as a function of ratio of primary amines to Ni(II) ions and Ni(II) concentration in the dendrimer precursor. Mean diameters (± one standard deviation {% size dispersity}) are significantly different beyond the 99.9% confidence level (as judged by application of the *t*-test to the average particle diameters of the next closest-sized particles). The number of particles used for calculating the average and standard deviation is 270, 395, 457, and 500 for the 2:1, 4:1, and 8:1 ratio scenarios. The BH_4^-:Ni(II) = 10:1.

NP Sample	**Ratio of NH_2 to Ni(II)** *n/x*	**[Ni(II)] (M)**	**Average $Ni(0)_{NP}$ Diameter ± 1s{%} (nm)**	**Number of Ni atoms per $Ni(0)_{NP}$**[a]	**Number of DAB-Am_{32}–Ni(II) Required to Make 1 $Ni(0)_{NP}$ [Aggregate Diameter, nm]**[b]	**Γ NH_2 on $Ni(0)_{NP}$ (mol cm^{-2})**[c]
DAB-Am_{32}–$Ni(0)_{NP}$	2:1	5×10^{-4}	2.43 ± 0.25 {10%}	702	44 [16]	2.51×10^{-8}
	4:1	5×10^{-4}	2.06 ± 0.31 {15%}	428	54 [17]	4.26×10^{-8}
		2×10^{-3}	2.73 ± 0.42 {15%}	996	125 [22]	5.65×10^{-8}
	8:1	5×10^{-4}	1.85 ± 0.35 {19%}	310	78 [20]	7.66×10^{-8}

[a]Calculated according to Leff *et al.* in *J. Phys. Chem.* **1995**, *99*, 7036-7041. [b]The aggregate diameter was computed using the method in footnote *a* and employed an estimated DAB-Am_{32}–$Ni(II)_x$ diameter of 2.72 nm. [c]Estimated using the surface area of all nanoparticles generated by reduction and the total amount of dendrimer in solution.

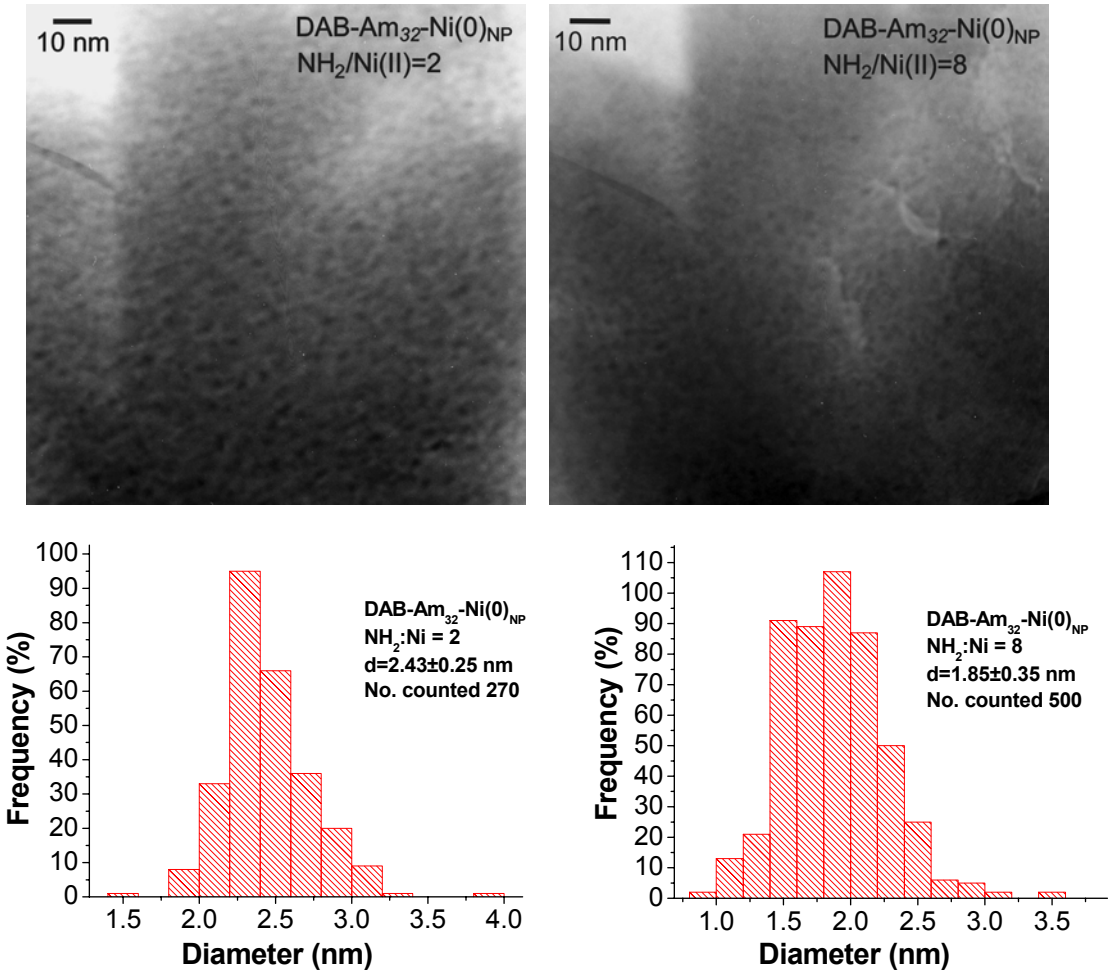

Figure 3.12 HR-TEM image and particle size distribution of nickel nanoparticles obtained by reduction of DAB-Am_{32}-Ni(II)$_x$, ($x = n/8$ and $n/2$); ($x = n/4$); [Ni(II)] = 5×10^{-4} M).

I observe very small $Ni(0)_{NP}$ sizes that are highly dependent on dendrimer generation (Table 3.1) and NH_2:Ni(II) values of $2 \leq n/x \leq 8$ (Table 3.2). $Ni(0)_{NP}$ size is inversely proportional to dendrimer generation and NH_2:Ni(II) ratio (n/x). Due to the sizes of the DAB-Am_n in solution, the $Ni(0)_{NP}$ produced here cannot reside completely inside the dendrimers, and it is concluded that the nanoparticles are coated with the DAB-Am_n (interdendrimer), yielding a nanocomposite material, similar to what we proposed in an initial study with Cu(II)-PPI complexes and that proposed by Gröhn et alia for PAMAM-Au(III) materials.[7,77] For example, in the case of the 5th-generation dendrimer in Table 3.1, the resulting Ni nanoparticle has a diameter of 1.88 nm that is only slightly smaller than that of DAB-Am_{64}

(~2.5 nm); these observations are in accord with those from our work with DAB-Am$_n$–Cu(0)$_{NP}$ nanocomposites.[7] In addition, it is clear that the number of Ni atoms contained in a single Ni(0)$_{NP}$ is more than that available in an individual precursor, DAB-Am$_n$–Ni(II)$_x$, which upon initial examination would seem to indicate that the growth process of the Ni(0) nuclei is not well separated from nuclei formation; however, this cannot be the case as the size dispersity of the Ni(0)$_{NP}$ is very low. Finally, the inverse relationship between Ni(0)$_{NP}$ size and *n*/*x* (NH_2:Ni(II) ratio, Table 3.2) would at first glance lead to the conclusion that the developing nanoparticle is stabilized by the presence of more amine groups on its surface (see last column in Table 3.2), but this argument does not hold for the generation-dependent effects observed in Table 3.1. Similar attempts on our part to describe the mechanism of DAB-Am$_n$–Cu(0)$_{NP}$ formation were met with similar frustration, but in that study we did not have detailed data regarding the effects of NH_2:metal ion ratio on nanoparticle size.[7]

I propose that the observed inverse relationship between Ni(0)$_{NP}$ size and both dendrimer generation and NH_2:Ni(II) ratio (*n*/*x*), and the larger-than-expected Ni(0)$_{NP}$ size, are due to the presence of DAB-Am$_n$–Ni(II)$_x$ complex aggregates, whose size is dependent on the concentration and generation of DAB-Am$_n$–Ni(II)$_x$ in the methanol solutions. As outlined in Scheme 3.2, I posit that upon {DAB-Am$_n$–Ni(II)$_x$}$_Y$ exposure to reducing agent, nanoparticles of a dimension corresponding to the total number of Ni atoms initially in the aggregate (*n***Y*/*x*) are formed, and the resulting Ni(0)$_{NP}$ are protected from further growth by their presence within the dendrimer aggregate. The aggregates of Ni(II)-dendrimer complexes form either as a result of the Ni(II) coordinating to pre-existing aggregates of the DAB-Am$_n$ (path A in Scheme 3.2), or they form by aggregation of the DAB-Am$_n$–Ni(II)$_x$ complexes (path B and C in Scheme 3.2). Upon reduction of the Ni(II)-complex aggregates, the concentration of the Ni(0)$_{atom}$ species is above the supersaturation value ("critical value"), and nucleation occurs inside the {DAB-Am$_n$}$_Y$

aggregate to yield DAB-Am$_n$–Ni(0)$_{NP}$. This model is in accord with the larger-than-expected sizes of the Ni(0)$_{NP}$ found here and those in our previous study of Cu(0)$_{NP}$,[7] as well as the small size dispersity of the nanoparticles. I conclude that aggregate formation would also occur for Ni(II), based on its similar chemical properties in comparison to Cu(II). At this time, I cannot discern between paths B and C in Scheme 3.2, but it is clear that aggregation of the DAB-Am$_{32}$–Ni(II)$_x$ would lead to the results noted in Table 3.1 and 3.2.

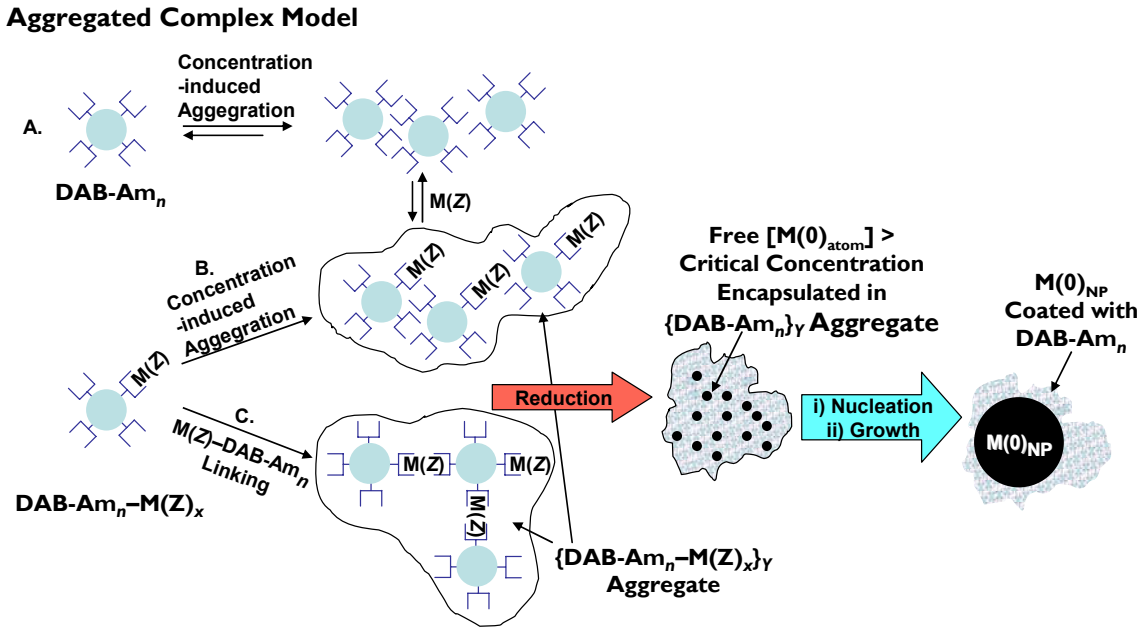

Scheme 3.2 Proposed path for formation of DAB-Am$_n$–Ni(0)$_{NP}$.

3.4 Conclusions

Ni(II) has been shown to form well-defined, stoichiometric complexes with DAB-Am$_n$ dendrimers. Using UV-Vis spectroscopy and the method of continuous variation, it was determined that the predominant complex between nickel and all DAB-Am$_n$ dendrimer generations studied exhibits a 2:1 ratio of NH_2 end groups to Ni(II). Nickel nanoclusters with diameters ranging from 1.85 to 2.70 nm have been prepared by $NaBH_4$ reduction of Ni(II) coordinated to various generations of DAB-Am$_n$ dendrimers (1, 2, 3, 4, and 5) under a variety of conditions. From XPS characterization studies, it was found that the Ni nanoparticles prepared

by the dendrimer-ligand-based method are in the metallic state without any Ni-B alloy present, and they possess an impurity of H_3BO_3 that forms during decomposition of $NaBH_4$ in methanol solution. The size of the Ni(0) nanoparticles can be precisely controlled (in order of impact) via dendrimer generation or the ratio of primary amines to Ni(II) ions in the dendrimer precursor. We would like to expand the variety of metal ions that can be complexed by DAB-Am_n dendrimers using the dendrimer-ligand-based method in order to create new hybrid materials, such as bimetallic nanoparticles supported on silica surfaces for environmental catalysis applications.

3.5 References

(1) Burda, C.; Chen, X. B.; Narayanan, R.; El-Sayed, M. A. Chemistry and properties of nanocrystals of different shapes. *Chem. Rev.* **2005**, *105*, 1025-1102.

(2) Zeng, F. W.; Zimmerman, S. C. Dendrimers in supramolecular chemistry: From molecular recognition to self-assembly. *Chem. Rev.* **1997**, *97*, 1681-1712.

(3) Bosman, A. W.; Janssen, H. M.; Meijer, E. W. About dendrimers: Structure, physical properties, and applications. *Chem. Rev.* **1999**, *99*, 1665-1688.

(4) Crooks, R. M.; Zhao, M. Q.; Sun, L.; Chechik, V.; Yeung, L. K. Dendrimer-encapsulated metal nanoparticles: Synthesis, characterization, and applications to catalysis. *Acc. Chem. Res.* **2001**, *34*, 181-190.

(5) Scott, R. W. J.; Wilson, O. M.; Crooks, R. M. Synthesis, characterization, and applications of dendrimer-encapsulated nanoparticles. *J. Phys. Chem. B* **2005**, *109*, 692-704.

(6) Bosman, A. W.; Schenning, A.; Janssen, R. A. J.; Meijer, E. W. Well-defined metallodendrimers by site-specific complexation. *Chem. Ber-Recl.* **1997**, *130*, 725-728.

(7) Floriano, P. N.; Noble, C. O.; Schoonmaker, J. M.; Poliakoff, E. D.; McCarley, R. L. Cu(0) nanoclusters derived from poly(propylene imine) dendrimer complexes of Cu(II). *J. Am. Chem. Soc.* **2001**, *123*, 10545-10553.

(8) Vassilev, K.; Ford, W. T. Poly(propylene imine) dendrimer complexes of Cu(II), Zn(II), and Co(III) as catalysts of hydrolysis of *p*-nitrophenyl diphenyl phosphate. *J. Polym. Sci., Part A: Polym. Chem.* **1999**, *37*, 2727-2736.

(9) Chai, M. H.; Ignash, M.; Holley, A. K. NMR investigation on the complexation of PPI-3 with zinc (II) ions. *Polym. Prepr. (Am. Chem. Soc., Div. Polym. Chem.)* **2004**, *45*, 581-582.

(10) Chai, M.; Holly, A. K.; Norton, M. L. Synthesis and characterization of PPI-3 encapsulated metal nanoparticles. *Polym. Prepr. (Am. Chem. Soc., Div. Polym. Chem.)* **2003**, *44*, 296-297.

(11) Esumi, K.; Isono, R.; Yoshimura, T. Preparation of PAMAM- and PPI-metal (silver, platinum, and palladium) nanocomposites and their catalytic activities for reduction of 4-nitrophenol. *Langmuir* **2004**, *20*, 237-243.

(12) Luo, Y.; Sun, X. Rapid, single-step preparation of dendrimer-protected silver nanoparticles through a microwave-based thermal process. *Mater. Lett.* **2007**, *61*, 1622-1624.

(13) Sun, X.; Dong, S.; Wang, E. One-step preparation and characterization of poly(propyleneimine) dendrimer-protected silver nanoclusters. *Macromolecules* **2004**, *37*, 7105-7108.

(14) Esumi, K. Synthesis and catalytic property of dendrimer-metal nanocomposites. *Polym. Prepr. (Am. Chem. Soc., Div. Polym. Chem.)* **2004**, *45*, 461-461.

(15) Esumi, K.; Matsumoto, T.; Seto, Y.; Yoshimura, T. Preparation of gold-, gold/silver-dendrimer nanocomposites in the presence of benzoin in ethanol by UV irradiation. *J. Colloid. Interface. Sci.* **2005**, *284*, 199-203.

(16) Vohs, J. K.; Brege, J. J.; Raymond, J. E.; Brown, A. E.; Williams, G. L.; Fahlman, B. D. Low-temperature growth of carbon nanotubes from the catalytic decomposition of carbon tetrachloride. *J. Am. Chem. Soc.* **2004**, *126*, 9936-9937.

(17) Esumi, K.; Hayakawa, K.; Yoshimura, T. Morphological change of gold-dendrimer nanocomposites by laser irradiation. *J. Colloid. Interface. Sci.* **2003**, *268*, 501-506.

(18) Esumi, K.; Miyamoto, K.; Yoshimura, T. Comparison of PAMAM-Au and PPI-Au nanocomposites and their catalytic activity for reduction of 4-nitrophenol. *J. Colloid. Interface. Sci.* **2002**, *254*, 402-405.

(19) Luo, Y. Size-controlled preparation of dendrimer-protected gold nanoparticles: A sunlight irradiation-based strategy. *Mater. Lett.* **2008**, *62*, 3770-3772.

(20) Sun, X.; Luo, Y. Size-controlled synthesis of dendrimer-protected gold nanoparticles by microwave radiation. *Mater. Lett.* **2005**, *59*, 4048-4050.

(21) Sun, X.; Jiang, X.; Dong, S.; Wang, E. One-step synthesis and size control of dendrimer-protected gold nanoparticles: A heat-treatment-based strategy. *Macromol. Rapid Commun.* **2003**, *24*, 1024-1028.

(22) Hayakawa, K.; Yoshimura, T.; Esumi, K. Preparation of gold-dendrimer nanocomposites by laser irradiation and their catalytic reduction of 4-nitrophenol. *Langmuir* **2003**, *19*, 5517-5521.

(23) Ponder, S. M.; Darab, J. G.; Mallouk, T. E. Remediation of Cr(VI) and Pb(II) aqueous solutions using supported, nanoscale zero-valent iron. *Environ. Sci. Technol.* **2000**, *34*, 2564-2569.

(24) Wang, C. B.; Zhang, W. X. Synthesizing nanoscale iron particles for rapid and complete dechlorination of TCE and PCBs. *Environ. Sci. Technol.* **1997**, *31*, 2154-2156.

(25) Born, J. G. P.; Mulder, P.; Louw, R. Fly-ash mediated reactions of phenol and monochlorophenols - oxychlorination, deep oxidation, and condensation. *Environ. Sci. Technol.* **1993**, *27*, 1849-1863.

(26) Buekens, A.; Stieglitz, L.; Huang, H.; Cornelis, E. Formation of dioxin in industrial combustors and pyrometallurgical plants. *Environ. Eng. Sci.* **1998**, *15*, 29-36.

(27) Froese, K. L.; Hutzinger, O. Polychlorinated benzene, phenol, dibenzo-*p*-dioxin, and dibenzofuran in heterogeneous combustion reactions of acetylene. *Environ. Sci. Technol.* **1996**, *30*, 998-1008.

(28) Lomnicki, S.; Dellinger, B. A detailed mechanism of the surface-mediated formation of PCDD/F from the oxidation of 2-chlorophenol on a CuO/silica surface. *J. Phys. Chem. A* **2003**, *107*, 4387-4395.

(29) Allouis, C.; Beretta, F.; D'Alessio, A. Structure of inorganic and carbonaceous particles emitted from heavy oil combustion. *Chemosphere* **2003**, *51*, 1091-1096.

(30) Rogge, W. F.; Hildemann, L. M.; Mazurek, M. A.; Cass, G. R.; Simoneit, B. R. T. Sources of fine organic aerosol .2. Noncatalyst and catalyst-equipped automobiles and heavy-duty diesel trucks. *Environ. Sci. Technol.* **1993**, *27*, 636-651.

(31) Haynes, B. S.; Neville, M.; Quann, R. J.; Sarofim, A. F. Factors governing the surface enrichment of fly-ash in volatile trace species. *J. Colloid. Interface. Sci.* **1982**, *87*, 266-278.

(32) Damle, A. S.; Ensor, D. S.; Ranade, M. B. Coal combustion aerosol formation mechanisms - a review. *Aerosol. Sci. Tech.* **1982**, *1*, 119-133.

(33) Murray, C. B. Synthesis and characterization of nearly monodisperse CdE (E = sulfur, selenium, tellurium) semiconductor nanocrystallites. *J. Am. Chem. Soc.* **1993**, *115*, 8706-8715.

(34) van den Brink, R. W.; Krzan, M.; Feijen-Jeurissen, M. M. R.; Louw, R.; Mulder, P. The role of the support and dispersion in the catalytic combustion of chlorobenzene on noble metal based catalysts. *Appl. Catal., B* **2000**, *24*, 255-264.

(35) Suh, Y. J.; Jang, H. D.; Chang, H. K.; Hwang, D. W.; Kim, H. C. Kinetics of gas phase reduction of nickel chloride in preparation for nickel nanoparticles. *Mater. Res. Bull.* **2005**, *40*, 2100-2109.

(36) Li, X. G.; Murai, T.; Chiba, A.; Takahashi, S. Particle features, oxidation behaviors and magnetic properties of ultrafine particles of Ni-Co alloy prepared by hydrogen plasma metal reaction. *J. Appl. Phys.* **1999**, *86*, 1867-1873.

(37) Rellinghaus, B.; Stappert, S.; Wassermann, E. F.; Sauer, H.; Spliethoff, B. The effect of oxidation on the structure of nickel nanoparticles. *Eur. Phys .J. D* **2001**, *16*, 249-252.

(38) Wu, S. H.; Chen, D. H. Synthesis and characterization of nickel nanoparticles by hydrazine reduction in ethylene glycol. *J. Colloid. Interface. Sci.* **2003**, *259*, 282-286.

(39) Chen, D. H.; Wu, S. H. Synthesis of nickel nanoparticles in water-in-oil microemulsions. *Chem. Mater.* **2000**, *12*, 1354-1360.

(40) Legrand, J.; Taleb, A.; Gota, S.; Guittet, M. J.; Petit, C. Synthesis and XPS characterization of nickel boride nanoparticles. *Langmuir* **2002**, *18*, 4131-4137.

(41) Chiang, S. J.; Liaw, B. J.; Chen, Y. Z. Preparation of NiB nanoparticles in water-in-oil microemulsions and their catalysis during hydrogenation of carbonyl and olefinic groups. *Appl. Catal. A* **2007**, *319*, 144-152.

(42) Hou, Y.; Kondoh, H.; Ohta, T.; Gao, S. Size-controlled synthesis of nickel nanoparticles. *Appl. Surf. Sci.* **2005**, *241*, 218-222.

(43) Chen, L.; Chen, J. M.; Zhou, H. D.; Zhang, D. J.; Wan, H. Q. Synthesis of dodecanethiol monolayer-stabilized nickel nanoparticles. *Mater. Sci. Eng. A* **2007**, *452*, 262-266.

(44) Couto, G. G.; Klein, J. J.; Schreiner, W. H.; Mosca, D. H.; de Oliveira, A. J. A.; Zarbin, A. J. G. Nickel nanoparticles obtained by a modified polyol process: Synthesis, characterization, and magnetic properties. *J. Colloid. Interface. Sci.* **2007**, *311*, 461-468.

(45) Roy, A.; Srinivas, V.; Ram, S.; De Toro, J. A.; Goff, J. P. A comprehensive structural and magnetic study of Ni nanoparticles prepared by the borohydride reduction of $NiCl_2$ solution of different concentrations. *J. Appl. Phys.* **2006**, *100*, 094307.

(46) Sidhaye, D. S.; Bala, T.; Srinath, S.; Srikanth, H.; Poddar, P.; Sastry, M.; Prasad, B. L. V. Preparation of nearly monodisperse nickel nanoparticles by a facile solution based methodology and their ordered assemblies. *J. Phys. Chem. C* **2009**, *113*, 3426-3429.

(47) Kudlash, A. N.; Vorobyova, S. A.; Lesnikovich, A. I. Interphase synthesis and some characteristics of aqueous nickel dispersions. *J. Phys. Chem. Solids* **2008**, *69*, 1652-1656.

(48) Boudjahem, A. G.; Monteverdi, S.; Mercy, M.; Bettahar, M. M. Study of support effects on the reduction of Ni^{2+} ions in aqueous hydrazine. *Langmuir* **2004**, *20*, 208-213.

(49) Estournes, C.; Lutz, T.; Happich, J.; Quaranta, T.; Wissler, P.; Guille, J. L. Nickel nanoparticles in silica gel: Preparation and magnetic properties. *J. Magn. Magn. Mater.* **1997**, *173*, 83-92.

(50) Chatterjee, A.; Chakravorty, D. Preparation of nickel nanoparticles by metalorganic route. *Appl. Phys. Lett.* **1992**, *60*, 138-140.

(51) Johnston-Peck, A. C.; Wang, J.; Tracy, J. B. Synthesis and structural and magnetic characterization of Ni(core)/NiO(shell) nanoparticles. *ACS Nano* **2009**, *3*, 1077-1084.

(52) Park, J.; Kang, E.; Son, S. U.; Park, H. M.; Lee, M. K.; Kim, J.; Kim, K. W.; Noh, H.-J.; Park, J.-H.; Bae, C. J.; Park, J.-G.; Hyeon, T. Monodisperse nanoparticles of Ni and NiO: Synthesis, characterization, self-assembled superlattices, and catalytic applications in the Suzuki coupling reaction. *Adv. Mater.* **2005**, *17*, 429-434.

(53) Wang, H.; Jiao, X.; Chen, D. Monodispersed nickel nanoparticles with tunable phase and size: Synthesis, characterization, and magnetic properties. *J. Phys. Chem. C* **2008**, *112*, 18793-18797.

(54) Winnischofer, H.; Rocha, T. C. R.; Nunes, W. C.; Socolovsky, L. M.; Knobel, M.; Zanchet, D. Chemical synthesis and structural characterization of highly disordered Ni colloidal nanoparticles. *ACS Nano* **2008**, *2*, 1313-1319.

(55) Knecht, M. R.; Garcia-Martinez, J. C.; Crooks, R. M. Synthesis, characterization, and magnetic properties of dendrimer-encapsulated nickel nanoparticles containing < 150 atoms. *Chem. Mater.* **2006**, *18*, 5039-5044.

(56) Job, P. Studies on the formation of complex minerals in solution and on their stability. *Annales De Chimie France* **1928**, *9*, 113-203.

(57) Huang, C. Y. Determination of binding stoichiometry by the continuous variation method - the job plot. *Methods Enzymol.* **1982**, *87*, 509-525.

(58) Cotton, F. A.; Wilkinson, G.; Murillo, C. A.; Bochmann, M. *Advanced inorganic chemistry*; 6th ed.; John Wiley & Sons, Inc.: New York, **1999**.

(59) Bosman, A. W. Dendrimers in action. Ph.D. Dissertation, Technische Universiteit Eindhoven, **1998**.

(60) P. Paoletti; Biagini, S.; Cannas, M. Internal strain in five- and six-membered chelate rings: Crystal structure of bisdi-(3-aminopropyl)aminenickel(II) perchlorate and of bisdi-(2-aminoethyl)aminenickel(II) chloride monohydrate. *J.Chem.Soc., Chem. Commun.* **1969**, 513-514.

(61) Pariya, C.; Ghosh, A.; Chaudhuri, N. R. Preparation, characterisation and thermal behaviour of n-(3-aminopropyl)- 1,3-propanediamine complexes of nickel(II) in the solid state. *Thermochim. Acta* **1995**, *249*, 199-210.

(62) Vacca, A.; Arenare, D.; Paoletti, P. Transition metal complexes of 3,3'-diaminodipropylamine: Stability constants. *Inorg. Chem.* **1966**, *5*, 1384-1389.

(63) Niu, Y.; Crooks, R. M. Preparation of dendrimer-encapsulated metal nanoparticles using organic solvents. *Chem. Mater.* **2003**, *15*, 3463-3467.

(64) Scott, R. W. J.; Ye, H. C.; Henriquez, R. R.; Crooks, R. M. Synthesis, characterization, and stability of dendrimer-encapsulated palladium nanoparticles. *Chem. Mater.* **2003**, *15*, 3873-3878.

(65) Glavee, G. N.; Klabunde, K. J.; Sorensen, C. M.; Hadjipanayis, G. C. Borohydride reduction of nickel and copper ions in aqueous and nonaqueous media - controllable chemistry leading to nanoscale metal and metal boride particles. *Langmuir* **1994**, *10*, 4726-4730.

(66) Grosvenor, A. P.; Biesinger, M. C.; Smart, R. S. C.; McIntyre, N. S. New interpretations of XPS spectra of nickel metal and oxides. *Surf. Sci.* **2006**, *600*, 1771-1779.

(67) Wagner, C. D.; Riggs, W. M.; Davis, L. E.; Moulder, J. F.; Muilenberg, G. E. *Handbook of x-ray photoelectron spectroscopy*; Perkin-Elmer Corporation Physical Electronics Division, Minnesota, U.S.A, 1979.

(68) Liu, Y. C.; Huang, C. Y.; Chen, Y. W. Hydrogenation of *p*-chloronitrobenzene on Ni-B nanometal catalysts. *J. Nanopart. Res.* **2006**, *8*, 223-234.

(69) Okamoto, Y.; Nitta, Y.; Imanaka, T.; Teranishi, S. Surface characterization of nickel boride and nickel phosphide catalysts by x-ray photoelectron-spectroscopy. *J. Chem. Soc., Faraday Trans. 1* **1979**, *75*, 2027-2039.

(70) Li, H.; Li, H. X.; Dai, W. L.; Wang, W. J.; Fang, Z. G.; Deng, J. F. XPS studies on surface electronic characteristics of Ni-B and Ni-P amorphous alloy and its correlation to their catalytic properties. *Appl. Surf. Sci.* **1999**, *152*, 25-34.

(71) Lee, S. P.; Chen, Y. W. Effects of preparation on the catalytic properties of Ni-P-B ultrafine materials. *Ind. Eng. Chem. Res.* **2001**, *40*, 1495-1499.

(72) Jackelen, A.-M. L.; Jungbauer, M.; Glavee, G. N. Nanoscale materials synthesis. 1. Solvent effects on hydridoborate reduction of copper ions. *Langmuir* **1999**, *15*, 2322-2326.

(73) Lo, C.-t. F.; Karan, K.; Davis, B. R. Kinetic studies of reaction between sodium borohydride and methanol, water, and their mixtures. *Ind. Eng. Chem. Res.* **2007**, *46*, 5478-5484.

(74) Il'inchik, E.; Volkov, V.; Mazalov, L. X-ray photoelectron spectroscopy of boron compounds. *J. Struct. Chem.* **2005**, *46*, 523-534.

(75) Esumi, K.; Suzuki, A.; Yamahira, A.; Torigoe, K. Role of poly(amidoamine) dendrimers for preparing nanoparticles of gold, platinum, and silver. *Langmuir* **2000**, *16*, 2604-2608.

(76) Esumi, K.; Suzuki, A.; Aihara, N.; Usui, K.; Torigoe, K. Preparation of gold colloids with UV irradiation using dendrimers as stabilizer. *Langmuir* **1998**, *14*, 3157-3159.

(77) Gröhn, F.; Bauer, B. J.; Akpalu, Y. A.; Jackson, C. L.; Amis, E. J. Dendrimer templates for the formation of gold nanoclusters. *Macromolecules* **2000**, *33*, 6042-6050.

(78) Lee, I. S.; Lee, N.; Park, J.; Kim, B. H.; Yi, Y.-W.; Kim, T.; Kim, T. K.; Lee, I. H.; Paik, S. R.; Hyeon, T. Ni/NiO core/shell nanoparticles for selective binding and magnetic separation of histidine-tagged proteins. *J. Am. Chem. Soc.* **2006**, *128*, 10658-10659.

(79) Finney, E. E.; Finke, R. G. Nanocluster nucleation and growth kinetic and mechanistic studies: A review emphasizing transition-metal nanoclusters. *J. Colloid. Interface. Sci.* **2008**, *317*, 351-374.

(80) Goldberg, D. E.; Fernelius, W. C. Formation constants of methylbis-(3-aminopropyl)-amine with per, nickel and cadmium ions. *J. Phys. Chem.* **1959**, *63*, 1328-1330.

CHAPTER 4

SILICA-SUPPORTED IRON OXIDE NANOPARTICLES SYNTHESIZED FROM FERROCENOYL DENDRIMERS

4.1 Introduction

Over the past decade, one of the greatest environmental concerns is the effect of combustion-generated fine particles on human health and the environment.[1-3] There is evidence that combustion-generated transition metal oxides[4,5] —particularly those containing copper, nickel, and iron—have been implicated in the production of pollutants.[6-10] Several studies[11-13] involving the surface-catalyzed formation of polychlorinated dibenzo-*p*-dioxins and dibenzofurans (PCDDs/PCDFs) have shown that supported transition metal oxides contribute to the production of PCDD/PCDF pollutants in the presence of a chlorine sources (e.g. chlorophenol, chlorobenzene) in the temperature range 200–600 °C.

Metal-containing dendrimers have been used for a number of years in nanofabrication because they combine the structural features of dendrimers with the function of metals.[14,15] Dendrimers are well suited as templates for synthesis of nanoscopic metals and metal oxides due to their propensity to coordinate or host a variety of metal ions at the periphery, interior or throughout all layers of the dendrimer "host."[16-18] The dendrimer-based nanoparticle precursors permit control over the average particle size, particle size distribution, and size dispersity of nanoparticles.[16] Ferrocene is the most widely-used functional moiety incorporated into dendrimers,[19-32] because ferrocene shows stable and useful redox properties and is easy to attach to materials. Modification of dendrimers with ferrocenoyl units has received considerable attention, as it has provided access to new materials useful in practical applications, such as modification of electrode surfaces,[33-37] molecular printboards,[38-41] chemical sensors,[42,43] electrochemical rectification,[44] multielectron redox materials,[21,24,45-47] and catalysis.[27,30] Another advantage of ferrocenoyl dendrimers is that they exibit chemical and electrochemical

reversibility (can be stabilized in both their oxidized and reduced forms).[27] Even though ferrocenoyl dendrimers have been used in many applications, no studies have been reported in the literature regarding the use of these dendrimers in the synthesis of iron oxide nanoparticles.

In the synthesis of iron oxide nanoparticles, a wide variety of factors can be adjusted (e.g. gelation process, nature of salt precursor, surface mobility of the species present during thermal oxidation) in order to control their size, shape, surface properties, types of phase transitions, and magnetic characteristics.[48,49] It is well known that the properties of nanomaterials strongly depend upon their dimensions;[50-53] therefore, the ability to make particles with small size dispersity is very important. Supported iron oxide catalysts are generally prepared from inorganic salt precursors via traditional methods, such as incipient-wetness impregnation,[54-58] sol-gel routes,[51,57,59-62] and spontaneous deposition on solid substrate,[63] followed by high temperature oxidation. Other methods, such as microcontact printing on silicon surfaces,[64] impregnation inside the pore system of mesoporous materials,[65-68] and incorporation of ferrocene into porous silica glass,[69] have also been used to prepare iron oxide nanoparticles on support. These preparation methods yield iron oxide nanoparticles having diameters ranging from approximately 3 nm to over 100 nm but with large size distributions (high size dispersity). Fe_2O_3 nanoparticles of a controlled size (diameter distribution in the range of 1–4 nm) have been prepared using a dendrimer template-based approach.[14,15,70] Choi et al.[14] prepared supported Fe_2O_3 nanoparticles (1.2 nm in diameter and 42% size dispersity) by using G6-OH PAMAM dendrimers loaded with 60 Fe(III) ions, and used them as catalytic metal seeds for the growth of carbon nanotubes. Amama et al.[15,70] used PAMAM dendrimers to deliver complexed Fe(III) ions to different substrates by dip coating, and they found that Fe_2O_3 nanoparticles obtained after calcination at high temperature are efficient catalysts for the growth of carbon nanotubes.

Here, I report the preparation and characterization of supported iron oxide nanoparticles

using the ferrocenoyl-functionalized dendrimers as precursors. The aim was to synthesize nanoparticles with a controllable size (smaller than 3 nm) and low size dispersity, that will be used as laboratory surrogates for combustion-generated particles to assess their role in pollutant formation (Chapter 5). The choice of iron oxide and support was based on the presence of these materials in the combustion processes. SiO_2 was used as material support for our nanoparticles because it is a relatively inert substrate, has large surface area, facilitates control of sample handling, and is a common inorganic material in combustion-generated particulate matter.[10,71] This chapter mainly focuses on the preparation and characterization of silica-supported iron oxide nanoparticles; the catalytic evaluations of these nanoparticles will be reported in the following chapter. To my knowledge, this is the first time that ferrocenoyl-functionalized dendrimers have been used as precursors in the synthesis of supported iron oxide nanoparticles. I used ferrocenoyl dendrimers as the particle precursor in the synthetic route because the number of active functional groups can be precisely controlled. The dendrimer generation, ferrocenoyl dendrimer loading on the silica surface, and calcination temperature of the dendrimer-based nanoparticle precursor are the key parameters that have been used to control the Fe_2O_3 nanoparticle sizes. After impregnation, the decomposition of the supported metallocene dendrimers was investigated by thermogravimetric analysis and X-ray photoelectron spectroscopy. It was observed that thermal decomposition at 450 °C in the presence of air leads to successful removal of the dendrimer from the silica surface, thereby yielding iron-oxide nanoparticles that are 2.48–3.65 nm in diameter. From HR-TEM studies it is demonstrated that the size of the iron oxide nanoparticles decreases with increasing generation of ferocenoyl-dendrimer and decreasing dendrimer loading as well as with decreasing the calcination temperature and time.

4.2 Experimental Section

4.2.1 Materials

The poly(propylene imine dendrimers) were obtained from Aldrich (generation 1 and 3) and SYMO-Chem (generations 2, 4, and 5) and used as received. Ferrocene carboxylic acid (97%), oxalyl chloride (≥96.0%), triethylamine (99%), tetrahydrofuran (ACS grade), and pentane (99%+ anhydrous) were from Sigma Aldrich. Dichloromethane (HPLC grade) was from J.T. Baker, *n*-hexane from EMD, $NaHCO_3$ and NaCl from Fisher, and Na_2SO_4 (anhydrous) from Mallinckrodt. Fumed silica, Cab-O-Sil EH-5, (surface area 380 $m^2\ g^{-1}$) was a gift from CABOT.

4.2.2 Synthesis of Ferrocenoyl-Functionalized Poly(propylene imine) Dendrimers

The nomenclature used to describe the dendrimers and dendrimer-nanoparticles in this paper is as follows: a given generation poly(propylene imine) dendrimer is denoted as DAB-Am_n, where *n* is the number of NH_2 terminal groups; ferrocenoyl dendrimers are referred to as DAB-$(NHCOFc)_n$ where *n* is the number of end groups, and Fc is the ferrocene group.

The synthesis of ferrocenoyl-functionalized dendrimers was achieved by condensation reactions of 1-(chlorocarbonyl)ferrocene with amine-terminated poly(propylene imine) dendrimer, similar to the procedure reported by Takada and co-workers.[34] In brief, under inert atmosphere, a mixture of DAB-Am_n and triethylamine in CH_2Cl_2 was added to a stirred CH_2Cl_2 solution containing the corresponding mole equivalent of 1-(chlorocarbonyl)ferrocene with respect to DAB-Am_n. The resulting ferrocenoyl dendrimers were purified by reprecipitations from CH_2Cl_2/*n*-hexane. All DAB-$(NHCOFc)_n$ dendrimers were isolated in 60–80% yields as air-stable orange solids, and they were characterized with ^1H NMR spectroscopy and electrospray ionization mass spectrometry (ESI-MS). Spectroscopic data for (DAB-$NHCOFc)_n$ modified dendrimers are as follows:

DAB-$(NHCOFc)_4$. ^1H-NMR (400 MHz, $CDCl_3$): δ 6.83 (t, 4H, NH), 4.77 (t, 8H, C_5H_4),

4.33 (t, 8H, C_5H_4), 4.21 (s, 20H, Cp), 3.45 (quartet, 8H, $NHCH_2$), 2.52 (t, 8H, $CH_2CH_2CH_2N$), 2.44 (br, 4H,$NCH_2CH_2CH_2CH_2N$), 1.77 (quint, 8H, $CH_2CH_2CH_2$), 1.45 (br, 4H, $NCH_2CH_2CH_2CH_2N$). MS (ESI-TOF; *m/z*) 1165.31 (calculated 1164.30 g $mole^{-1}$).

DAB-$(NHCOFc)_8$. ^{1}H-NMR (400 MHz, $CDCl_3$): δ 7.3 (t, 8H, NH), 4.93 (t, 16H, C_5H_4), 4.34 (t, 16H, C_5H_4), 4.22 (s, 40H, Cp), 3.42 (br, 16H, $NHCH_2$), 2.47 and 2.41 (br, 36H, CH_2NCH_2), 1.74 (br, 28H, $CH_2CH_2CH_2$), 1.43 (br, 4H, $NCH_2CH_2CH_2CH_2N$). MS (ESI-TOF; *m/z*) 2469.75 (calculated 2469.74 g $mole^{-1}$).

DAB-$(NHCOFc)_{16}$. ^{1}H-NMR (400 MHz, $CDCl_3$): δ 7.52 (t, 16H, NH), 4.94 (t, 32H, C_5H_4), 4.34 (t, 32H, C_5H_4), 4.22 (s, 80H, Cp), 3.42 (br, 32H, $NHCH_2$), 2.47 and 2.38 (br, 84H, CH_2NCH_2), 1.75 (m, 56H, $CH_2CH_2CH_2$), 1.43 (br, 4H, $NCH_2CH_2CH_2CH_2N$). MS (ESI-TOF; *m/z*) 5079.66 (calculated 5079.61 g $mole^{-1}$).

DAB-$(NHCOFc)_{32}$. ^{1}H-NMR (400 MHz, $CDCl_3$): δ 7.68 (t, 32H, NH), 4.97 (t, 64H, C_5H_4), 4.34 (t, 64H, C_5H_4), 4.22 (s, 160H, Cp), 3.42 (br, 64H, $NHCH_2$), 2.46 and 2.38 (br, 180H, CH_2NCH_2), 1.75 (br, 60H, $CH_2CH_2CH_2$), 1.43 (br, 4H, $NCH_2CH_2CH_2CH_2N$). MS (ESI-TOF; *m/z*) 10298.82 (calculated 10300.35 g $mole^{-1}$).

DAB-$(NHCOFc)_{64}$. ^{1}H-NMR (400 MHz, $CDCl_3$): δ 7.86 (br, 64H, NH), 5.00 (br, 128H, C_5H_4), 4.33 (br, 128H, C_5H_4), 4.21 (s, 320H, Cp), 3.40 (br, 128H, $NHCH_2$), 2.40 (br, 372H, CH_2NCH_2), 1.75 and 1.67 (br, 252H, $CH_2CH_2CH_2$). MS (ESI-TOF; m/z) presented many peaks because of fragmentation and was unable to resolve the reconstruction, MS (MALDI-TOF;*m/z*): broad and noisy around *m/z* 20000.

1-(Chlorocarbonyl)ferrocene was prepared by treatment of ferrocene carboxylic acid with oxalyl chloride according to a previously reported procedure.[72]

4.2.3 Synthesis of Silica-Supported Iron Oxide Nanoparticles

DAB-$(NHCOFc)_n$ dendrimers were deposited onto silica supports at room temperature. Solutions of DAB-$(NHCOFc)_n$ were made by placing the modified dendrimers in tetrahydrofuran, followed by sonication for 30 min to ensure complete dissolution. Impregnation on Cab-O-Sil EH-5 silica was carried out by mixing an appropriate concentration of DAB-$(NHCOFc)_n$ solution with a known weight of silica to achieve different iron loading (5, 2, or 1 wt.% Fe_2O_3 on silica) after calcination. The resulting mixture was allowed to equilibrate for 1 h with occasional stirring. After impregnation, the sample was dried by rotary evaporation. The precursor was calcined for 4 h at 450 °C in a tube furnace under a constant flow of air (70 mL min^{-1}) to convert ferrocene to iron oxide and to remove the organic material. An additional experiment was performed at 450 °C with an extended calcination time (total time 8 h). Two other temperatures (400 and 550 °C) were used for DAB-$(NHCOFc)_{16}$ to examine the effect of temperature on the final structural state and size of the particles. As a reference control, a silica sample was prepared using the same reaction conditions without any dendrimer. In order to determine the role of DAB-Am_n dendrimer in preventing agglomeration of ferrocenoyl-modified dendrimers on the support, I also prepared Fe_2O_3 nanoparticles on silica support starting from a precursor where DAB-$(NHCOFc)_8$ was dissolved in tetrahydrofuran containing 5-fold excess unmodified dendrimer, DAB-Am_8. Then the same steps were followed, namely evaporation of solvent and subsequent calcination at 450 °C for 4 h.

4.2.4 Characterization

4.2.4.1 HR-TEM Images of Silica-Supported Iron Oxide Nanoparticles

Electron microscopy images were obtained with a JEOL-2010 high-resolution transmission electron microscope. The supported iron oxide nanoparticles were first dispersed in methanol, after which a drop of the suspension was placed on a holey carbon-coated copper grid

(400 mesh from SPI supplies), and the solvent was allowed to evaporate. The instrument was operated at an accelerating voltage of 200 KV and different standard magnifications (400–600 K). For each sample, histograms of particle size distributions were obtained through measurement of minimum 400 randomly selected particles from at least 5 images that were taken from different parts of the grid. The images were acquired using a digital camera with Gatan software.

4.2.4.2 X-Ray Photoelectron Spectroscopy (XPS)

The X-ray photoelectron spectra were acquired using an AXIS 165 photoelectron spectrometer using monochromatic Al Kα radiation with a base pressure of 2×10^{-9} Torr. The samples were prepared by pressing the powdered silica-supported iron oxide nanoparticles onto double-sided copper tape and degassed in the pretreatment chamber overnight. After that, the samples were moved into the analysis chamber for XPS study. A 15 eV pass energy was used to examine the chemical state of elements in the target products. Low-resolution survey spectra (40 eV pass energy) were recorded for the 0–1200 eV region to determine the elements present in the sample. High-resolution spectra (160 eV pass energy was used in order to increase the signal intensity) were recorded in the appropriate energy range for all elements present in the sample (Fe 2p, N 1s, C 1s, O 1s, Si 2p).

4.2.4.3 Thermogravimetric Analysis (TGA)

The TGA experiments were carried out on a Mettler instrument with a heating rate of 10 °C/min. Weight changes were recorded as a function of temperature between 25 and 700 °C in both air and nitrogen environments.

4.3 Results and Discussion

The synthesis of the dendrimers, DAB-$(NHCOFc)_n$, was achieved by condensation reactions of 1-(chlorocarbonyl)ferrocene with amine-terminated poly(propylene imine)

dendrimer,[34] as in Scheme 4.1. The advantage of using a ferrocenoyl-modified dendrimer as the precursor to Fe_2O_3 nanoparticles is that it allows for precise control over the number and placement of functional groups at the periphery of the dendrimer.

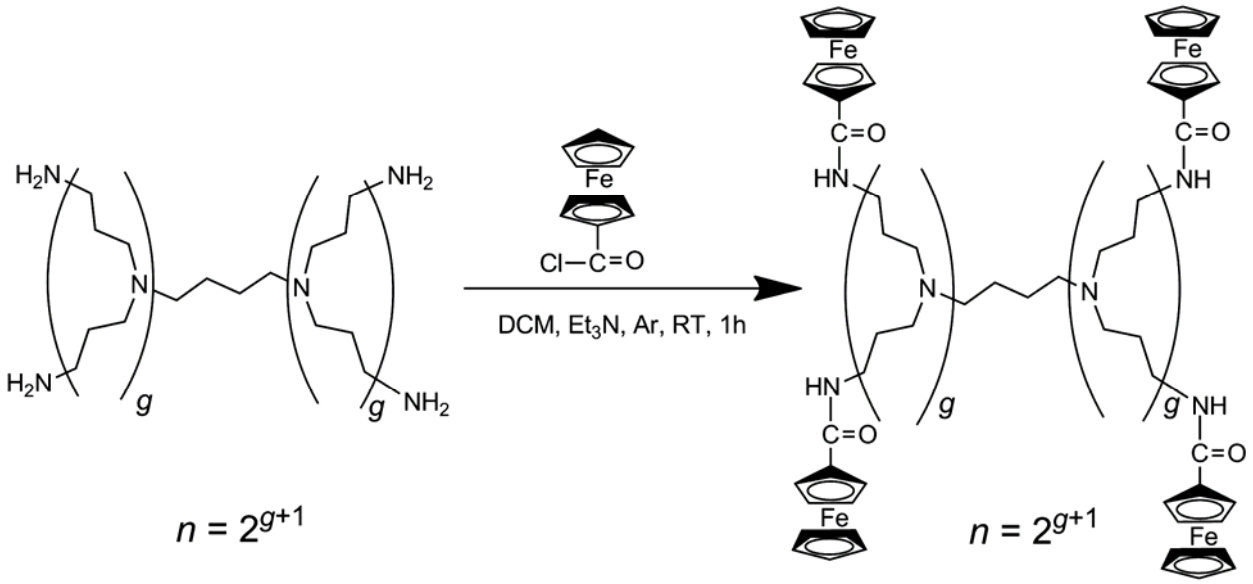

Scheme 4.1 Synthesis of ferrocenoyl-modified dendrimer, DAB-$(NHCOFc)_n$.

Supported metal nanoparticles (zerovalent) are generally prepared via impregnation of dendrimer templated metal onto support followed by thermal treatment.[73-75] In this research the synthesis of silica-supported Fe_2O_3 nanoparticles was achieved from supported ferrocenoyl-functionalized poly(propylene imine) dendrimers (as shown in Scheme 4.2) in two steps. First, the silica support was impregnated with ferrocenoyl-modified dendrimers by a standard impregnation procedure at room temperature. Then, the impregnated silica was calcined in air at high temperatures (400–550 °C), resulting in formation of iron oxide nanoparticles. Thermal decomposition and oxidation of precursor leads to a color change of impregnated silica from yellow-orange to reddish-brown, indicating the formation of iron oxide nanoparticles.[76] A crucial parameter in the synthesis of supported metal oxide nanoparticles is the activation temperature, because removal of the dendrimer precursor by calcination at high temperatures may result in nanoparticle sintering.

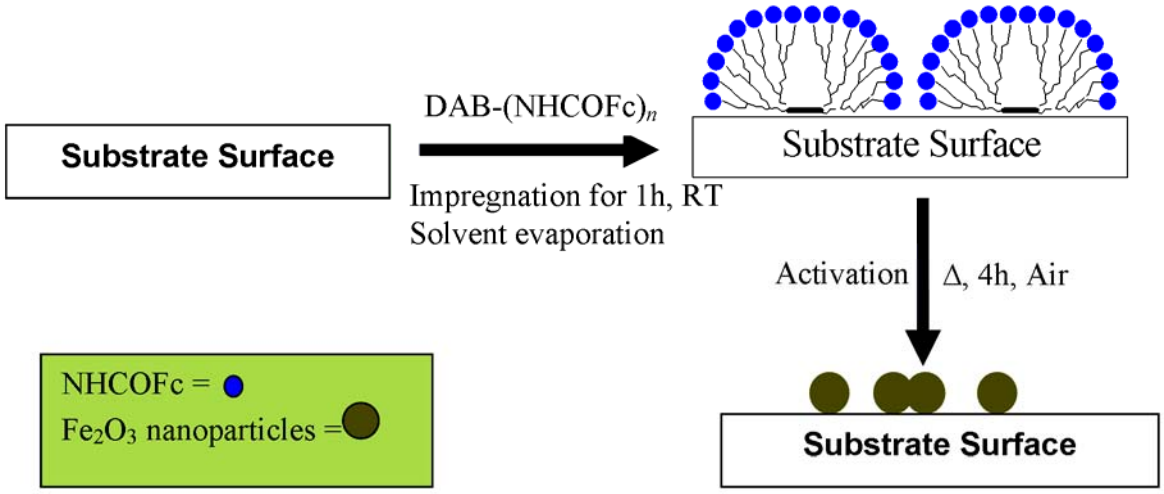

Scheme 4.2 Synthesis of silica-supported Fe_2O_3 nanoparticles.

Activation conditions for the supported DAB-(NHCOFc)$_n$ were chosen on the basis of X-ray photoelectron spectroscopy (XPS) experiments and thermal decomposition as measured by thermogravimetric analysis (TGA). Thermogravimetric experiments for decomposition of silica-supported ferrocenoyl-modified dendrimer both in air and argon environments are shown in Figure 4.1.

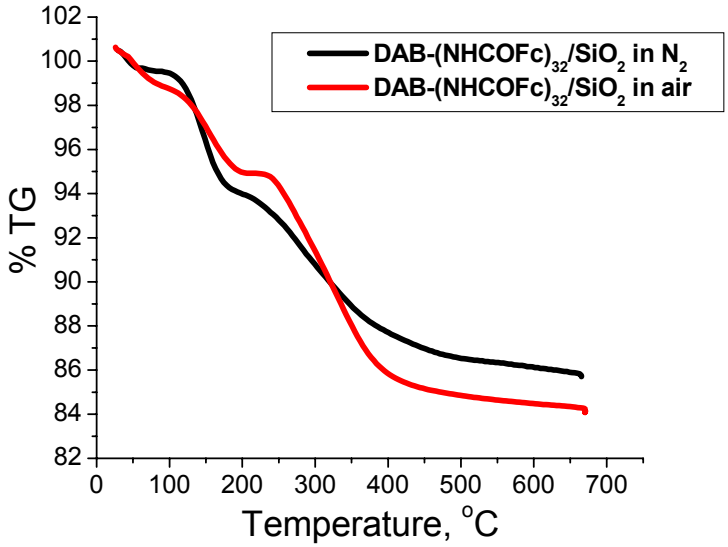

Figure 4.1 Thermogravimetric analysis data for the decomposition of DAB-(NHCOFc)$_{32}$/SiO_2 in air and N_2 environments (rate of heating 10 °C/min).

The decomposition profile is similar in both environments; the major differences are that under oxygen at higher temperature (after 350 °C) there is more weight loss and the weight loss attained its maximum value (about 15%) around 400 °C in the case of oxidation conditions. It is clear that dendrimer decomposition starts at about 150 °C and is complete by 500 °C, an observation that is in agreement with the literature data for other metal-dendrimer decompositions.[77]

4.3.1 Characterization of DAB-(NHCOFc)$_n$/SiO$_2$ Precursors by XPS

X-ray photoelectron spectroscopy was used to determine the chemical state and relative abundance of iron species on the silica support surface and also to monitor the removal of organic material after various thermal decompositions. In Figure 4.2 are shown the N1s high-resolution spectra for DAB-(NHCOFc)$_{16}$/SiO$_2$ before and after calcination at different temperatures.

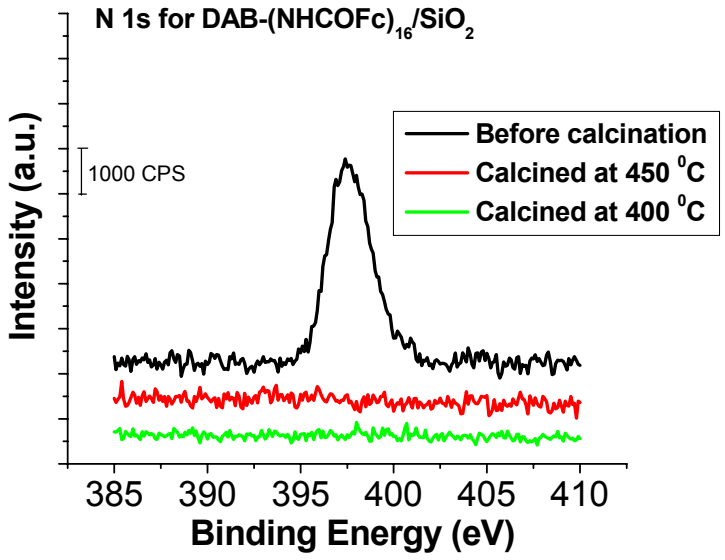

Figure 4.2 N 1s high-resolution X-ray photoelectron spectra for DAB-(NHCOFc)$_{16}$/SiO$_2$ before and after calcination at 400 and 450 °C for 4 h. Green line: calcined at 400 °C, red line: calcined at 450 °C, and black line: before calcination. Number of scans is two for all spectra.

As can be seen at 400 °C, there is no residual nitrogen in the calcined sample for this ferrocenoyl-functionalized dendrimer indicating the decomposition of the dendrimer. According to these XPS experiments, 450 °C was selected as the calcination temperature to be sure that the dendrimer is removed completely in the case of higher generation ferrocenoyl dendrimers. The XPS data are in good agreement with TGA results shown in Figure 4.1, confirming that at 400 °C in air the dendrimer is decomposed. Iron oxide nanoparticles could have a catalytic effect on the decomposition of the dendrimer during calcination, because previously it has been shown that Cu(II) ions accelerated dendrimer decomposition.[78] This metals catalytic effect has been found to be typical for supported metal nanoparticles synthesized by calcination of dendrimers.[78,79] Velarde-Ortiz and Larsen[78] showed that poly(propylene) imine dendrimers could be removed from a silica matrix (sol-gel derive) at temperatures around 300 °C when Cu(II) ions were complexed with the dendrimer. In the absence of Cu(II) ions, the dendrimer was removed at much higher temperatures (550–600 °C) indicating that the Cu(II) ions are catalytic centers that accelerate the decomposition of dendrimer.[78]

Analysis of the N 1s region by high-resolution X-ray photoelectron spectroscopy (Figure 4.3) indicates the presence of N with a binding energy at ~397 eV in samples before calcination. The lack of any detectable N 1s peak after oxidation at 450 °C for 4 h confirms that all N have been removed and no dendrimer is present on silica support. I choose to monitor just the nitrogen as an indicator of dendrimer removal because carbon is always an environmental contamination in XPS spectra.

Before and after the calcination at 450 °C, X-ray photoelectron survey spectra were recorded for DAB-$(NHCOFc)_n/SiO_2$ with a 5% formal content of Fe_2O_3 on the silica support to determine the elements present in the precursors and calcined samples (Figure 4.4). Examination of the survey spectra of samples before calcinations (Figure 4.4) leads to the observation that the

only atomic species detected on the surface are carbon, nitrogen, oxygen, and iron, in addition to silicon from the support.

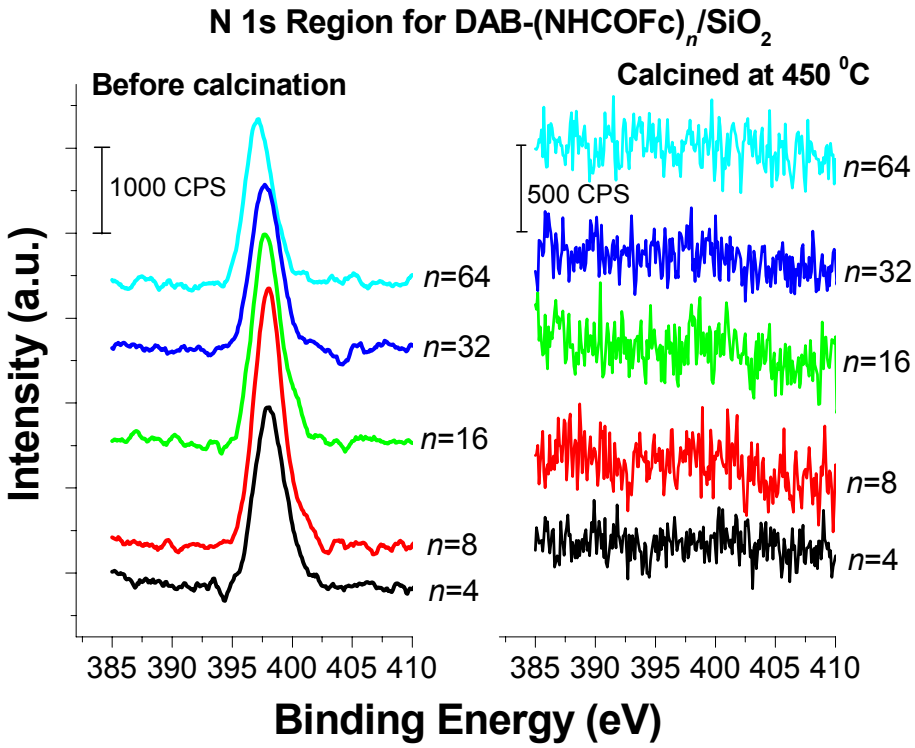

Figure 4.3 N 1s high-resolution X-ray photoelectron spectra for DAB-(NHCOFc)$_n$/SiO$_2$ (n = 4, 8, 16, 32, and 64) before and after calcination at 450 °C for 4 h. Number of scans is two for all spectra.

After calcination at 450 °C (Figure 4.4), the surface species detected by XPS are oxygen, iron, silicon and a very small amount of carbon (less than 5 atomic %).

In Figure 4.5 is shown the XPS Fe 2p region (high-resolution) of uncalcined and calcined DAB-(NHCOFc)$_n$/SiO$_2$. For all five dendrimer generations, the Fe 2p$_{3/2}$ peak lies at ~706.7 eV for uncalcined samples and ~710.7 eV for calcined samples. These binding energies (Table 1) are in excellent agreement with those reported for Fe (II) in organometallic species and Fe(III) in Fe$_2$O$_3$.[80] The XPS data clearly indicate that Fe is present in two distinct oxidation states, Fe(II) before calcination and Fe(III) after calcination at 450 °C, confirming oxidation.

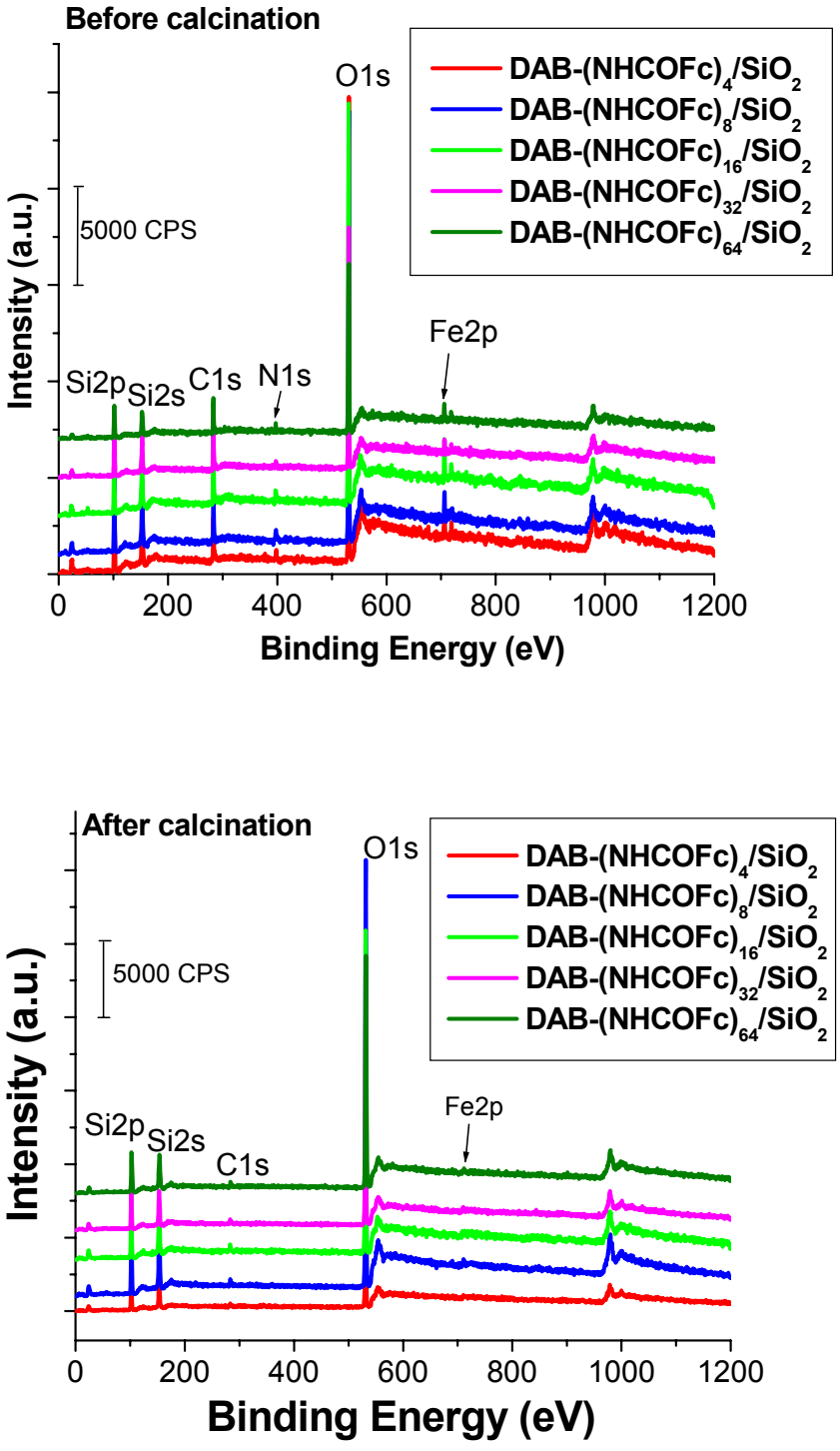

Figure 4.4 Survey X-ray photoelectron spectra for DAB-(NHCOFc)$_n$/SiO$_2$ before and after calcination at 450 °C for 4 h.

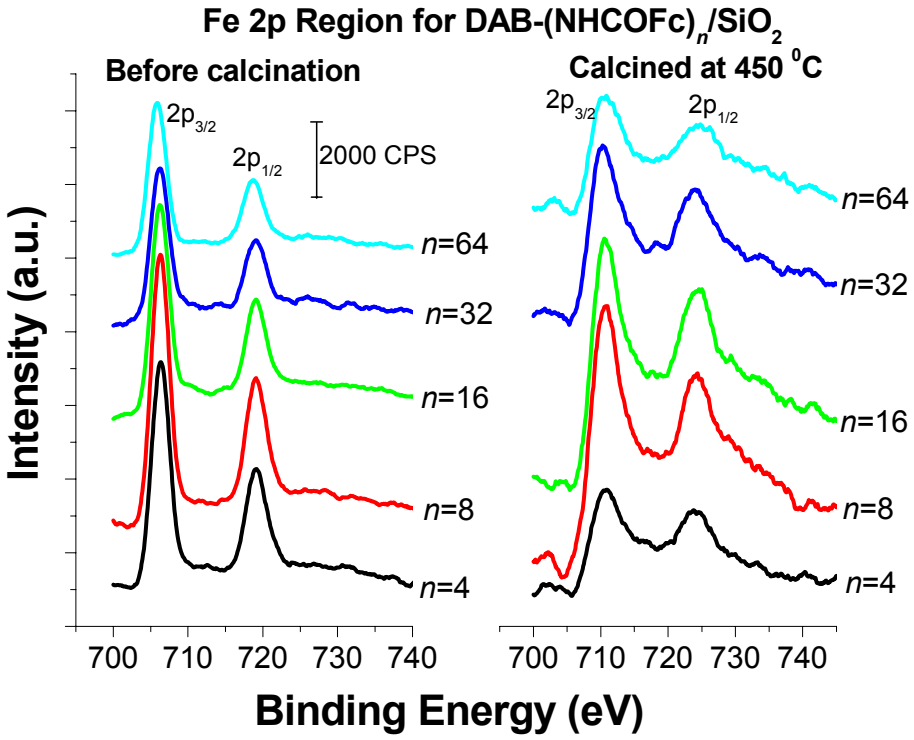

Figure 4.5 Fe 2p high-resolution X-ray photoelectron spectra for DAB-$(NHCOFc)_n/SiO_2$ (n = 4, 8, 16, 32, and 64) before and after calcination at 450 °C for 4 h. Number of scans is two for all spectra.

The oxidation of DAB-$(NHCOFc)_n/SiO_2$ leads to ~ 4.0 eV binding energy shift to higher values, with the final value being consistent with the presence of Fe_2O_3 species.[80] Assigning of the valency of the iron oxide species was achieved using a peak-fitting procedure. In Figure 4.6 is shown the peak-fitted Fe 2p core level spectrum of the oxidized DAB-$(NHCOFc)_{16}/SiO_2$ calcined at 450 °C. As can be seen, from examining Figure 4.6 two peaks are present in the Fe $2p_{3/2}$ region. The first peak at 710.4 eV and the second peak at 712.5 eV are assigned to Fe(III) as in Fe_2O_3 (the second one is a shake up peak). In table 4.1 are summarized the Fe 2p binding energies for DAB-$(NHCOFc)_n/SiO_2$ before and after calcination at 450 ºC and the reference data for Fe(II) and Fe_2O_3.[54,80-83] As can be seen for all calcined DAB-$(NHCOFc)_n/SiO_2$ samples, the Fe $2p_{3/2}$ binding energy corresponds to Fe_2O_3.

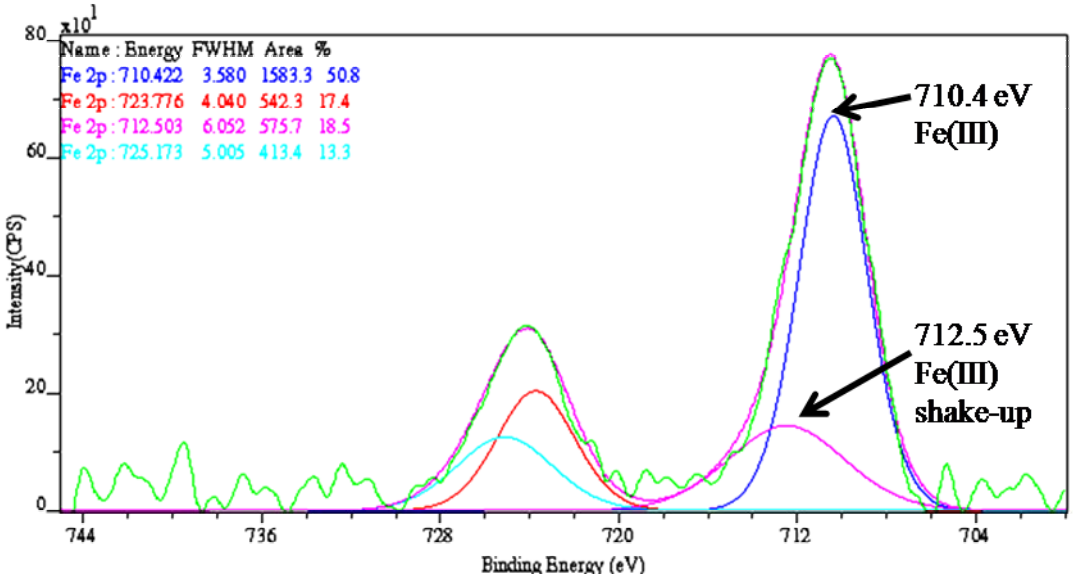

Figure 4.6 Peak-fitted Fe2p X-ray photoelectron spectra for DAB-$(NHCOFc)_{16}/SiO_2$ calcined at 450 °C for 4 h.

Table 4.1 Fe 2p binding energies for DAB-$(NHCOFc)_n/SiO_2$ before and after calcination at 450 °C for 4 h. Reported values for Fe(II) and Fe(III) are also shown.[80]

Sample	Binding Energy Before Calcination (eV)		Binding Energy After Calcination at 450 °C (eV)	
	Fe $2p_{3/2}$	**Fe $2p_{1/2}$**	**Fe $2p_{3/2}$**	**Fe $2p_{1/2}$**
DAB-$(NHCOFc)_4$	706.9	719.4	710.9	723.7
DAB-$(NHCOFc)_8$	706.5	719.3	710.7	724.1
DAB-$(NHCOFc)_{16}$	706.7	719.5	710.7	724.8
DAB-$(NHCOFc)_{32}$	706.7	719.6	710.6	724.3
DAB-$(NHCOFc)_{64}$	706.7	719.4	710.5	724.6
Fe(II)	**706.7**	**719.9**	-	-
Fe_2O_3	-	-	**710.7**	**724.3**

The "bare" SiO_2 support was examined with XPS to check for possible residual impurity species. The survey and Fe2p high-resolution spectra for a SiO_2 sample calcined at 450 °C for 4 h are presented in Figure 4.7. The survey spectrum shows no other species other than silicon and oxygen, as expected. XPS data of amine-terminated poly(propylene imine) dendrimers, DAB-Am_n, supported on silica, and made using conditions identical to DAB-$(NHCOFc)_n/SiO_2$, indicated that at this calcination temperature the dendrimers were completely removed.

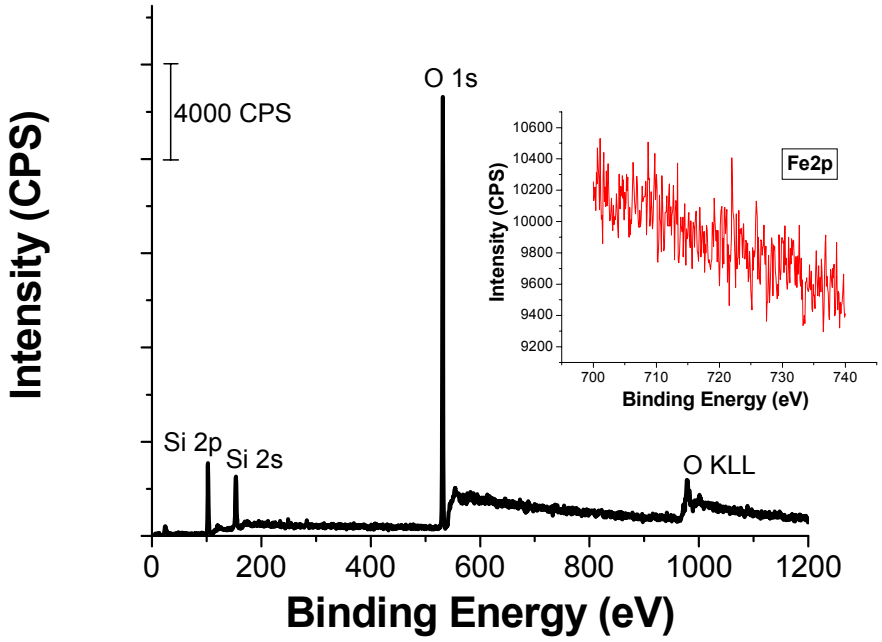

Figure 4.7 Survey X-ray photoelectron spectra for SiO_2 calcined at 450 °C for 4 h. (Inset is the high-resolution spectrum for Fe 2p).

The effect of heat treatment was investigated to follow the formation of iron oxides on the silica support. A set of DAB-$(NHCOFc)_{16}/SiO_2$ having an iron content that would lead to 5% iron oxide (expressed as Fe_2O_3) loading was prepared and calcined at three different temperatures (400, 450, and 550 °C). In Figure 4.8 are presented the high-resolution XPS data for samples calcined at 400 and 550 °C. It can be seen that the Fe $2p_{3/2}$ peak is situated at ~710.7 eV, which is virtually identical in energy to that for the peak of the sample calcined at 450 °C (Figure 4.5). This result indicates that higher temperature has no effect on the iron oxidation state for the studied temperature range (400–550 °C).

Quantitative analyses of the XPS core level spectra samples resulting from calcination of DAB-$(NHCOFc)_n/SiO_2$ at 450 °C for 4 h, with a 5% formal content of Fe_2O_3 on silica support, shows that an average of 5% Fe_2O_3 is present on the surface of the samples. These observations indicate that the resulting iron oxide coverage values are close to those predicted from the

amount of DAB-$(NHCOFc)_n/SiO_2$ placed on silica. In addition, these values provide strong support in the conclusion that the ferrocene units are not desorbed from the silica (volatilized) to any significant degree.

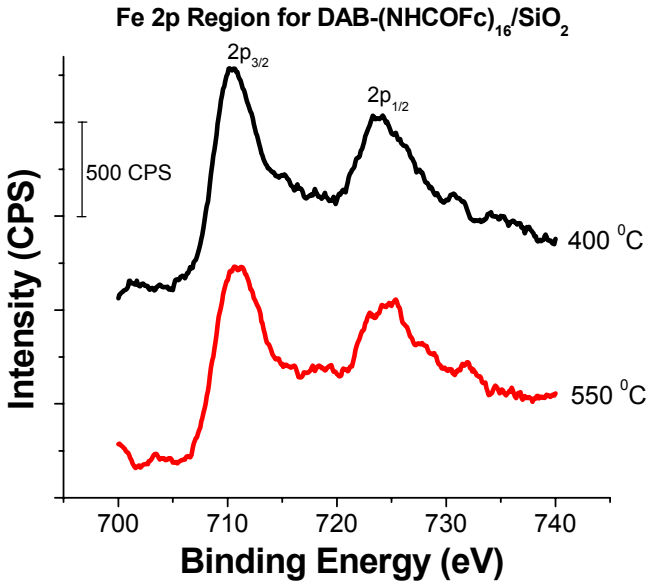

Figure 4.8 Fe 2p high-resolution X-ray photoelectron spectra for DAB-$(NHCOFc)_{16}/SiO_2$ calcined at 400 and 550 °C for 4 h. Number of scans is two for all spectra.

4.3.2 Characterization of Calcined DAB-$(NHCOFc)_n/SiO_2$ by High-Resolution Transmission Electron Microscopy (HR-TEM)

The calcined samples were examined with HR-TEM with the aim to determine the existence and the shape size, and size distribution of Fe_2O_3 nanoparticles on the silica surface. The dendrimer generation, Fe_2O_3 surface coverage on the silica surface, and the calcination temperature are the key parameters that were used to determine how to control nanoparticle size. The influence of other parameters on Fe_2O_3 nanoparticle size and dispersity was examined by varying the time of calcination, and by diluting the ferrocenoyl-modified dendrimers with non-modified dendrimer. During the thermal treatment, I propose that the dendrimer molecules work as a sintering-control agent, where in the degree to which iron oxide nanoparticle can agglomerate and coalesce into large particles on the silica surface is retarded or eliminated. In

all cases, the HR-TEM images revealed the presence of small pseudo-spherical and well-dispersed nanoparticles on the silica surface (Figures 4.9–4.10) that possess small size dispersities.

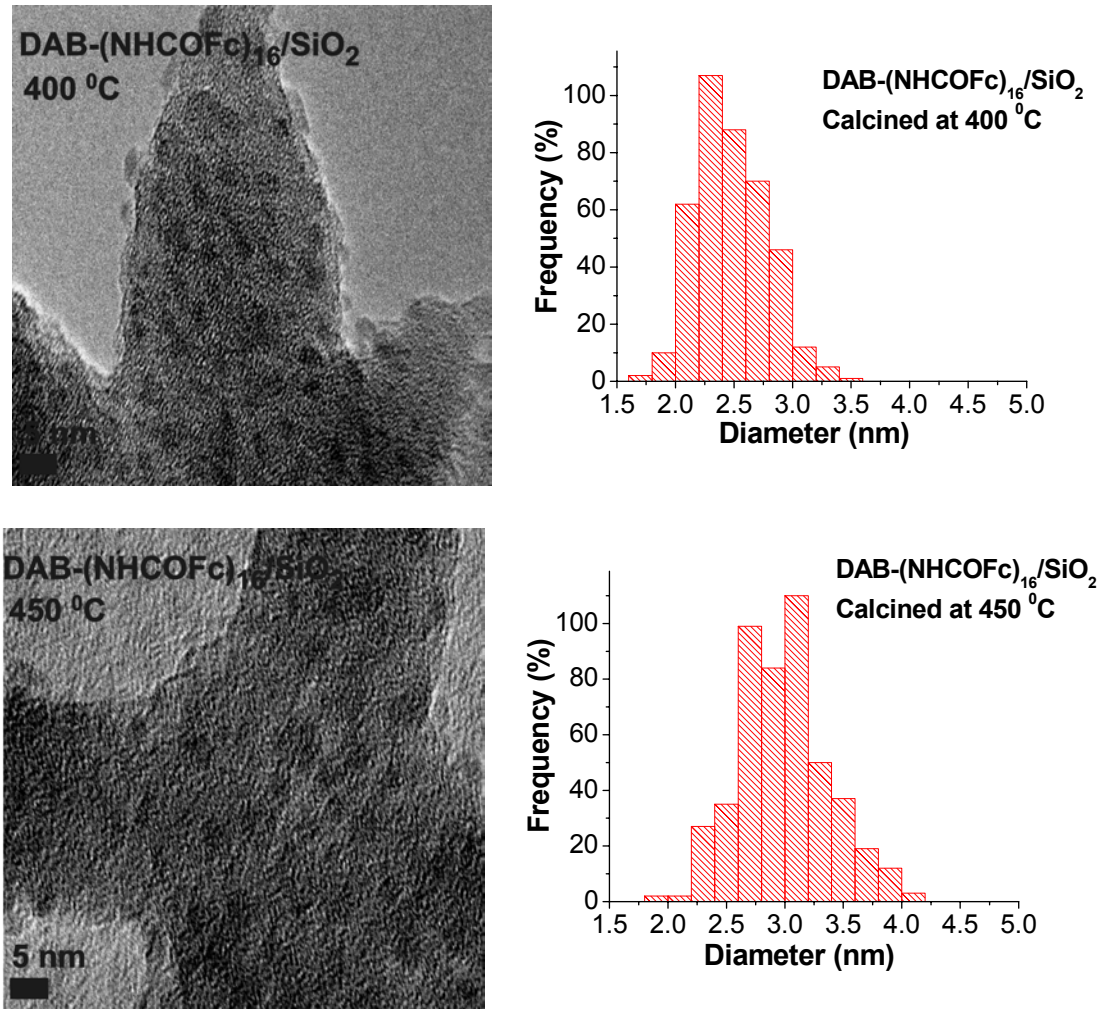

Figure 4.9 HR-TEM images and particle size distributions of Fe_2O_3/SiO_2 nanoparticles obtained by calcination of DAB-$(NHCOFc)_{16}/SiO_2$ at 400 and 450 °C (5% Fe_2O_3) for 4 h. The number of particles used for the particle size distribution calculations is 403 for 400 °C and 480 for 450 °C.

In Table 4.2 are summarized the mean diameters of iron oxide nanoparticles as a function of dendrimer generation. The important thing to notice here is that the Fe_2O_3 nanoparticle size decreases with increased dendrimer generation and the size dispersity is quite small (< 15%).

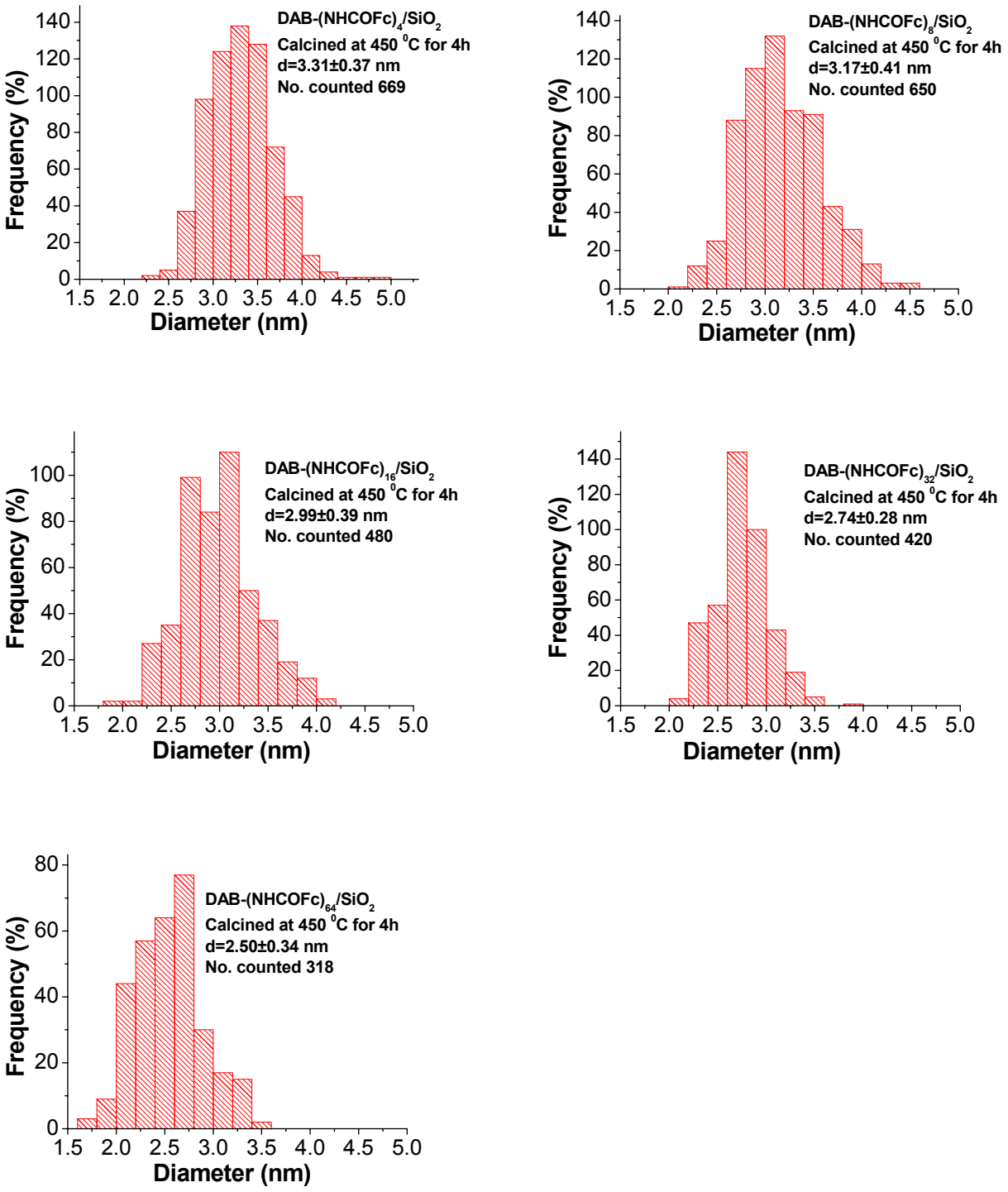

Figure 4.10 Particle size distributions of Fe_2O_3/SiO_2 nanoparticles obtained by calcination of DAB-$(NHCOFc)_n/SiO_2$ (n = 4, 8, 16, 32, and 64) precursors at 450 °C (5% Fe_2O_3 loading) for 4 h.

Upon statistical treatment of the Fe_2O_3 nanoparticle diameter data, it was found that the differences in diameters are significant beyond the 99.9% confidence level (*t*-test). There is a roughly 25% decrease in particle size when the generation of dendrimer is increased from 1 to 5 (n = 4 to n = 64 ferrocene units dendrimer). I propose that this decrease in silica-supported Fe_2O_3 nanoparticle size with increasing dendrimer generation is due to decreased diffusion of iron species during the conversion of the ferrocene units into Fe_2O_3 nanoparticles.

Table 4.2 Mean diameters of iron oxide nanoparticles as a function of dendrimer generation (calcination temperature 450 °C for 4 h and 5% Fe_2O_3 loading).

Sample	Average Diameter ± 1s (% Size Dispersity) (nm)	Number of Particles Evaluated
DAB-$(NHCOFc)_4/SiO_2$	3.31±0.37 (11%)	669
DAB-$(NHCOFc)_8/SiO_2$	3.17±0.41 (13%)	650
DAB-$(NHCOFc)_{16}/SiO_2$	2.99±0.39 (13%)	480
DAB-$(NHCOFc)_{32}/SiO_2$	2.74±0.28 (10%)	420
DAB-$(NHCOFc)_{64}/SiO_2$	2.50±0.34 (14%)	318

Investigation of particle size as a function of calcination temperature was also carried out. The results in Table 4.3 and Figures 4.11 reveal that the size of the resulting iron oxide nanoparticles obtained from DAB-$(NHCOFc)_{16}/SiO_2$ with a 5% iron oxide loading is affected somewhat by the calcination temperature at a fixed calcination time of 4 h.

Table 4.3 Mean diameter of iron oxide nanoparticles as a function of calcination temperature and iron loading for DAB-$(NHCOFc)_{16}/SiO_2$. Samples were calcined for 4 h.

Sample (precursor)	Average Diameter ± 1s (% Size Dispersity) (nm)	Number of particles evaluated	Calcination temperature (°C)	Iron loading in the form of Fe_2O_3 (%)
DAB-$(NHCOFc)_{16}/SiO_2$	2.41±0.32 (13%)	405	450	1
	2.56±0.29 (11%)	398	450	2
	2.60±0.30 (11%)	479	550	
	2.47±0.31 (14%)	403	400	5
	2.99±0.39 (14%)	480	450	
	3.17±0.41 (12%)	439	550	

When the calcinations temperature is varied from 400 to 550 °C, there is only a 28% increase in Fe_2O_3 particle size. A 60% increase in Au(0) nanoparticle size was observed for Au(0)-PAMAM composites embedded in TiO_2 by sol-gel method when the calcination temperature was changed for 500 to 550 °C.[84]

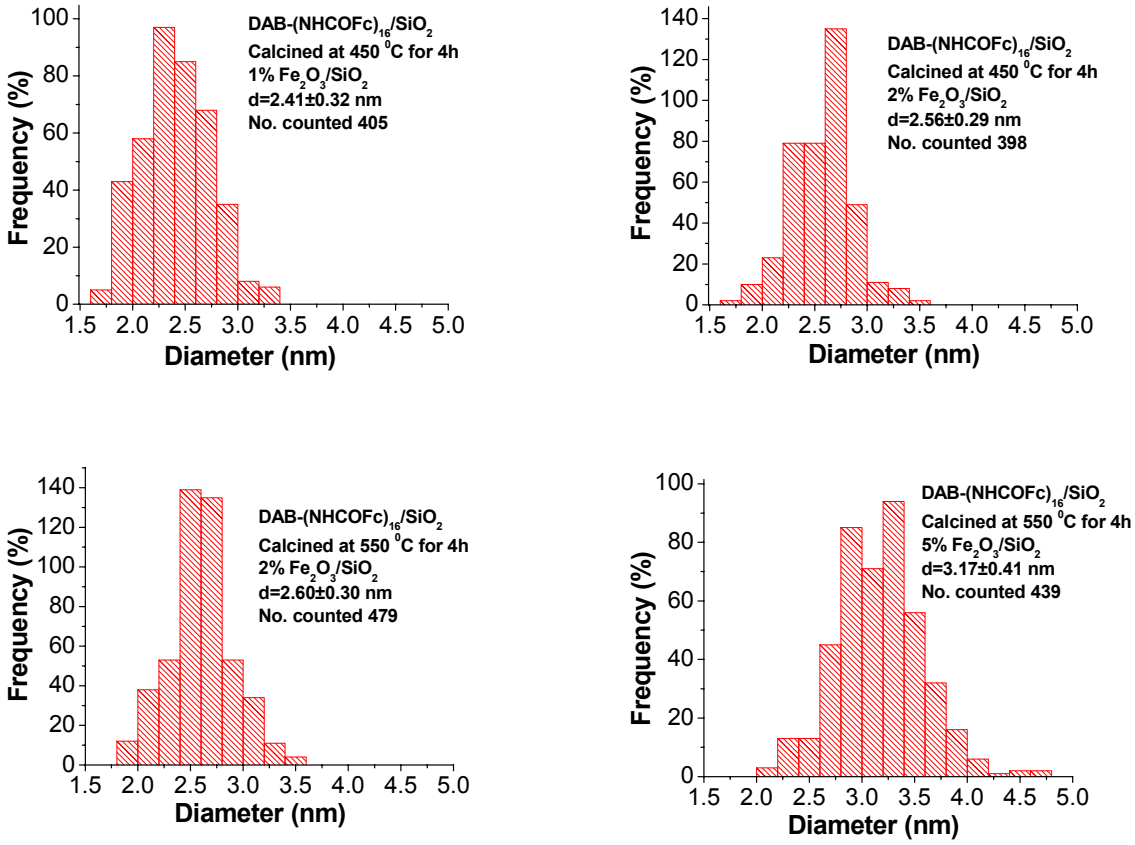

Figure 4.11 Particle size distributions of Fe_2O_3/SiO_2 nanoparticles obtained by calcination of DAB-$(NHCOFc)_{16}/SiO_2$, with 1–5% Fe_2O_3 at 450 and 550 °C for 4 h.

To examine the effect of iron loading on the nanoparticle size, a set of DAB-$(NHCOFc)_{16}/SiO_2$ precursors with a formal iron content (expressed as Fe_2O_3) in the range 1–5% was prepared and calcined at different temperatures for 4 h. From the data in Table 4.3 and Figures 4.11 and 4.12, it is clear that the particle size decreases with decreasing metal oxide loading. Upon statistical treatment of the Fe_2O_3 nanoparticle diameter data, it was found that the differences in diameters are significant beyond the 99.9% confidence level (*t*-test). It is found

that a significant decrease (24%) in the iron oxide nanoparticle size was obtained by decreasing the metal oxide loading from 5 to 1%.

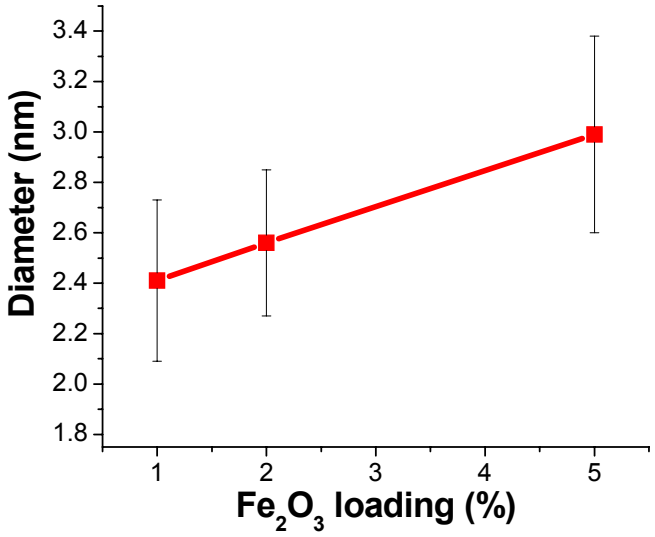

Figure 4.12 Mean diameter of Fe_2O_3-supported nanoparticles as a function of metal oxide loading on SiO_2 for DAB-$(NHCOFc)_{16}$/SiO_2 calcined at 450 °C for 4 h.

This result can be explained by my hypothesis that at lower iron coverage values the ferrocenoyl-dendrimers are more dispersed on the silica surface (further apart) and the chance of initial dendrimer agglomeration during thermal treatment is less because of the increased distance over which the ferrocenoyl-dendrimers must diffuse. This hypothesis is supported by the results obtained for 2% Fe_2O_3 loading (Table 4.3). Here, the change in temperature from 450 to 550 °C results in a slight increase (1%) in the nanoparticle size. Smaller diameters for samples containing 1–2% Fe_2O_3 loading indicate that better dispersion of the active phase DAB-$(NHCOFc)_{16}$/SiO_2 is achieved for these samples. The observed variation in Fe_2O_3 nanoparticle size with metal loading and calcination temperature is in agreement with literature information where these factors have been reported to have an important influence on the particle size, the size distribution and the nature of iron oxide phase (γ or α) in the Fe_2O_3 nanoparticle.[51,59]

Other parameters have been studied (such as the presence of unmodified DAB-Am_n dendrimer on the surface with DAB-$(NHCOFc)_n/SiO_2$, calcination for a longer period of time) in order to see if they influence the average size of silica-supported Fe_2O_3 nanoparticles. In order to increase the space between adsorbed ferrocenoyl dendrimers on silica surface unmodified dendrimers were used in solution. For the experiments with unmodified DAB-Am_n dendrimer in solution, the ferrocenoyl-modified dendrimer was mixed in solutions containing unmodified poly(propylene imine) dendrimer in excess (that was 5 times more molar ratio with respect to primary amine end group than the ferrocene end groups) before the impregnation of the silica support. The formal content of iron (expressed as Fe_2O_3) was 5% on silica and the sample were calcined at 450 °C for 4 h under a flow of air. The results are presented in Table 4.4. As can be seen, there is a ~10 % decrease in Fe_2O_3 nanoparticle size when unmodified dendrimer was present in solution.

Table 4.4 Mean diameter of iron oxide nanoparticles prepared from DAB-$(NHCOFc)_8/SiO_2$ in the presence of DAB-Am_8 dendrimer (calcination temperature 450 °C for 4 h and 5% Fe_2O_3 loading).

Sample	**Average Diameter ± 1s (% Size Dispersity) (nm)**	**Number of particles evaluated**	**DAB-Am_8 in solution**
DAB-$(NHCOFc)_8/SiO_2$	3.17±0.41 (13%)	650	no
	2.87±0.35 (12%)	256	yes

Upon statistical treatment of the Fe_2O_3 nanoparticle diameter data, it was found that the differences in diameters are significant beyond the 99.9% confidence level (*t*-test). This outcome is most likely due to the nanoparticles being better dispersed on the silica surface suggesting that agglomeration can be avoided by impregnating the SiO_2 support with solution having more amine-terminated dendrimer template. This can be explained by having the unmodified dendrimers compete for the silica binding sites with the ferrocenoyl-modifed

dendrimers, and the agglomeration of nanoclusters during thermal treatment would be less than in the case when just ferrocene dendrimer was used. Also, experiments done with ferrocene carboxylic acid instead of ferrocenoyl dendrimers leads to 3 nm Fe_2O_3 nanoparticles but with larger size dispersity (data not shown here).

In an additional experiment, Fe_2O_3/SiO_2 nanoparticles were prepared from the DAB-$(NHCOFc)_{16}/SiO_2$ precusor and calcined at 450 °C with an extended calcination time (for 8 h versus 4 h). A representative TEM image and the resulting particle size distribution are presented in Figure 4.13. During this experiment, the size of the nanoparticles increased to 3.65 nm compared to 2.99 nm for the 4 h calcination time (22% increase). It is clear that with identical calcination temperature but longer calcination time the Fe_2O_3 nanoparticles grow in size, suggesting that further heating induce agglomeration via surface diffusion. It seems like the Fe_2O_3 nanoparticles are not crystalline, thereby allowing Fe_2O_3 "units" to be removed from nanoparticles and then diffuse on SiO_2 surface.

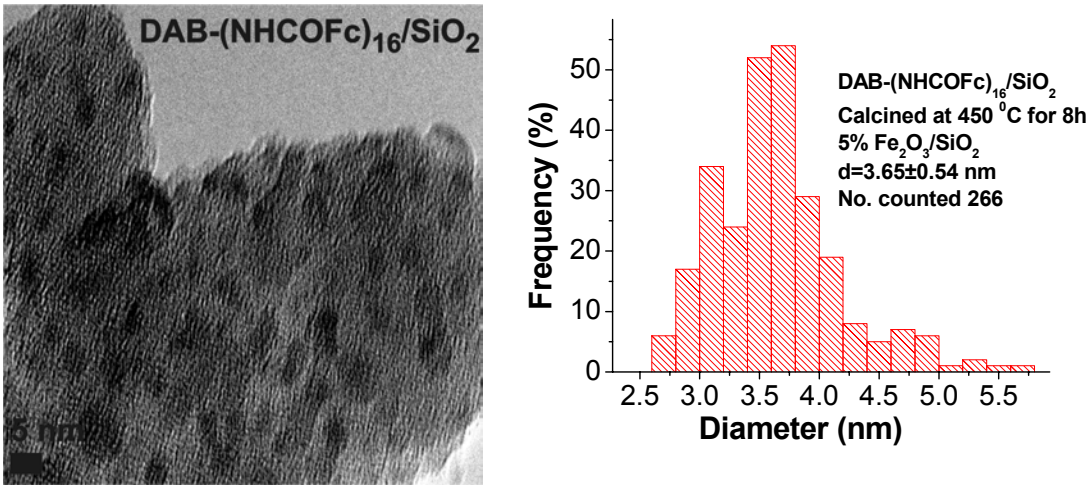

Figure 4.13 HR-TEM image and particle size distributions of Fe_2O_3/SiO_2 nanoparticles obtained by calcination of DAB-$(NHCOFc)_{16}/SiO_2$ precursors at 450 °C for 8 h (5% Fe_2O_3).

Silica supports impregnated with only THF and calcinated at 450 °C for 4 h were also investigated. TEM images (Figure 4.14) from control experiments using SiO_2 without modified

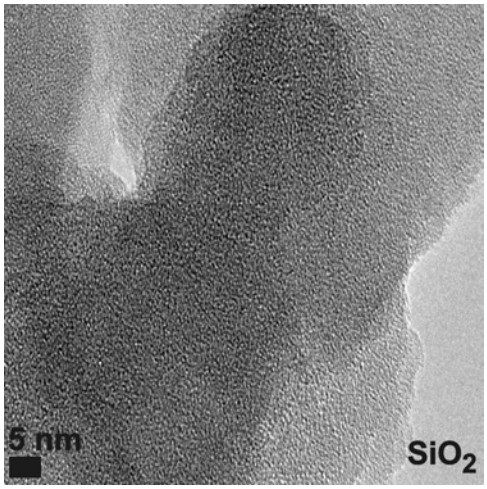

Figure 4.14 HR-TEM image for SiO_2 support calcined at 450 °C for 4 h after impregnation with THF.

dendrimer did not possess any particulates at all.

It is very important to understand the interaction of dendrimers with silica surface in order to interpret the TEM and XPS data. The size of nanocluster obtained can be related to the adsorption and packing of dendrimers on silica and to the activation conditions. The interaction of different dendrimers with solid surfaces has been studied extensively.[34,85,86] It was shown that the amount of dendrimers adsorbed on the investigated porous surfaces depends on the combination of size/shape characteristics, concentration of dendrimer solutions, surface area of support, chemical structure of the dendrimers and solid supports. The saturation coverage of the ferrocenoyl modified dendrimers on platinium surfaces has been described by Moran and co-workers.[34] They reported on a comprehensive study involving the adsorption process of three generations of DAB-$(NHCOFc)_n$ (n = 8, 32, and 64) on platinum electrodes. The experimental values (Γ = (6.5±1.1) × 10^{-12} for DAB-$(NHCOFc)_{64}$, (1.4±0.2) × 10^{-11} for DAB-$(NHCOFc)_{32}$, and (3.5±0.4) × 10^{-11} mol cm^{-2} for DAB-$(NHCOFc)_8$) for the saturation coverage were in good accordance with theoretical ones (Γ = 7.37 × 10^{-12} for DAB-$(NHCOFc)_{64}$, 9.06 × 10^{-12} for DAB-$(NHCOFc)_{32}$, and 2.45 × 10^{-11} mol cm^{-2} for DAB-$(NHCOFc)_8$) calculated

assuming that the adsorbed film has a hexagonal close-packed structure. This suggests that the surface coverage for these dendrimers is likely controlled by their calculated molecular sizes that are 5.1, 4.6, and 2.8 nm for generation 5, 4, and 2, respectively.

I chose to work with a low concentration of dendrimer and low loading of metal (1–5% Fe_2O_3) so that less than a fraction of a full dendrimer monolayer would be formed. The available surface area of the silica support (380 m^2/g) limits the amount of ferrocenoyl-modified dendrimer that can be adsorbed. The calculation of surface coverage for ferrocenoyl dendrimers (generation 2, 4, and 5) on silica surfaces using the theoretical surface coverage reported in the literature for Pt,[34] indicated that for all three ferrocenoyl dendrimer generations, less than a monolayer (< 0.8 monolayer) is formed. For DAB-$(NHCOFc)_4$ the surface coverage should be close or maybe a little over an monolayer. This may explain the higher sizes for nanoparticles obtained from precursors with high percent loading and for DAB-$(NHCOFc)_4$. Also, I cannot exclude the possibility of localized multilayers of the dendrimer on the silica surface during the solvent evaporation, especially for 5% Fe_2O_3 loading and for lower generations of dendrimers (DAB-$(NHCOFc)_4$ and maybe DAB-$(NHCOFc)_8$). First and second generations of dendrimers possess an open structure that makes the internal dendrimer moiety more accessible, resulting in better packing on silica surface compared with higher generations that have a more compact structure.

I propose that adsorption of ferrocenoyl-modified dendrimers on silica is governed by the surface–dendrimer interaction, with small or no interactions between the adsorbed dendrimers, as reported previously for DAB-$(NHCOFc)_n$ on Pt.[34] Another factor that influences ferrocenoyl-dendrimer coverage on silica is the size of the ferrocenoyl-modified dendrimers. The size of the ferrocenoyl dendrimers was measured by DLS for generation 3 to 5 and the results , presented in Table 4.5, were in good agreement with those calculated in the literature.[34]

Table 4.5 The sizes of DAB-(NHCOFc)$_n$ dendrimers in THF determined by DLS.

Sample	Size (nm)	
	Experimental	**Theoretical Diameter**[34]
DAB-(NHCOFc)$_{16}$	3.56 ± 0.26	3.8
DAB-(NHCOFc)$_{32}$	4.35 ± 0.08	4.6
DAB-(NHCOFc)$_{64}$	5.00 ± 0.06	5.1

There are two possible sources of interaction between the dendrimer and the SiO_2 surface: by the surface ferrocene end groups or/and by the internal amine groups. At this moment I do not know the exact interaction of the dendrimers with the silica support. Attempts to ascertain how ferrocenoyl-modified dendrimers adsorb on silica surfaces by X-ray absorption near-edge spectroscopy (XANES) experiments were inconclusive.

All these experiments indicate that the Fe_2O_3 nanoparticle sizes are precisely controlled by the selection of dendrimer generation, iron oxide loading, calcination temperature and time, and the presence of amine-terminated poly(propylene imine) dendrimers. Scheme 4.3 outlines the formation of iron oxide nanoparticles onto silica surfaces from ferrocenoyl dendrimers, either in the absence (path A) or presence (path B) of unmodified poly(propylene imine) dendrimers. The dendrimers are modeled as being adsorbed on silica surface in less than a monolayer. Upon heating in oxidative environment, dendrimer removal occurs by the decomposition of the dendrimer skeleton and ferrocenoyl groups to form adsorbed species (dendrimer fragments) onto silica surface (first step in Scheme 4.3, path A) followed by removal of these fragments from the silica surface at higher temperature and oxidation of iron species to form Fe_2O_3 nanoparticles (second step in Scheme 4.3, path A). Further heat treatment or longer activation time at elevated temperature results in nanoparticle growth on the silica surface (third step in Scheme 4.3, path A). When amine-terminated poly(propylene imine) dendrimers are present in solution (path B in Scheme 4.3), the nanoparticle size decreases because there is an adsorptive competition between amine dendrimers and ferrocenoyl dendrimers on the silica support. During adsorption the

amine-terminated dendrimers bind on the surface and keep the ferrocenoyl dendrimers further apart (first step in scheme 4.3, path B), increasing the distance over which the ferrocenoyl dendrimer must diffuse to agglomerate during calcination.

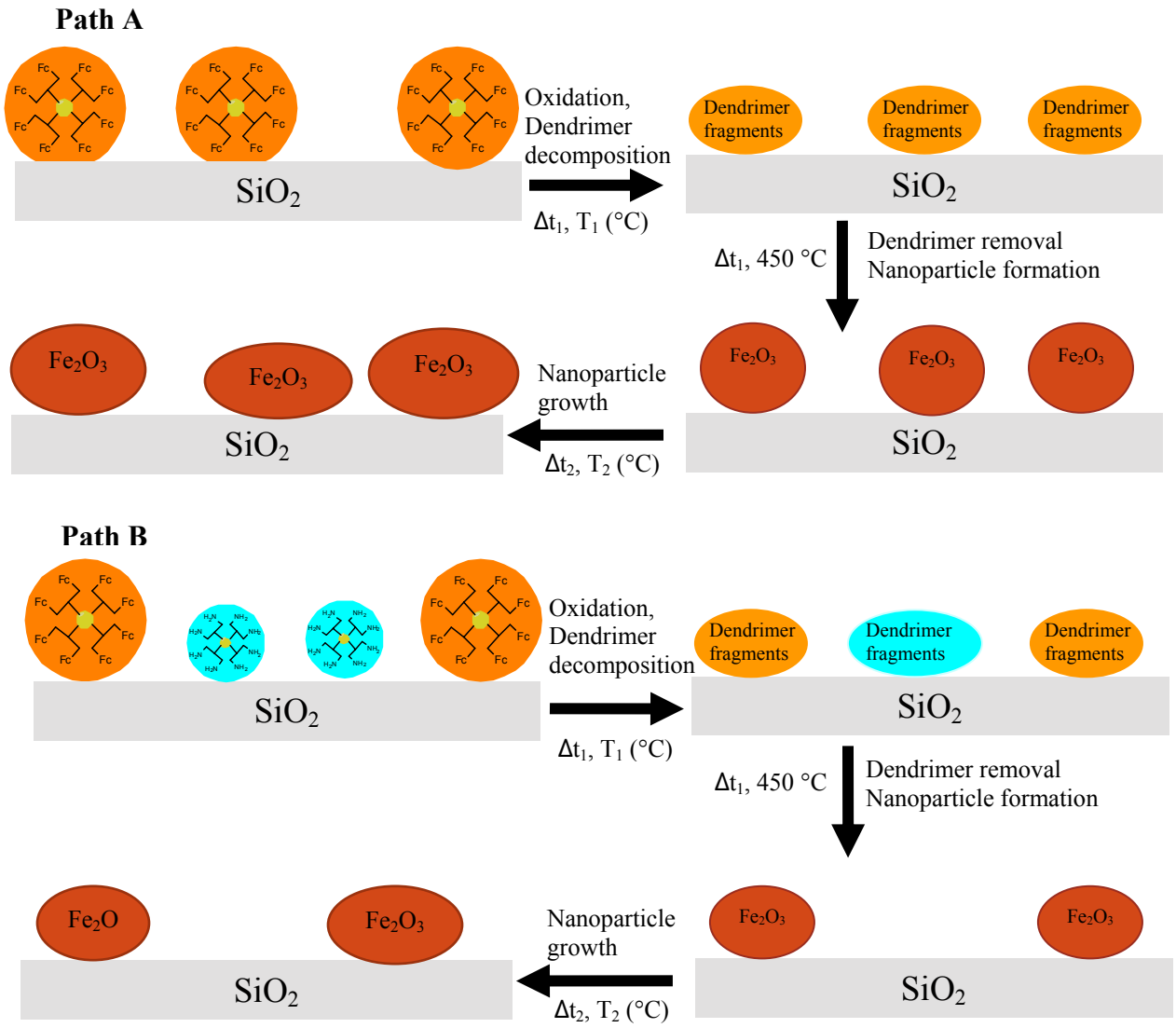

Scheme 4.3 Proposed path for the formation of Fe_2O_3 nanoparticles on silica surfaces.

The Fe_2O_3 nanoparticle size decreases with increasing dendrimer generation, decreasing iron oxide loading, and decreasing calcination temperature. For extended period of calcination 8 vs. 4 h, there is a 22% increase in the nanoparticle size. The dependence of the nanoparticle size on these parameters can be explained as follows. First, the observed inverse relationship

between the Fe_2O_3 nanoparticle size and dendrimer generation is proposed to be due to the size of the dendrimers and the packing on the silica surface during the impregnation process (lower generations of dendrimers have better packing on silica surface compared with higher generations that have a globular structure). By increasing the dendrimer generation, the diffusion of iron species during the conversion from ferrocene units to Fe_2O_3 nanoparticles decreases. Second, the observed increased nanoparticle size with increasing calcination temperature and time is most likely due to the diffusion of nanoparticles on silica surface. The presence of iron in the ferrocenoyl dendrimers has a catalytic effect for oxidative decomposition of dendrimer, which is decomposed at 450 °C (as observed by X-ray photoelectron spectroscopy and thermogravimetric analyses). Upon increasing the temperature, after the dendrimer was already removed, "units" of Fe_2O_3 nanoparticles are removed from the original nanoparticles and diffuse on the silica surface causing agglomeration and an increase in the nanoparticle size. This supposition is supported by the fact that the volume/size of the nanoparticles obtained by calcination at 450 °C for 8 h is not that expected from two particles (obtained by calcination at 450 °C for 4 h) coming together to form a larger particle.

4.4 Conclusions

The use of ferrocenoyl-functionalized dendrimers as precursors offers a reliable, flexible, and reproducible means of producing supported iron oxide nanoparticles with very narrow size distributions and controlled shape. A set of DAB-$(NHCOFc)_n/SiO_2$ samples with a formal content of iron oxide phases in the range of 1–5% was prepared by an impregnation method and subsequent air calcination at different temperatures (400–550 °C). Control of iron oxide nanoparticle size is shown to be possible by manipulating the dendrimer generation, calcination time and temperature, and ferrocenoyl dendrimer loading on silica support. Modification of these parameters serve as a simple way to tune nanoparticle sizes, yielding to silica-supported

iron oxide nanoparticles that are 2.41 to 3.65 nm in diameter with low size dispersity (less than 15%). The HR-TEM studies demonstrate that the size of the iron oxide nanoclusters decrease with increasing generation of ferrocenoyl-dendrimer and decreasing Fe_2O_3 loading on silica support. The calcination temperature was selected according to XPS and TGA data, showing that 450 °C was a good temperature for decomposition and oxidation of DAB-$(NHCOFc)_n$ dendrimer without causing substantial agglomeration of nanoparticles. Increasing the calcination temperatures from 450 to 550 ° C for 2% metal oxide loading on silica support had little effect on the final particle size distributions. For 5% metal oxide loading increasing the temperature caused a 28% increase in Fe_2O_3 nanoparticle size. Smaller diameters for samples containing 1–2% Fe_2O_3 indicates that better dispersion of the active phase is achieved for these samples. The variation of particle size with extended thermal calcination was also observed, indicating that at high temperature the Fe_2O_3 "units" are removed from Fe_2O_3 nanoparticles diffusing on silica surface and causing nanoparticle coalescence and growth. When amine-terminated poly(propylene imine dendrimers) were used in competition with ferrocenoyl dendrimers in iron oxide synthesis method the size of Fe_2O_3 nanoparticles decreased 10%.

4.5 References

(1) Li, N.; Xia, T.; Nel, A. E. The role of oxidative stress in ambient particulate matter-induced lung diseases and its implications in the toxicity of engineered nanoparticles. *Free Radical Bio. Med.* **2008**, *44*, 1689-1699.

(2) Buonanno, G.; Ficco, G.; Stabile, L. Size distribution and number concentration of particles at the stack of a municipal waste incinerator. *Waste Manage.* **2009**, *29*, 749-755.

(3) Lewtas, J. Air pollution combustion emissions: Characterization of causative agents and mechanisms associated with cancer, reproductive, and cardiovascular effects. *Mutat. Res.* **2007**, *636*, 95-133.

(4) Mohapatra, R.; Rao, J. R. Some aspects of characterisation, utilisation and environmental effects of fly ash. *J. Chem. Technol. Biotechnol.* **2001**, *76*, 9-26.

(5) Allouis, C.; Beretta, F.; D'Alessio, A. Structure of inorganic and carbonaceous particles emitted from heavy oil combustion. *Chemosphere* **2003**, *51*, 1091-1096.

(6) Born, J. G. P.; Mulder, P.; Louw, R. Fly-ash mediated reactions of phenol and monochlorophenols - oxychlorination, deep oxidation, and condensation. *Environ. Sci. Technol.* **1993**, *27*, 1849-1863.

(7) Buekens, A.; Stieglitz, L.; Huang, H.; Cornelis, E. Formation of dioxin in industrial combustors and pyrometallurgical plants. *Environ. Eng. Sci.* **1998**, *15*, 29-36.

(8) Froese, K. L.; Hutzinger, O. Polychlorinated benzene, phenol, dibenzo-*p*-dioxin, and dibenzofuran in heterogeneous combustion reactions of acetylene. *Environ. Sci. Technol.* **1996**, *30*, 998-1008.

(9) Thomas, V. M.; McCreight, C. M. Relation of chlorine, copper and sulphur to dioxin emission factors. *J. Hazard. Mater.* **2008**, *151*, 164-170.

(10) Quina, M. J.; Bordado, J. C.; Quinta-Ferreira, R. M. Treatment and use of air pollution control residues from MSW incineration: An overview. *Waste Manage.* **2008**, *28*, 2097-2121.

(11) Alderman, S. L.; Farquar, G. R.; Poliakoff, E. D.; Dellinger, B. An infrared and x-ray spectroscopic study of the reactions of 2-chlorophenol, 1,2-dichlorobenzene, and chlorobenzene with model CuO/silica fly ash surfaces. *Environ. Sci. Technol.* **2005**, *39*, 7396-7401.

(12) Lomnicki, S.; Dellinger, B. A detailed mechanism of the surface-mediated formation of PCDD/F from the oxidation of 2-chlorophenol on a CuO/silica surface. *J. Phys. Chem. A* **2003**, *107*, 4387-4395.

(13) Nganai, S.; Lomnicki, S.; Dellinger, B. Ferric oxide mediated formation of PCDD/Fs from 2-monochlorophenol. *Environ. Sci. Technol.* **2009**, *43*, 368-373.

(14) Choi, H. C.; Kim, W.; Wang, D. W.; Dai, H. J. Delivery of catalytic metal species onto surfaces with dendrimer carriers for the synthesis of carbon nanotubes with narrow diameter distribution. *J. Phys. Chem., B* **2002**, *106*, 12361-12365.

(15) Amama, P. B.; Maschmann, M. R.; Fisher, T. S.; Sands, T. D. Dendrimer-templated Fe nanoparticles for the growth of single-wall carbon nanotubes by plasma-enhanced CVD. *J. Phys. Chem., B* **2006**, *110*, 10636-10644.

(16) Crooks, R. M.; Zhao, M. Q.; Sun, L.; Chechik, V.; Yeung, L. K. Dendrimer-encapsulated metal nanoparticles: Synthesis, characterization, and applications to catalysis. *Acc. Chem. Res.* **2001**, *34*, 181-190.

(17) Bosman, A. W.; Janssen, H. M.; Meijer, E. W. About dendrimers: Structure, physical properties, and applications. *Chem. Rev.* **1999**, *99*, 1665-1688.

(18) Zeng, F. W.; Zimmerman, S. C. Dendrimers in supramolecular chemistry: From molecular recognition to self-assembly. *Chem. Rev.* **1997**, *97*, 1681-1712.

(19) Casado, C. M.; Cuadrado, I.; Moran, M.; Alonso, B.; Garcia, B.; Gonzalez, B.; Losada, J. Redox-active ferrocenyl dendrimers and polymers in solution and immobilised on electrode surfaces. *Coord. Chem. Rev.* **1999**, *186*, 53-79.

(20) Chase, P. A.; Gebbink, R. J. M. K.; van Koten, G. Where organometallics and dendrimers merge: The incorporation of organometallic species into dendritic molecules. *J. Organomet. Chem.* **2004**, *689*, 4016-4054.

(21) Alvarez, J.; Ren, T.; Kaifer, A. E. Redox potential selection in a new class of dendrimers containing multiple ferrocene centers. *Organometallics* **2001**, *20*, 3543-3549.

(22) Sengupta, S.; Sadhukhan, S. K. Convergent synthesis of ferrocene dendrimers: The use of multitopic dendrons with disrupted conjugation. *Organometallics* **2001**, *20*, 1889-1891.

(23) Cardona, C. M.; McCarley, T. D.; Kaifer, A. E. Synthesis, electrochemistry, and interactions with beta-cydodextrin of dendrimers containing a single ferrocene subunit located "Off-center". *J. Org. Chem.* **2000**, *65*, 1857-1864.

(24) Cuadrado, I.; Moran, M.; Casado, C. M.; Alonso, B.; Lobete, F.; Garcia, B.; Ibisate, M.; Losada, J. Ferrocenyl-functionalized poly(propylenimine) dendrimers. *Organometallics* **1996**, *15*, 5278-5280.

(25) Salmon, A.; Jutzi, P. Water soluble ferrocenyl and polyferrocenyl compounds: Synthesis and electrochemistry. *J. Organomet. Chem.* **2001**, *637*, 595-608.

(26) Astruc, D.; Blais, J. C.; Daniel, M. C.; Gatard, S.; Nlate, S.; Ruiz, J. Metallodendrimers and dendronized gold colloids as nanocatalysts, nanosensors and nanomaterials for molecular electronics. *C.R. Chimie* **2003**, *6*, 1117-1127.

(27) Astruc, D.; Ornelas, C.; Ruiz, J. Metallocenyl dendrimers and their applications in molecular electronics, sensing, and catalysis. *Acc. Chem. Res.* **2008**, *41*, 841-856.

(28) Astruc, D.; Ornelas, C.; Aranzaes, J. R. Ferrocenyl-terminated dendrimers: Design for applications in molecular electronics, molecular recognition and catalysis. *J. Inorg. Organomet. P.* **2008**, *18*, 4-17.

(29) Astruc, D. Organometallic chemistry at the nanoscale. Dendrimers for redox processes and catalysis. *Pure Appl. Chem.* **2003**, *75*, 461-481.

(30) Astruc, D.; Blais, J. C.; Daniel, M. C.; Martinez, V.; Nlate, S.; Ruiz, J. Nano-scale metallodendritic complexes in electron-transfer processes and catalysis. *Macromol. Symp.* **2003**, *196*, 1-25.

(31) Daniel, M. C.; Ruiz, J.; Nlate, S.; Blais, J. C.; Astruc, D. Nanoscopic assemblies between supramolecular redox active metallodendrons and gold nanoparticles: Synthesis, characterization, and selective recognition of $H2PO_4^-$, HSO_4^-, and adenosine-5 '-triphosphate (ATP(2-)) anions. *J. Am. Chem. Soc.* **2003**, *125*, 2617-2628.

(32) Ravoo, B. J. Nanofabrication with metal containing dendrimers. *Dalton Trans.* **2008**, 1533-1537.

(33) Alonso, B.; Moran, M.; Casado, C. M.; Lobete, F.; Losada, J.; Cuadrado, I. Electrodes modified with electroactive films of organometallic dendrimers. *Chem. Mater.* **1995**, *7*, 1440-1442.

(34) Takada, K.; Diaz, D. J.; Abruna, H. D.; Cuadrado, I.; Casado, C.; Alonso, B.; Moran, M.; Losada, J. Redox-active ferrocenyl dendrimers: Thermodynamics and kinetics of adsorption, in-situ electrochemical quartz crystal microbalance study of the redox process and tapping mode AFM imaging. *J. Am. Chem. Soc.* **1997**, *119*, 10763-10773.

(35) Diaz, I.; Garcia, B.; Alonso, B.; Casado, C. M.; Moran, M.; Losada, J.; Perez-Pariente, J. Ferrocenyl dendrimers incorporated into mesoporous silica: New hybrid redox-active materials. *Chem. Mater.* **2003**, *15*, 1073-1079.

(36) Alonso, B.; Armada, P. G.; Losada, J.; Cuadrado, I.; Gonzalez, B.; Casado, C. M. Amperometric enzyme electrodes for aerobic and anaerobic glucose monitoring prepared by glucose oxidase immobilized in mixed ferrocene-cobaltocenium dendrimers. *Biosens. Bioelectron.* **2004**, *19*, 1617-1625.

(37) Zamora, M.; Herrero, S.; Losada, J.; Cuadrado, I.; Casado, C. M.; Alonso, B. Synthesis and electrochemistry of octamethylferrocenyl-functionalized dendrimers. *Organometallics* **2007**, *26*, 2688-2693.

(38) Nijhuis, C. A.; Yu, F.; Knoll, W.; Huskens, J.; Reinhoudt, D. N. Multivalent dendrimers at molecular printboards: Influence of dendrimer structure on binding strength and stoichiometry and their electrochemically induced desorption. *Langmuir* **2005**, *21*, 7866-7876.

(39) Tokuhisa, H.; Zhao, M. Q.; Baker, L. A.; Phan, V. T.; Dermody, D. L.; Garcia, M. E.; Peez, R. F.; Crooks, R. M.; Mayer, T. M. Preparation and characterization of dendrimer monolayers and dendrimer-alkanethiol mixed monolayers adsorbed to gold. *J. Am. Chem. Soc.* **1998**, *120*, 4492-4501.

(40) Nijhuis, C. A.; Boukamp, B. A.; Ravoo, B. J.; Huskens, J.; Reinhoudt, D. N. Electrochemistry of ferrocenyl dendrimer - beta-cyclodextrin assemblies at the interface of an aqueous solution and a molecular printboard. *J. Phys. Chem., C* **2007**, *111*, 9799-9810.

(41) Ling, X. Y.; Malaquin, L.; Reinhoudt, D. N.; Wolf, H.; Huskens, J. An in situ study of the adsorption behavior of functionalized particles on self-assembled monolayers via different chemical interactions. *Langmuir* **2007**, *23*, 9990-9999.

(42) Valerio, C.; Fillaut, J. L.; Ruiz, J.; Guittard, J.; Blais, J. C.; Astruc, D. The dendritic effect in molecular recognition: Ferrocene dendrimers and their use as supramolecular redox sensors for the recognition of small inorganic anions. *J. Am. Chem. Soc.* **1997**, *119*, 2588-2589.

(43) Ruiz, J.; Medel, M. J. R.; Daniel, M. C.; Blais, J. C.; Astruc, D. Redox-robust pentamethylamidoferrocenyl metallodendrimers that cleanly and selectively recognize the $H_2PO_4^-$ anion. *Chem. Commun.* **2003**, 464-465.

(44) Oh, S. K.; Baker, L. A.; Crooks, R. M. Electrochemical rectification using mixed monolayers of redox-active ferrocenyl dendrimers and n-alkanethiols. *Langmuir* **2002**, *18*, 6981-6987.

(45) Shu, C. F.; Shen, H. M. Organometallic ferrocenyl dendrimers: Synthesis, characterization and redox properties. *J. Mater. Chem.* **1997**, *7*, 47-52.

(46) Suzuki, M.; Nakajima, R.; Tsuruta, M.; Higuchi, M.; Einaga, Y.; Yamamoto, K. Synthesis of ferrocene-modified phenylazomethine dendrimers possessing redox switching. *Macromolecules* **2006**, *39*, 64-69.

(47) Gonzalez, B.; Cuadrado, I.; Alonso, B.; Casado, C. M.; Moran, M.; Kaifer, A. E. Mixed cobaltocenium-ferrocene heterobimetallic complexes and their binding interactions with beta-cyclodextrin. A three-state, host-guest system under redox control. *Organometallics* **2002**, *21*, 3544-3551.

(48) Latham, A. H.; Williams, M. E. Controlling transport and chemical functionality of magnetic nanoparticles. *Acc. Chem. Res.* **2008**, *41*, 411-420.

(49) Laurent, S.; Forge, D.; Port, M.; Roch, A.; Robic, C.; Elst, L. V.; Muller, R. N. Magnetic iron oxide nanoparticles: Synthesis, stabilization, vectorization, physicochemical characterizations, and biological applications. *Chem. Rev.* **2008**, *108*, 2064-2110.

(50) Knecht, M. R.; Crooks, R. M. Magnetic properties of dendrimer-encapsulated iron nanoparticles containing an average of 55 and 147 atoms. *New J. Chem.* **2007**, *31*, 1349-1353.

(51) delMonte, F.; Morales, M. P.; Levy, D.; Fernandez, A.; Ocana, M.; Roig, A.; Molins, E.; OGrady, K.; Serna, C. J. Formation of gamma-Fe_2O_3 isolated nanoparticles in a silica matrix. *Langmuir* **1997**, *13*, 3627-3634.

(52) Eustis, S.; El-Sayed, M. A. Why gold nanoparticles are more precious than pretty gold: Noble metal surface plasmon resonance and its enhancement of the radiative and nonradiative properties of nanocrystals of different shapes. *Chem. Soc. Rev.* **2006**, *35*, 209-217.

(53) Chiang, S. J.; Liaw, B. J.; Chen, Y. Z. Preparation of NiB nanoparticles in water-in-oil microemulsions and their catalysis during hydrogenation of carbonyl and olefinic groups. *Appl. Catal. A* **2007**, *319*, 144-152.

(54) O'Shea, V. A. D.; Alvarez-Galvan, M. C.; Campos-Martin, J. M.; Menendez, N. N.; Tornero, J. D.; Fierro, J. L. G. Surface and structural features of Co-Fe oxide nanoparticles deposited on a silica substrate. *Eur. J. Inorg. Chem.* **2006**, 5057-5068.

(55) Hong, F.; Yang, B. L.; Schwartz, L. H.; Kung, H. H. Crystallite size effect in the selective oxidation of butene to butadiene on iron-oxide .1. Mossbauer, X-ray, and magnetization characterization of the catalysts. *J. Phys. Chem.* **1984**, *88*, 2525-2530.

(56) Lund, C. R. F.; Dumesic, J. A. Strong oxide-oxide interactions in silica-supported magnetite catalysts .1. X-ray-diffraction and mossbauer-spectroscopy evidence for interaction. *J. Phys. Chem.* **1981**, *85*, 3175-3180.

(57) Ida, T.; Tsuiki, H.; Ueno, A.; Tohji, K.; Udagawa, Y.; Iwai, K.; Sano, H. Characterization of iron-oxide in Fe_2O_3/SiO_2 catalyst. *J. Catal.* **1987**, *106*, 428-439.

(58) Alcala, M. D.; Real, C. Synthesis based on the wet impregnation method and characterization of iron and iron oxide-silica nanocomposites. *Solid State Ionics* **2006**, *177*, 955-960.

(59) Ennas, G.; Musinu, A.; Piccaluga, G.; Zedda, D.; Gatteschi, D.; Sangregorio, C.; Stanger, J. L.; Concas, G.; Spano, G. Characterization of iron oxide nanoparticles in an Fe_2O_3-SiO_2 composite prepared by a sol-gel method. *Chem. Mater.* **1998**, *10*, 495-502.

(60) Bruni, S.; Cariati, F.; Casu, M.; Lai, A.; Musinu, A.; Piccaluga, G.; Solinas, S. Ir and nmr study of nanoparticle-support interactions in a Fe_2O_3-SiO_2 nanocomposite prepared by a sol-gel method. *Nanostruct. Mater.* **1999**, *11*, 573-586.

(61) Chaneac, C.; Tronc, E.; Jolivet, J. P. Thermal behavior of spinel iron oxide-silica composites. *Nanostruct. Mater.* **1995**, *6*, 715-718.

(62) Solinas, S.; Piccaluga, G.; Morales, M. P.; Serna, C. J. Sol-gel formation of gamma-Fe_2O_3/SiO_2 nanocomposites. *Acta. Mater.* **2001**, *49*, 2805-2811.

(63) Choi, H. C.; Kundaria, S.; Wang, D. W.; Javey, A.; Wang, Q.; Rolandi, M.; Dai, H. J. Efficient formation of iron nanoparticle catalysts on silicon oxide by hydroxylamine for carbon nanotube synthesis and electronics. *Nano Lett.* **2003**, *3*, 157-161.

(64) Ding, L.; Zhou, W. W.; Chu, H. B.; Jin, Z.; Zhang, Y.; Li, Y. Direct preparation and patterning of iron oxide nanoparticles via microcontact printing on silicon wafers for the growth of single-walled carbon nanotubes. *Chem. Mater.* **2006**, *18*, 4109-4114.

(65) Kohn, R.; Froba, M. Nanoparticles of 3d transition metal oxides in mesoporous MCM-48 silica host structures: Synthesis and characterization. *Catal. Today* **2001**, *68*, 227-236.

(66) Huwe, H.; Froba, M. Synthesis and characterization of transition metal and metal oxide nanoparticles inside mesoporous carbon CMK-3. *Carbon* **2007**, *45*, 304-314.

(67) Kohn, R.; Paneva, D.; Dimitrov, M.; Tsoncheva, T.; Mitov, I.; Minchev, C.; Froba, M. Studies on the state of iron oxide nanoparticles in MCM-41 and MCM-48 silica materials. *Micropor. Mesopor. Mat.* **2003**, *63*, 125-137.

(68) Tsoncheva, T.; Rosenholm, J.; Teixeira, C. V.; Dimitrov, M.; Linden, M.; Minchev, C. Preparation, characterization and catalytic behavior in methanol decomposition of nanosized iron oxide particles within large pore ordered mesoporous silicas. *Micropor. Mesopor. Mat.* **2006**, *89*, 209-218.

(69) Schnitzler, M. C.; Mangrich, A. S.; Macedo, W. A. A.; Ardisson, J. D.; Zarbin, A. J. G. Incorporation, oxidation and pyrolysis of ferrocene into porous silica glass: A route to different silica/carbon and silica/iron oxide nanocomposites. *Inorg. Chem.* **2006**, *45*, 10642-10650.

(70) Amama, P. B.; Cola, B. A.; Sands, T. D.; Xu, X. F.; Fisher, T. S. Dendrimer-assisted controlled growth of carbon nanotubes for enhanced thermal interface conductance. *Nanotechnology* **2007**, *18*, 385303-385306.

(71) Saffarzadeh, A.; Shimaoka, T.; Motomura, Y.; Watanabe, K. Characterization study of heavy metal-bearing phases in MSW slag. *J. Hazard. Mater.* **2009**, *164*, 829-834.

(72) Bordelanne, O.; Delville, M. H. Metal oxide modification via transition metal complexes: Hybrid materials characterizations and potential applications in molecular recognition. *Solid. State. Sci.* **2002**, *4*, 851-858.

(73) Sun, L.; Crooks, R. M. Dendrimer-mediated immobilization of catalytic nanoparticles on flat, solid supports. *Langmuir* **2002**, *18*, 8231-8236.

(74) Singh, A.; Chandler, B. D. Low-temperature activation conditions for PAMAM dendrimer templated Pt nanoparticles. *Langmuir* **2005**, *21*, 10776-10782.

(75) Deutsch, D. S.; Lafaye, G.; Liu, D. X.; Chandler, B.; Williams, C. T.; Amiridis, M. D. Decomposition and activation of Pt-dendrimer nanocomposites on a silica support. *Catal. Lett.* **2004**, *97*, 139-143.

(76) Cornell, R. M.; Schwertmann, U. *The iron oxides structure, properties, reactions, occurences and uses*; second ed.; WILEY-VCH, 2003.

(77) Rogers, M. C.; Adisa, B.; Bruce, D. A. Synthesis and characterization of dendrimer-templated mesoporous oxidation catalysts. *Catal. Lett.* **2004**, *98*, 29-36.

(78) Velarde-Ortiz, R.; Larsen, G. A poly(propylene imine) (dap-am-64) dendrimer as Cu^{2+} chelator for the synthesis of copper oxide clusters embedded in sol-gel derived matrixes. *Chem. Mater.* **2002**, *14*, 858-866.

(79) Lang, H. F.; May, R. A.; Iversen, B. L.; Chandler, B. D. Dendrimer-encapsulated nanoparticle precursors to supported platinum catalysts. *J. Am. Chem. Soc.* **2003**, *125*, 14832-14836.

(80) Wagner, C. D.; Riggs, W. M.; Davis, L. E.; Moulder, J. F.; Muilenberg, G. E. *Handbook of x-ray photoelectron spectroscopy*; Perkin-Elmer Corporation Physical Electronics Division, Minnesota, U.S.A, 1979.

(81) Teng, F.; Guan, Y. T.; Zhu, W. P. Effect of biofilm on cast iron pipe corrosion in drinking water distribution system: Corrosion scales characterization and microbial community structure investigation. *Corros. Sci.* **2008**, *50*, 2816-2823.

(82) Pech-Canul, M. A.; Bartolo-Perez, P. Inhibition effects of *n*-phosphono-methyl-glycine/Zn^{2+} mixtures on corrosion of steel in neutral chloride solutions. *Surf. Coat. Technol.* **2004**, *184*, 133-140.

(83) Olivares, O.; Likhanova, N. V.; Gomez, B.; Navarrete, J.; Llanos-Serrano, M. E.; Arce, E.; Hallen, J. M. Electrochemical and XPS studies of decylamides of alpha-amino acids adsorption on carbon steel in acidic environment. *Appl. Surf. Sci.* **2006**, *252*, 2894-2909.

(84) Scott, R. W. J.; Wilson, O. M.; Crooks, R. M. Titania-supported Au and Pd composites synthesized from dendrimer-encapsulated metal nanoparticle precursors. *Chem. Mater.* **2004**, *16*, 5682-5688.

(85) Ottaviani, M. F.; Turro, N. J.; Jockusch, S.; Tomalia, D. A. EPR investigation of the adsorption of dendrimers on porous surfaces. *J. Phys. Chem., B* **2003**, *107*, 2046-2053.

(86) Esumi, K.; Goino, M. Adsorption of poly(amidoamine) dendrimers on aluminan-water and silica/water interfaces. *Langmuir* **1998**, *14*, 4466-4470.

CHAPTER 5

IRON OXIDE NANOPARTICLE-CATALYZED REACTIONS WITH MONOCHLOROBENZENE

5.1 Introduction

Polychlorinated dibenzo-*p*-dioxins (PCDDs) and polychlorinated dibenzofurans (PCDFs) are among the most toxic pollutants in the environment, and are formed in many combustion processes from any combination of C, H, and O, in the presence of Cl under suitable conditions of time and temperature.[1,2] There are at least two formation mechanisms of PCDD/Fs in combustion systems: homogeneous, which occurs in the gas phase between 500–800 °C, and heterogeneous, which is characterized by surface-mediated processes occurring at lower temperatures (200–500 °C) by two routes, *de novo* and catalytically-assisted coupling of precursors.[1,2] Formation of PCDD/Fs in the *de novo* route takes place via oxidation and chlorination of the carbonaceous material of the fly ash. In the catalytically-assisted coupling of precursors, the reaction proceeds by combination of organic precursors on solid surfaces in the presence of a catalyst. Heterogeneous formation of PCDD/Fs in the post-combustion region (temperatures of 200–500 °C) requires the presence of transition metal catalysts, whether formation is from aromatic precursors or *de novo* processes. Copper oxides and chlorides have been the most studied catalysts in the production of PCDD/Fs.[3-7] The precursor surface-mediated reactions, catalyzed by transition metal oxides, are suspected of accounting for the majority of PCDD/Fs formed in combustion reactions.[3,8]

Iron oxide is one of the highest concentration transition metals present in combustion processes,[9-11] and it has the potential to be a significant source of polychlorinated PCDD/F emissions.[12,13] Previous research has focused on iron oxide (micron-sized particles) mediated formation of PCDD/Fs from chlorinated phenol and benzene precursors[12,13] and iron oxide-mediated destruction of PCDD/Fs.[14-17] For PCDD/Fs formed from precursors, such as

2-monochlorophenol, over iron oxides supported on silica substrates, Nganai and co-workers[12] found that iron oxides mediate the formation of both dioxins and furans. Dibenzo-*p*-dioxin, 1-monochlorodibenzo-*p*-dioxin, 4,6-dichlorodibenzofuran and dibenzofuran, were formed in maximum yields (0.2%, 0.1%, 0.4%, and 0.3%, respectively) under pyrolytic conditions, between 200–500 °C for 1 h reaction time.

Chlorobenzenes and chlorophenols are both found in the flue gas of municipal waste incinerators and are precursors for PCDD/Fs.[3,18] Investigations and discussions regarding the mechanism of PCDD/Fs formation from aromatic precursors have focused primarily on chlorophenols.[4,6,19,20] In the case of chlorophenols, it is proposed that the precursor molecules interact with the metal oxide surface, chemisorbed, organic–metal oxide complexes that subsequently undergo electron transfer to form surface associated persistent free radicals.[21] The authors posit that these radicals subsequently react via Eley–Rideal and/or Langmuir–Hinshelwood mechanism to form PCDD/Fs.[4] Very few studies have shown the formation of PCDD/Fs from chlorinated benzenes as precursors,[3,22] with most of the papers being focused on the catalytic destruction of monochlorobenzene.[23-26] Supported metal oxides and noble metals are the most studied catalysts in the decomposition reactions of chlorobenzene.[17,22,27,28]

Studies of catalytic degradation of chlorobenzene (in the presence of 16% O_2 in nitrogen) on 2 wt.% Pt/γ-Al_2O_3 led to formation of polychlorobenzenes and albeit in low levels, PCDDs and PCDFs at about 400 °C.[22] Upon exposure to *tert*-butyl chloride, as an additional chlorine source, much higher levels of polychlorinated benzenes and PCDD/Fs were obtained. A model mixture of products of incomplete combustion was also used in this reaction, and the results revealed that the yields of PCDD/Fs were higher compared with the results obtained from combustion of chlorobenzene.[22] Addink et al.[3] studied the formation of PCDD/Fs on fly ash

from the point of view of both pathways: precursors (such as chlorobenzene, 1,2,4,5-tetrachlorobenzene, pentachlorobenzene and phenol) and *de novo* reactions from carbon model compounds (such as toluene, hexane, and three antraquinone derivatives) under oxidative conditions. It was found that both chlorobenzenes and phenol form PCDD/Fs via condensation reactions. Experiments with model carbon compounds showed that they formed PCDD/Fs, with the anthraquinone derivatives being the most reactive.

However, other experiments did not result in PCDD/F formation from monochlorobenzene combustion in an oxidative atmosphere.[28-31] Iron oxide supported on titanium dioxide and iron-titanium mixed-oxide catalysts were studied by Khaleel and Al-Nayli[27] in the oxidative decomposition of chlorobenzene. It was found that mixed iron-titanium oxide catalysts showed the highest activity for the complete oxidation of chlorobenzene at 325 °C, without the formation of other chlorinated organics. Nakka et al.[29] studied the combustion of chlorobenzene in the temperature interval 300–600 °C in the presence of CuO and HCl. Tetrachloroethylene and higher chlorobenzenes were the only products observed in this study. Van den Brink et al.[30] also observed considerable amounts of polychlorinated benzenes (varying from dichlorobenzene to hexachlobenzene) as by-products formed from the combustion of chlorobenzene over Pt/γ-Al_2O_3 between 200–600 °C. Furthermore, they studied the combustion of chlorobenzene on supported Pt and Pd nanoparticle catalysts.[28] The experimental results showed that polychlorinated benzenes are the only by-products obtained from chlorobenzene decomposition carried out under oxidative conditions (15% O_2/N_2) on 2% Pt with different supports (γ-Al_2O_3, SiO_2, and ZrO_2). In addition, the concentrations of polychlorinated benzenes correlated with the dispersion of Pt on supports, as very small Pt crystallites (1.6-nm diameter) were more active in formation of polychlorinated benzene.[28] When Pd/γ-Al_2O_3 catalysts were used, the conversion of chlorobenzene was lower, but the concentration of by-products was

higher.[28] The formation of polychlorinated benzenes was also been confirmed experimentally by Scirè et al.[31] between 200–550 °C with Pt catalysts supported on H-type zeolites. Liu et al.[32] reported the formation of poly(chlorinated biphenyls) from the pyrolysis of chlorinated benzene over a $CuCl_2$ catalyst in an HCl atmosphere. Kinetic and FT-IR studies were conducted by Lichtenberger and Amiridis[33] to investigate the oxidation mechanism of chlorinated benzenes over V_2O_5/TiO_2 catalysts. It was found that chlorobenzene oxidation proceeds by the adsorption of chlorobenzenes onto the catalytic sites via nucleophilic attack at the ring chlorine position, followed by subsequent oxidation of the remaining aromatic ring.

Although extensive research has been performed on the formation of PCDD/Fs in combustion processes using micron-size particles of transition metal oxides, no studies exist that address how smaller, potentially more reactive nanoscale particles affect the products. It is hypothesized that transition metal oxide nanoparticles present in ultrafine particles ($PM_{0.1,}$ particles with a mean aerodynamic diameter of less than 0.1 μm) emitted from the combustion sources may be responsible for the formation of gas-phase pollutants through catalytic reactions occurring on their surface. It is expected that nanoparticles would be at least as active as or even more active than micron-sized particles for the production of combustion by-products, because the extremely small size of nanoparticles will maximize the surface area exposed to the organic precursor during combustion processes, thereby allowing a larger variety of reactions to occur.

To test this hypothesis, well-defined iron oxide nanoparticles supported on silica surfaces were prepared using organometallic dendrimers. For comparison purposes, silica-supported iron oxide nanoparticles were prepared by the method of incipient wetness, using an iron(III) nitrate precursor. The prepared nanoparticles were characterized by HR-TEM, and it was found that their size and dispersity were dependent on the preparation method. Surface-mediated reactions of monochlorobenzene over these iron oxide nanoparticles (prepared

by the two different methods) were studied using a system for thermal diagnostic studies.[34] These studies were performed over silica surfaces having between 2 and 5% Fe_2O_3, under pyrolytic and oxidative conditions, in a temperature range of 300–550 °C. Besides benzofuran and dibenzofuran as the only furans detected under pyrolytic conditions, considerable amounts of benzene were formed. Phenols and chlorinated phenols (monochlorophenol and dichlorophenol), dichlorobenzene, biphenyl, and naphthalene were also detected. Under oxidative conditions, the only by-products detected were benzene, dichlorobenzene, trichloroethylene, and tetrachloroethylene, indicating that the presence of oxygen in the feed gas promotes the breakdown of molecules, thereby resulting in lower molecular weight combustion products (CO, CO_2, C2 and C3 organics, HCl) that were not analyzed.

5.2 Experimental Section

5.2.1 Materials

All commercial-grade reagents were used without further purification. The poly(propylene imine) dendrimers were obtained from SYMO-Chem and used as received. The following chemicals were purchased from Sigma-Aldrich: iron(III) nitrate nonahydrate (99.99+%), chlorobenzene (99.8%), trichloroethylene (ACS reagent, ≥99.5%), benzene (puriss, p.a., standard for GC, ≥99.9%), 1,2-dichlorobenzene (HPLC grade, 99%), dibenzofuran (99+%), 2,3-benzofuran (99%), biphenyl (99.5%), 2-chlorophenol (99+%), tetrahydrofuran (ACS grade), and pentane (99%+ anhydrous). Other chemicals used were tetrachloroethylene (99+%), from Fisher, phenol (puriss p.a.) from Riedel-deHaën, 2,4-dichlorophenol (99%) from Acros Organics, and naphthalene (99+%) from Aldrich Chemical Co. The solvents used were HPLC-grade methanol from Mallinckrodt, and HPLC-grade dichloromethane from J.T. Baker. Fumed silica, Cab-O-Sil EH-5, (surface area 380 $m^2 g^{-1}$ and submicron particle size) was a gift from CABOT.

5.2.2 Synthesis of Silica-Supported Iron Oxide Nanoparticles

The Fe_2O_3/SiO_2 samples used in this study were prepared by two different procedures: adsorption of organometallic dendrimers on SiO_2, denoted as FD, and incipient wetness of SiO_2 with iron(III) nitrate nonahydrate, refered to as IN.

The ferrocenoyl-functionalized DAB-$(NHCOFc)_n$ dendrimers were deposited onto silica at room temperature. The synthesis of DAB-$(NHCOFc)_n$ dendrimers was achieved by condensation reactions of 1-(chlorocarbonyl)ferrocene with amine-terminated poly(propylene imine) dendrimers as described in Chapter 4. Impregnation on Cab-O-Sil EH-5 silica was carried out by mixing an appropriate concentration of DAB-$(NHCOFc)_{32}$ solution with a known weight of silica to achieve different iron loadings (5 and 2 wt.% Fe_2O_3 on silica) after calcination. The resulting mixture was allowed to equilibrate for 1 h with occasional stirring. After impregnation, the sample was dried by rotary evaporation. The precursor was calcined for 4 h at 450 ºC in a tube furnace under a constant flow of air (70 mL min^{-1}) to convert ferrocene to iron oxide and to remove the organic material. As a reference control, a silica sample was prepared using the same reaction conditions without any dendrimer present.

For comparison, Fe_2O_3/SiO_2 samples were prepared by the method of incipient wetness. Cab-O-Sil silica was introduced into a methanol solution of iron(III) nitrate nonahydrate (with a concentration chosen to obtain a 5 or 2 wt.% Fe_2O_3 on silica support) for the incipient wetness to occur. The mixture was stirred well and then kept overnight at room temperature in a desiccator. The samples were then calcined at 450 ºC for 4 h in a tube furnace under a constant flow of air (70 mL min^{-1}).

The prepared catalysts were labeled as follows: ferrocenoyl poly(propylene imine) dendrimers are referred to as DAB-$(NHCOFc)_n$, where *n* is the number of end groups and Fc is the ferrocene group; silica-supported iron oxide nanoparticles prepared from ferrocenoyl

dendrimer precursor are *x*% Fe_2O_3FD/SiO_2, where *x* is the loading of metal oxides (5 or 2 wt.%) and FD stands for ferrocenoyl dendrimer; and silica-supported iron oxide nanoparticles prepared by incipient wetness of SiO_2 with iron nitrate precursors are *x*% Fe_2O_3IN/SiO_2, where *x* is the loading of metal oxides (5 or 2 wt.%) and IN stands for iron nitrate.

5.2.3 System for Thermal Diagnostic Studies

Surface-mediated reactions of monochlorobenzene over Fe_2O_3/SiO_2 were studied using a system for thermal diagnostic studies (STDS) built by the Dellinger group. The STDS consists of a high-temperature fused-silica flow reactor inside a furnace whose temperature is controlled by a separate temperature controller. The furnace is housed inside the thermal reactor compartment, namely a gas chromatograph (GC) oven. The GC oven is designed to act as a temperature controller that maintains the temperature of all the connections and lines coming from the injection port to the reactor and the lines going from the reactor to the heated transfer line. A gas chromatograph mass spectrometer (GC-MS) system is interfaced in-line with the thermal reactor for chemical analysis of the reactor effluent.

In all cases, 10 mg of the Fe_2O_3/SiO_2 catalyst were mixed with 40 mg of quartz, and placed between quartz wool plugs in a fused silica reactor (0.4 cm inside diameter, 18 cm length) in the STDS. All transfer lines were maintained at a constant temperature of 200 °C to facilitate the transport of gas-phase reactants and products. The reactant, monochlorobenzene, was introduced into the flow stream using a digital syringe pump (KD Scientific, model 100) through a vaporizer maintained at 135 °C. A constant rate of injection was selected to obtain gas-phase concentration of monochlorobenzene of 184 ppm for all experiments. Helium (UHP) was used as the carrier gas for pyrolytic conditions, while a mixture of oxygen-helium (20%) was the carrier gas for oxidative conditions, with an overall flow rate at 20 mL min^{-1}. The reaction time of monochlorobenzene over the catalytic bed was 5 min for all experiments and the space

velocity was 9550 h^{-1}. The flow reactor effluent was transported through a heated, temperature-controlled transfer line where it was trapped cryogenically at the head of the capillary column of gas chromatograph mass spectrometry (GC-MS) system (Varian, Saturn 2000). Liquid nitrogen was used to cryogenically trap gas-phase products at the head of the capillary column (Chrompack, CP SIL 8CB 30m × 0.32 i.d., stationary phase film thickness of 0.25μm) inside GC (Varian, CP 3800). Initially, all of the products were trapped in the head of capillary column at –60 °C, followed by temperature programmed ramping of the column from –60 °C to 300 °C at 15 °C min^{-1}. Separated products with molecular weights from 40 to 650 amu were analyzed with a mass spectrometer (MS) operating in the full-scan mode. The mass-spectral library (NIST 98 version 1.6d) was used to identify the products.

The conversion of monochlorobenzene, and the yields of the products were calculated using the expressions:

$$\text{Conversion} = \{([MCBz]_0\text{-}[MCBz])/[MCBz]_0\} \times 100 \qquad \textbf{Equation 5.1}$$

$$\text{Yield} = \{[product]A/[MCBz]_0\} \times 100 \qquad \textbf{Equation 5.2}$$

$$\text{Selectivity} = \{[product]/([MCBz]_0 - [MCBz])\} \times 100 \qquad \textbf{Equation 5.3}$$

where $[MCBz]_0$ is the initial concentration of monochlorobenzene injected into the reactor (in moles), [MCBz] is the concentration of monochlorobenzene transformed, [product] is the concentration of the particular product formed (in moles), and A is the molar stoichiometric factor (2 in this case, as one product molecule is formed from two MCBz molecules). The concentrations of the products calculated were based on the calibration with standards of the products and the peak area counts from the chromatogram. The temperature studied was 300–550 °C, and fresh catalyst beds were used for each reaction temperature run. Each data point reflects an average result of at least three experimental runs.

5.2.4 High-Resolution Transmision Electron Microscopy (HR-TEM)

Electron microscopy images were obtained with a JEOL-2010 high-resolution transmission electron microscope. The nanoparticles were first dispersed in methanol, after which a drop of the suspension was placed on a holey copper grid (400 mesh from SPI supplies) and the solvent was allowed to evaporate. The instrument was operated at an accelerating voltage of 200 KV. The images were recorded with a Gatan digital camera. For each sample, HR-TEM images were taken from different parts of the grid and used to estimate the average diameter and size distribution of particles. The nanoparticles sizes were measured using an ImageJ program (image processing and analysis JAVA-based software developed by the National Institutes of Health (NIH)) and the histograms were plotted using OriginPro 6.1. The nanoparticle size measurements are mean values ± standard deviation calculated from at least 200 measurements.

5.2.5 X-Ray Photoelectron Spectroscopy (XPS)

The XPS data were obtained with an AXIS 165 photoelectron spectrometer using a monochromatized Al Kα X-ray radiation source. The samples were prepared by pressing the powdered silica-supported iron oxide nanoparticles onto double-sided copper tape. The samples were degassed in the pretreatment chamber overnight and then moved into the analysis chamber for XPS study. A charge neutralizer was used to minimize/eliminate sample charging. High-resolution spectra (160 eV pass energy was used to increase the signal intensity) were recorded for the Fe 2p and C 1s regions. The binding energies were calibrated with respect to the signal of C1s (binding energy 283.5 eV). A commercially available Fe_2O_3 reference (99.98% trace metal basis, from Sigma-Aldrich) and a mixture of Fe_2O_3-SiO_2 reference (which was prepared by mixing in a mortar Fe_2O_3 reference with SiO_2 (calcined before at 450 °C for 4 h) were evaluated for comparison purposes.

5.3 Results and Discussion

Monochlorobenzene was chosen as a model precursor in our study because it has been found in relatively high amounts in the stack gases from municipal waste incinerators and it has also been reported that exists a good correlation between the international toxicity equivalent (I-TEQ) value of PCDD/Fs and measured monochlorobenzene.[3,22,35,36] Furthermore, this good correlation can give an estimation of the PCDD/Fs emission in the flue gases by measuring the monochlorobenzene on-line.[36] The combustion experiments were performed under pyrolytic and oxidative conditions with the aim to evaluate the catalytic performance of iron oxide nanoparticles in the decomposition of monochlorobenzene, focusing attention on the formation of by-products. In order to investigate the influence of nanoparticle size and dispersity on the catalytic activity of silica-supported iron oxide nanoparticles, two preparation methods and two iron oxide loadings (2 and 5%) were studied.

5.3.1 Characterization of Silica-Supported Iron Oxide Nanoparticles by HR-TEM

The silica-supported iron oxide samples, obtained by calcination of ferrocenoyl dendrimer (DAB-$(NHCOFc)_{32}$/SiO_2) and iron nitrate ($Fe(NO_3)_3$/SiO_2) on silica at 450 °C in air, were analyzed by HR-TEM with the aim to determine the existence of iron oxide nanoparticles and the shape size, and size distribution of the nanoparticles on silica. In Table 5.1 are displayed the diameter averages of iron oxide nanoparticles as a function of precursor and iron oxide loading. Typical high-resolution electron microscopy images and particle size distributions of iron oxide nanoparticles supported on silica are displayed in Figure 5.1 for nanoparticles obtained from the ferrocenoyl dendrimer and Figure 5.2 for nanoparticles obtained from the iron nitrate. In the HR-TEM images, the nanoparticles are small dark spots observed on the gray silica background.

Table 5.1 Mean diameters of iron oxide nanoparticles as a function of precursor and Fe_2O_3 loading (calcination temperature, 450 °C).

Sample	Fe_2O_3 loading (wt.%)	Average Diameter ± 1s (Size Dispersity) (nm)	No. of particles evaluated
Fe_2O_3FD/SiO_2	5	2.80±0.31 (12%)	274
	2	2.36±0.25 (10%)	309
Fe_2O_3IN/SiO_2	5	5.06±1.72 (33%)	490
	2	3.91±0.93 (24%)	324

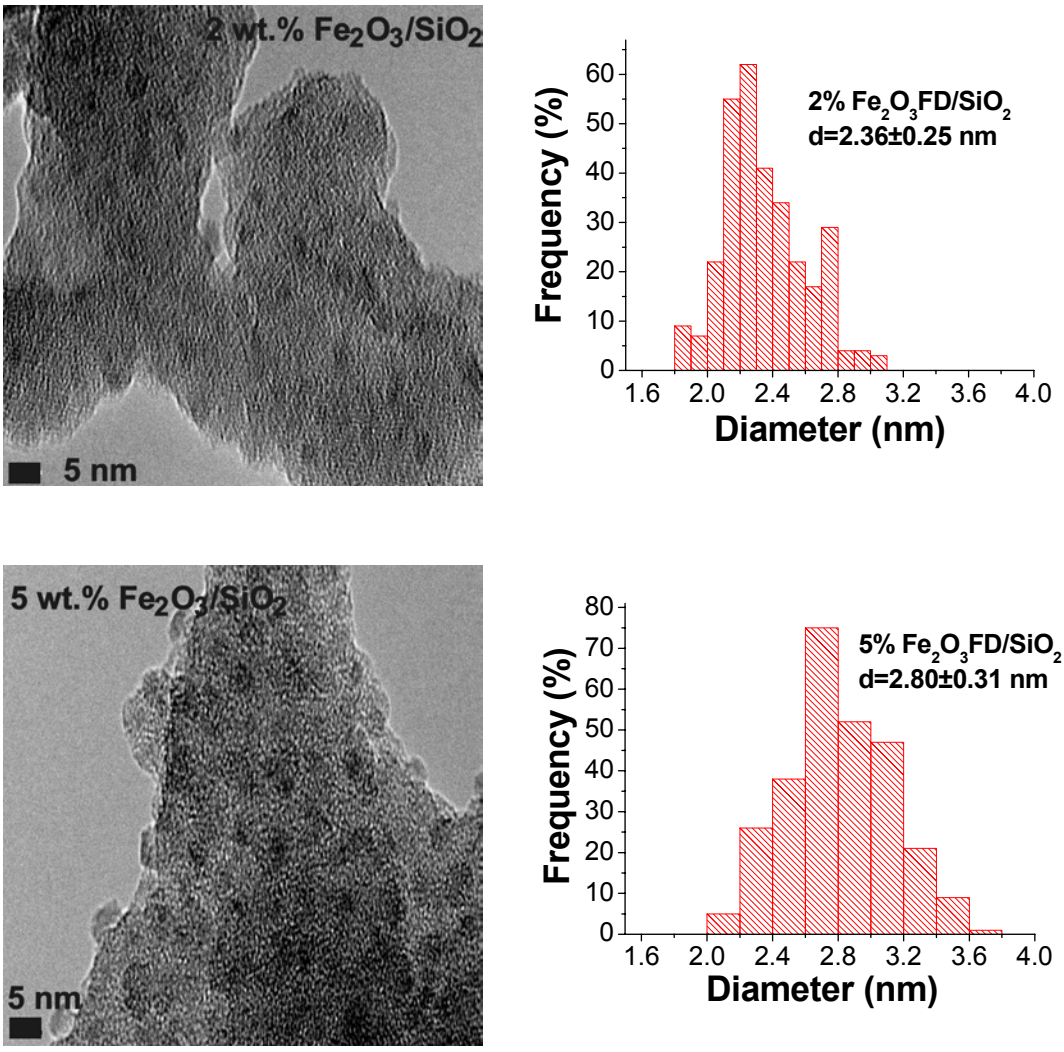

Figure 5.1 HR-TEM images and particle size distributions of Fe_2O_3FD/SiO_2 nanoparticles obtained by calcination of DAB-$(NHCOFc)_{32}/SiO_2$ precursors at 450 °C (with 2 and 5% Fe_2O_3) for 4 h.

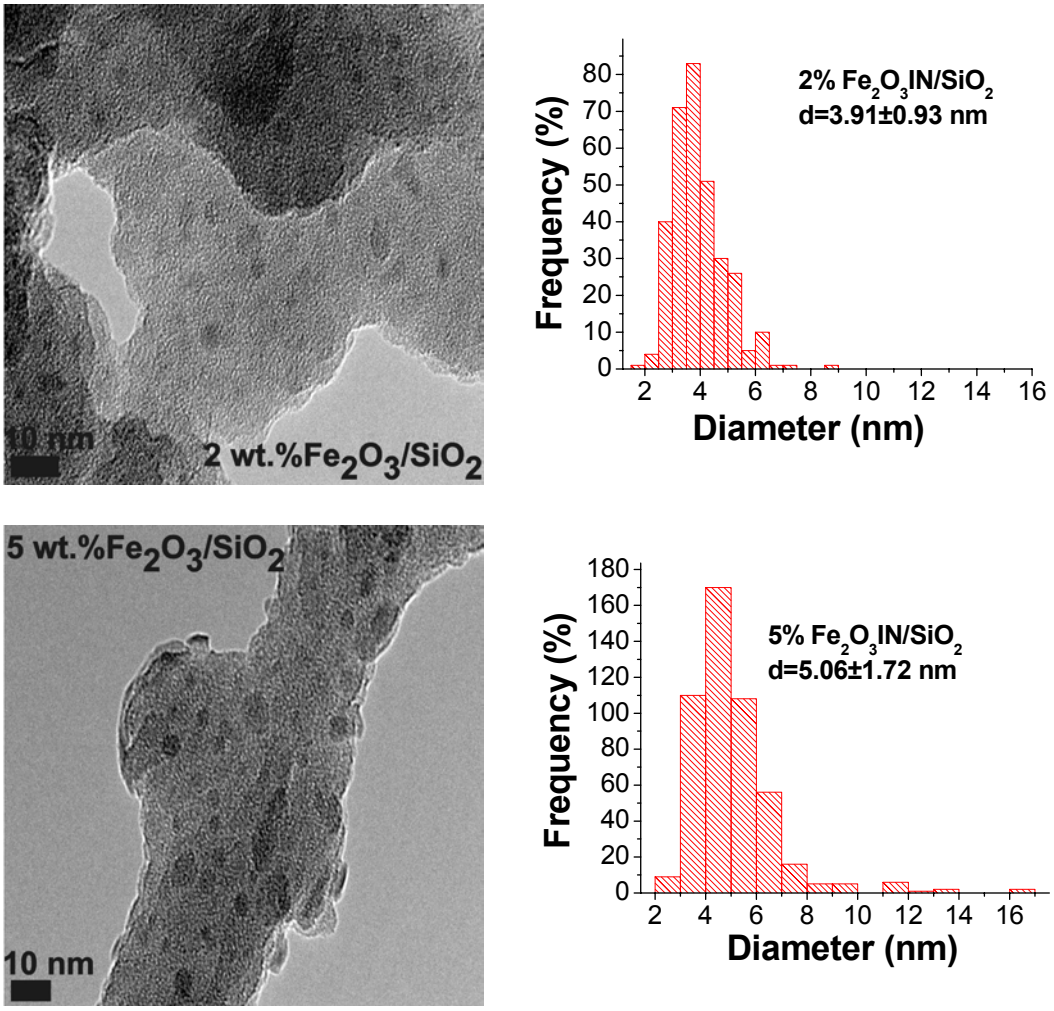

Figure 5.2 HR-TEM images and particle size distributions of Fe_2O_3IN/SiO_2 nanoparticles obtained by calcination of $Fe(NO_3)_3/SiO_2$ precursors at 450 °C (with 2 and 5% Fe_2O_3) for 4 h.

From the data in Table 5.1 and Figures 5.1 and 5.2, it is clear that the particle size decreases with decreasing metal oxide loading. The samples obtained from the dendrimer precursors have a very small size distribution (< 12%). Smaller diameters for samples containing 2% Fe_2O_3 indicate that better dispersion of the active phase (dendrimer) is achieved for these samples. It was found that a significant increase (81%) in the iron oxide cluster size was obtained in the case of the iron nitrate/SiO_2 precursor with 5% loading.

5.3.2 Characterization of Silica-Supported Iron Oxide Nanoparticles by XPS

The silica-supported iron oxide samples obtained by calcination of DAB-$(NHCOFc)_{32}/SiO_2$ and $Fe(NO_3)_3/SiO_2$ at 450 °C for 4 h were analyzed by XPS with the

aim to determine the oxidation state of iron oxide nanoparticles on silica support surfaces. For comparison purposes, a commercially-available Fe_2O_3 reference (99.98% trace metal basis) and a mixture of a Fe_2O_3 reference (99.98% trace metal basis) with SiO_2 (which was calcinated at 450 °C for 4 h) were evaluated. In Figure 5.3 are shown representative high-resolution Fe 2p region spectra of Fe_2O_3/SiO_2 samples obtained by the two procedures and the references.

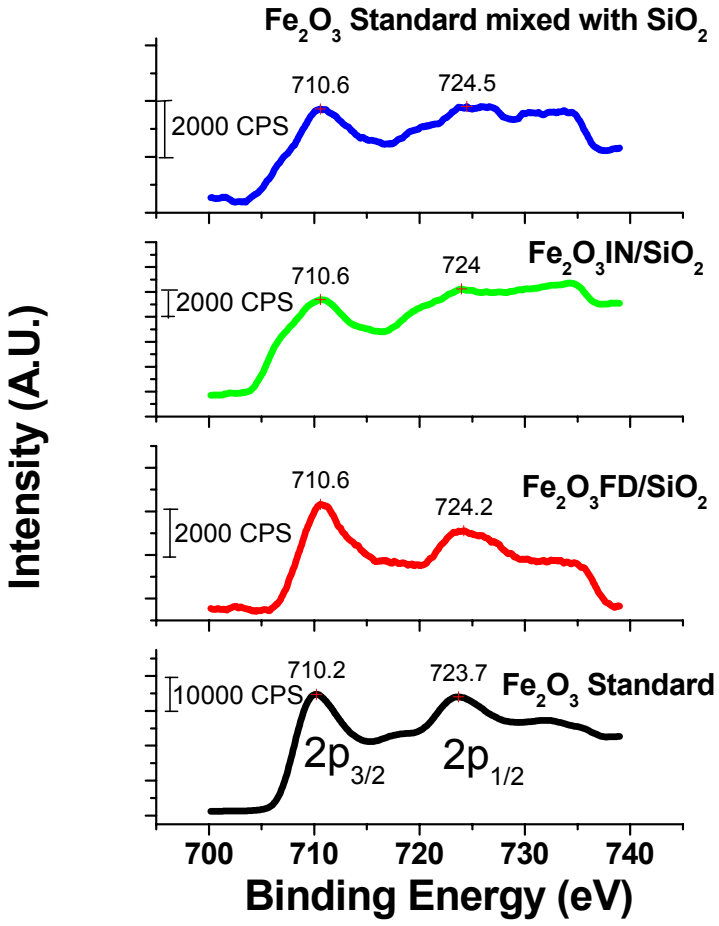

Figure 5.3 Fe 2p high-resolution X-ray photoelectron spectra. Black line: Fe_2O_3 reference from Sigma-Aldrich, red line: Fe_2O_3 nanoparticles obtained by calcination of ferrocenoyl dendrimer (5% Fe_2O_3 loading); green line: Fe_2O_3 nanoparticles obtained by calcination of iron(III) nitrate (5% Fe_2O_3 loading); and blue line: Fe_2O_3 reference mixed with SiO_2.

The peak shape and position of the Fe $2p_{3/2}$ at 710.6 eV binding energy is indication of the presence of Fe(III) oxide (Fe_2O_3) in the sample. Confirmation of Fe(III) state in the nanoparticles comes also from the observed 13.6 eV binding energy difference between the Fe

$2p_{1/2}$ and $2p_{3/2}$ transitions.[37] For the case of the Fe_2O_3IN/SiO_2 and the Fe_2O_3 standard mixed with SiO_2, the binding energy difference between the Fe $2p_{1/2}$ and $2p_{3/2}$ transitions was found to be 13.4 and 13.9 eV, respectively. Interestingly, the Fe_2O_3IN/SiO_2 and the Fe_2O_3 standard mixed with SiO_2 samples, the Fe $2p_{1/2}$ peak is not well resolved, and also for Fe_2O_3IN/SiO_2 the spectra presents a small shoulder at ~707 eV that can be due to the presence of Fe(II).

Further chemical/structural information about the iron oxide nanoparticles was obtained using X-ray diffraction (XRD). X-ray diffraction pattern (see Appendix) for Fe_2O_3/SiO_2 nanoparticles obtained by the dendrimer method and the iron nitrate incipient wetness method did not show any sharp peaks leading to the conclusion that these samples are likely amorphous or that the particle sizes are very small to allow for proper diffraction.

5.3.3 Pyrolytic Conditions

Surface-mediated reactions of monochlorobenzene were studied under pyrolytic conditions between 300–550 °C over silica-supported iron oxide nanoparticles (with 2 and 5% iron oxide coverage on silica surface) prepared by two different methods. Fe_2O_3FD/SiO_2 was prepared by air calcination of a ferrocenoyl dendrimer supported on silica at 450 °C for 4 h, while Fe_2O_3IN/SiO_2 was prepared by incipient wetness of SiO_2 and air calcination at 450 °C of the silica-supported iron(III) nitrate.

5.3.3.1 Catalytic Activities of 5% Fe_2O_3/SiO_2 Nanoparticles in Surface-Mediated Pyrolysis of Monochlorobenzene

The conversion of monochlorobenzene over samples containing 5% Fe_2O_3 was studied as function of temperature, and the results are shown in Figure 5.4. The results indicate that Fe_2O_3/SiO_2 catalysts (obtained by the two different methods) had similar activity for monochlorobenzene decomposition (statistical treatment by use of the *t*-test indicated that these average values are not different at the 95% confidence level). It can be seen that the reaction

becomes discernable at temperatures above 400 °C, and 50% of monochlorobenzene is converted at about 450 °C and approaches almost complete decomposition (96%) at 550 °C.

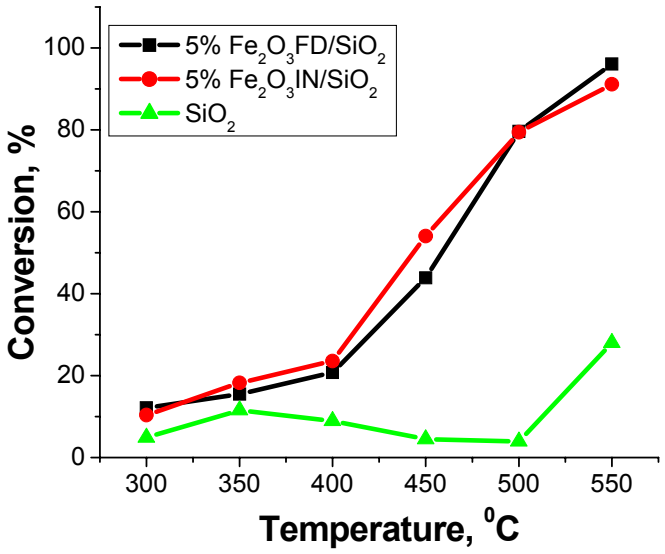

Figure 5.4 Chlorobenzene conversions over 5% Fe_2O_3/SiO_2 catalysts and SiO_2 (control) under pyrolytic conditions.

SiO_2 by itself exhibits some activity for the conversion of monochlorobenzene above 500 °C (between 300–500 °C the conversion is less than 10%), indicating that the iron oxide sites on the silica surfaces are the main active phase in monochlorobenzene conversion. The results on bare silica are probably due to the thermal decomposition of monochlorobenzene at this relatively high temperature (550 °C) and not to the surface-mediated reactions, because it was found that monochlorobenzene chemisorbs onto silica surfaces just after a few hours of exposure.[38]

Benzofuran and dibenzofuran are formed on both samples as shown in Figure 5.5. The 5% Fe_2O_3 nanoparticles (obtained from ferrocenoyl dendrimer), having an average diameter of 2.8 nm are more active for dibenzofuran formation than those obtained from iron nitrate, with those from the latter having a diameter of 5.06 nm and a broad size distribution of 33%. There is clearly a correlation between nanoparticle size and production of furans. Benzofuran production

reached maximum yields of 0.31% and 0.20% at 550 °C for Fe_2O_3FD/SiO_2 and Fe_2O_3IN/SiO_2, respectively; but, this difference between the average values is not significant upon statistical treatment (*t*-test at the 95% confidence interval).

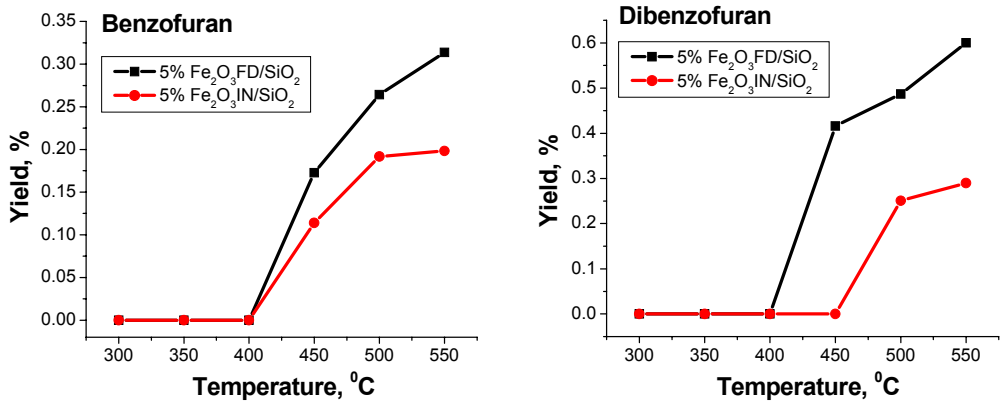

Figure 5.5 Formation of PCDF from the pyrolysis of monochlorobenzene over 5% Fe_2O_3FD/SiO_2 and 5% Fe_2O_3IN/SiO_2.

Dibenzofuran formation achieved a maximum yield at the same temperature, with 0.60% for Fe_2O_3FD/SiO_2 and 0.29% for Fe_2O_3IN/SiO_2. Moreover, on the 5% Fe_2O_3FD/SiO_2 catalyst, dibenzofuran starts to form at lower temperature (450 °C). The statistical treatment with *t*-test indicated that these average values are significantly different at the 95% confidence level. Interestingly, no PCDDs or other chlorinated PCDFs were detected under the reaction conditions studied.

Besides benzofuran and dibenzofuran, the by-products obtained from monochlorobenzene pyrolysis over 5% Fe_2O_3/SiO_2 nanoparticles are benzene, dichlorobenzene, phenol, chlorophenol, naphthalene, and biphenyl. Figure 5.6 depicts the yields obtained for these by-products as a function of temperature and catalyst. Benzene, produced via dechlorination of monochlorobenzene, was the major product obtained for both catalysts with a yield that increased with increasing temperature, achieving 35% at 550 °C for the Fe_2O_3FD/SiO_2 catalyst. For phenol, the maximum yields were obtained at 500 °C, namely 1.54% for the Fe_2O_3FD/SiO_2

and 0.45% for the Fe_2O_3IN/SiO_2 samples. The same trend was also observed for chlorophenol, but in this case, use of Fe_2O_3IN/SiO_2 catalyst slightly increased the yield of chlorophenol versus the Fe_2O_3FD/SiO_2 catalyst (with maximum yields of 0.30% and 0.28% at 500 °C). The only chlorinated benzene detected was dichlorobenzene at very low yields, less than 0.17% at 450 °C for both catalysts studied.

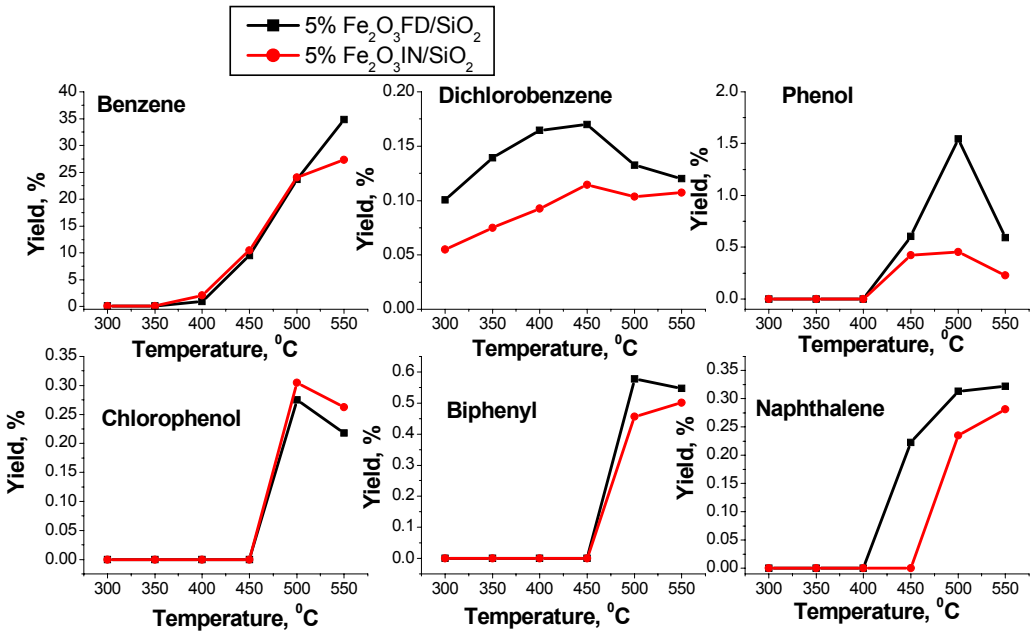

Figure 5.6 Formation of by-products from the pyrolysis of monochlorobenzene over 5% Fe_2O_3FD/SiO_2 and 5% Fe_2O_3IN/SiO_2.

The maximum yields of biphenyl were just slightly lower (0.46%) on the Fe_2O_3IN/SiO_2 catalyst than on the Fe_2O_3FD/SiO_2 catalyst (0.58%) at 500 °C. Naphthalene was achieved in maximum yields of 0.32% and 0.28% at 550°C using Fe_2O_3FD/SiO_2 and Fe_2O_3IN/SiO_2 catalysts, respectively. Each of these by-products started to form at temperatures between 400–450 °C, with the exception of benzene and dichlorobenzene being detected at temperatures as low as 300 °C. On the basis of these results presented in Figure 5.6 and statistical treatment (*t*-test at 95% confidence level), 5%Fe_2O_3FD/SiO_2 catalysts have higher catalytic activity compared to

5%Fe_2O_3IN/SiO_2 in conversion of monochlorobenzene to benzene (at 550 °C), dichlorobenzene, naphthalene, and phenol by-products. For the other by-products, the statistical treatment indicated that the results are not significantly different at the 95% confidence interval.

5.3.3.2 Catalytic Activities of 2% Fe_2O_3/SiO_2 Nanoparticles in Surface-Mediated Pyrolysis of Monochlorobenzene

Samples with 2% Fe_2O_3 loading were also prepared and tested under pyrolytic conditions. In Figure 5.7 are shown the relationship between the conversion of monochlorobenzene and reaction temperature.

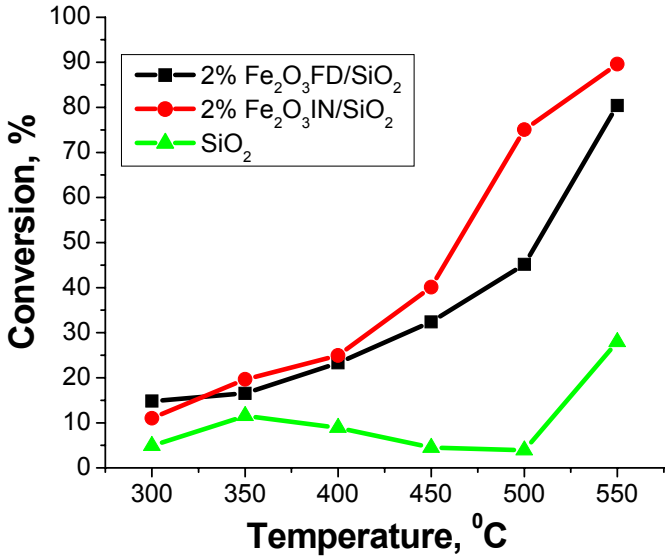

Figure 5.7 Chlorobenzene conversion with 2% Fe_2O_3/SiO_2 catalysts and SiO_2 (control) under pyrolytic conditions.

Monochlorobenzene conversion gradually increased over the temperature range of 300 to 450 °C, where the conversion rate accelerated and led to ~90% destruction at 550 °C. The 2% Fe_2O_3IN/SiO_2 catalyst exhibits better activity for monochlorobenzene conversion with values reaching 40% conversion at 450 °C.

The by-products detected for surface-mediated pyrolysis of monochlorobenzene over 2% Fe_2O_3/SiO_2 were the same as those obtained under pyrolysis over 5% Fe_2O_3 loading (benzofuran,

dibenzofuran, benzene, dichlorobenzene, phenol, chlorophenol, naphthalene, and biphenyl) but with the additional product of dichlorophenol that was not observed for samples with 5% Fe_2O_3 loading. Figure 5.8 displays data for the formation of furans from pyrolysis of monochlorobenzene as a function of temperature. The yields of benzofuran on the 2% Fe_2O_3/SiO_2 catalysts are slightly different only at 550 °C, with maximum values of 0.30% for Fe_2O_3FD/SiO_2 and 0.20% for Fe_2O_3IN/SiO_2. Dibenzofuran yields are significantly different for the two catalysts with the same Fe_2O_3 loading and reached 0.55% for samples obtained from ferrocenoyl dendrimer (FD) and 0.14% for samples prepared from iron nitrate (IN) at 550 °C. The statistical treatment by *t*-test indicated that these average yields from the two catalysts are different at the 95% confidence level.

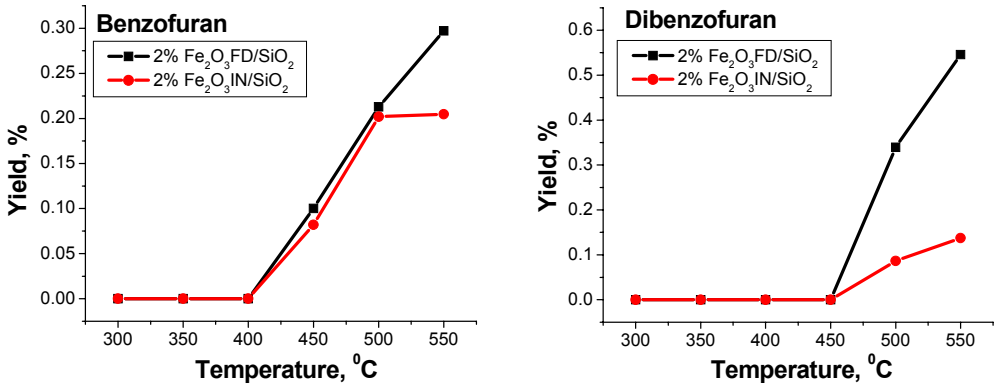

Figure 5.8 Formation of PCDF from the pyrolysis of monochlorobenzene over 2% Fe_2O_3FD/SiO_2 and 2% Fe_2O_3IN/SiO_2

The yields of non-furan by-products are displayed in Figure 5.9. As with the 5% Fe_2O_3 loading results, benzene was the major product obtained for both catalyst preparations with yields that increased with increasing temperature, with 42% being observed for Fe_2O_3FD/SiO_2 and 30% for Fe_2O_3IN/SiO_2 at 550 °C. For phenol, the maximum yields were 2.87% at 550 °C for Fe_2O_3FD/SiO_2 and 1.65% at 500 °C for Fe_2O_3IN/SiO_2. Interestingly, the phenol yields are considerably higher (~ 5 fold increase) for samples with 2% compared to 5% iron oxide content.

The same trend was observed for chlorophenol but only for the samples prepared from ferrocenoyl dendrimer. For the same 2% Fe_2O_3 loading, a maximum yield of 0.58% for chlorophenol was obtained at 550 °C with Fe_2O_3FD/SiO_2 and 0.24% at 500 °C with Fe_2O_3IN/SiO_2. Dichlorophenol, which was observed only for the sample with 2% Fe_2O_3 loading and on bare silica, had a maximum yield of ~0.5 % at 500 °C for all samples.

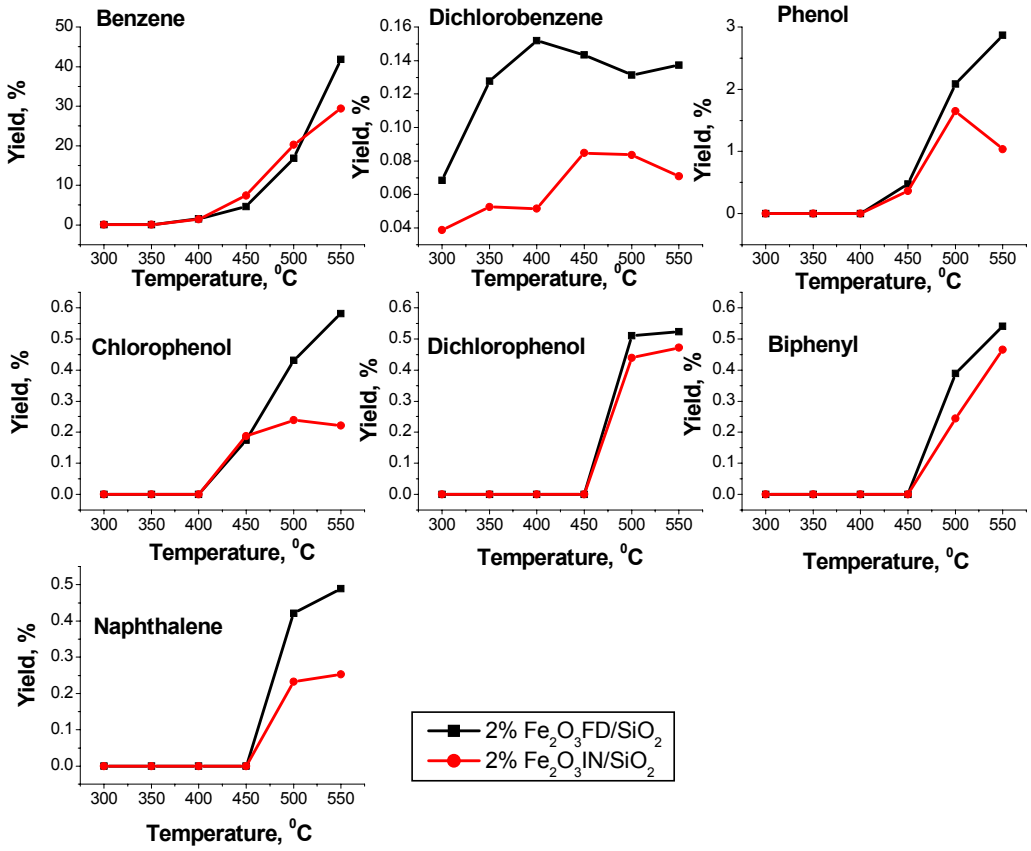

Figure 5.9 Formation of by-products from the pyrolysis of monochlorobenzene over 2% Fe_2O_3FD/SiO_2 and 2% Fe_2O_3IN/SiO_2.

Dichlorobenzene yields do not change substantially with reaction temperature, although the maximum yields are a little higher for the samples obtained from the ferrocenoyl dendrimer, 0.15% at 400 °C. The yields of biphenyl increased with increasing temperature after 450 °C, reaching values of 0.54% and 0.47% at 550 °C for the Fe_2O_3FD/SiO_2 and Fe_2O_3IN/SiO_2

catalysts, respectively. The maximum yield of naphthalene was significantly higher (0.49% at 550 °C) for the Fe_2O_3FD/SiO_2 catalyst than for the Fe_2O_3IN/SiO_2 (0.25% at 550 °C). Statistical treatment (*t*-test) indicated that the yields are higher for Fe_2O_3FD/SiO_2 compared to Fe_2O_3IN/SiO_2 catalyst for the following by-products: dichlorobenzene, phenol, chlorophenol, and naphthalene. For the other by-products (benzene and biphenyl) statistical treatment indicated that the results are not significantly different at the 95% confidence interval.

Silica supports having no iron oxide nanoparticles present were studied for the ability to decompose monochlorobenzene; the identity and by-products formed are shown in Table 5.2. It can be seen that silica by itself displayed significant activity in the formation of phenol and chlorinated phenols at temperatures ≥ 500 °C which is due to the reaction of monochlorobenzene in the gas phase.

Table 5.2 Percent yield of by-products from the pyrolysis of monochlorobenzene over SiO_2 surfaces.

Byproduct	**% Yield By-products**					
	Temperature (°C)					
	300	**350**	**400**	**450**	**500**	**550**
Benzene	0.03	0.03	0.03	0.03	0.04	0.16
Dichlorobenzene	0.05	0.06	0.06	0.06	0.05	0.07
Benzofuran	0.00	0.00	0.00	0.00	0.00	0.00
Dibenzofuran	0.00	0.00	0.00	0.00	0.00	0.00
Phenol	0.00	0.00	0.00	0.00	0.18	0.61
Chlorophenol	0.00	0.00	0.00	0.00	0.11	0.15
Dichlorophenol	0.00	0.00	0.00	0.00	0.42	0.34
Biphenyl	0.00	0.00	0.00	0.00	0.00	0.00
Naphthalene	0.00	0.00	0.00	0.00	0.00	0.00

5.3.3.3 The Effect of the Preparation Method and Iron Oxide Loading on Monochlorobenzene Decomposition under Pyrolytic Conditions.

Surface-mediated reaction of monochlorobenzene was studied under pyrolytic conditions over a temperature range of 300–550 °C using silica-supported iron oxide nanoparticles (prepared by the two distinct methods as in the previous section of this chapter) as catalysts.

The temperature dependence of the surface-mediated pyrolytic degradation of monochlorobenzene was presented in Figures 5.4 and 5.7 for 5 and 2% Fe_2O_3 loading, respectively. As depicted in Figure 5.4, the thermal decomposition of monochlorobenzene for the two catalysts followed the same trend, indicating that for the same 5% Fe_2O_3 loading, the two catalysts have similar activities in decomposition of monochlorobenzene to by-products. On the contrary for 2% Fe_2O_3 loading (as shown in Figure 5.7), the performance of the two catalysts, Fe_2O_3FD/SiO_2 and Fe_2O_3IN/SiO2, was different. The decomposition of monochlorobenzene increased significantly over 2% Fe_2O_3IN/SiO_2 in the temperature range 450–500 °C, with the monochlorobenzene conversion shifted to lower temperatures for the catalysts that have larger Fe_2O_3 nanoparticle size. When the Fe_2O_3 loadings are compared (as shown in Figures 5.4 and 5.7), the 5% Fe_2O_3/SiO_2 catalysts showed higher activity in decomposition of monochlorobenzene than the 2% Fe_2O_3/SiO_2 catalysts, especially for catalysts obtained from ferrocenoyl dendrimer. This is expected, because for 5% iron oxide loading there are more active iron oxide species participating in the reaction, allowing more reaction to occur between monochlorobenzene and Fe_2O_3/SiO_2. Therefore, it can be concluded that the surface-mediated thermal degradation of monochlorobenzene is influenced by the loading of iron oxide on the silica surface, and for 2% Fe_2O_3 loading, the particle size also plays a significant role.

In terms of by-product formation, the conversion of monochlorobenzene to specific by-products (selectivity) as a function of temperature for Fe_2O_3FD/SiO_2 and Fe_2O_3IN/SiO_2 with 5 and 2% loadings are depicted in Figure 5.10. The by-products were observed by 450 °C in accordance with conversion graphs that indicated a significant increase in monochlorobenzene decomposition above 450 °C. Generally, selectivity is higher for catalysts that have smaller dimensions. As can be seen in Figure 5.10, the low size dispersity Fe_2O_3 nanoparticles obtained from the ferrocenoyl dendrimer exhibit more activity in the formation of benzofuran,

dibenzofuran, dichlorobenzene, phenol, chlorinated phenols, biphenyl, and naphthalene by-products. The 2% Fe_2O_3FD/SiO_2 catalyst, —having the smallest nanoparticles size— is the most active in the decomposition of monochlorobenzene to by-products.

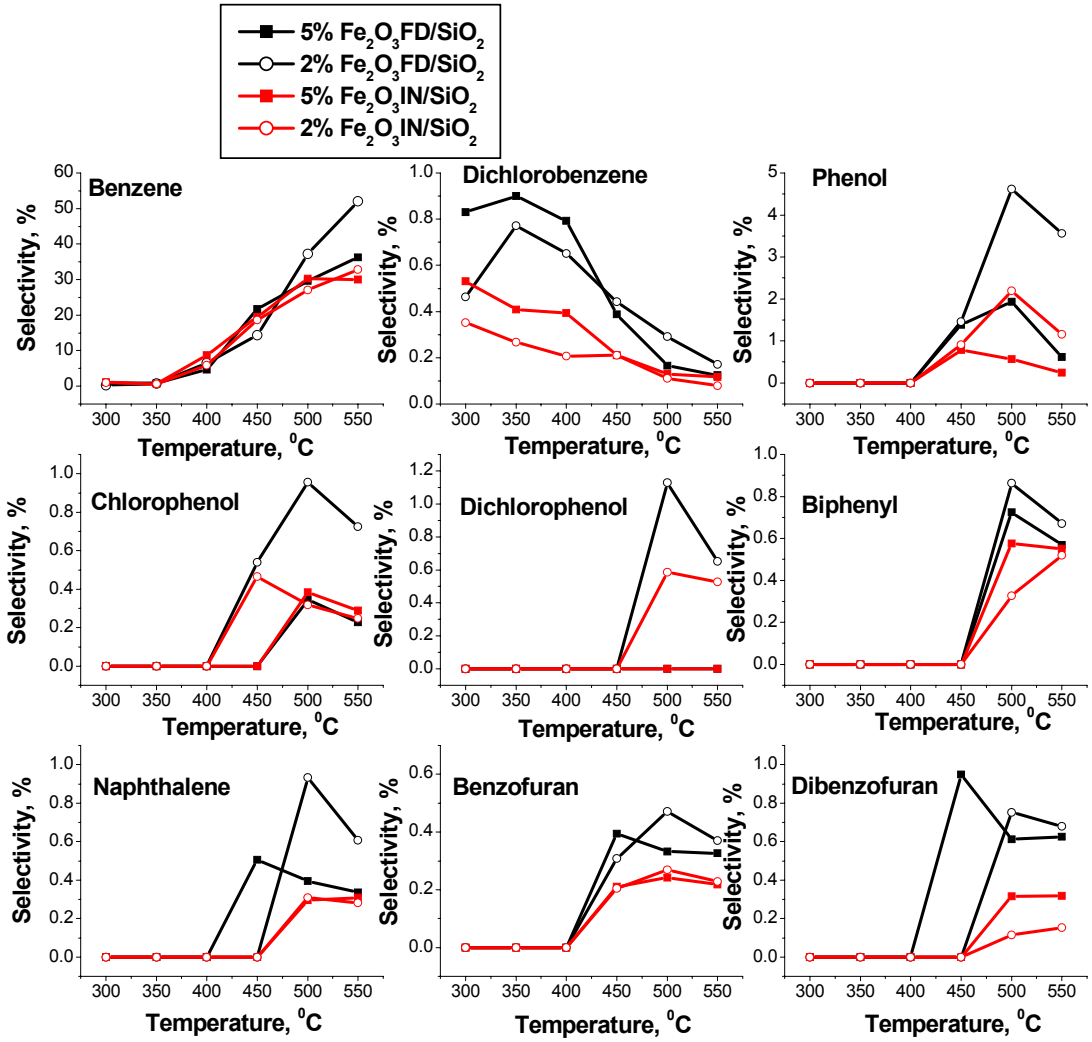

Figure 5.10 Surface-mediated pyrolytic selectivity of monochlorobenzene conversion to by-products with Fe_2O_3/SiO_2 catalysts prepared under various conditions.

This outcome is in agreement with other results found in the literature for other nanoparticle catalysts. When supported platinum catalysts were used in the oxidative decomposition of monochlorobenzene, smaller Pt crystallites gave rise to chlorinated benzenes in concentration

higher than those from larger particles; the result was attributed to the fact that in large particles, most of the Pt that is responsible for polychlorinated benzene formation is not accessible to the reactant.[28]

The benzene yield appears independent of nanoparticle size and iron oxide loading, with the exception of the 2% Fe_2O_3FD/SiO_2 catalyst, where higher amounts of benzene were detected above 500 °C. Dichlorobenzene was detected by 300 °C, with a maximum yield of 0.9% at 350 °C for 5% Fe_2O_3FD/SiO_2 and then decreased with increasing temperature. The phenol by-products were detected after 400 °C with maximum observed at ~500 °C. High concentrations of monochlorophenol and dichlorophenol were observed in the case of 2% Fe_2O_3 loading, especially for the catalyst obtained from the ferrocenoyl dendrimer. The increased amount of chlorophenol for the 2% Fe_2O_3 catalysts is most likely due to the size of the nanoparticles and maybe to different interactions with the silica support (because of the increased exposure of the surface hydroxyl groups of the silica support to the reactants). As was shown in Table 5.2, phenol and chlorinated phenols (monochlorophenol and dichlorophenol) were detected above 500 °C during monochlorobenzene reactions with silica surfaces that can be attributed to monochlorobenzene thermal decomposition in the gas phase.

Biphenyl is obtained with a maximum value of ~0.9% for the 2% Fe_2O_3FD/SiO_2 at 500 °C. Naphthalene, benzofuran, and dibenzofuran presented a different trend. At 450 °C, more by-products were obtained with 5% Fe_2O_3FD/SiO_2 catalyst, while at 500 °C, higher yields were detected with 2% Fe_2O_3FD/SiO_2 catalyst.

Above 500 °C the by-products formation decreased (except benzene) for all catalysts, indicating Fe_2O_3/SiO_2 promoted destruction of all by-products or the chlorobenzene did not chemisorbs and react at higher temperatures.

5.3.4 Oxidative Conditions

Oxidation of monochlorobenzene was investigated with Fe_2O_3/SiO_2 nanoparticles using 20% O_2 in He (UHP), as a carrier gas. This study was also performed using the 5 and 2% Fe_2O_3/SiO_2 nanoparticles, prepared by ferrocenoyl dendrimer method and by incipient wetness of SiO_2 with iron(III) nitrate.

5.3.4.1 Catalytic Activities of 5% Fe_2O_3/SiO_2 Nanoparticles in the Surface-Mediated Oxidation of Monochlorobenzene

Although statistical analysis (*t*-test) indicated that these values are not significantly different at the 95% confidence interval, the Fe_2O_3FD/SiO_2 catalyst exhibited a slight increase for the conversion of monochlorobenzene versus the Fe_2O_3IN/SiO_2 catalyst, as depicted in Figure 5.11. Under oxidative conditions, the conversion becomes observable at 350 °C for both catalysts and increases with increasing temperature. SiO_2 exhibits a small activity in the conversion of monochlorobenzene, with only 30% of monochlorobenzene converted at 550 °C which is attributed to monochlorobenzene decomposition in the gas-phase.

The only by-products obtained under oxidative conditions were benzene, dichlorobenzene, trichloroethylene, and tetrachloroethylene, and their yields are presented in Figure 5.12. Dichlorobenzene was the only chlorinated benzene detected, with its yield achieving a maximum of ~1% at 400–450 °C for both Fe_2O_3/SiO_2 catalysts. Benzene and trichloroethylene were detected in trace amounts (less than 0.1%), with a slight increase in yields for both around 400–450 °C. The Fe_2O_3IN/SiO_2 catalyst exhibited an increased activity in the production of benzene and trichloroethylene. Tetrachloroethylene yields increase slowly with increasing temperature, achieving values of 0.18% for Fe_2O_3FD/SiO_2 and 0.14% for Fe_2O_3IN/SiO_2 at 550 °C. Statistical treatments of these data indicated that, with the exception of benzene, the average values for the other by-products yields are not significantly different at the 95% confidence level for the two catalysts.

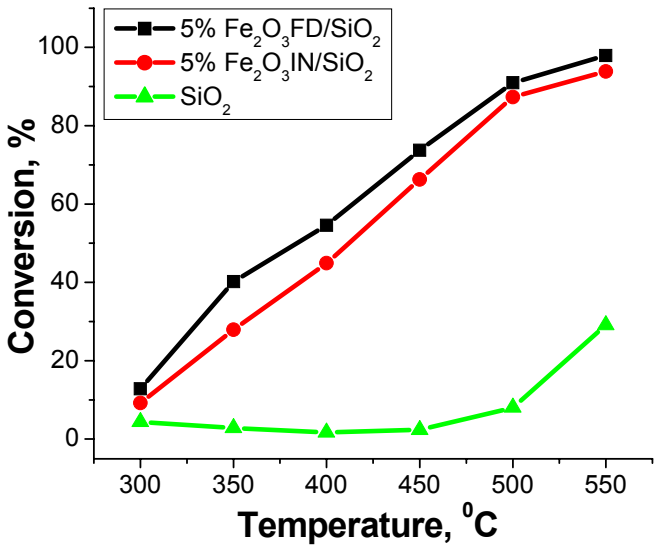

Figure 5.11 Chlorobenzene conversion over 5% Fe_2O_3/SiO_2 catalysts and SiO_2 (control) under oxidative conditions.

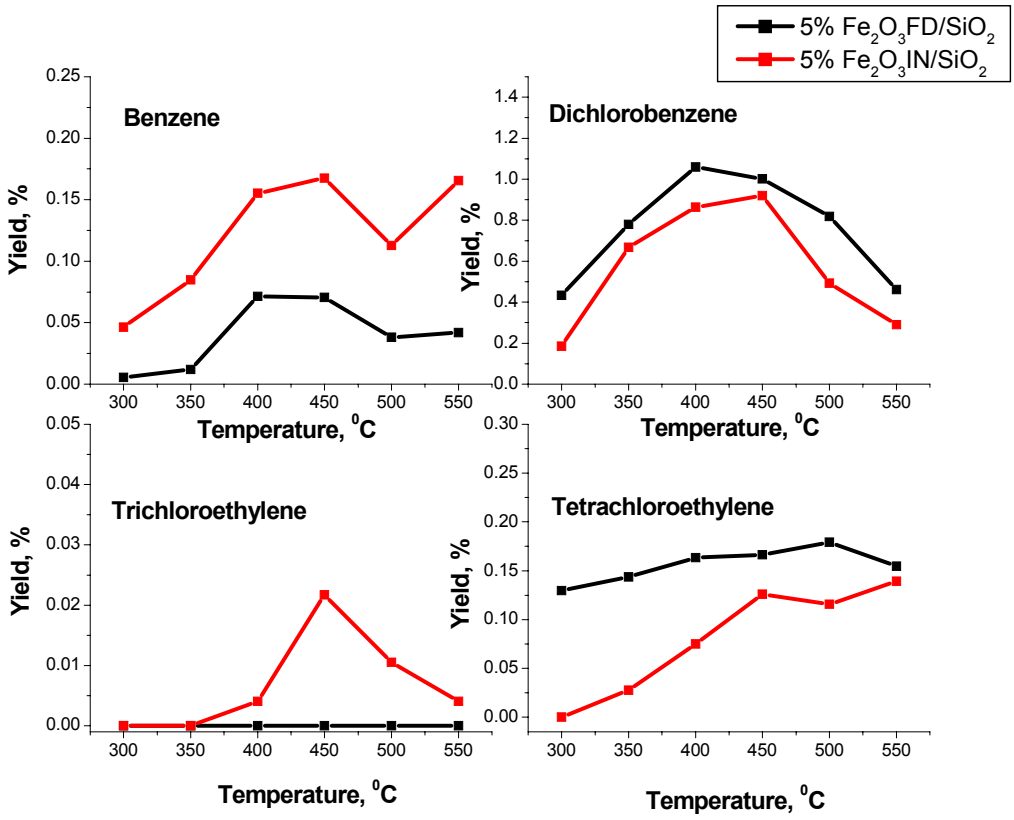

Figure 5.12 Formation of by-products from the surface-mediated oxidation of monochlorobenzene using 5% Fe_2O_3FD/SiO_2 and 5% Fe_2O_3IN/SiO_2 catalysts.

5.3.4.2 Catalytic Activities of 2% Fe_2O_3/SiO_2 Nanoparticles in the Surface-Mediated Oxidation of Monochlorobenzene

Figure 5.13 depicts data for the surface-mediated oxidation of monochlorobenzene with 2% Fe_2O_3FD/SiO_2 and Fe_2O_3IN/SiO_2 catalysts in the temperature range 300–550 °C. Fe_2O_3FD/SiO_2 leads to a better conversion of monochlorobenzene than Fe_2O_3IN/SiO_2 between 350–450 °C.

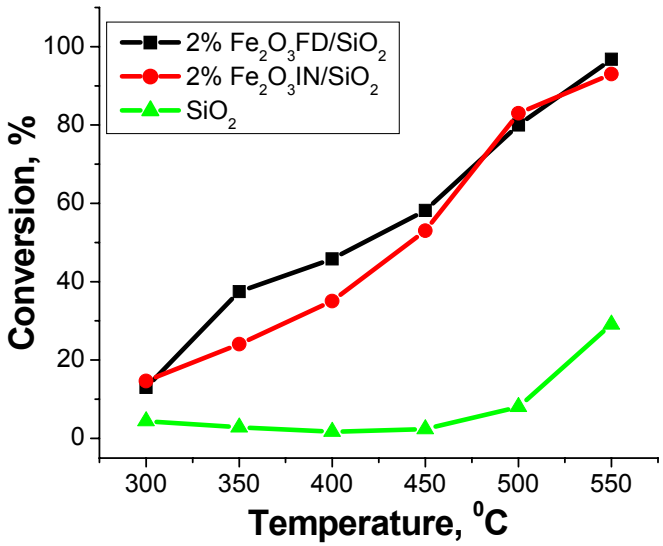

Figure 5.13 Chlorobenzene conversion with 2% Fe_2O_3/SiO_2 catalysts and SiO_2 (control) under oxidative conditions.

Under oxidative conditions, the samples with 2% iron oxide exhibited a lower activity in surface-mediated oxidation of monochlorobenzene than the catalyst with 5% loading.

The by-products obtained under oxidative conditions with the 2% Fe_2O_3/SiO_2 catalysts are presented in Figure 5.14. In this case, the sample prepared by incipient wetness of the silica support with iron nitrate (IN) exhibited a slight increase in the benzene yields compared to the ones prepared by the ferrocenoyl dendrimer (FD) method. Dichlorobenzene achieved a maximum yield of 1.99% at 450 °C for Fe_2O_3IN/SiO_2 catalyst and 1.52% obtained at 500 °C for Fe_2O_3FD/SiO_2.

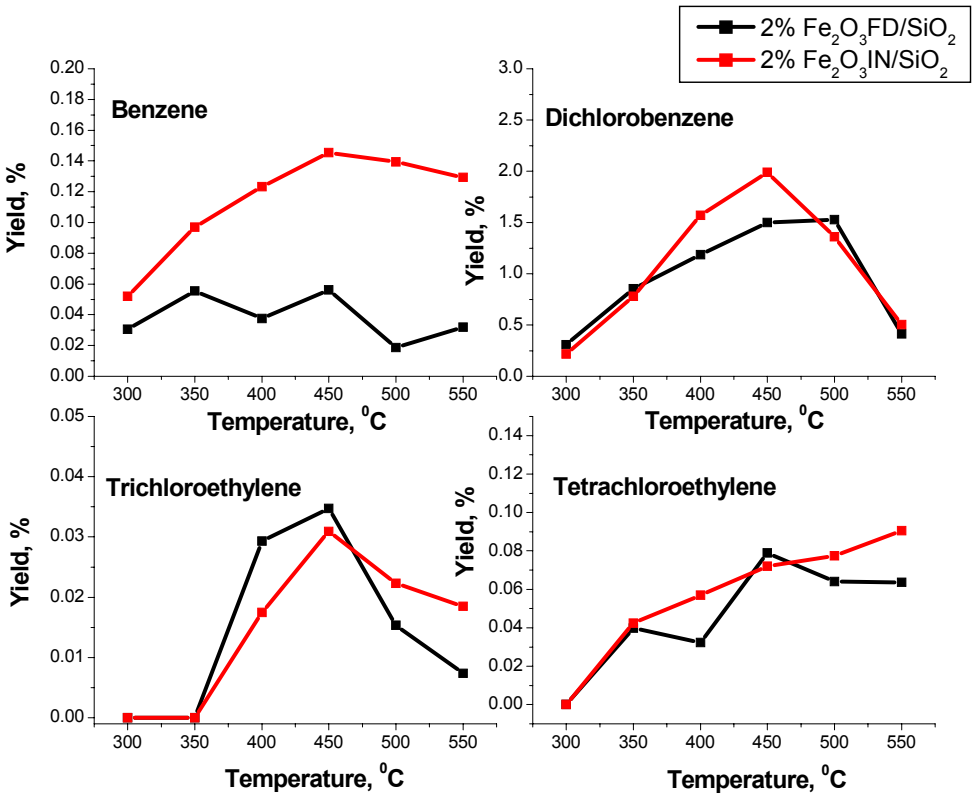

Figure 5.14 Formation of by-products from the surface-mediated oxidation of monochlorobenzene with 2% Fe_2O_3FD/SiO_2 and 2% Fe_2O_3IN/SiO_2 catalysts.

Trichloroethylene and terachloroethylene were also detected in very small amounts (less than 0.1%) with the yields increasing slightly up to 450 °C. The results obtained for the by-products yields (in the case of dichlorobenzene, trichloroethylene and tetrachloroethylene) are not significantly different at 95% confidence level for the 2% Fe_2O_3FD/SiO_2 catalyst compared to the 2% Fe_2O_3IN/SiO_2 catalyst.

The silica support alone by itself showed a very low activity in the oxidation of monochlorobenzene to by-products, and the by-products yield obtained are presented in Table 5.3.

Table 5.3 Percent yield of by-products from the oxidation of monochlorobenzene over SiO_2 surfaces.

Byproduct	% Yield By-products					
	Temperature (°C)					
	300	**350**	**400**	**450**	**500**	**550**
Benzene	0.01	0.01	0.01	0.01	0.05	0.20
Dichlorobenzene	0.00	0.07	0.09	0.10	0.63	0.38
Trichloroethylene	0.00	0.00	0.00	0.00	0.00	0.00
Tetrachloroethylene	0.00	0.00	0.00	0.00	0.09	0.13

5.3.4.3 The Effect of Preparation Method and Iron Oxide Loading on Monochlorobenzene Decomposition under Oxidative Conditions.

Under oxidative conditions (20% oxygen), the destruction of monochlorobenzene improved in the lower temperature range compared with pyrolytic conditions. For example at 350 °C, monochlorobenzene was 45% converted for the 5% Fe_2O_3FD/SiO_2 catalyst versus 18% at the same temperature under pyrolytic conditions (as shown in Figures 5.11 and 5.13). Iron oxide nanoparticles prepared from ferrocenoyl dendrimers exhibited an increase in the surface-mediated oxidation of monochlorobenzene versus that obtained for nanoparticles prepared by incipient wetness impregnation for 2% Fe_2O_3 loading. Increasing the reaction temperature resulted in increased conversion; however, full conversion is reached at temperatures above 550 °C.

The conversion of monochlorobenzene to specific by-products (selectivity) under oxidative conditions is presented in Figure 5.15, and it appears that there is no general trend. For example, monochlorobenzene conversion to trichloroethylene and tetrachloroethylene was higher over 5% Fe_2O_3FD/SiO_2, while benzene was obtained in greater quantities with 5% Fe_2O_3IN/SiO_2 catalyst. On the contrary, in the case of the 2% catalysts, the conversion of monochlorobenzene to by-products was better over the catalyst obtained from iron nitrate precursor.

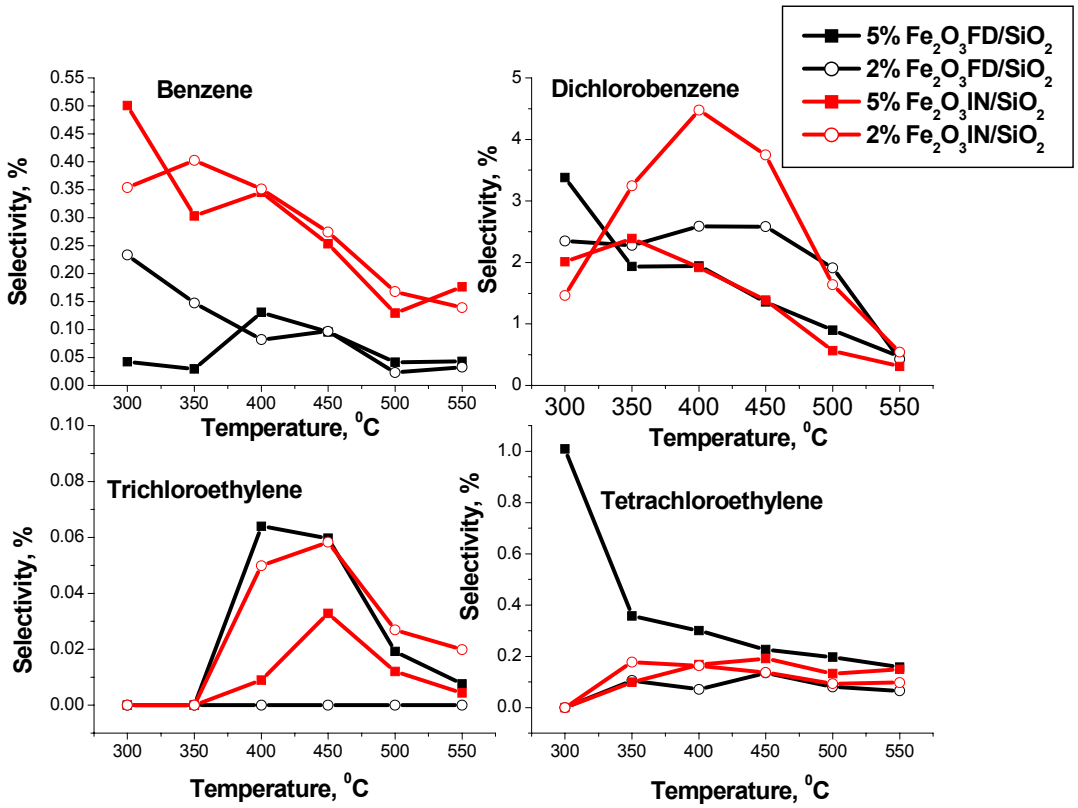

Figure 5.15 Surface-mediated oxidative selectivity of monochlorobenzene conversion to by-products with Fe_2O_3/SiO_2 catalysts prepared under various conditions.

The complete absence of furans and chlorinated phenols indicates that Fe_2O_3/SiO_2 nanoparticles are also suitable catalysts for monochlorobenzene destruction under oxidative conditions. Under pyrolytic conditions, it is clear that the surface oxygen units of the catalysts acted in the oxidation of monochlorobenzene. I propose this resulted in monochlorobenzene remaining adsorbed onto the Fe_2O_3/SiO_2 surface rather than being oxidized and participating in further reactions. The presence of oxygen, under oxidative conditions, would yield more oxygen on the Fe_2O_3/SiO_2 surface that promotes combustion of the phenyl ring and breakdown to lower molecular weight molecules. This might also be due to the strong oxidant character of Fe_2O_3 catalysts, some of which have been reported to exhibit oxidation activity in the destruction of chlorobenzene and also dioxins and furans.[17,27]

5.3.5 Proposed Reaction Mechanism for the Formation of By-products under Pyrolytic and Oxidative Conditions

In order for the pyrolytic and oxidative decomposition of monochlorobenzene to furans and other by-products to occur at low temperature, monochlorobenzene must attach to the Fe_2O_3/SiO_2 surface. In this research, low-temperature conversion (300–550 °C) of monochlorobenzene to by-products indicates that iron oxide nanoparticles on the silica surface mediated this reaction. The surface-mediated formation of furans from the decomposition of monochlorobenzene over silica-supported iron oxides nanoparticles occurs only under pyrolytic conditions, at temperatures between 450–550 °C. Iron oxide species clearly promote furan formation after monochlorobenzene chemisorption, but the mechanism is not fully understood. A detailed study of surface mediated reactions of 2-chlorophenol, 1,2-dichlorobenzene, and monochlorobenzene with CuO/SiO_2 was reported by Alderman and co-workers[39] using FT-IR and XANES. They determined that chlorinated phenols and chlorinated benzenes chemisorbed onto the surface of CuO/SiO_2 to form chlorophenolate via H_2O and/or HCl elimination. EPR experiments indicated that monochlorobenzene chemisorbed onto CuO/Silica, similar to 1,2-dichlorobenzene, by forming mostly semiquinone radicals at lower temperatures and both semiquinone and phenoxyl-type radical at higher temperatures.[21] It was also found that monochlorobenzene was easily chlorinated to dichlorobenzene, and the chemisorption mechanism on the CuO surface is similar to 1,2-dichlorobenzene.[21] Based on these results,[21,39] and a mechanism proposed in the literature for the conversion of monochlorophenol over Fe_2O_3/SiO_2 catalyst,[12] I posit the chemisorption of monochlorobenzene onto the Fe_2O_3/SiO_2 catalysts probably occurs via a mechanism similar to the CuO/Silica system, outlined in Scheme 5.1. First, monochlorobenzene is chemisorbed onto the support surface via HCl elimination.[21,33,40] As previously determined in the literature, the resulting chemisorbed species undergo electron transfer with the metal center, resulting in the formation of persistent free

radicals and the reduction of the metal.[12] The surface-associated phenoxyl radical can exist as an oxygen-centered (intermediate II in Scheme 5.1) or carbon-centered mesomer (intermediate III in Scheme 5.1). Future EPR experiments are needed to confirm the presence of such radicals.

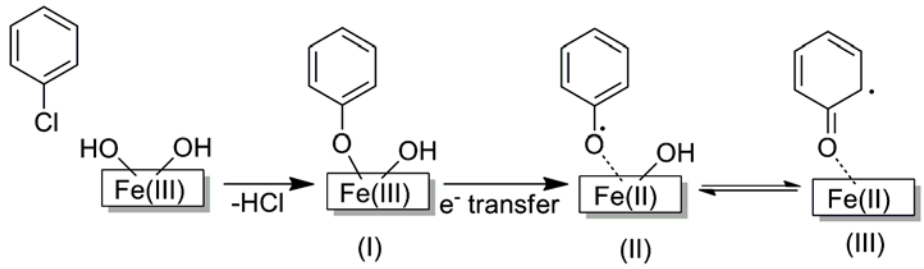

Scheme 5.1 Proposed mechanism for adsorption of monochlorobenzene onto Fe_2O_3/SiO_2 catalysts.

Chlorine atom displacement can facilitate formation of other chlorinated by-products. In addition to chlorine displacement, many other reactions (such as hydrogen abstraction by chlorine atoms, chlorine atom transfer, and radical addition) can participate in the formation of by-products. Significant amounts of benzene were detected from surface-mediated pyrolysis of monochlorobenzene at temperatures as low as 400 °C. In this route, benzene is most likely formed, starting from surface phenolate by the scission of the C-O bond to form a free phenyl radical that can scavenge a hydrogen to form benzene,[41] see pathway 1 in Scheme 5.2. Phenol can then be formed by the scission of one M-O bond[12,41] in the surface phenolate to yield phenoxyl radical that is subsequently converted to phenol by scavenging a hydrogen atom, see pathway 2 in Scheme 5.2. The only chlorinated by-products obtained are dichlorobenzene and chlorinated phenols (monochlorophenol and dichlorophenol). The low supply of chlorine atoms in the reaction studied here could be one of the factors that influence the pattern of chlorinated products. Conversion of monochlorobenzene to chlorinated phenols could occur on the surface of Fe_2O_3/SiO_2 by chlorination of surface phenolate with chlorine coming from surface hypochlorite species,[4] pathway 3 in Scheme 5.2.

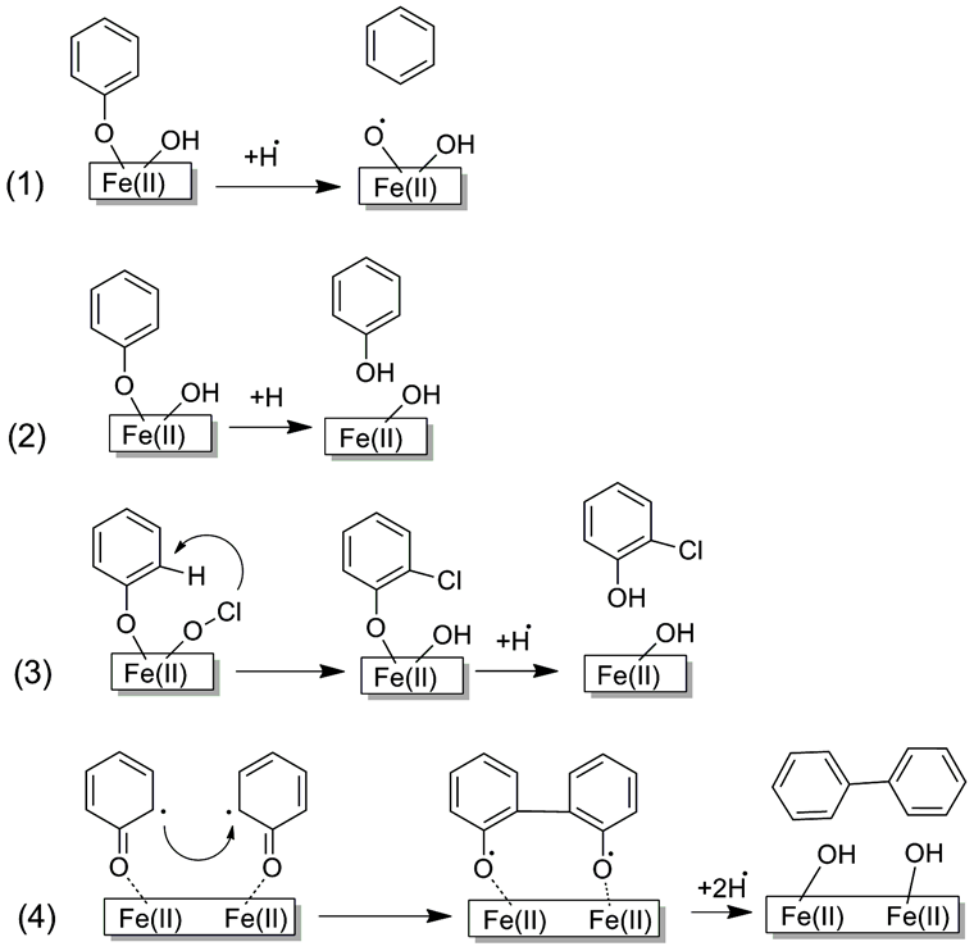

Scheme 5.2 Proposed mechanism for the formation of benzene, phenol, chlorophenol, and biphenyl on Fe_2O_3/SiO_2 catalysts from monochlorobenzene.

Additional chlorination to form dichlorophenol requires abstraction of a hydrogen and addition attack of chlorine. Biphenyl might be formed by the reaction of two keto mesomers, pathway 4 in Scheme 5.2. The formation of naphthalene is a more complicated process that can occur by the recombination of two cyclopentadienyl radicals,[42] followed by rearrangement and hydrogen radical elimination or via reaction of a phenyl radical with the species resulting from the aromatic ring breakdown at high temperatures (CH_4, C_2H_2, C_4H_4, and H_2).[43-45] However, none of these naphthalene formation mechanisms have been determined experimentally in the catalyst surfaces.

The adsorption mechanism of monochlorobenzene on the Fe_2O_3/SiO_2 catalysts to form furans may be explained by a mechanism similar to that proposed for 2-monochlorophenol destruction on Fe_2O_3/SiO_2.[12] The formation of dibenzofuran occurs by a Langmuir-Hinshelwood (L-H) mechanism that implies reaction between two surface-adsorbed species (likely by keto mesomers).[4,12] Two of these keto mesomers react and, after recombination-electron transfer, dibenzofurans are desorbed from the iron oxide surface, Scheme 5.3.

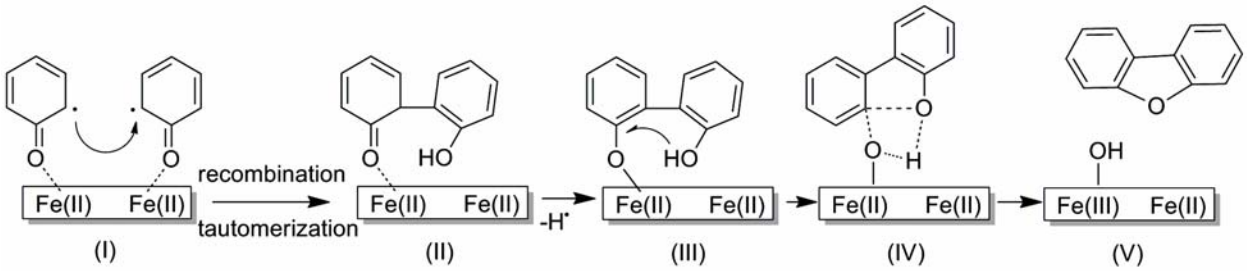

Scheme 5.3 Proposed reaction mechanism for the formation of dibenzofuran on Fe_2O_3/SiO_2.

Previous experimental results indicated that when the pyrolysis of monochlorobenzene was performed at higher temperature (800–1200 °C) in the gas phase, no PCDD/Fs were detected,[43] an outcome that supports the conclusion that iron oxides on silica surfaces are reactive sites for the formation of furans under pyrolytic conditions at low temperature.

Under oxidative conditions, the only by-products detected in this work were dichlorobenzene, benzene, trichloroethylene, and tetrachloroethylene. It was shown in the literature that, in the presence of oxygen and suitable conditions (temperature, H_2O, and catalyst), most of the adsorbed aromatics are completely oxidized to their final products (CO_2, H_2O and HCl).[23,26] Chlorinated benzenes are by-products formed during almost all monochlorobenzene catalytic oxidative decomposition experiments.[26,30,31] Under oxidative conditions, two processes are likely to occur: the chlorination of monochlorobenzene to form dichlorobenzene, and the scission of the carbon-carbon and carbon-oxygen bond to form lower molecular weight products. In the presence of oxygen, no furans were detected from

surface-mediated oxidative degradation of monochlorobenzene over any of the Fe_2O_3/SiO_2 nanoparticles, indicating that the excess of oxygen in the reaction promotes combustion of the phenyl ring. Iron oxides are better catalysts for monochlorobenzene destruction than other studied catalysts in the literature, such as noble metals and fly ash, which promotes formation of PCDD/Fs from monochlorobenzene under oxidative conditions.[3,22]

Mechanistic studies of the catalytic oxidation of chlorinated benzenes over metal oxides or noble metal catalysts were proposed in the literature.[25,33,40] Based on the data published in the literature and my experimental data, the surface-mediated oxidation of monochlorobenzene over Fe_2O_3/SiO_2 could proceed through the same mechanism depicted in Scheme 5.1. The surface oxygen from the iron oxide surface participates in the oxidation of monochlorobenzene, according to the Mars-van Krevelen mechanism wherein the surface oxygen atoms are consumed by the reagents, leaving oxygen vacancies on the catalyst surface.[46] The presence of chlorine on the surface can block further reactions. The surface hydrogens in our case are effective donor sites that can convert, to some extent, the surface chlorine into HCl, thereby restoring the active sites.

In the second step, the surface phenolate could react further with chlorine atoms to form dichlorobenzene or could suffer bond rupture of the aromatic ring to give nonaromatic intermediates.[33] These intermediates would then react further with chlorine atoms to form trichloroethylene or tetrachloroethylene, as observed in this study. The partial oxidation products formed on silica-supported iron oxide nanoparticle catalysts can undergo further oxidation reactions to form complete oxidation products (CO, CO_2, HCl and H_2O) as observed in other studies.[33]

5.4 Conclusions

Surface-mediated reaction of monochlorobenzene was studied under pyrolytic and oxidative conditions, over a temperature range of 300–550 °C, in the presence of silica-supported iron oxide nanoparticles catalysts. The preparation of the catalysts was focused on obtaining nanoparticles with different sizes and low size dispersity and different iron oxide loadings. In order to achieve this, two preparation methods were used: deposition of ferrocenoyl-modified poly(propylene imine) dendrimers on silica support and incipient wetness of silica with iron(III) nitrate salt. After impregnation, the samples were calcined at 450 °C in air flow for 4 h. HR-TEM characterization showed that the iron oxide sizes are in the nanometer regime (less than 5 nm in average diameter) for both methods, and the size and size dispersity are dependent on the preparation method, with the smallest size dispersity obtained from ferrocenoyl dendrimer. XPS experiments confirmed that Fe_2O_3 is present in the calcined samples.

In the monochlorobenzene combustion experiments at 300–550 °C, after 5 min reaction time, the by-products detected under pyrolytic conditions were furan, dibenzofuran, chlorobenzenes, chlorophenols, biphenyl, and naphthalene. The experiments with Fe_2O_3/SiO_2 catalysts illustrated that the catalytic decomposition of monochlorobenzene to by-products depends on the number of iron oxide active sites present on the support as well as on the size of iron oxide nanoparticles. The 2% Fe_2O_3FD/SiO_2 catalyst was the most active one in the formation of by-products from monochlorobenzene under pyrolytic conditions. Under oxidative conditions, the iron oxide catalysts mediated monochlorobenzene destruction to lower molecular weight products. The only by-products detected under oxidative conditions were dichlorobenzene, benzene, trichloroethylene and tetrachloroethylene. The 2% Fe_2O_3IN/SiO_2 catalyst was more active in the formation of benzene and dichlorobenzene while the 5%

Fe_2O_3FD/SiO_2 catalyst was more active in the formation of trichloroethylene and tetrachloroethylene.

The heterogeneous reactions occurring on the surface of silica-supported iron oxide nanoparticles under pyrolytic conditions promoted the formation of the lower chlorinated products (dichlorobenzene, monochlorophenol, and dichlorophenol), and this is most likely due to the low supply of chlorine species in the reaction (just one chlorine from the monochlorobenzene precursor). Additional experiments with highly chlorinated benzene seem necessary to support this conclusion, because it was shown that the presence of supplementary chlorine sources in the reaction increase the production of more chlorinated congeners.[22]

5.5 References

(1) Altarawneh, M.; Dlugogorski, B. Z.; Kennedy, E. M.; Mackie, J. C. Mechanisms for formation, chlorination, dechlorination and destruction of polychlorinated dibenzo-p-dioxins and dibenzofurans (PCDD/Fs). *Prog. Energy Combust. Sci.* **2009**, *35*, 245-274.

(2) Stanmore, B. R. The formation of dioxins in combustion systems. *Combust. Flame* **2004**, *136*, 398-427.

(3) Addink, R.; Cnubben, P. A. J. P.; Olie, K. Formation of polychlorinated dibenzo-*p*-dioxins dibenzofurans on fly-ash from precursors and carbon model compounds. *Carbon* **1995**, *33*, 1463-1471.

(4) Lomnicki, S.; Dellinger, B. A detailed mechanism of the surface-mediated formation of PCDD/F from the oxidation of 2-chlorophenol on a CuO/silica surface. *J. Phys. Chem. A* **2003**, *107*, 4387-4395.

(5) Pekarek, V.; Weber, R.; Grabic, R.; Solcova, O.; Fiserova, E.; Syc, M.; Karban, J. Matrix effects on the de novo synthesis of polychlorinated dibenzo-*p*-dioxins, dibenzofurans, biphenyls and benzenes. *Chemosphere* **2007**, *68*, 51-61.

(6) Ryu, J. Y.; Mulholland, J. A. Metal-mediated chlorinated dibenzo-*p*-dioxin (CDD) and dibenzofuran (CDF) formation from phenols. *Chemosphere* **2005**, *58*, 977-988.

(7) Thomas, V. M.; McCreight, C. M. Relation of chlorine, copper and sulphur to dioxin emission factors. *J. Hazard. Mater.* **2008**, *151*, 164-170.

(8) Dickson, L. C.; Lenoir, D.; Hutzinger, O. Quantitative comparison of denovo and precursor formation of polychlorinated dibenzo-*p*-dioxins under simulated municipal solid-waste incinerator postcombustion conditions. *Environ. Sci. Technol.* **1992**, *26*, 1822-1828.

(9) Quina, M. J.; Bordado, J. C.; Quinta-Ferreira, R. M. Treatment and use of air pollution control residues from MSW incineration: An overview. *Waste Manage.* **2008**, *28*, 2097-2121.

(10) Born, J. G. P.; Mulder, P.; Louw, R. Fly-ash mediated reactions of phenol and monochlorophenols - oxychlorination, deep oxidation, and condensation. *Environ. Sci. Technol.* **1993**, *27*, 1849-1863.

(11) Allouis, C.; Beretta, F.; D'Alessio, A. Structure of inorganic and carbonaceous particles emitted from heavy oil combustion. *Chemosphere* **2003**, *51*, 1091-1096.

(12) Nganai, S.; Lomnicki, S.; Dellinger, B. Ferric oxide mediated formation of PCDD/Fs from 2-monochlorophenol. *Environ. Sci. Technol.* **2009**, *43*, 368-373.

(13) Kasai, E.; Kobayashi, T.; Nakamura, T. Formation of PCDD/Fs on iron oxides from chlorobenzene and chlorophenol. *Organohalogen Compd.* **1999**, *41*, 187-190.

(14) Lomnicki, S.; Dellinger, B. Development of supported iron oxide catalyst for destruction of PCDD/F. *Environ. Sci. Technol.* **2003**, *37*, 4254-4260.

(15) Wang, H. C.; Chang, S. H.; Hung, P. C.; Hwang, J. F.; Chang, M. B. Catalytic oxidation of gaseous PCDD/Fs with ozone over iron oxide catalysts. *Chemosphere* **2008**, *71*, 388-397.

(16) Wang, H. C.; Chang, S. H.; Hung, P. C.; Hwang, J. F.; Chang, M. B. Synergistic effect of transition metal oxides and ozone on PCDD/F destruction. *J. Hazard. Mater.* **2009**, *164*, 1452-1459.

(17) Hung, W.-T.; Lin, C.-F. Use of regenerated ferric oxide for CO destruction and suppressing dioxin formation in flue gas in a pilot-scale incinerator. *Chemosphere* **2003**, *53*, 727-735.

(18) Lavric, E. D.; Konnov, A. A.; De Ruyck, J. Surrogate compounds for dioxins in incineration. A review. *Waste Manage.* **2005**, *25*, 755-765.

(19) Briois, C.; Ryan, S.; Tabor, D.; Touati, A.; Gullett, B. K. Formation of polychlorinated dibenzo-*p*-dioxins and dibenzofurans from a mixture of chlorophenols over fly ash: Influence of water vapor. *Environ. Sci. Technol.* **2007**, *41*, 850-856.

(20) Ryu, J.-Y.; Mulholland, J. A. Dioxin and furan formation on $CuCl_2$ from chlorinated phenols with one ortho chlorine. *Proc. Combust. Inst.* **2002**, *29*, 2455-2461.

(21) Lomnicki, S.; Truong, H.; Vejerano, E.; Dellinger, B. Copper oxide-based model of persistent free radical formation on combustion-derived particulate matter. *Environ. Sci. Technol.* **2008**, *42*, 4982-4988.

(22) De Jong, V.; Cieplik, M. K.; Louw, R. Formation of dioxins in the catalytic combustion of chlorobenzene and a micropollutant-like mixture on Pt/γ-Al_2O_3. *Environ. Sci. Technol.* **2004**, *38*, 5217-5223.

(23) Xingyi, W.; Qian, K.; Dao, L. Catalytic combustion of chlorobenzene over MnOx-CeO_2 mixed oxide catalysts. *Appl. Catal., B* **2009**, *86*, 166-175.

(24) Moon, S. W.; Lee, G. D.; Park, S. S.; Hong, S. S. Catalytic combustion of chlorobenzene over V_2O_5/TiO_2 catalysts prepared by the precipitation-deposition method. *React. Kinet. Catal. Lett.* **2004**, *82*, 303-310.

(25) de Jong, V.; Cieplik, M. K.; Reints, W. A.; Fernandez-Reino, F.; Louw, R. A mechanistic study on the catalytic combustion of benzene and chlorobenzene. *J. Catal.* **2002**, *211*, 355-365.

(26) Taralunga, M.; Mijoin, J.; Magnoux, P. Catalytic destruction of chlorinated POPs - catalytic oxidation of chlorobenzene over PtHFAU catalysts. *Appl. Catal., B* **2005**, *60*, 163-171.

(27) Khaleel, A.; Al-Nayli, A. Supported and mixed oxide catalysts based on iron and titanium for the oxidative decomposition of chlorobenzene. *Appl. Catal., B* **2008**, *80*, 176-184.

(28) van den Brink, R. W.; Krzan, M.; Feijen-Jeurissen, M. M. R.; Louw, R.; Mulder, P. The role of the support and dispersion in the catalytic combustion of chlorobenzene on noble metal based catalysts. *Appl. Catal., B* **2000**, *24*, 255-264.

(29) Nakka, H.; Fullana, A.; Sidhu, S. Surface catalyzed chlorobenzene transformation reactions in post-combustion zone. *Organohalogen Compd.* **2004**, *66*, 1140-1145.

(30) van den Brink, R. W.; Louw, R.; Mulder, P. Formation of polychlorinated benzenes during the catalytic combustion of chlorobenzene using a Pt/γ-Al_2O_3 catalyst. *Appl. Catal., B* **1998**, *16*, 219-226.

(31) Scirè, S.; Minicò, S.; Crisafulli, C. Pt catalysts supported on H-type zeolites for the catalytic combustion of chlorobenzene. *Appl. Catal., B* **2003**, *45*, 117-125.

(32) Liu, P. Y.; Zheng, M. H.; Zhang, B.; Xu, X. B. Mechanism of PCBs formation from the pyrolysis of chlorobenzenes. *Chemosphere* **2001**, *43*, 783-785.

(33) Lichtenberger, J.; Amiridis, M. D. Catalytic oxidation of chlorinated benzenes over V_2O_5/TiO_2 catalysts. *J. Catal.* **2004**, *223*, 296-308.

(34) Rubey, W. A.; Grant, R. A. Design aspects of a modular instrumentation system for thermal diagnostic studies. *Rev. Sci. Instrum.* **1988**, *59*, 265-269.

(35) Blumenstock, M.; Zimmermann, R.; Schramm, K. W.; Kaune, A.; Nikolai, U.; Lenoir, D.; Kettrup, A. Estimation of the dioxin emission (PCDD/FI-TEQ) from the concentration of low chlorinated aromatic compounds in the flue and stack gas of a hazardous waste incinerator. *J. Anal. Appl. Pyrolysis* **1999**, *49*, 179-190.

(36) Zimmermann, R.; Heger, H. J.; Blumenstock, M.; Dorfner, R.; Schramm, K. W.; Boesl, U.; Kettrup, A. On-line measurement of chlorobenzene in waste incineration flue gas as a surrogate for the emission of polychlorinated dibenzo-*p*-dioxins/furans (I-TEQ) using mobile resonance laser ionization time-of-flight mass spectrometry. *Rapid Commun. Mass Spectrom.* **1999**, *13*, 307-314.

(37) Wagner, C. D.; Riggs, W. M.; Davis, L. E.; Moulder, J. F.; Muilenberg, G. E. *Handbook of x-ray photoelectron spectroscopy*; Perkin-Elmer Corporation Physical Electronics Division, Minnesota, U.S.A, **1979**.

(38) Alderman, S. L. Infrared and x-ray spectroscopic studies of the copper(II) oxide mediated reactions of chlorinated aromatic precursors to PCDD/F. *Dissertation*, Louisiana State University, **2005**.

(39) Alderman, S. L.; Farquar, G. R.; Poliakoff, E. D.; Dellinger, B. An infrared and x-ray spectroscopic study of the reactions of 2-chlorophenol, 1,2-dichlorobenzene, and chlorobenzene with model CuO/silica fly ash surfaces. *Environ. Sci. Technol.* **2005**, *39*, 7396-7401.

(40) van den Brink, R. W.; de Jong, V.; Louw, R.; Maggi, P.; Mulder, P. Hydrogen–deuterium isotope effects in the reactions of chlorobenzene and benzene on a Pt/γ-Al_2O_3 catalyst. *Catal. Lett.* **2001**, *71*, 15-20.

(41) Ihm, H.; White, J. M. Stepwise dissociation of thermally activated phenol on Pt(111). *J. Phys. Chem., B* **2000**, *104*, 6202-6211.

(42) Mebel, A. M.; Kislov, V. V. Can the $C_5H_5 + C_5H_5 \rightarrow C_{10}H_{10} \rightarrow C_{10}H_9 + H/C_{10}H_8 + H_2$ reaction produce naphthalene? An Ab initio/RRKM study. *J. Phys. Chem. A* **2009**, *113*, 9825-9833.

(43) Rouzet, G.; Schwartz, D.; Gadiou, R.; Delfosse, L. The formation of chlorinated aromatic hydrocarbons during high temperature pyrolysis of chlorobenzene. *J. Anal. Appl. Pyrolysis* **2001**, *57*, 153-168.

(44) Appel, J.; Bockhorn, H.; Frenklach, M. Kinetic modeling of soot formation with detailed chemistry and physics: Laminar premixed flames of C2 hydrocarbons. *Combust. Flame* **2000**, *121*, 122-136.

(45) Lindstedt, R. P.; Rizos, K. A. The formation and oxidation of aromatics in cyclopentene and methyl-cyclopentadiene mixtures. *Proc. Combust. Inst.* **2002**, *29*, 2291-2298.

(46) Lomnicki, S.; Dellinger, B. Formation of PCDD/F from the pyrolysis of 2-chlorophenol on the surface of dispersed copper oxide particles. *Proc. Combust. Inst.* **2002**, *29*, 2463-2468.

CHAPTER 6

CONCLUSIONS AND OUTLOOK

6.1 Summary of Results

Methods to synthesize well-defined metal and metal oxide nanoparticles with small sizes (less than 3 nanometers) and low size dispersity (less than 20%) in solution or on surfaces using either amine-terminated poly(propylene imine) dendrimers or ferrocenoyl-modified poly(propylene imine) dendrimers on silica surfaces have been developed in this research. The purpose of this research was to synthesize well-defined nanoparticles and to use them as laboratory surrogates for combustion-generated nanoparticles to assess their role in mediating the formation of surface-associated pollutants; this has been demonstrated for Fe_2O_3 nanoparticles supported on SiO_2.

In general, the preparation of stable Ni metal nanoparticles is relatively difficult because they are easily oxidized, and sometimes Ni-reducing agent alloys are formed instead of pure Ni. Prior work on chemical reduction with sodium borohydride reported the formation of either Ni metal nanoparticles or a mixture of metal, metal oxides and metal borides, indicating that the mechanism and the end product depends drastically on the reaction conditions, such as aqueous or nonaqueous media, inert or ambient atmosphere.[1,2] In this research, well-defined Ni nanoparticles of controllable size and having low size dispersity were prepared by anaerobic chemical reduction of DAB-Am$_n$-Ni(II)$_x$ complexes with sodium borohydride in methanol. Five generations of amine-terminated poly(propylene imine) dendrimers, DAB-Am$_n$ (n = 4, 8, 16, 32, 64) were used as multifunctional ligands for Ni(II) ions. UV-vis spectroscopy and the method of continuous variation (Job plot) allowed for determination of the complexation and the stoichiometry of the predominant DAB-Am$_n$-Ni(II)$_x$ complex. It was found that Ni(II) coordinates with NH_2 end groups of the dendrimer in a mole ratio of 1:2, similar to that found for

complexation of Cu(II) with poly(propylene imine) dendrimers.[3] The results support the conclusion that complexation of Ni(II) by DAB-Am_n dendrimers occurs in a site-selective way wherein dipropylenetriamine (dpt) end groups act as very strong coordinating units. In order to obtain information about the oxidation state of Ni nanoparticles prepared by borohydride reduction of the DAB-Am_n-$Ni(II)_x$ complex and the possible presence of other elements in the nanoparticles, X-ray photoelectron spectroscopy was used. XPS confirmed that the particles are composed of Ni(0) nanoparticles with a borate contaminant. Nanoparticles size is precisely controlled in the 1.85 to 2.70 nm range by manipulating the dendrimer generation, the ratio of primary amines to Ni(II) ions, and the $NiCl_2$ concentration, as shown by high-resolution transmission electron microscopy (HR-TEM).

Another aim of this research was the synthesis of metal oxide nanoparticles on a solid surface. Silica-supported iron oxide nanoparticles of controllable size and having low size dispersity were synthesized by using ferrocenoyl-modified poly(propylene imine) dendrimers. The syntheses were carried out by impregnating a series of poly(propylene imine) dendrimers functionalized with peripheral ferrocenoyl units, DAB-$(NHCOFc)_n$ (n = 4, 8, 16, 32, and 64), onto a high-surface-area silica, followed by thermal treatment to remove the organic materials. In order to find the optimum calcination temperature, decomposition of the supported ferrocenoyl-modified dendrimers was investigated by thermogravimetric analysis (TGA) and XPS. From TGA results it was showen that the weight loss of organic material attained its maximum value around 400 °C under oxidative conditions. XPS confirmed successful removal of the dendrimers (absence of N 1s peak at approximately 400 eV) after calcination at 450 ºC for 4 h in a tube furnace with controlled air flow. Formation of iron oxide nanoparticles after air calcination was also confirmed by XPS. Control over nanoparticle diameter was shown to be possible by manipulating the ferrocenoyl dendrimer generation, calcination temperature and

time, the ferrocenoyl dendrimer loading on silica support, and the presence of unmodified poly(propylene imine) dendrimer in reaction. Modification of these parameters served as a simple way to tune nanoparticle sizes, yielding silica-supported iron oxide nanoparticles that are 2.41 to 3.65 nm in diameter with very low size dispersities (less than 15%).

To test the hypothesis that the transition metal oxide nanoparticles present in the ultrafine particulate materials emitted from combustion sources may be responsible for the formation of gas-phase pollutants through catalytic reactions occurring on their surface, I have performed a study of the pyrolytic and oxidative combustion of chlorobenzene with silica-supported Fe_2O_3 nanoparticles between 300–550 ºC. For comparison purposes, the Fe_2O_3 nanoparticles supported on silica were prepared by two methods: standard impregnation with ferrocenoyl dendrimers and incipient wetness impregnation with iron(III) nitrate dissolved in methanol, followed by calcination at 450 °C in a tube furnance with controlled air flow. The obtained iron oxide nanoparticles were characterized by HR-TEM and it was found that their size and dispersity are dependent on the preparation method. The use of ferrocenoyl dendrimers as iron oxide nanoparticles precursors resulted in well-defined nanoparticles with a very small size distribution. The mean diameter of the nanoparticles was 2.36±0.25 nm for 2% iron oxide loading and increased to 2.80±0.31 nm with an iron oxide loading of 5%. When the iron nitrate was used in the synthesis, the nanoparticles increased in size and had a larger size distribution. For example, for 5% Fe_2O_3 coverage, the average size of nanoparticles obtained was 5.06±1.72 nm, while for 2% coverage the average size was 3.91±0.93 nm. The results obtained from pyrolysis experiments indicated that the Fe_2O_3 nanoparticles promote furans formation and other byproducts (benzene, dichlorobenzene, phenols, chlorinated phenols, biphenyl, and naphthalene). It was also found that the Fe_2O_3 nanoparticles obtained from ferrocenoyl-modified dendrimers had higher activity in production of furans than the ones obtained from iron nitrate.

Furthermore, the nanoparticles with the smallest size, obtained using ferocenoyl dendrimer and 2% Fe_2O_3 loading, were generally the most active in the formation of byproducts from pyrolytic decomposition of monochlorobenzene.

Under oxidative conditions, iron oxide-mediated monochlorobenzene destruction to lower molecular weight products occured rather than the formation of furans and chlorinated byproducts. The only byproducts detected from surface-mediated oxidative decomposition of monochlorobenzene with the Fe_2O_3/SiO_2 catalysts were benzene, dichlorobenzene, trichloroethylene, and tetrachloroethylene, indicating that the presence of oxygen in the feed gas promotes chlorobenzene combustion.

6.2 Conclusions

The results of this research revealed that the developed synthetic methods using dendritic complexes, employing amine-terminated poly(propylene imine) dendrimers or ferrocenoyl-modified poly(propylene imine) dendrimers, were successful in the preparation of well-defined Ni(0) nanoparticles in solution and iron oxide nanoparticles on silica surface with low size dispersities (less than 20%). The well-defined iron oxide nanoparticles were used as laboratory surrogates for combustion-generated nanoparticles to assess their role in pollutant formation. Surface-mediated reaction of an organic precursor (monochlorobenzene) was studied under pyrolytic and oxidative conditions over silica-supported Fe_2O_3 nanoparticles between 300–550 °C. It was found that silica-supported Fe_2O_3 nanoparticles have different properties under pyrolytic and oxidative conditions. The iron oxide nanoparticles mediated decomposition of monochlorobenzene to furans and other byproducts only under pyrolytic conditions. Under oxidative conditions no furans were detected. With these findings, it is clear that metal oxide nanoparticles play a significant role in mediating the formation of surface-associated pollutants from organic precursors in combustion processes.

6.3 Outlook

The dendrimer-ligand-based method can be used to create new hybrid materials, such as bimettalic nanoparticles supported on silica surfaces. This work and the previous work in the McCarley group[3] demonstrated that Ni(II) and Cu(II) form well-defined complexes with poly(propylene imine) dendrimers, DAB-Am_n-$M(II)_x$ (where $x = n/2$, and M is Ni(II) or Cu(II)). This known complexation can be extended to synthesize Cu-Ni bimetallic nanoparticles supported on silica surface. The synthesis will be carried out by complexation of DAB-Am_n dendrimer with Ni(II) and Cu(II) in different NH_2:M(II) molar ratios, followed by deposition on the silica surface, to obtain supported Cu-Ni bimetallic nanoparticles. The activation of dendrimer-metal complex/SiO_2 at high temperature in a tube furnace with controlled air flow will result in formation of NiO-CuO nanoparticles/SiO_2. These new materials could be also used as laboratory surrogates for combustion-generated nanoparticles to assess their role in mediating the formation of surface-associated pollutants from organic precursors.

6.4 References

(1) Glavee, G. N.; Klabunde, K. J.; Sorensen, C. M.; Hadjipanayis, G. C. Borohydride reduction of nickel and copper ions in aqueous and nonaqueous media - controllable chemistry leading to nanoscale metal and metal boride particles. *Langmuir* **1994**, *10*, 4726-4730.

(2) Legrand, J.; Taleb, A.; Gota, S.; Guittet, M. J.; Petit, C. Synthesis and XPS characterization of nickel boride nanoparticles. *Langmuir* **2002**, *18*, 4131-4137.

(3) Floriano, P. N.; Noble, C. O.; Schoonmaker, J. M.; Poliakoff, E. D.; McCarley, R. L. Cu(0) nanoclusters derived from poly(propylene imine) dendrimer complexes of Cu(II). *J. Am. Chem. Soc.* **2001**, *123*, 10545-10553.

APPENDIX

X-RAY DIFFRACTOGRAMS (XRD) FOR Fe_2O_3/SiO_2

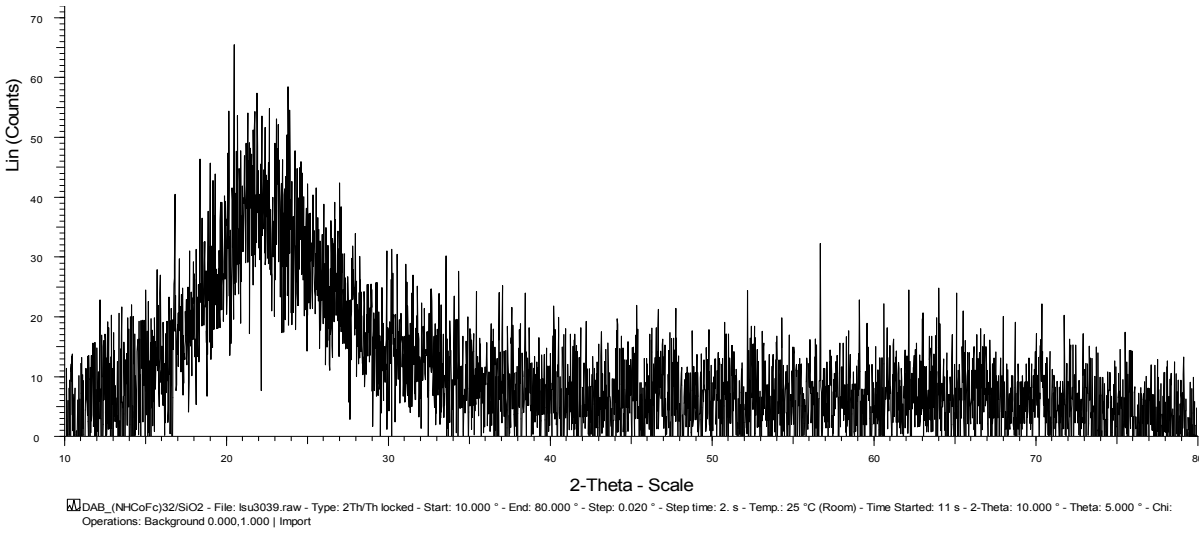

Figure A.1 XRD pattern for Fe_2O_3FD/SiO_2 obtained by calcination of DAB-$(NHCOFc)_{32}/SiO_2$ at 450 °C for 4 h.

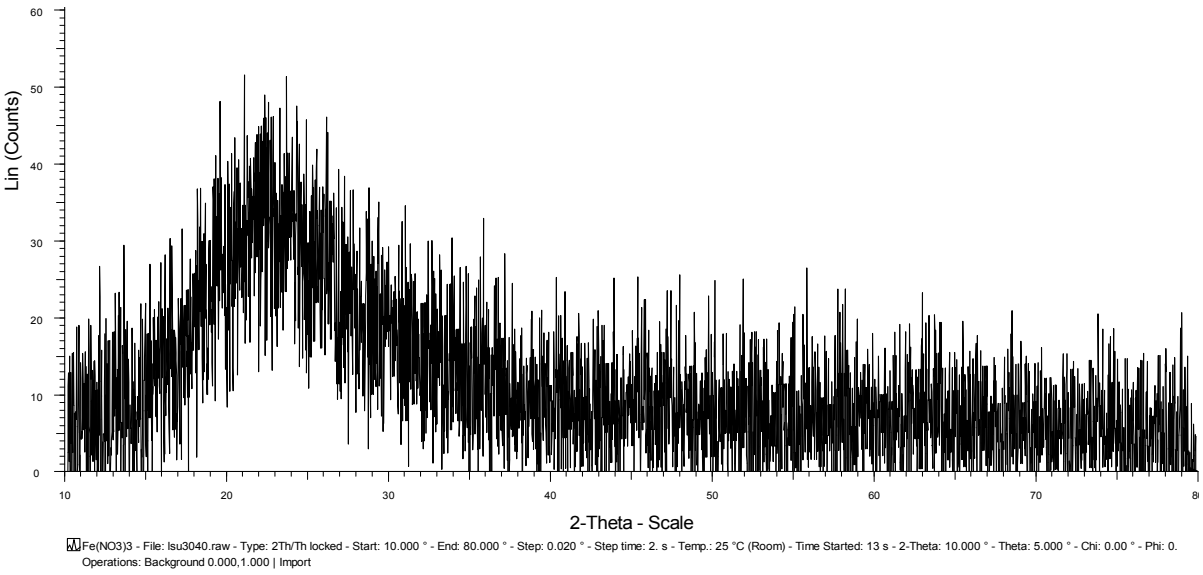

Figure A.2 XRD pattern for Fe_2O_3IN/SiO_2 obtained by calcination of $Fe(NO_3)_3/SiO_2$ at 450 °C for 4 h.

VITA

Elisabeta Mitran was born in Romania. She received her Bachelor of Science degree in chemistry from the University of Bucharest in 1995 and master's degree from the same university in 1997. After graduation, she worked as a research chemist at The National Research and Development Institute for Industrial Ecology, Department of Air Pollution (ECOIND) in Bucharest, Romania, until 2004, where she had the opportunity to work with very talented people and learn how to do quality research. She came to the United States in the fall of 2004 and enrolled in the doctoral program in the Department of Chemistry at Louisiana State University where she joined the research group of Dr. Robin L. McCarley. The degree of Doctor of Philosophy will be conferred at the Spring 2010 Commencement.